High-Resolution X-ray Diffraction Imaging using Ptychography

Isaac Russell Peterson

Submitted in total fulfilment
of the requirements of the degree of
Doctor of Philosophy

March, 2015

School of Physics,
The University of Melbourne

Abstract

Coherent Diffractive Imaging (CDI) is a promising form of X-ray microscopy that delivers high resolution imaging without the limitations imposed by an image-forming optic. Instead the image is recovered from diffraction data using computational techniques with foundations in crystallography. The important distinction is that CDI can be performed on non-crystalline samples. This has major implications in both biological and material sciences as many samples of interest cannot be formed into crystals and are therefore not accessible to conventional crystallographic analysis. Unfortunately these advances are accompanied by limitations on the useable sample size and a number of convergence issues in the image retrieval algorithms. These issues have been largely addressed by ptychography, a recent development of CDI that uses large datasets acquired by translating the target sample through the illuminating probe. Importantly, the technique allows non-crystalline samples to be imaged over an extended field of view, with the additional benefit of resolving a number of the convergence issues encountered in CDI.

This thesis proposes a number of modifications to the ptychographic algorithm that extend and improve its use in high-resolution X-ray imaging. These include the use of ptychography in conjunction with computed tomography, a new method for using additional ptychographic data obtained by scanning the target sample through multiple illuminating probes, an algorithm that can iteratively correct for sample scanning trajectory errors during the sample image construction, and an algorithm that can iteratively characterise and correct for partial spatial coherence in a high flux ptychographic dataset, enabling high-resolution sample image reconstruction using high-flux X-ray data. The proposed algorithms are tested using synchrotron X-ray data and shown to yield significant improvements in the reconstructed sample image compared to the results obtained using a standard ptychographic algorithm.

Declaration

This is to certify that:

i. The thesis comprises only my original work towards the PhD except where indicated.

ii. Due acknowledgement has been made in the text to all other material used.

iii. The thesis is fewer than 100 000 words in length, exclusive of tables, maps, bibliographies and appendices.

_____

Acknowledgments

The work in this thesis was conducted with the support and assistance of the ARC Centre of Excellence in Coherent X-ray Science (CXS). I would particularly like to express thanks and recognition to my three supervisors, Prof. Keith Nugent, A/Prof Harry Quiney and Prof. Ian Robinson. I also acknowledge the support from collaborators at the Advanced Photon Source in Chicago, in particular to David Vine, Ian McNulty and Ross Harder.

The author acknowledges the receipt of a Melbourne Research Scholarship, support from the Australian Research Council Centre of Excellence for Coherent X-ray Science, as well as travel funding provided by the International Synchrotron Access Program (ISAP), managed by the Australian Synchrotron and funded by the Australian Government. Use of the Advanced Photon Source was supported by the U.S. Department of Energy, Office of Science, and Office of Basic Energy Sciences, under Contract No. DE-AC02-06CH11357.

Statement Of Contributions

Throughout this thesis valuable guidance, advice, and support has been provided by my supervisors, Prof. Keith Nugent, A/Prof Harry Quiney and Prof. Ian Robinson. Both Prof. Keith Nugent and A/Prof Harry Quiney have also provided valuable guidance in the writing of this thesis.

Chapters $4-7$ use synchrotron X-ray data obtained at the Advanced Photon Source by myself in collaboration with a number of researchers. Ian McNulty, David Vine, and Ross Harder of the Advanced Photon Source provided their valuable time and experience in these experiments. Collaborators from the Australian Research Council (ARC) Centre of Excellence for Coherent X-ray Science (CXS) groups at the University of Melbourne and La Trobe University, as well as the London Centre for Nanotechnology have provided support during X-ray data collection and sample preparation. These collaborators are duly noted as authors on the subsequent publications "Nanoscale Fresnel coherent diffraction imaging tomography using ptychography", "Translation position determination in ptychographic coherent diffraction imaging", and "Quantitative X-ray wavefront measurements of Fresnel zone plate and K-B mirrors using phase retrieval". The data used in Appendix B was obtained at the SPring-8 source in Japan by myself, Brian Abbey, Rebecca Ryan and A/Prof. Andrew Peele. The source code used in the data analysis, processing, and phase retrieval was my own except where specified.

CONTENTS

LIST OF FIGURES

CHAPTER

ONE

INTRODUCTION

"Where the telescope ends, the microscope begins. Which of the two has the grander view?"

- Victor Hugo

1.1 Background

Research across a broad range of sciences including molecular biology, pharmacology, material science and nanotechnology has continued to drive the improvement of the resolution and contrast of a wide array of imaging techniques including X-ray and electron microscopy. This progression has resulted in imaging techniques capable of resolving mesoscopic-scale structures, such as cellular organelles and nanoparticles. The characteristic size of systems in this scale range from approximately 100 nm (the size of a typical virus or nano-particle) to 1 μm (the size of a typical bacterium) and play a key role in understanding the connection between macroscopic properties and atomic structures. Knowledge of their function and structural configuration requires detailed analysis of the internal sample structure at nanoscale or ideally at atom-scale resolution. Imaging at this scale lies beyond the limitations imposed by the diffraction limit of visible light, requiring X-rays, or the even shorter wavelengths associated with electrons in order to access this information.

At present, atom-scale resolution is only attainable using electron and X-ray crystallographic techniques developed throughout the 20^{th} century. These techniques illuminate a crystal lattice and can provide atom-scale information using recorded diffraction patterns. The structural information obtained using crystallography has proven critical in understanding many material and biological systems,

in particular protein structures, but is restricted by the availability of crystalline samples. This has continued to drive the rapid and continual growth of sample crystallisation procedures as well as ever brighter and correspondingly ever more coherent sources. These include the aforementioned third generation synchrotron sources and fourth generation X-ray free electron laser (XFEL) facilities. Unfortunately many biological samples, in particular many membrane proteins, either undergo structural damage during the crystallisation process, or cannot be formed into sufficiently large crystals, rendering crystallographic techniques unusable.

Coherent Diffractive Imaging (CDI), a diffraction-based imaging technique under intensive development in the past decade, possesses the required resolution and contrast for nanoscale imaging and promises to deliver atom-scale imaging for non-periodic samples. Critically there is no requirement for sample crystallisation and no restrictions imposed by an objective lens on the achievable resolution. Instead the sample image is obtained from diffraction data using computational techniques with their origins in crystallography. For biological materials the ability to record high angle scatter is limited by radiation damage. However, it has been demonstrated [2] that if the sample is exposed to a sufficiently rapid and intense pulse (e.g. the pulse from an X-ray free-electron laser), the scattered wave can exit the target sample before significant structural damage occurs. Under these circumstances atom-scale resolution imaging for non-crystalline samples is a real possibility, allowing access to previously unexplored structural information in both material samples and biomolecules. Though much work remains to be completed, this area is currently under intensive development as access to this information would revolutionise material science, molecular biology and medical research.

Reconstructing a scattering sample from a single diffraction image imposes a strict limitation on the useable sample size, and can lead to a number of convergence issues in the reconstruction algorithms. These issues have been largely solved by ptychography, a recent development of CDI, and the focus of this thesis. It has recently been applied using X-rays to image non-crystalline material and biological samples over an extended field of view [3, 4, 5]. The ability to obtain nanoscale images of a broad range of non-crystalline samples, without resorting to sample sectioning, addresses a number of the short comings in several competing techniques including Scanning Electron Microscopy (SEM) and Scanning X-ray Transmission Microscopy. As in CDI, X-ray ptychography requires a highly coherent and sufficiently brilliant X-ray source. The historical developments that have led to the advent of ultra brilliant X-ray sources including third generation synchrotrons and the X-ray free electron laser are now briefly overviewed. The discussion includes an

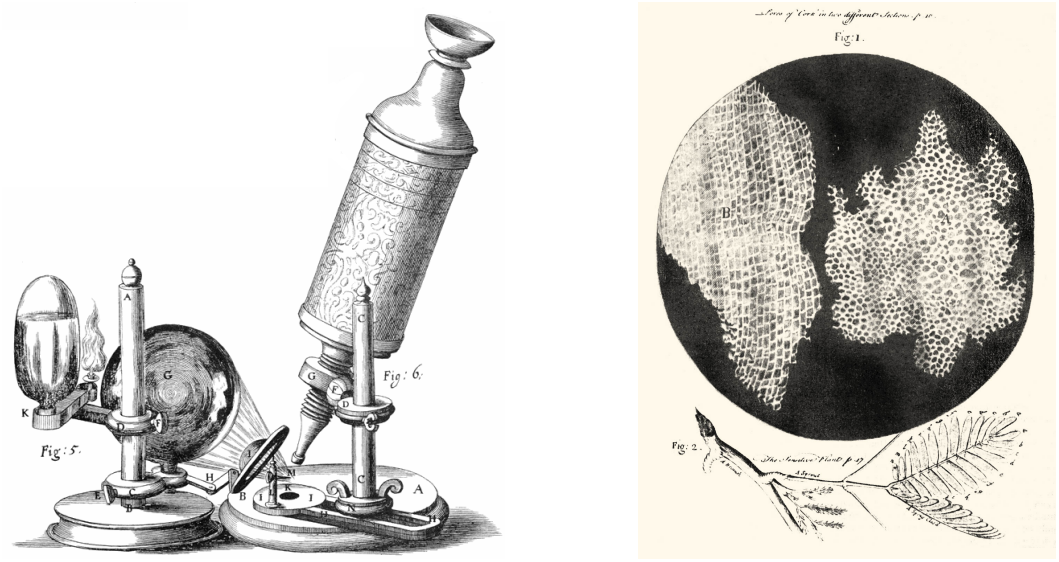

(a) (b)

Figure 1.1: With the advent of the optical microscope in (a), Hooke observed the repeated "cell" structure in a magnified cork section in (b). Image reprinted from [7].

overview of high resolution imaging techniques that either relate to or compete with the ptychographic CDI methods explored in this thesis.

1.2 Microscopy

Modern light microscopy traces its roots back to the 10^{th} century, when Arabic opticians discovered the foundations of modern physical optics. In particular, the law of refraction was first accurately described as early as 984 in Ibn Sahl's treatise *On Burning Mirrors and Lenses* [6]. These ideas were developed in the 12^{th} century by Francis Bacon, who studied the optical properties of lenses and mirrors, in particular the effects of lenses in combination. It was not until the latter part of the 16^{th} century that the first microscope, (a single lens and sample plate arrangement) was invented. Shortly afterwards an eyepiece or *ocular* lens was used in conjunction with a secondary *objective* lens positioned near the sample, producing the first compound microscope.

Hooke, using convex lenses with short focal lengths, significantly improved upon the available magnification and resolution of the compound microscope, producing a microscope strikingly similar to its modern counterpart in widespread use today. The subsequent discoveries by Hooke in his seminal work *Micrographia* [7], in particular the first published depiction of a microorganism (the microfungus *Mucor*), revolutionised thinking in medicine, biology and the material sciences. Later

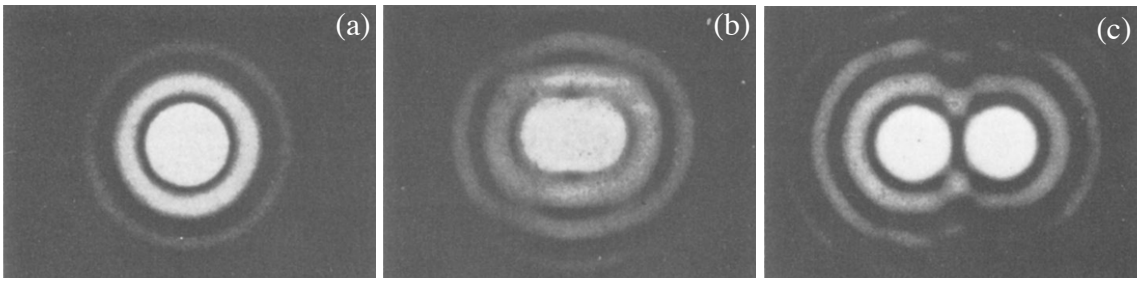

Figure 1.2: Two monochromatic point sources focused by an objective lens. (a) The sources are spaced too close to resolve. (b) The sources are at an angular separation satisfying the Rayleigh criterion - i.e. the first minimum of each disk overlaps the central maximum of the other. (c) The sources are spaced sufficiently wide to easily resolve.

work by Leeuwenhoek observed and described microscopic protozoa and bacteria. Leeuwenhoek was also the first to record microscopic observations of muscle fibres, bacteria, spermatozoa and capillary blood flow.

Among the most important subsequent medical advances was the discovery of *Mycobacterium tuberculosis*, the bacterium that causes tuberculosis [8]. This led shortly afterwards to the discovery of the *Mycobacterium tuberculosis* vaccine [9], a groundbreaking step in medical research. Along with mechanical improvements, a series of new sample preparation techniques were later developed to enhance the view of the sample, leading to higher quality images of the system under study. The progression and refinement of visible light microscopy led to the eventual development of complex lens arrangements with the ability to resolve features as small as 250 nm within a compact instrument, a resolving power $\sim 20,000$ times greater than the first compound microscope.

In all optical systems there is a limit beyond which additional magnification and improvements in the lens quality ceases to improve resolution and instead simply enlarges features without resolving them. The diffraction limit is a consequence of the wave nature of light and may be described as the smallest distance at which two distinct features can be resolved before the system fails to identify them as individual objects [10]. The resolution of an imaging system can be determined by considering the overlapping Airy disks from two point sources. The Rayleigh criterion [10] defines the resolution limit as the point where the central maximum of each disk lies above the first minimum of the other (as shown in Fig. 1.2).

For a microscope with objective focal length f and lens diameter d, the spatial resolution is determined using the Rayleigh criterion

$$\Delta l = \frac{1.22 f \lambda}{d}, \tag{1.1}$$

where λ is the illumination wavelength. The "1.22" factor is derived from the first zero of a Bessel function of the first kind, of order one and relates to the first minimum surrounding the central Airy disc. An alternate formulation suggested by Abbé [10] relates the diffraction limited resolution from the Rayleigh criterion to the angle subtended by an objective lens as

$$\begin{aligned} \Delta &= \frac{0.61\lambda}{n \sin\theta} \\ &= \frac{0.61\lambda}{\mathrm{NA}}, \end{aligned} \tag{1.2}$$

where Δ is the achievable resolution, n is the refractive index of the medium, θ is half the angle subtended by the lens and $\mathrm{NA} = n \sin\theta$ is the numerical aperture of the lens.

The Abbé criterion in Eq. 1.2 strictly limits the achievable resolution in conventional light microscopy. As a result, a precise wide-field microscope with high numerical aperture can achieve a resolution of $\sim$ 250 nm using visible light. Recent emerging techniques, known collectively as "super-resolution light microscopy", have overcome the diffraction barrier using fluorophores, a fluorescent chemical compound that absorbs light energy of a specific wavelength and re-emits light at a longer wavelength. In conventional fluorescence microscopy all the fluorophores in the sample are fluorescent, their diffraction limited images overlap, creating a smooth but blurred picture. This issue has been addressed using super-resolution techniques such as Stochastic Optical Reconstruction Microscopy (STORM) [11], which activates distinct fluorophore molecular states to obtain the temporal discrimination of objects that are otherwise unresolved or blurred within the spatial resolution of the microscope. This is achieved through fluorescent probes that can switch between fluorescent and dark states, such that only a small, optically resolvable fraction of the fluorophores is detected in every "snap-shot". A final super-resolution image can be reconstructed from the accumulated positions in a series of these snap-shots. These advances have resulted in spatial resolutions as high as $\sim$ 20 nm using visible light, a remarkable achievement. The requirement for fluorophores unfortunately introduces highly complicated staining procedures, an issue that has been addressed by recent advances in label free localisation microscopy using Spectral Precision Distance Microscopy (SPDM) [12, 13]. This technique has achieved optical resolutions of cellular structures in the range of approximately 50 nm. Though these super-resolution techniques represent major advances in light microscopy, they are limited to nanoscale studies of optically thin samples. Studying structures with atom-scale precision requires the use of shorter wavelength probe particles such as electrons and

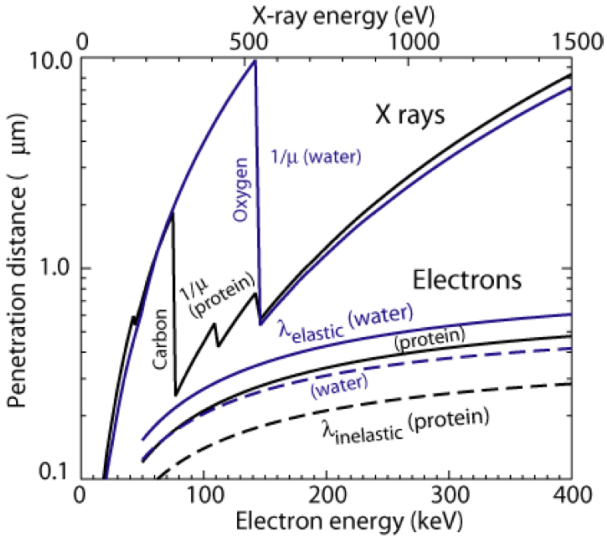

Figure 1.3: Penetration distance of X-rays and electrons for water and proteins. The "water window" lies between the K absorption edges of carbon (285 eV) and oxygen (543 eV), providing high contrast between water and proteins. Image reprinted from Kirz *et al.* [14]

X-rays, where the penetrating power of the latter probe particle provides access to internal sample structures without the need for invasive sample sectioning.

The discovery of X-rays and the subsequent extension of optical microscope techniques to X-ray wavelengths throughout the mid to late 20^{th} century led to the entirely new field of X-ray microscopy. In addition to exploiting the increased resolution associated with shorter X-ray wavelengths ($\sim$ Å), the correspondence between X-ray photon energies and electron shell energies provides access to a natural spectroscopic probe. These energies range from soft X-rays (250 eV $-$ 1.8 keV) to the hard X-ray regime (8 keV $-$ 100 keV). Soft X-rays are particularly suitable when imaging biological samples as they exhibit high intrinsic contrast between water and proteins in the "water window" (see Fig. 1.3). This is an energy band between the K-edges (a sudden increase in the attenuation coefficient of photons occurring at a photon energy just above the binding energy of the K-shell electrons) of carbon (285 eV) and oxygen (543 eV). The available contrast in this energy band allows imaging of biological samples in their natural state without the need for disruptive sample preparation.

The two main X-ray microscopy techniques currently in use are Scanning Transmission X-ray Microscopy (STXM) [15] and full-field Transmission X-ray Microscopy (TXM) [16]. While the principles of these techniques have remained unchanged since their introduction, their constituent elements including the source, optics, stages and detectors have undergone revolutionary advancements over the last few

decades. STXM imaging scans a finely focused X-ray beam across the sample using a two-dimensional raster grid scanning trajectory, recording an absorption contrast map. The resolution of the technique is limited by the spot size that can be produced by the X-ray focusing optics. Using a Fresnel zone plate (FZP) Chao *et al.* achieved a spot size of approximately 15 nm [17] at 815 eV, i.e. within the soft X-ray regime. Additional information can be extracted from the STXM setup by using an additional energy resolving detector to measure the fluorescence signal of the illuminated spot. The use of Kirkpatrick-Baez (KB) mirrors as the focusing mechanism has realised a spot size of 7 nm [18].

Full field Transmission X-ray Microscopy uses both a condenser to illuminate the sample and a secondary objective X-ray lens. The objective is usually a Fresnel zone plate owing to its high angular acceptance (KB mirrors are not suitable for this purpose due to their low acceptance angle and large off-axis aberrations). To date the best resolution achieved by soft X-ray TXM is approximately 12 nm [17, 19]. The achievable resolution of these techniques is governed by the limitations in the manufacture of the focusing optics, in both the achievable width of the outermost zone and the effective absorption in the opaque zones. Advances in focused ion beam and electron beam lithography have enabled the manufacture of zone plates with an outermost zone width $\sim$ 10nm. Despite the revolutionary advancements in their constituent optical elements, the achievable resolutions ($\sim$ 10 nm) for both STXM and TXM are approximately an order of magnitude greater than the wavelength of the X-rays used. It appears unlikely that either STXM or TXM will achieve Angstrom resolution.

The explosive growth in X-ray and electron science during the twentieth century also led to the development of Transmission Electron Microscopy (TEM) [20, 21, 22] and Scanning Electron Microscopy (SEM). The extremely short electron wavelength and corresponding improvement in the achievable resolution has resulted in many insights into nanoscale and atom-scale structures. In scanning electron microscopy an electron beam is scanned across the target sample, forming images from the elastically and inelastically scattered electrons as well as from photon emission. Though this can provide extremely rich nanoscale surface detail, the technique is surface limited as the images are formed from scattered electrons rather than transmitted electrons. The internal structures are consequentially not visible using SEM. This detail can sometimes be attained through Transmission Electron Microscopy, though due to the adverse effect of multiple electron scattering in the target sample, the process is limited to very thin samples ($<$ 100 nm). Transmission electron microscopes commonly operate at 100 kV, with an associated electron wavelength

of 3.7 pm - three orders of magnitude smaller than soft X-ray wavelengths and sufficiently small to attain atomic information. Imaging of internal biological structures through TEM requires sample sectioning and corresponding preparation including chemical fixation using formaldehyde and gluteraldehyde, staining with heavy elements such as uranium salts and sample dehydration using successively greater concentrations of acetone. This is a time consuming and structurally disruptive process with particular implications for biology as the process prevents the possibility of imaging live cells or even undisturbed cells. Nonetheless, the technique has provided many insights in structural biology, primarily due to the short wavelength and strong Coulomb interaction associated with electrons.

The imaging methods discussed thus far use an arrangement of lenses in which the image obtained requires very little processing and is indicative of the target sample. Although X-ray imaging offers sample penetration and has sufficiently short wavelengths for the study of nanoscale and atom scale structures, the achievable resolution is fundamentally limited by the X-ray optics rather than the wavelength. These limitations are bypassed in X-ray crystallography by removing the objective lens altogether, relying instead on a periodic lattice of scattering centres to massively amplify and coherently reinforce weak scatter into a useable Bragg diffraction signal. Inversion of the collected diffraction data reproduces an average estimate of the unit cell through the solution of the crystallographic "phase problem". This process circumvents the weak sample scattering problem (a particular issue for biological samples), enabling high resolution imaging with sufficiently low radiation dose for imaging biological materials. These techniques remain the primary access to molecular and atom-scale structural information. Their refinement has progressed with the advent of ultra bright, highly coherent X-ray light sources including third generation synchrotron and fourth generation X-ray free electron (XFEL) sources. The result is the routine application of crystallography to atom-scale imaging of many material and bio-molecules, in particular proteins. Unfortunately many material science and biologically important samples (e.g. membrane proteins), either undergo structural damage during the crystallisation process, or obstinately refuse to crystallise at all. Without sufficient amplification of the sample scatter the Bragg diffraction signal is too weak for crystallographic techniques to be useable.

1.3 Coherent Diffractive Imaging

The possibility of combining the penetrating power of coherent X-rays with the resolution and contrast of crystallographic techniques was first suggested by Sayre

in 1952 [23]. It was noted that the diffraction data resulting from a finite non-periodic object illuminated by a fully coherent wave might be used to reconstruct the sample image. Rather than directly imaging a sample, the method relies on the Fourier relationship between a coherent wave exiting a scattering object and its far-field diffracted wave. The wavefield is iteratively reconstructed from the diffraction intensity through the application of *a priori* information. Applying ideas from information theory, Sayre identified the critical role played by sampling the diffraction data at twice the Nyquist frequency [23], where the Nyquist frequency is the sampling rate required in conventional crystallography. This study concluded that if this condition is satisfied and the scattering sample extent is known, the wavefield phase may be retrieved from diffraction intensity data. These ideas form the basis for Coherent Diffractive Imaging [23, 24] (CDI), a lensless imaging technique that provides the contrast and resolution necessary for nanoscale X-ray imaging.

1.3.1 Phase Retrieval Algorithms

The simplest phase retrieval technique using diffraction data was introduced by Gerchberg and Saxton [25] for applications in electron microscopy. This pioneering study demonstrated an iterative method to retrieve the phase of a wave function from simultaneous measurement of the intensity in the sample and far-field diffraction planes. The study also suggested the extension of this method to X-ray crystallography, but the technical difficulties involved in performing a measurement in the sample plane limited the application.

This problem was addressed by Fienup [26], who lifted the restriction on measurement in the sample plane, requiring only measurement of the diffraction data. The routine, known as "Error Reduction" or "ER", involved the sequential application of constraints to the current estimate of the wavefield in the detector and sample planes. These constraints are consistency with the measured intensity or "modulus" and knowledge of the object extent or "support". The latter constraint is enforced by setting the wavefield outside a region known to contain the sample to zero. Fienup found that the process was sufficiently robust to noise to converge on a solution to within experimental error. If the iterate lies within the basin of attraction of the global error minimum, i.e. a set of initial conditions leading to long-time behaviour that approaches the global minimum, ER generally exhibits quadratic convergence characteristics. Though these findings were promising, the method was initially plagued by non-unique solutions and points where the solution trajectory "stagnated" in a local (false) minima. In the context of phase retrieval this may occur when the current wavefield estimate obeys one of the iterative constraints (e.g.

the modulus constraint), yet violates the other (e.g. the support constraint). ER was later shown to be a method of "steepest descents" [27], an iterative technique known to be prone to stagnation in local minima. Despite the tendency towards iterative stagnation, the ER algorithm retains widespread use as a highly useful tool in CDI, frequently used in conjunction with the phase retrieval algorithms detailed below.

The stagnation and slow convergence issues of the ER algorithm led Fienup to combine phase retrieval techniques with control theory, developing a class of feedback algorithm that used the current estimate of the wavefield in conjunction with output from the previous iteration. Known as the Basic Input-Output (BIO) [28] and the Hybrid Input-Output (HIO) [29] algorithms, they are essentially the ER algorithm with an added feedback loop such that output from the previous iteration is included with the current iteration to produce each successive iterate. The HIO algorithm as originally formulated applies strictly only to a support constraint (with positivity), together with the Fourier modulus constraint. These restrictions were lifted somewhat with the HIO generalisation developed by Millane [30]. HIO has been shown to be associated with conjugate gradient optimisation [31], providing a phase retrieval imaging method that can avoid stagnation, resulting in improved accuracy and robustness in the sample image retrieval when combined with ER.

Marchesini *et al.* later made an important modification to the support constraint known as "shrink-wrap" [32]. Rather than supplying *a priori* information about the object extent, the support constraint is dynamically updated by iteratively thresholding the current estimate of the wavefield in the sample plane. Recent iterative algorithms based around the original ideas proposed by Gerchberg and Saxton include Difference Map (DM), Relaxed Averaged Alternating Reflections (RAAR) and saddle-point optimisation [33]. A summary of modern phase retrieval techniques is provided in the review by Marchesini [31], comparing iterative projection methods with conventional non-linear optimisation techniques.

1.3.2 Experimental Coherent X-ray Diffractive Imaging

The geometrical arrangement for a CDI experiment shown in Fig. 1.4. In this arrangement a coherent plane wave illuminates a target sample and the resulting far-field diffraction intensity patterns are recorded on a detector with a sufficiently fine sampling grid. When the scattering signal is small compared to the direct X-ray beam (as is the case for biological samples), a beamstop is used to prevent damage to the detector. This consequently blocks the low frequency diffraction data associated with sample shape information, making the sample phase retrieval significantly more

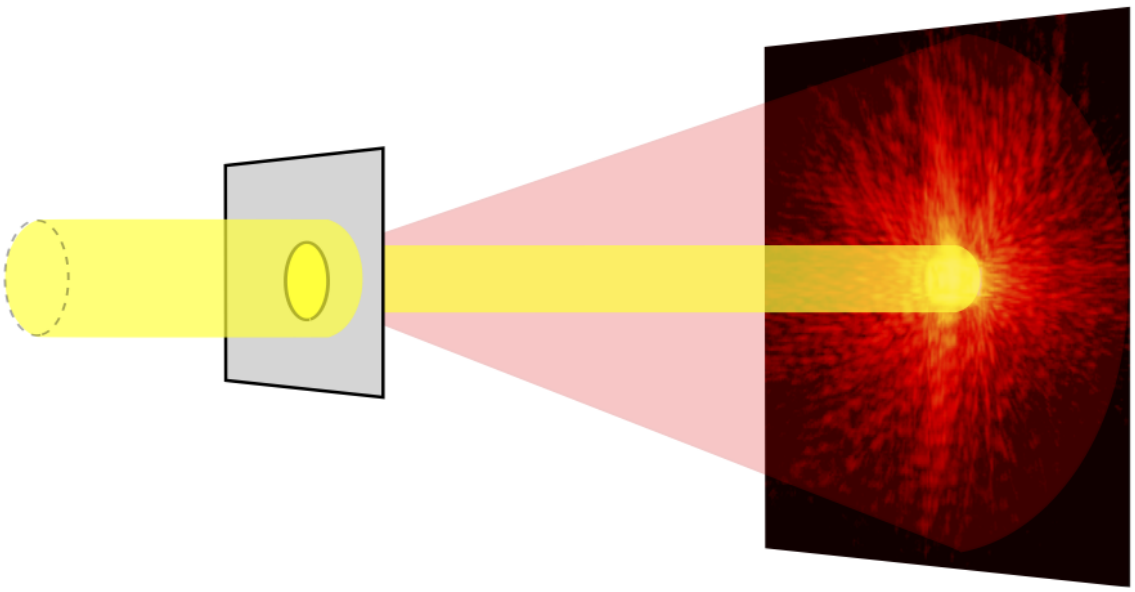

Figure 1.4: Experimental coherent diffractive imaging. Coherent plane wave X-rays illuminate a sample and the resulting diffraction intensity is recorded by a detector placed in the far-field. The direct beam (yellow) is usually blocked by a beamstop to avoid damage to the detector.

difficult to achieve.

The first application of CDI phase-retrieval methods to X-ray diffraction data from a non-crystalline sample was performed by Miao *et al.* [24, 34], who applied iterative electron microscopy algorithms to Sayre's ideas on oversampling to successfully reconstruct patterned groupings of gold nanoscale dots (shown in Fig. 1.5). This highly influential work successfully demonstrated a diffractive imaging technique for non-crystalline samples, performed without an objective lens, and may be regarded as the ignition point for the subsequent development of CDI. The experiment used a beamstop to block the direct beam, resulting in a missing central region in the diffraction data. This was addressed by splicing in synthesised data generated from an optical image of the sample. Provided a sufficiently small number of pixels are lost due to the beamstop, current methods account for the data loss by allowing the algorithm to estimate the low spatial frequency information, making the use of supplementary data unnecessary. This is possible only when the over-sampling rate is significantly in excess of the critical oversampling rate defined by Bates [35]. These and other ideas on restoration of lower frequency information were explored in later work [36]. Miao later demonstrated the ability to retrieve structured, layered, and amorphous samples using CDI [37], with the important distinction that the information could be obtained without resorting to sample sectioning.

CDI was first used to obtain images of a biological sample by Miao, imaging

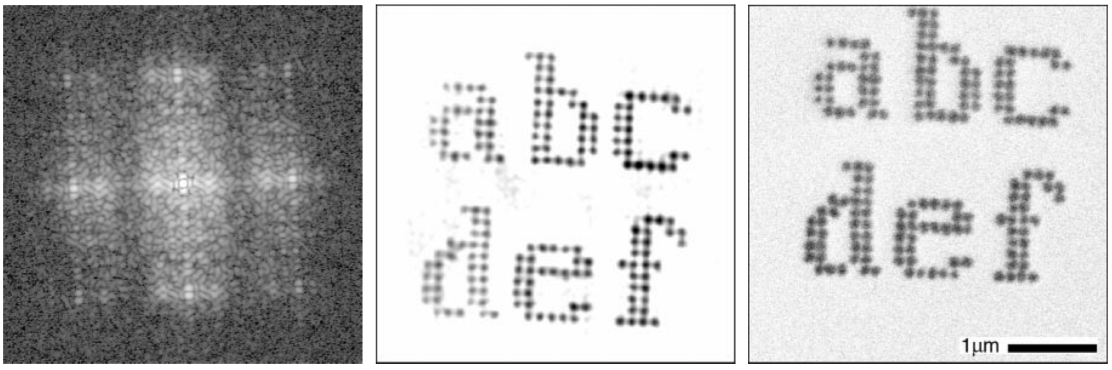

(a) (b) (c)

Figure 1.5: The first experimental demonstration of CDI. (a) shows an example sample diffraction image, with the resulting reconstructed sample image in (b). An SEM image of the sample in shown in (c). Image reprinted from [24].

E. coli bacteria at 30 nm [38] resolution. Subsequent work included imaging a freeze-dried yeast cell [36, 39], quantitative imaging of a freeze dried bacterium [40], demonstrations of frozen hydrated biological samples with a yeast cell [41] and bacteria [42], as well as three-dimensional mappings of an unstained human chromosome at 120 nm resolution [43]. The ability to obtain detailed high resolution images of the internal structures of biological samples without the need for staining or dehydration is an important distinction, as it allows biological samples to be imaged close to their natural state. CDI can reveal sample structure by elemental specific contrast imaging near absorption edges. The structure of biological samples is related to the location of carbon-heavy proteins surrounded by oxygen-heavy water molecules. Water-window energies are therefore particularly suitable to CDI of biological samples. Studies in this area include soft X-ray imaging of yeast cells [41], and diatoms [44].

Early CDI results on two-dimensional crystalline samples were obtained by Vartanyants *et al.* using the beam coherence characteristics to reconstruct the surface morphology of the Si(111) crystal surface [45]. Other notable work includes that by Robinson *et al.* [46, 47] and Vartanyants *et al.* [48], who applied CDI to the detailed characterisation of nanocrystalline samples. In these experiments the diffracted intensity is recorded about a Bragg diffraction peak, requiring the detector to be placed at the Bragg angle characteristic to the crystalline sample under study. The diffracted intensity distribution can be used in conjunction with CDI algorithms to retrieve structural information on the nanocrystal sample. In later work, Williams *et al.* extended this two-dimensional technique to obtain three-dimensional images of gold nano-crystals [49]. In addition to providing information on the crystal size and shape, Bragg CDI has been used to map the crystal strain (defects and dislocations

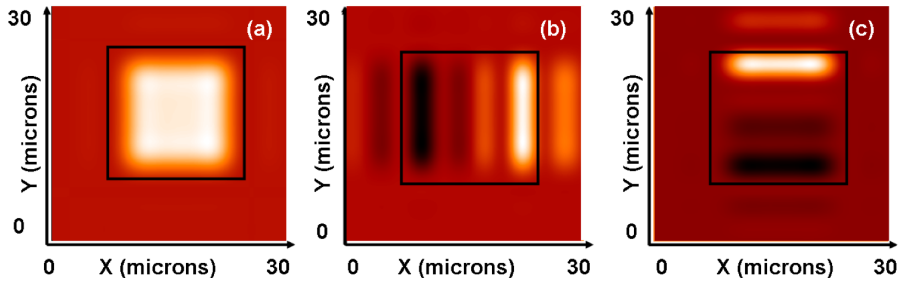

Figure 1.6: The three modes required to adequately account for partial coherence at APS endstation 2-ID-B. Image reprinted from [1].

in the crystal lattice) [50]. The ability to extract this detailed structural information from diffraction data has established Bragg CDI as an important imaging tool.

1.3.3 Partially Coherent CDI

The effect of partial spatial coherence in CDI was discussed by Vartanyants *et al.* [48] and later by Spence *et al.* [51], who suggested that the success of phase retrieval algorithms requires the coherence length of the incident illumination to be at least twice the lateral dimensions of the target sample. A later study [52] placed a stricter requirement on the beam coherence properties, concluding that a small departure from full coherence is sufficient to formally render the scattered wave irretrievable from its diffraction data using any conventional iterative method based on coherent propagation. When the full coherence assumption is invalid the reconstructed object is unable to simultaneously satisfy both the modulus and support constraints. Depending on the level of partial coherence in the illuminating wavefield, the sample reconstruction may show significant artefacts including incorrect intensity fluctuation or a total failure to converge [52, 53]. This places a major restriction on the useable flux as third generation synchrotron sources are inherently partially coherent sources with full spatial and temporal coherence at the sample plane achieved at the expense of discarding over 99% of the available radiated flux.

Partially coherent wavefields can be accounted for in CDI by incorporating a series of coherent modes into the phase retrieval scheme [53, 1]. This first requires a modal decomposition of the incident wavefront into mutually orthogonal modes that interact with the sample and are propagated independently. An example modal decomposition of a partial spatially coherent wavefield obtained at the 2-ID-B beam line at the Advanced Photon Source is shown in Fig. 1.6, where it was found that only three coherent modes contributed significantly to the modal expansion of the mutual optical intensity [1]. The first experimental demonstration of partially co-

herent diffractive imaging was performed by Whitehead *et al.* [53], who successfully reconstructed a gold test pattern illuminated by a partial spatially coherent incident wavefront assumed to have a Gaussian coherence function. CDI algorithms, with the inherent assumption of a spatially coherent illumination, were shown to be unable to produce reconstruction images of comparable quality. The method also demonstrated superior results compared to CDI for data that would normally be considered fully spatially coherent. The modal decomposition method has also proved effective for temporally coherent sources [54], where the modes can be used to sufficiently sample the frequencies in a broadband source. This study achieved a reduction in exposure times by a factor of 60 [54]. These algorithms extend CDI to both spatially and temporally partially coherent sources, allowing CDI to be performed under a broader range of experimental conditions. In particular the useable flux is significantly increased, enabling a significant reduction in the data acquisition times.

1.3.4 Fresnel CDI

Despite continual development and improvement, plane-wave CDI is affected by a range of convergence issues related to reflection and translation ambiguities in the phase retrieval schemes. Nugent *et al.* [55, 56] demonstrated that these ambiguities could be removed by using an illumination with known curvature. This exploratory study used astigmatic diffraction from a cylindrical wavefront, requiring two data sets with orthogonal cylindrical phase curvatures in addition to the original plane wave dataset. This also removed the need for any *a priori* information about the sample extent. Rather than the Fraunhofer diffraction associated with plane wave illumination [10], curved illumination propagates according to Fresnel theory. Using three data sets to perform these measurements is somewhat cumbersome, as the geometric parameters and separate illuminations must be highly characterised. Nonetheless, the ideas and algorithmic implementation proposed by Nugent *et al.* demonstrated rapid and consistent conversion in the algorithms, providing promising results for a new imaging technique. The method was later optimised by Quiney *et al.* [57], who discussed the application of a Fresnel zone plate to produce a spherical wavefront with sufficient phase curvature.

The technique proposed by Quiney *et al.* (known as Fresnel CDI or FCDI) requires detailed characterisation of the illumination phase. This is obtained using a separate measurement of the illumination intensity. Recovery of the illumination phase proceeds in a similar fashion to ER, using the Fresnel free space propagator rather than the Fraunhofer propagator associated with plane wave propagation, and

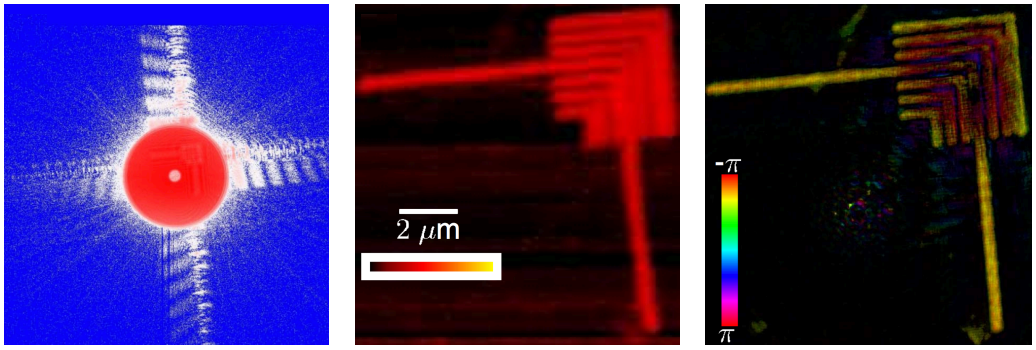

(a) (b) (c)

Figure 1.7: The first demonstration of experimental Fresnel CDI. (a) shows an example data frame from a nested chevron target sample. The reconstructed sample transmission phase is shown in (b), with a STXM image provided for comparison in (c). Image reprinted from [59].

with the additional requirement of a three-plane propagation through the pupil, focus and detector planes. The finite support is enforced in the focusing optic, or "pupil" plane, where the extent of the illumination is well characterised. In subsequent work [58] Quiney *et al.* reconstructed the illumination at the focus of a Fresnel zone plate. This work demonstrated an accelerated convergence of the iterative algorithms compared to plane wave illumination while operating under the assumptions of fully coherent illumination and a finite support. Fresnel CDI was later shown to demonstrate greater robustness to partial coherence when compared to plane wave illumination [52, 53].

The first experimental demonstration of Fresnel CDI was performed by Williams *et al.* [59], achieving a resolution of 24 nm. In this study a nested group of chevrons (shown in Fig. 1.7) was placed approximately 1 mm downstream of the zone plate focus, resulting in a flux density an order of magnitude greater than the equivalent plane wave experiment. The reconstructed transmission function is shown in Fig. 1.7, demonstrating a strong qualitative agreement with the STXM image. It was later shown that Fresnel CDI can yield a quantitative estimate of the sample transmission function [60]. As a demonstration, the thickness of a series of gold nano-structures was determined to within an accuracy of 10%, at a spatial resolution of 50 nm. Incorporating iterative transmission function constraints led to further quantitative and qualitative improvements in the sample image reconstruction [61]. The technique has also been applied to biological samples including *plasmodium falciparum*-infected red blood cells [62]. Aside from a high sensitivity to sample drift, Fresnel CDI has proven to be a robust method for recovering high-resolution, quantitative images of the target sample.

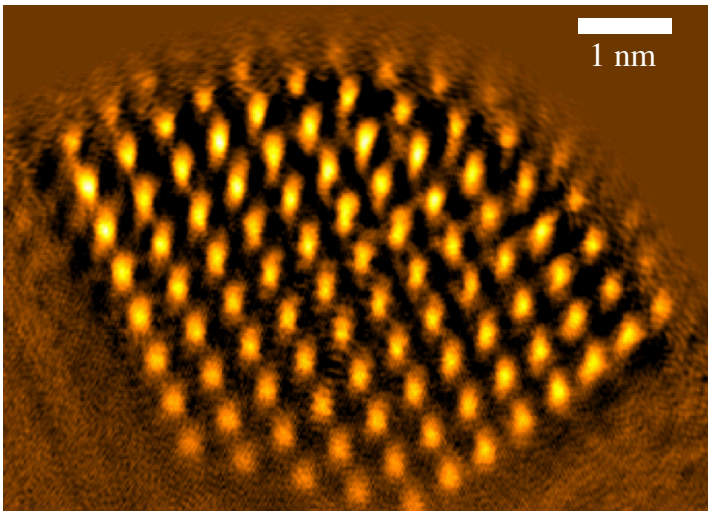

Figure 1.8: Ptychographic reconstruction of a cerium dioxide nanoparticle specimen at atomic resolution using an aberration-corrected electron microscope. Image reprinted from [70].

1.4 Ptychography

"Ptychography" (derived from the greek words "ptyché", meaning "fold", and "gráphein", meaning "to write"), was originally proposed by Hoppe [63] as a method to retrieve phase information using the coherent interference of adjacent Bragg reflections from a crystalline sample. In the original formulation, Hoppe suggested this could be achieved by placing an aperture in the specimen plane such that each reciprocal-lattice point would overlap and interfere with its neighbours. The method was later optimised for imaging non-periodic and extended scattering samples [64, 65, 66]. The current method involves step-wise translation of the target sample across a coherent, localised illuminating probe (sharing much in common with scanning microscopy). The resulting ptychographic dataset is used in conjunction with an extension of iterative phase retrieval algorithms to retrieve the complex sample transmission function and complex illuminating wavefield [3, 4, 40, 67, 68, 69].

Ptychography has seen much recent interest and development in the diffractive X-ray imaging community, primarily due to the fact that in addition to improved convergence characteristics compared to CDI, it removes the restriction on the permissible sample size enforced by the sampling requirements for single diffraction patterns, allowing extended samples to be imaged. The effective sample extent is defined through the use of an aperture placed upstream of the sample. The sample is scanned in steps small enough to ensure a sufficient probe overlap [71] and the resulting diffraction intensity is recorded for each sample translation. This provides a significant amount of data redundancy, resulting in improved convergence charac-

teristics in the iterative phase reconstruction compared to CDI. The technique has proven useful for imaging various material and biological [5, 40, 72] samples. As distinct from conventional scanning microscopy, the achievable spatial resolution in ptychography is not limited by the beam size and is ideally wavelength limited. Recent demonstrations with X-rays have achieved a spatial resolution of approximately 10 nm [73]. In an interesting development, ptychography was recently performed using electrons as the probe particle [70, 74, 75] (see Fig. 1.8). These exploratory studies have achieved atom-scale resolution for simple test samples, promising an atom-scale technique for non-crystalline biological and material samples.

1.5 Three-Dimensional CDI

Recent technical and computational advances have led to the development of three-dimensional nanoscale CDI using both biological [5] and material [49, 76] samples. Considering the exit surface wave as a projection through the sample [77], the diffraction data series may be assembled into a three-dimensional diffraction volume and determining the sample distribution using the three-dimensional implementation of standard phase retrieval algorithms such as ER or HIO [76]. This was first performed by Chapman *et al.* [76] on a 2 μm wide pyramidal arrangement of gold nano-spheres mounted on a silicon nitride window. The dataset was composed from approximately 120 projections taken at 1° rotation intervals. The edges of the silicon nitride window mount blocked approximately 30° of the available projections on either side of the available rotations. In addition to reconstructing the target sample (shown in Fig. 1.9) the study demonstrated the ability to retrieve the missing "wedge" of data. Subsequent three-dimensional CDI demonstrations in material science include work on gold and ceramic foams [78].

Alternately, the three-dimensional sample distribution may be retrieved by rotating the sample through a series of angular projections, individually retrieving each projected sample transmission functions and assembling the projected reconstruction series into a three-dimensional sample image using computed tomography [79]. Recent work in biological applications includes an impressive three-dimensional mapping of a mouse femur sample using ptychographic CDI tomography [5] (see Fig. 1.10), with an achieved resolution of approximately 100 nm. Though three-dimensional atom-scale CDI is yet to be achieved, the possibility of using XFEL sources to obtain three-dimensional mappings of material and biological molecules is arguably the most exciting area in diffractive imaging and currently under intensive investigation.

1.6 Tabletop and XFEL sources

A major CDI research ambition is to apply the techniques developed at large scale facilities to table-top laboratory sources. The current leading technology in this area is high-harmonic generation (HHG), a relatively inexpensive yet highly coherent table-top source suitable for CDI [51, 80]. Though several demonstrations have shown HHG sources to be capable of producing coherent X-rays in the water-window [81, 82, 83], the available flux is currently too small to realise scientifically significant biological imaging. A recent study demonstrated the possibility to reconstruct the scattering sample using higher flux broadband HHG diffraction data in conjunction with polychromatic CDI algorithms [84]. Despite these advances, tabletop CDI remains a goal rather an established procedure.

About a decade ago it was suggested that non-crystalline nanoscale objects might be imaged with atom-scale precision using ultra-high brilliance fourth-generation X-ray free-electron laser sources [85]. Recent proposals have suggested X-ray crystallographic and CDI methods might be applied to this problem, exploiting the ultra-high brilliance femtosecond pulses at these facilities. These ultra-brilliant femtosecond strategies are attractive as they bypass the requirement for high quality crystalline forms of the target sample, compensating for the decrease in scatter by an increase in the number of incident coherent photons (XFEL radiation is $\sim 10^{10}$ times brighter than synchrotron radiation). Initial studies [2] suggest the brilliance of these sources may circumvent resolution limitations due to radiation dose, offering the possibility to attain wavelength limited resolution for non-crystalline samples. These considerations have profound implications for imaging bio-molecules, in particular membrane

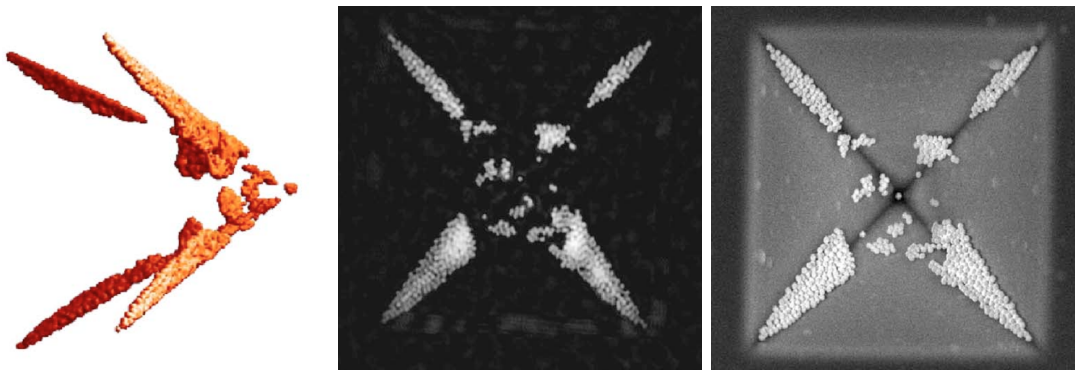

(a) (b) (c)

Figure 1.9: The first demonstration of 3D CDI. Three-Dimensional reconstructions of a 2 μm wide pyramidal arrangement of gold nano-spheres on a Si_3N_4 window. The projection through the sample in (b) shows an excellent agreement with the SEM image in (c). Image reprinted from [76].

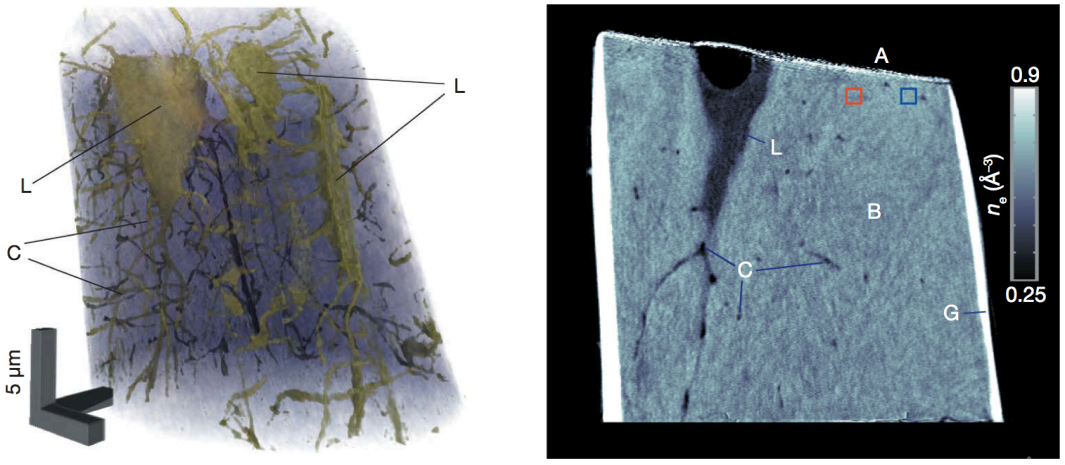

(a) (b)

Figure 1.10: 3D CDI reconstruction of a mouse femur using ptychography. (a) Volume rendering with the bone matrix in translucent colours to show osteocyte lacunae (L) and the connecting canaliculi (C). (b) A projection through the sample. Image reprinted from [5].

proteins, with the promise to revolutionise molecular imaging.

The successful operation of the Stanford XFEL marked the beginning of a new phase in X-ray microscopy, in which coherent X-ray diffractive imaging techniques have the potential to image the structure of matter at atom-scale resolution. This is clearly an exciting research area and preliminary work has recently been performed in a research program with the ultimate goal of the structural determination of isolated bio-molecules using CDI. Similar ambitions are being pursued at other emerging XFEL imaging facilities. Progress in this field will need to overcome several formidable obstacles. The principal challenge is to develop techniques capable of extracting structural information using a probe that destroys the target sample within a few femto-seconds. The rapid development of the electron distribution during this brief instant couples the effect of diffraction from the undisturbed target sample with the rapidly changing electrodynamics of the molecule. Photoionisation, Auger emission and electron capture all contribute to the evolution of the electron density in the target molecule, producing incoherent superpositions of diffraction data. Despite these challenges, major progress has already been made in the provision of a suitably bright X-ray source, the experimental design, and the theoretical and computational tools required to interpret the data of these atom-scale experiments.

The first experimental demonstration of free-electron laser CDI was performed by Chapman *et al.* [2], using VUV radiation at the FLASH facility to illuminate a lithographed silicon nitride window. Though not in the X-ray regime, this exploratory work demonstrated the possibility of capturing diffraction patterns in the

extremely brief time ($\sim$ femtoseconds) before the sample was destroyed. High-level computational models indicate that the nuclei remain relatively stable during the pulse and their arrangement may be determined from the determination of the recovered electron structure. Due to the destruction of each sample, one scheme is to pass a stream of reproducible molecules through the XFEL beam with diffraction patterns being recorded from random orientations [86]. The orientations for each diffraction pattern can be determined *post facto* [87, 88], yielding a three-dimensional diffraction volume ready for phase retrieval. An alternate method takes an "all of data" approach in the manner described by Saldin *et al.* [89]. The possibility of imaging two-dimensional crystals using an XFEL has also been demonstrated [90]. This is significant as many biological samples such as *bacteriorhodopsin* form two-dimensional, but not three-dimensional crystals. In other developments, the SACLA XFEL facility at Spring-8 in Japan has recently become operational while the FLASH facility in Hamburg, operational since 2005, will shortly operate in the X-ray regime. A number of other facilities including the European XFEL are in the construction stage or planning stage of development.

1.7 Thesis Overview

This thesis is primarily concerned with ptychography, a robust, high-resolution diffractive imaging method that solves a number of the issues in CDI, in particular the ability to image extended samples. Throughout the following chapters, a number of modifications and extensions to the ptychographic algorithm are proposed that can yield significant improvement in the reconstructed sample image compared to the images obtained using currently practiced ptychographic methods. The operation and accuracy of the proposed algorithms are tested using ptychographic X-ray data obtained at the Advanced Photon Source. The thesis is structured as follows:

Chapter 2 develops the mathematical framework used to describe a synchrotron X-ray wavefield, in particular the interactions of the illuminating wavefield with the scattering sample, the wavefield propagation, and the coherence theory used to account for deviations from full spatial or temporal coherence.

Chapter 3 uses the formalism developed in Chapter 2 to describe the experimental and computational aspects required to reconstruct a non-crystalline scattering sample from synchrotron X-ray diffraction data. This includes a discussion on the X-ray source, X-ray focussing optics, as well as the detectors used to record the diffraction data. The standard CDI algorithms used to reconstruct the scattering sample from the diffraction data are also described, along with their extension to

ptychography.

Chapter 4 extends two-dimensional ptychography (performed in a Fresnel geometry) to a three-dimensional technique using computed tomography. The method uses X-ray diffraction data recorded over a series of sample rotations to obtain a quantitative, high-contrast three-dimensional map of a lithographed borosilicate test sample.

Chapter 5 details a number of applications and extensions in coherent plane wave ptychography. These include a quantitative study of the evolution of the illuminating wavefield under propagation, a method for generating additional data redundancy by scanning the target sample through several distinct illuminating probes, and the use of undersampled ptychographic data to obtain extended images of the illuminating wavefield.

Uncertainty in the sample positions is a particular issue in ptychography as it limits the achievable sample image resolution. In Chapter 6 an iterative cross-correlation gradient-descent scan trajectory optimisation scheme is proposed, allowing the ptychographic scan trajectory to be corrected simultaneously with the retrieval of the sample transmission function and illuminating wavefield.

Chapter 7 proposes two modifications to the standard ptychographic algorithm that enable ptychography to be performed using a high-flux, partially coherent ptychographic dataset. Under the assumption of a Gaussian coherence function, it is shown that a coherence characterisation and correction can be performed simultaneously with the sample transmission and illumination probe retrievals, using only the partially coherent ptychographic diffraction data.

CHAPTER

TWO

FUNDAMENTALS

This chapter discusses the theory required to describe the X-ray source, illuminating wavefield, scattering material, scattered wavefield and the interpretation of the diffraction patterns arising from the interference effects of light waves. A classical model is adopted to describe the light field and particle interactions.

2.1 Coherent Wave Propagation

This field has been reviewed extensively for general wavefields in a number of texts including Born and Wolf's comprehensive work [10] and more specifically for X-ray propagation [77, 91, 92] and the reader is directed to those texts for a comprehensive treatment on the subject. The treatment below summarises the theoretical background used to describe the propagation of partially-coherent X-ray light sources. The reader is referred to Appendix A for a brief overview of the preliminaries.

2.1.1 Helmholtz Wave Equation

Derivations of the Helmholtz wave equation from Maxwell's equations can be found in standard electromagnetism [93] or optics [10] texts. The free-space Maxwell equations for an electric field, $\mathbf{E}(\rho, t)$, and magnetic field $\mathbf{B}(\rho, t)$, in the absence of

a charge or current are

$$\nabla \cdot \mathbf{E}(\rho, t) = 0 \tag{2.1a}$$

$$\nabla \cdot \mathbf{B}(\rho, t) = 0 \tag{2.1b}$$

$$\nabla \times \mathbf{E}(\rho, t) = -\frac{\partial}{\partial t}\mathbf{B}(\rho, t) \tag{2.1c}$$

$$\nabla \times \mathbf{B}(\rho, t) = \epsilon_0 \mu_0 \frac{\partial}{\partial t}\mathbf{E}(\rho, t), \tag{2.1d}$$

where ϵ_0 is the electric permittivity and μ_0 is the magnetic permeability of free space. Taking the curl of Eq. 2.1c, using the identity, $\nabla \times (\nabla \times \mathbf{A}) = \nabla(\nabla \cdot \mathbf{A}) - \nabla^2 \mathbf{A}$, and substituting Eq. 2.1d yields

$$\nabla^2 \mathbf{E}(\rho, t) - \nabla \left[\nabla \cdot \mathbf{E}(\rho, t)\right] = \epsilon_0 \mu_0 \frac{\partial^2}{\partial^2 t}\mathbf{E}(\rho, t). \tag{2.2}$$

Assuming the length scale of the variations in the dielectric medium is much longer than the wavelength associated with the oscillating field, the source term, $\nabla \left[\nabla \cdot \mathbf{E}(\rho, t)\right]$, may be neglected. Vector diffraction effects do not contribute significantly in the synchrotron applications used in this thesis. Eq. 2.2 may therefore be expressed in terms of the scalar quantity, $\Psi(\rho, t)$ as

$$\left(\nabla^2 - \frac{1}{c^2}\right) \Psi(\rho, t) = 0. \tag{2.3}$$

Separating the scalar wave-field into spatial and temporal components, i.e. writing $\Psi(\rho, t) = \Psi(\rho) e^{-i\omega t}$ and substitution into Eq. 2.3 yields the *Helmholtz wave equation*

$$\left(\nabla^2 + k^2 n^2\right) \Psi(\rho) = 0. \tag{2.4}$$

Formal solutions of the scalar wave vector, $\Psi(\mathbf{r})$, in Eq. 2.4 require specification of boundary conditions. For all practical purposes this requires that $\Psi(\mathbf{r})$ satisfies free-space propagation as $|\mathbf{r}| \to \infty$. The region of space occupied by the sample satisfies the Helmholtz wave equation with

$$\begin{aligned} n &= 1 - (\delta + i\beta) \\ &= 1 - \delta n \end{aligned} \tag{2.5}$$

the quantity, n, is known as the complex refractive index. In free space $\delta n = 0$ (i.e. $n = 1$), yielding the *free space Helmholtz Equation*

$$\left(\nabla^2 + k^2\right) \Psi(\rho) = 0. \tag{2.6}$$

2.1.2 Free-space Propagation

The Fourier transform of Eq. 2.6 is:

$$(k^2 - \mathbf{q}^2)\tilde{\Psi}(\mathbf{q}) = 0. \tag{2.7}$$

For non-zero values of $\tilde{\Psi}(\mathbf{q})$, this is satisfied by a sphere in reciprocal space defined by $|\mathbf{q}| = k$, i.e. the superposition of all plane waves with wavenumber k (this is a restatement of energy conservation). The construction is known as the "Ewald Sphere" [10] and is described in greater detail in Section 2.3). Defining $\mathbf{q} = (q_\perp, q_z)$ and taking the Fourier transform of Eq. 2.6 in the *transverse* plane yields

$$\left[(k^2 - {\mathbf{q}_\perp}^2) + \partial_z^2\right] \tilde{\Psi}(\mathbf{q}_\perp, z) = 0. \tag{2.8}$$

Eq. 2.8 has the general solution

$$\tilde{\Psi}(\mathbf{q}_\perp, z) = \tilde{\Psi}^+(\mathbf{q}_\perp)e^{i\sqrt{k^2-\mathbf{q}_\perp^2}z} + \tilde{\Psi}^-(\mathbf{q}_\perp)e^{-i\sqrt{k^2-\mathbf{q}_\perp^2}z} \tag{2.9}$$

For X-ray scattering experiments the scatter is forward propagating, i.e. $\tilde{\Psi}^+(\mathbf{q}_\perp)$ is interpreted as the wavefield at a distance z and the backward propagating term, $\tilde{\Psi}^-(\mathbf{q}_\perp)$, is set to zero. The evolution in the direction of propagation is

$$\begin{aligned}\Psi(\mathbf{r}_\perp, z) &= \mathscr{F}^{-1}\left[\tilde{\Psi}(\mathbf{q}_\perp)\exp\left[iz\sqrt{k^2 - \mathbf{q}_\perp^2}\right]\right] \\ &\propto \int \tilde{\Psi}(\mathbf{q})\exp\left[iz\sqrt{k^2 - \mathbf{q}_\perp^2}\left(\sqrt{1 - (\mathbf{q}/k)^2} + \mathbf{q}\cdot\mathbf{r}/kz\right)\right] d\mathbf{q}.\end{aligned} \tag{2.10}$$

Far-field diffraction is obtained when $z \to \infty$, i.e. the integrand in Eq. 2.10 vanishes unless the phase is stationary, yielding

$$\frac{\mathbf{r}_\perp}{z} = \frac{\mathbf{q}_\perp}{\sqrt{k^2 - \mathbf{q}_\perp^2}} \tag{2.11}$$

The far-field intensity may be obtained through standard asymptotic methods, yielding

$$\begin{aligned} I(\mathbf{r}_\perp) &= \left|\Psi_{\text{far field}}(\mathbf{r}_\perp)\right|^2 \\ &\propto \frac{1}{1+(\mathbf{r}_\perp/z)^2}\left|\tilde{\Psi}\left(\mathbf{q}_\perp\right)\right|^2, \end{aligned} \tag{2.12}$$

where $\mathbf{q}_\perp$ is as defined in Eq. 2.11. In other words the far-field diffraction intensity is proportional to the square of the two-dimensional Fourier transform of the sample exit surface wave. This is commonly referred to as "Fraunhofer" diffraction and is often derived from the Kirchhoff-Fresnel integral (see Eq. 2.15 for $z \to \infty$).

2.1.3 Paraxial Free Space Fresnel Propagation

Under the *paraxial approximation*, i.e.

$$|\mathbf{q}_\perp| \ll k, \tag{2.13}$$

the substitution of Eq. 2.13 into Eq. 2.10 along with the first order expansion of $\sqrt{k^2-\mathbf{q}_\perp^2}$ yields

$$\begin{aligned} \Psi(\mathbf{r}_\perp, z) &\approx \mathscr{F}^{-1}\left[\tilde{\Psi}(\mathbf{q}_\perp)\exp\left(ikz(1-\frac{\mathbf{q}_\perp^2}{2k^2})\right)\right] \\ &= \mathscr{F}^{-1}\left[\tilde{\Psi}(\mathbf{q}_\perp)\exp\left(ikz-\frac{iz}{2k}\mathbf{q}_\perp^2\right)\right]. \end{aligned} \tag{2.14}$$

For small propagation distances (i.e. $z \ll 1$), the quadratic phase factor in Eq. 2.14 is also small and Eq. 2.14 can be used to obtain an estimate of the near-field propagation of the wavefield via the *angular spectrum* method. For larger propagation distances, Eq. 2.14 is written as the convolution

$$\begin{aligned} \Psi(\mathbf{r}_\perp, z) &= \Psi(\mathbf{r}_\perp) \otimes \mathscr{F}^{-1}\left[\exp\left(ikz(1-\frac{\mathbf{q}_\perp^2}{2k^2})\right)\right] \\ &= -\frac{i\pi}{\lambda z}e^{ikz}\int \Psi(\mathbf{r'}_\perp)\exp\left[\frac{ik}{2z}(\mathbf{r}_\perp-\mathbf{r'}_\perp)^2\right]d\mathbf{r'}_\perp \\ &= -\frac{i\pi}{\lambda z}e^{ikz}e^{i\pi\mathbf{r}_\perp^2/\lambda z}\int \Psi(\mathbf{r'}_\perp)\exp\left(\frac{i\pi\mathbf{r'}_\perp{}^2}{\lambda z}\right)\exp\left[-\frac{2\pi i}{\lambda z}\mathbf{r}_\perp\cdot\mathbf{r'}_\perp\right]d\mathbf{r'}_\perp \\ &= -\frac{i\pi}{\lambda z}e^{ikz}e^{i\pi\mathbf{r}_\perp^2/\lambda z}\mathscr{F}\left[\Psi(\mathbf{r'}_\perp)\exp\left(\frac{i\pi\mathbf{r'}_\perp{}^2}{\lambda z}\right)\right]. \end{aligned} \tag{2.15}$$

Under the paraxial approximation, free space propagation is therefore performed via the Fourier transform of a planar wavefield multiplied by a rapidly oscillating spherical wave phase-factor, $\exp\left(i\pi {\mathbf{r}'_\perp}^2/\lambda z\right)$, with a uniform phase advancement of magnitude kz. This has an interesting consequence for an ideal thin lens (for example a zone plate), introducing a phase change to the wavefield such that $\Psi \rightarrow \Psi e^{\pm i\pi {\mathbf{r}_\perp}^2/\lambda z}$ for a diverging/converging lens. This removes the rapidly oscillating phase term that would otherwise prevent sufficient sampling of the wavefield and is the formulation that underpins theoretical work by Quiney *et al.* [58] for reconstructing the illuminating field of a spherically expanding wavefront, with a zone plate as the focusing mechanism.

In the case where $\Psi(\mathbf{r}'_\perp)$ is non-zero only within a finite region of space, the quantity $i\pi {\mathbf{r}'_\perp}^2/\lambda z$ reaches a maximum along the edge of the non-zero region. The phase change $\Delta\phi$ due to the path length difference between rays from the edge of a scattering object of width L and through the object centre is

$$\begin{aligned}\Delta\phi &= \frac{2\pi}{\lambda}\left(r - z\right) \\ &= \frac{2\pi}{\lambda}\left(\sqrt{z^2 + (L/2)^2} - z\right) \\ &\approx \frac{\pi(L/2)^2}{\lambda z} \\ &= \pi N_F, \end{aligned} \tag{2.16}$$

N_F is known as the *Fresnel Number* and is a measure of the number of maxima and minima in the interference pattern. If $N_F \ll 1$, i.e. when z is large, the quadratic phase term in Eq. 2.15 is small, recovering the small angle Fraunhofer propagation in Eq. 2.12.

2.2 X-ray interactions with Matter

The fundamental scattering agent for X-rays is the electron. In the discussion below the kinematic limit is assumed, i.e. each scattering centre is assumed to elastically interact with the incident illumination only once. This treatment ignores the photoelectric effect as well as minor inelastic scattering events due to the Compton effect, in which X-rays are inelastically scattered from weakly bound or free electrons in the scattering medium. The discussion below follows the classical approach adopted by Als-Nielsen & McMorrow [94], deriving single electron scatter, extending this to describe the scatter from discrete and continuous charge distributions.

2.2.1 Discrete and continuous charge distribution

An electromagnetic wave incident on a sample interacts with both the charge and spin of the electrons present in the material. The electrical interactions are stronger than the magnetic interactions by a factor of $\hbar\omega/mc$, corresponding to a factor of approximately 10^4 for intensity measurements. Magnetic interactions are therefore neglected for the remainder of the discussion. Assuming the electromagnetic wave is polarised, the electric field at a time, t, is

$$\mathbf{E} = E_0 e^{i(\mathbf{k}\cdot\mathbf{r}-\omega t)}\hat{\epsilon}, \tag{2.17}$$

where $\mathbf{k}$ is the wave vector in the direction of propagation with magnitude $|\mathbf{k}| = 2\pi/\lambda$, angular frequency, $\omega = 2\pi/f$, and direction of polarisation, $\hat{\epsilon}$. An electron with charge, e, and mass, m_e, at position, $\mathbf{r}'$, under the influence of an electric field with the form in Eq. 2.17, has (classical) acceleration

$$\mathbf{a} = \frac{e}{m_e}\mathbf{E} = \frac{e}{m_e}E_0 e^{i(\mathbf{k}\cdot\mathbf{r}'-\omega t)}\hat{\epsilon}. \tag{2.18}$$

The accelerating electron emits radiation with an electric field,

$$\mathbf{E}' = \frac{ea}{c^2 R}\sin\theta = \frac{e^2\sin\theta}{mc^2 R}E_0 e^{i(\mathbf{k}\cdot\mathbf{r}'-\omega t')}\hat{\epsilon}, \tag{2.19}$$

where $R = |\mathbf{R}|$ is the distance from the electron and θ is the angle between the acceleration direction and the vector connecting the charge and the point where the field is measured [93]. Distortions in the electric field caused by this acceleration propagate relativistically with time of emission $t' = t - R'/c$, yielding

$$\mathbf{E}' = \frac{e^2\sin\theta}{mc^2 R}E_0 e^{i(\mathbf{k}\cdot\mathbf{r}'+\mathbf{k}'\cdot\mathbf{R}'-\omega t)}\hat{\epsilon}. \tag{2.20}$$

Introducing the momentum transfer vector $\mathbf{q} = \mathbf{k}' - \mathbf{k}$, writing $\mathbf{R}' = \mathbf{R} - \mathbf{r}'$ and assuming $|\mathbf{r}| \ll |\mathbf{R}|$ yields

$$\mathbf{E}' = \frac{e^2\sin\theta}{mc^2 R}E_0 e^{i(\mathbf{k}'\cdot\mathbf{R}-\omega t)}e^{i\mathbf{q}\cdot\mathbf{r}'}\hat{\epsilon}. \tag{2.21}$$

The electric field for a distribution of N identical charges at position $\mathbf{r}$ is

$$\mathbf{E}' = \frac{e^2\sin\theta}{mc^2 R}E_0 e^{i(\mathbf{k}'\cdot\mathbf{R}-\omega t)}\sum_{j=1}^{N} e^{i\mathbf{q}\cdot\mathbf{r}}\hat{\epsilon}. \tag{2.22}$$

For a continuous charge distribution with charge density, $\rho(\mathbf{r})$, the total number of electrons, N_e, is $N_e = \int \rho(\mathbf{r}) d\mathbf{r}$, the scattered radiation is the superposition of the radiated fields from each volume element $\rho(\mathbf{r})d\mathbf{r}$. The scattered wavefield can then be written as

$$\mathbf{E}' = \frac{e^2 \sin\theta}{mc^2 R} E_0 \int \rho(\mathbf{r}) e^{i\mathbf{q}\cdot\mathbf{r}} d\mathbf{r}, \tag{2.23}$$

i.e. the scattered field is directly proportional to the Fourier transform of the electron density. These ideas are now developed using wave theory.

2.2.2 The Projection Approximation

The interaction of a wavefield with a scattering sample is described by considering solutions to the Helmholtz wave equation (Eq. 2.4) with $\delta n \neq 0$. For a plane wave incident on a scattering object with a thickness, z_0, assuming the scattering is only at small angles from the direction of incident propagation, the wave field at $z = z_0$ can be described by the deviations in phase and amplitude as the wave passes through the medium. Under the paraxial approximation, for weakly diffracting samples, with a planar illumination, or spherical expanding waves with a very low curvature across the sample, there is minimal divergence of both the unperturbed illumination and the diffracted wavefield propagating through the sample. Under these assumptions the exit surface wave is the product of the incident illumination, $\Psi_0(\mathbf{r}_\perp)$, and the sample transmission function, $O(\mathbf{r}_\perp)$.

If the wavefield has the separable form $\psi(\mathbf{r}) = \Psi(\mathbf{r}_\perp)e^{-ikz}$, the Helmholtz wave equation (Eq. 2.4) is

$$\left[\nabla^2 + 2ik\partial_z + k^2(n^2 - 1)\right] \Psi(\mathbf{r}) = 0. \tag{2.24}$$

At X-ray wavelengths the refractive index is close to unity (i.e. $|\delta n| \ll 1$). Substitution of Eq. 2.5 into Eq. 2.24 yields

$$\left[(\nabla_\perp^2 + \partial_z^2) + 2ik\partial_z - 2k^2\delta n\right] \psi(\mathbf{r}) = 0. \tag{2.25}$$

where $n^2 \approx 1 - 2\delta n$ to first order. Under the paraxial approximation (Eq. 2.13), $\partial_z^2 \psi(\mathbf{r}) \approx 0$. In the limit $k \to \infty$ the $\nabla_\perp^2$ term may be neglected, yields the first order *eikonal* approximation:

$$\partial_z \psi(\mathbf{r}) = -ik\delta n(\mathbf{r})\psi(\mathbf{r}). \tag{2.26}$$

The solution to Eq. 2.26 is

$$\begin{aligned}\psi(\mathbf{r}_\perp) &= \psi_0(\mathbf{r}_\perp)\exp\left[-ik\int\left(\delta(\mathbf{r}_\perp,z)-i\beta(\mathbf{r}_\perp,z)\right)dz\right]\\ &= \psi_0(\mathbf{r}_\perp)O(\mathbf{r}_\perp),\end{aligned} \tag{2.27}$$

where $O(\mathbf{r}_\perp)$ is the complex transmission function. Eq. 2.27 is known as the *projection approximation*. The complex transmission function, $O(\mathbf{r}_\perp)$, may be separated into amplitude and phase components $O(\mathbf{r}_\perp) = A(\mathbf{r}_\perp)\exp\left[i\phi(\mathbf{r}_\perp)\right]$, where

$$\begin{aligned}A(\mathbf{r}_\perp) &= \exp\left[-k\int\beta(\mathbf{r})dz\right]\\ \phi(\mathbf{r}_\perp) &= -k\int\delta(\mathbf{r})dz.\end{aligned} \tag{2.28}$$

This formulation is useful for the two dimensional description of sample interactions in Chapter 4, where knowledge of the illumination function, $\psi_0(\mathbf{r}_\perp)$, yields the sample transmission function, $O(\mathbf{r}_\perp)$, that may be constrained using Eq. 2.28.

2.2.3 The Born Approximation

The Helmholtz wave equation (Eq. 2.4) can be solved in a perturbative manner by considering an expansion parameter η for δn, yielding Eq. 2.4 as

$$\nabla^2\Psi + k^2\Psi = -2k^2\eta\delta n\Psi, \tag{2.29}$$

where $\Psi(\mathbf{r})$ is expanded into the form

$$\Psi(\mathbf{r}) = \Psi_0(\mathbf{r}) + \eta\Psi_1(\mathbf{r}) + \eta^2\Psi_2(\mathbf{r}) + ... \tag{2.30}$$

Eq. 2.30 is known as the known as the *Born series*. The zero order solution to Eq. 2.29 is the homogenous equation

$$\nabla^2\Psi_0 + k^2\Psi_0 = 0. \tag{2.31}$$

Higher order "correction" terms are determined using the recursive relation

$$\nabla^2\Psi_n + k^2\Psi_n = -2k^2\delta n\Psi_{n-1}. \tag{2.32}$$

Kinematically these represent multiple scattering events with each successive term, Ψ_n, generated as a response to the source, Ψ_{n-1}. The task is to find the general

solution to the *inhomogenous* Helmholtz equation

$$\nabla^2\Psi_n + k^2\Psi_n = -2k^2 f(\mathbf{r}), \tag{2.33}$$

where $-2k^2 f(\mathbf{r})$ is a source term. The standard method for solving an equation of the form in Eq. 2.33 uses *Green's functions*. The Fourier transform of Eq. 2.33 yields

$$\left(k^2 - \mathbf{q}^2\right)\tilde{\Psi}(\mathbf{q}) = -2k^2\tilde{f}(\mathbf{q}). \tag{2.34}$$

Defining

$$G(\mathbf{q}) = -(2\pi)^{-\frac{3}{2}}\left(\frac{2k^2}{k^2 - \mathbf{q}^2}\right) \tag{2.35}$$

leads to the convolution relation $\Psi(\mathbf{r}) = G(\mathbf{r}) \otimes f(\mathbf{r})$, where $G(\mathbf{r})$ is the Greens' function

$$G(\mathbf{r}) = -\frac{2k^2}{(2\pi)^{3/2}}\frac{e^{ik|\mathbf{r}|}}{4\pi|\mathbf{r}|}. \tag{2.36}$$

The recursive relationship in Eq. 2.32 is

$$\Psi_n = G \otimes (\delta n \Psi_{n-1}). \tag{2.37}$$

In the *first Born approximation* only the first term in δn is retained,

$$\Psi_B = \Psi_0 + G \otimes (\delta n \Psi_0)\,. \tag{2.38}$$

The propagated wave is

$$\tilde{\Psi}_B = \mathscr{F}[\Psi_B] = \mathscr{F}[\Psi_0] + \mathscr{F}[G] \otimes (\mathscr{F}[\delta n] \otimes \mathscr{F}[\Psi_0])\,, \tag{2.39}$$

where

$$\begin{aligned}
\mathscr{F}[G] \otimes \mathscr{F}[f] &= \sqrt{2\pi}\mathscr{F}_z^{-1}\left[\mathscr{F}[G(\mathbf{q})]\,\mathscr{F}[f(\mathbf{q})]\right] \\
&= \int \frac{2k^2}{(2\pi)^{3/2}}\frac{1}{|\mathbf{q}|^2 - k^2}\mathscr{F}[f(\mathbf{q})]\, e^{iq_z z} dq_z \\
&= \frac{1}{\sqrt{2\pi}}\frac{ik^2}{\sqrt{k^2 - q_\perp^2}}\mathscr{F}[f(\mathbf{q}_\perp, q_z)]\, e^{i\sqrt{k^2 - \mathbf{q}_\perp^2}z}.
\end{aligned} \tag{2.40}$$

The integral in the second line is performed in the complex plane with $z > 0$. Substitution of the plane wave illumination $\Psi_0 = Ae^{ikz}$ and the above form for

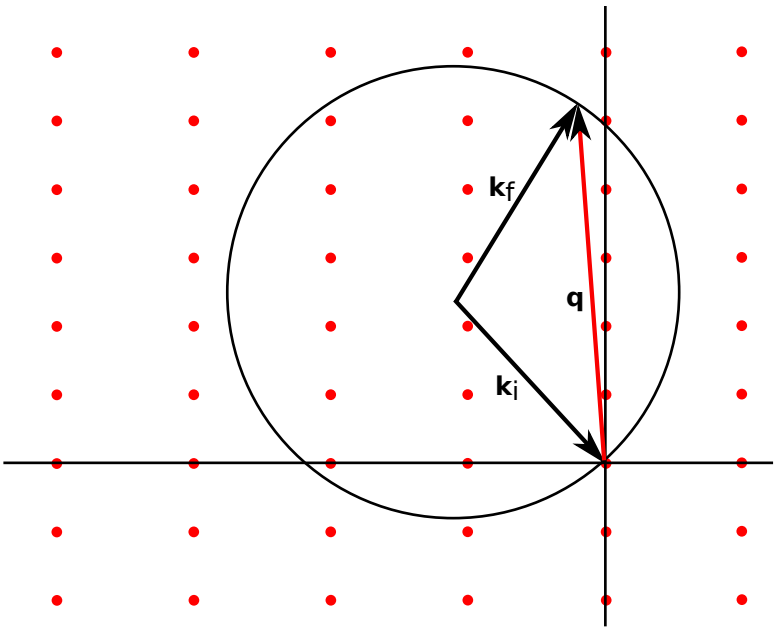

Figure 2.1: Construction of the Ewald Sphere

$\mathscr{F}[G] \otimes \mathscr{F}[f]$ into 2.39 yields the propagated wave as

$$\tilde{\Psi}_B = 2\pi A\delta(\mathbf{q}_\perp)e^{ikz} + \frac{\sqrt{2\pi}Aik^2}{\sqrt{k^2 - q_\perp^2}}\mathscr{F}\left[\delta n(\mathbf{q}_\perp, q_z)\right] e^{i\sqrt{k^2-\mathbf{q}_\perp^2}}. \tag{2.41}$$

When $k \to \infty$

$$\begin{aligned}\Psi_B &= \mathscr{F}^{-1}_{\mathbf{q}_\perp}\left[\tilde{\Psi}_B\right] \\ &\approx Ae^{ikz} + ikAe^{ikz}\mathscr{F}^{-1}_{\mathbf{q}_\perp}\left[\mathscr{F}[\delta n(\mathbf{q}_\perp, q_z = 0)]\right] \\ &= Ae^{ikz}\left(1 + ik\delta n_\perp\right),\end{aligned} \tag{2.42}$$

recovering the projection approximation. The condition for the first Born approximation, $|\Psi_1| \ll |\Psi_0|$, yields $|k\delta n| \ll 1$, i.e. the first Born approximation is valid for optically thin samples. The result in Eq. 2.41 is particularly important in three-dimensional diffraction theory as it allows the assembly of two dimensional diffraction measurements taken over a series of incidence angles into a three-dimensional diffraction volume. This is possible because each diffraction pattern is the three-dimensional Fourier transform of the scattering strength measured on the Ewald sphere.

2.3 The Ewald Sphere

The measurements in a scattering experiment can be understood through a simple graphical method known as the Ewald Construction [10] (see Fig. 2.1). In this scheme a coherent quasi-monochromatic plane wave illumination is described by the wave-vector, $\mathbf{k}$, where $\mathbf{k}$ is aligned with the direction of wave propagation and terminates at the origin of reciprocal space. For an elastic scattering event the *scattered* wave-vector, $\mathbf{k}'$, has magnitude $|\mathbf{k}'| = |\mathbf{k}|$. The direction of the scattered wave sweeps out the sphere indicated in Fig. 2.1. A Bragg peak at $\mathbf{q} = \mathbf{k}' - \mathbf{k}$ can be measured when it lies on the surface of the Ewald sphere. Experimentally, the illumination is not perfectly monochromatic (the APS beamline 34-ID has $\Delta\lambda/\lambda \approx 10^{-4}$ [52]). The spread of wavelengths in the beam transforms the Ewald construction from the surface of a sphere into a measurable small volume contained between spheres of different radii at the end of the $\mathbf{k}$ vector. The use of a two-dimensional detector such as a CCD camera allows the simultaneous probing of many orientations of the $\mathbf{k}'$ vector depending on the detector size and the sample-detector geometry.

2.4 Partial Coherence

A proper treatment of problems involving light from a finite source with a finite spectral range requires knowledge of the correlations that exist between light disturbances at two arbitrary points in the wave field. This topic has been extensively reviewed in many texts [10, 77, 91, 92, 95]. A review of the central concepts is provided below.

The theory of partial coherence is generally formulated in terms of space-time correlations, where the field has statistical properties independent of the origin of time. Recent measurements [96, 97] appear to confirm these assumptions for third generation synchrotron sources. Coherence may be described by considering a collection of two-pinhole experiments wherein the location and contrast of the interference fringes are described by the first order correlation function. This is commonly referred to as the Mutual Coherence Function, $\Gamma(\mathbf{r}_1, \mathbf{r}_2, \tau)$, of the wave field and defined in terms of its associated fluctuating time-dependent electric fields, $\mathbf{E}(\mathbf{r}, t)$, as

$$\Gamma(\mathbf{r}_1, \mathbf{r}_2, \tau) = \langle \mathbf{E}(\mathbf{r}_1, t)\mathbf{E}^*(\mathbf{r}_2, t+\tau) \rangle \,, \tag{2.43}$$

where τ is the time separation between the two fields and the angular brackets indicate an ensemble average. The MCF describes the time correlation between points in the electromagnetic field and is used to measure the degree that the field

at one point can be predicted, if known at some other point, as a function of space and time.

Measurement of the coherence function over the four dimensional data from the pinholes at $\mathbf{r}_1$ and $\mathbf{r}_2$, requires measurement of the intensity distribution. In this context this is the self-correlation of the field, i.e.

$$I(r) = \Gamma(\mathbf{r}, \mathbf{r}, 0). \tag{2.44}$$

Defining the complex degree of coherence, $\gamma_{12}(\mathbf{r}_1, \mathbf{r}_2, \tau)$, as

$$\gamma_{12}(\mathbf{r}_1, \mathbf{r}_2, \tau) = \frac{\Gamma(\mathbf{r}_1, \mathbf{r}_2, \tau)}{\sqrt{\Gamma(\mathbf{r}_1, \mathbf{r}_1, 0)\Gamma(\mathbf{r}_2, \mathbf{r}_2, 0)}}, \tag{2.45}$$

and the degree of coherence, μ_{12}, as

$$\begin{aligned} \mu_{12} &= \gamma_{12}(\mathbf{r}_1, \mathbf{r}_2, 0) \\ &= \frac{\Gamma(\mathbf{r}_1, \mathbf{r}_2, 0)}{\sqrt{I(\mathbf{r}_1)I(\mathbf{r}_2)}}, \end{aligned} \tag{2.46}$$

provides a means of measuring the coherence of the illumination.

2.4.1 Spectral Decomposition

The interaction of light with matter is dominated by frequency effects rather than time dependent effects, motivating a discussion of the interactions via the cross-spectral density, $W(\mathbf{r}_1, \mathbf{r}_2, \omega)$, defined as

$$W(\mathbf{r}_1, \mathbf{r}_2, \omega) = \frac{1}{2\pi} \int \Gamma(\mathbf{r}_1, \mathbf{r}_2, \tau) e^{i\omega\tau} d\tau. \tag{2.47}$$

The essential property of the cross-spectral density function is that it is a Hermitian nonnegative definite function in $\mathbf{r}_1$ and $\mathbf{r}_2$.

2.4.2 Quasi-monochromatic light

The use of a device such as a double crystal monochromator allows the light source to be considered to be quasi-monochromatic, i.e. to consist of spectral components that cover an angular frequency range, $\Delta\omega$, that is small compared to the mean frequency, $\bar{\omega}$, and where the time separation, τ, approaches zero. Under these conditions, Eq. 2.47 is multiplied by $e^{-i\bar{\omega}\tau}$ and the delta sifting properties allow the

MCF to be written in the separable form

$$\Gamma(\mathbf{r}_1, \mathbf{r}_2, \tau) \approx e^{-i\bar{\omega}\tau} J(\mathbf{r}_1, \mathbf{r}_2), \tag{2.48}$$

where $J(\mathbf{r}_1, \mathbf{r}_2)$ is the Mutual Optical Intensity (MOI) [91] and

$$J(\mathbf{r}_1, \mathbf{r}_2) = \Gamma(\mathbf{r}_1, \mathbf{r}_2, 0). \tag{2.49}$$

Eq. 2.48 is the cornerstone of the quasi-monochromatic approximation. It means that for a limited range of τ the quasi-monochromatic field is well approximated by harmonic variations in time, or equivalently to behave like a monochromatic field with frequency $\bar{\omega}$.

Substituting Eq. 2.48 into Eq. 2.47 yields the spectral density $W(\mathbf{r}_1, \mathbf{r}_2, \omega)$ for a quasi-monochromatic field as

$$W(\mathbf{r}_1, \mathbf{r}_2, \omega) \approx J(\mathbf{r}_1, \mathbf{r}_2)\delta(\omega - \omega_0), \tag{2.50}$$

where $\delta(\omega - \omega_0)$ is the Dirac delta function. The quasi-monochromatic field may therefore be considered fully temporally coherent with a single optical frequency ω_0.

In order to adequately describe interference with partially coherent light, it is thus necessary to know the mutual coherence function, $\Gamma(\mathbf{r}_1, \mathbf{r}_2, \tau)$, or equivalently the intensity, $I(\mathbf{r})$, along with the complex degree of coherence, $\gamma(\mathbf{r}_1, \mathbf{r}_2, \tau)$. Unlike the field theory for the disturbance at $\Psi(\mathbf{r}, t)$, a great advantage of this formulation is that it allows correlation functions and time averaged intensities to be described in a way that may be determined experimentally.

2.4.3 Modal Expansion

The following analysis is a summary of the modal framework set out with specific reference to synchrotron radiation in a recent overview on CDI [92]. As the cross spectral density $W(\mathbf{r}_1, \mathbf{r}_2, \omega)$ is by construction, a non-negative definite Hermitian function, the modal expansion of the cross spectral density function may be written in terms of the wavefields or *modes*, $\psi_n(\mathbf{r})$, i.e.

$$W(\mathbf{r}_1, \mathbf{r}_2, \omega) = \sum_n \alpha_n(\omega)\psi_n(\mathbf{r}_1, \omega)\psi_n^*(\mathbf{r}_2, \omega). \tag{2.51}$$

In this context the modes $\psi_n(\mathbf{r}, \omega)$ form the eigenvectors of the spectral density function, with associated real non-negative eigenvalues, $\alpha_n(\omega)$. The modes propagate

through free space according to the Wolf equations [10]

$$(\nabla_j^2 + k^2)W(\mathbf{r}_1, \mathbf{r}_2, \omega) = 0. \tag{2.52}$$

Each mode, $\psi_n(\mathbf{r}, \omega)$, satisfies the free space Helmholtz wave equation

$$(\nabla^2 + k^2)\psi_n(\mathbf{r}, \omega) = 0, \tag{2.53}$$

Multiplying Eq. 2.51 by $\psi_n(\mathbf{r}_2, \omega)$, integrating over $\mathbf{r}_2$ and using the orthonormality of the modes, $\psi_n(\mathbf{r})$, yields the Fredholm integral equation

$$\int W(\mathbf{r}_1, \mathbf{r}_2, \omega)\psi_n(\mathbf{r}_2, \omega)d\mathbf{r}_2 = \alpha_n(\omega)\psi_n(\mathbf{r}_1, \omega). \tag{2.54}$$

The quasi-monochromatic case, identified above in Eq. 2.50, allows the corresponding equation for the Mutual Optical Intensity, $\mathbf{J}(\mathbf{r}_1, \mathbf{r}_2)$, to be written as

$$\mathbf{J}(\mathbf{r}_1, \mathbf{r}_2) = \sum_n \alpha_n \psi_n(\mathbf{r}_1)\psi_n^*(\mathbf{r}_2), \tag{2.55}$$

where the label, ω, is suppressed for quasi-monochromatic sources. Multiplying Eq. 2.55 by $\psi_n(\mathbf{r}_2)$, integrating over $\mathbf{r}_2$, and using the orthonormality of the modes yields

$$\int \mathbf{J}(\mathbf{r}_1, \mathbf{r}_2)\psi_n(\mathbf{r}_2)d\mathbf{r}_2 = \alpha_n\psi_n(\mathbf{r}_1). \tag{2.56}$$

Multiplying Eq. 2.56 by $\psi_m(\mathbf{r}_2)$ and integrating over $\mathbf{r}_1$, yields

$$\iint \psi_m(\mathbf{r}_2)\mathbf{J}(\mathbf{r}_1, \mathbf{r}_2)\psi_n(\mathbf{r}_2)d\mathbf{r}_2 d\mathbf{r}_1 = \alpha_n \int \psi_m(\mathbf{r}_2)\psi_n(\mathbf{r}_1)d\mathbf{r}_1. \tag{2.57}$$

The coherent modes are themselves expanded in a complete basis set, $P_k(\mathbf{r})$, with the form

$$\psi_n(\mathbf{r}) = \sum_k c_n^k P_k(\mathbf{r}). \tag{2.58}$$

Eq 2.57 may be written as

$$\sum_i \sum_j c_m^i c_n^j \int P_i(\mathbf{r}_1)\mathbf{J}(\mathbf{r}_1, \mathbf{r}_2)P_j(\mathbf{r}_2)d\mathbf{r}_2 d\mathbf{r}_1 = \alpha_n \sum_k \sum_l c_m^k c_n^l \int P_k(\mathbf{r}_2)P_l(\mathbf{r}_1)d\mathbf{r}_1 \tag{2.59}$$

This is may be written as a matrix eigenvalue equation of the form

$$\mathbb{JC} = \mathbf{a}\mathbb{SC}, \tag{2.60}$$

where $\mathbb{C}$ is a matrix containing the eigenvectors, $\mathbf{a}$ is diagonal matrix containing the corresponding eigenvalues, and the elements of $\mathbb{J}$ and $\mathbb{S}$ are

$$J_{kl} = \iint P_k(\mathbf{r}_1) J(\mathbf{r}_1, \mathbf{r}_2) P_l(\mathbf{r}_2) d\mathbf{r}_2 d\mathbf{r}_1 \tag{2.61}$$

$$S_{tu} = \int P_t(\mathbf{r}_2) P_u(\mathbf{r}_1) d\mathbf{r}_1 \tag{2.62}$$

Any basis set, $P_k(x)$, that is complete over the defined domain may be chosen for the application. Choosing $P_k(\mathbf{r}) = L_k(\mathbf{r})$, where $L_k(\mathbf{r})$ are the Legendre polynomials, collapses $\mathbb{S}$ to a diagonal matrix with elements determined using the Legendre orthonormality relation

$$\int L_m(\mathbf{r}_2) L_n(\mathbf{r}_1) d\mathbf{r}_1 = \frac{2n}{2n+1} \delta_{mn}, \tag{2.63}$$

where δ_{mn} is the Kronecker delta function. The modal decomposition has now been reduced to a system of linear equations defined by Eq. 2.60 that may be solved by well established methods in linear algebra. The non-negative definite requirement on $\mathbf{J}(\mathbf{r}_1, \mathbf{r}_2)$ forces the eigenvalues to take either real non-negative or zero values. $\mathbf{J_x}(x_1, x_2)$ and $\mathbf{J_y}(y_1, y_2)$ may be approximated by a sum of two dimensional modes with form in Eq. 2.55. Substitution of the resulting modal expansions for $\mathbf{J_x}$ and $\mathbf{J_y}$ into Eq. 7.3 gives the expansion of the four dimensional $\mathbf{J}(\mathbf{r}_1, \mathbf{r}_2)$ in terms of the two dimensional modes $\psi_n(\mathbf{r}_1)$ and $\psi_m(\mathbf{r}_2)$:

$$\begin{aligned} \mathbf{J}(\mathbf{r}_1, \mathbf{r}_2) &= \sum_n \alpha_n \psi_n(x_1) \psi_n^*(x_2) \\ &= \sum_n \sum_m \gamma_n \beta_m \psi_n(\mathbf{r}_1) \psi_m^*(\mathbf{r}_2). \end{aligned} \tag{2.64}$$

The four-dimensional MOI is expressed as a modal sum of $n \times m$ two-dimensional modes with the form $\psi_n(\mathbf{r}_1)\psi_m^*(\mathbf{r}_2)$, and with associated modal occupancies, $\alpha_n = \gamma_n \beta_n$. The intensity distribution in the detector plane, $I(\mathbf{q})$, is constructed using

the known modal occupancies (these are preserved under free space propagation) as

$$\begin{aligned} I(\mathbf{q}) &= \sum_n \alpha_n \Psi_n(\mathbf{q}) \Psi_n^*(\mathbf{q}) \\ &= \sum_n \alpha_n I_n(\mathbf{q}) \end{aligned} \tag{2.65}$$

2.4.4 Gaussian-Schell model for partially coherent sources

The general characteristics of a partially coherent synchrotron beam may be accounted for by assuming a source with an ellipsoidal Gaussian amplitude and a mutual coherence function as defined by the Gaussian-Schell model [95]. In this model the MOI is separable in Cartesian coordinates, such that

$$\mathbf{J}(\mathbf{r_1}, \mathbf{r_2}) = \mathbf{J_x}(x_1, x_2) \times \mathbf{J_y}(y_1, y_2), \tag{2.66}$$

where

$$\mathbf{J_x}(x_1, x_2) = J_0^x e^{-\alpha_x x_1^2} e^{-\alpha_x^* x_2^2} e^{-\beta_x (x_1 - x_2)^2} \tag{2.67}$$

This approximation allows the Cartesian components of the MOI function to be propagated separately via

$$\mathbf{J_x}(x_1', x_2') = J_0^x \frac{1}{\lambda z} \int e^{-\alpha_x x_1^2} e^{-\alpha_x^* x_2^2} e^{-\beta_x (x_1 - x_2)^2} e^{-\frac{i\pi}{\lambda z}(x_1 - x_1')^2} e^{-\frac{i\pi}{\lambda z}(x_2 - x_2')^2} dx_1 dx_2 \tag{2.68}$$

This may be treated analytically [92], leading to the solution

$$\mathbf{J}(x_1', x_2'; z') = J_0'^x e^{-\alpha_x' x_1^2} e^{-\alpha'^*_x x_2^2} e^{-\beta_x' (x_1' - x_2')^2} \tag{2.69}$$

The main feature to note is the preservation of the general Gaussian-Schell form of both amplitude and MCF under propagation. In the more general frequency-dependent context of the cross-spectral density coherent mode expansion [98], the intensity distribution and MCF assume the forms

$$\begin{aligned} I(x, \omega) &= A(\omega) e^{-\frac{x^2}{2\sigma_I^2}} \\ \mu(x_1, x_2) &= e^{-\frac{(x_1 - x_2)^2}{2\sigma_\mu^2}} \end{aligned} \tag{2.70}$$

where $\mu(x_1, x_2)$ is the Fourier transform of the complex degree of coherence $\gamma(\mathbf{r}_1, \mathbf{r}_2, \tau)$ in Eq. 2.45. In particular, the one-dimensional modes in the cross spectral density

expansion are

$$\psi_n(x,\omega) = \left(\frac{2c_\omega}{\pi}\right)^{1/4} \frac{1}{\sqrt{2^n n!}} H_n(\sqrt{2c_\omega}x) e^{-c_\omega x^2}, \tag{2.71}$$

where $c_\omega = \sqrt{a_\omega^2 + 2a_\omega b_\omega}$ and $a_\omega = 1/4\sigma$ and $b_\omega = 1/2\xi_t^2$. H_n are the Hermite polynomials and the associated eigenvalues in Eq. 2.45 are

$$\alpha_n(\omega) = A(\omega) \left(\frac{\pi}{a_\omega + b_\omega + c_\omega}\right)^{1/2} \left(\frac{b_\omega}{a_\omega + b_\omega + c_\omega}\right)^n \tag{2.72}$$

CHAPTER

THREE

COHERENT X-RAY DIFFRACTION MICROSCOPY

Diffraction microscopy is an imaging technique based on the reconstruction of a scattering specimen from its diffraction pattern. In crystallography the orientation and symmetry of the crystal determines the distribution of the diffraction peaks from scattered X-rays. These Bragg peaks are the result of constructive interference between the periodic scattering centres within the crystal. The crystal amplification of the scattering signal enables measurement of diffraction data using low intensity and low-coherence X-ray sources. This has enabled fundamentally important atom-scale structural information to be obtained using a wide range of X-ray sources and remains the primary access to atomic sample structure information in the biological and material sciences. CDI also measures X-ray diffraction from a scattering sample, with the distinction that there is no longer a periodic array of scattering centres. The diffracted intensity distribution no longer exhibits systematic concentration of the scattering signal into Bragg peaks. This places higher demands on detector sensitivity, but more importantly, the reduction in signal amplification necessitates a massive increase in the number of coherent incident photons, as without access to a periodic scattering array, coherence in the scattering information is almost entirely dependent on the source coherence.

A synchrotron beamline consists of a series of X-ray optical devices including slits, attenuators, crystal monochromators and mirrors that control the bandwidth, photon flux, beam dimensions, focus and collimation of the X-rays before they enter the experimental endstation, where the CDI experiments are performed. This chapter details the X-ray source, optics, and detectors required to measure diffrac-

tion intensities that may be used to obtain images of the scattering sample using CDI. This is followed by a discussion of the sampling requirements and algorithms required to reconstruct the target sample from diffraction data using CDI and for extended samples using ptychography.

3.1 Synchrotron X-ray Sources

Retrieval of a scattering sample from diffraction data using CDI requires the source to be sufficiently brilliant and coherent (both spatially and temporally). The source brilliance, defined as the number of photons per second per mm^2 per $mrad^2$ per 0.1% bandwidth, is a measure of the available flux normalized for the divergence and monochromaticity. Third-generation synchrotrons are capable of producing quasi-monochromatic radiation with a negligible degree of temporal coherence. Although highly spatially coherent, the spatial coherence characteristics fall short of the essentially perfect coherence exhibited by a modern optical laser. This is a particularly important issue in CDI as the algorithms require a sufficiently coherent illumination to converge. The need to supply a sufficiently spatially coherent illumination enforces a practical limit on the usable flux that is further limited by the requirement to select out an appropriately narrow bandwidth to satisfy the quasi-monochromatic condition. Later in this thesis the theoretical, computational and experimental framework required to lift these restrictions is discussed.

Synchrotron radiation is emitted by relativistic charged particles as they are accelerated along curved trajectories [94]. The loss of energy due to synchrotron radiation was initially regarded as an undesirable side effect of electron acceleration and only later developed into the primary vehicle for coherent X-ray science. A synchrotron initially accelerates electrons in several stages to relativistic speeds, directing the high-energy electrons into a closed circular path through a series of devices including an undulator or wiggler where the actual radiative emission occurs. A schematic of an undulator is provided in Fig. 3.1, showing a periodic electromagnetic structure designed to produce synchrotron radiation in a spectrum of high order harmonics [99].

The periodic magnetic field of a planar undulator is applied at right angles to the longitudinal electron path. Moving electrons are subjected to a corresponding Lorentz force at right angles to the direction of electron motion and the applied magnetic field. This causes the electrons to undulate in the direction transverse to their motion. The ultra-brightness of synchrotron radiation is derived from two fundamental results related to the nature of radiation emitted by relativistic electrons

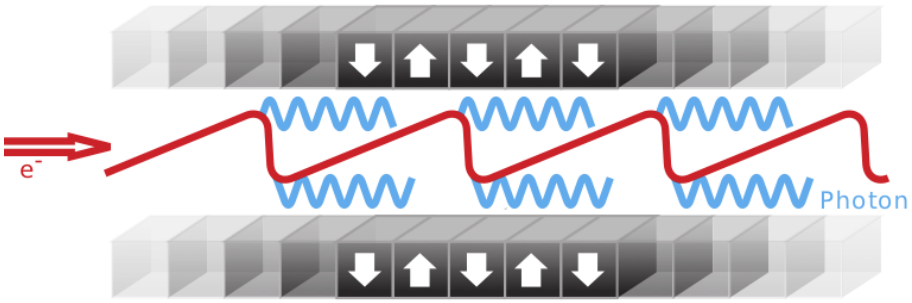

Figure 3.1: X-Ray radiation from a synchrotron source. The transverse electron oscillation causes photon emission

travelling in a circular orbit, namely a spontaneous energy emission proportional to the fourth power of the electron energy and the spread of the radiation into an extremely narrow forward-pointing radiation cone centred on the direction of electron velocity. The cone half angle is

$$\theta_r = \gamma^{-1} = \sqrt{1 - \frac{|\mathbf{v}|^2}{c^2}}.$$

In an undulator these radiation cones overlap and coherently interfere, producing a spectrum of bright harmonics, rather than the smooth spectrum characteristics associated with wiggler radiation. The relativistic Doppler effect and Lorentz contraction increase the observed frequency by the Lorentz contraction factor γ. These effects allow the undulator to accelerate the electrons into the X-Ray emitting range, producing the ultra-brilliant X-ray illumination used in CDI experiments

3.2 X-ray Optics

The advancement of X-ray microscopy has critically relied on the development of X-ray focusing technologies using diffraction (e.g. Fresnel zone plates), refraction (e.g. Compound reflective lenses) and total external reflection (e.g. Kirkpatrick-Baez mirrors). The synchrotron X-ray data used in this thesis was obtained using KB mirrors as the focusing mechanism, with the exception of the study in Chapter 4, where a Fresnel zone plate (FZP) was used.

The crossed-mirror configuration widely used for micro-focusing in the hard X-ray regime was first devised by Kirkpatrick and Baez [100, 101], resolving astigmatism focusing issues (primarily due to mirror surface aberrations) in spherical and cylindrical grazing-incidence optics. Kirkpatrick-Baez (KB) mirrors (see Fig.3.2 (a)) consist of two elliptically curved mirrors arranged such that the horizontal focus of the first mirror and the vertical focus of the second mirror coincide in the same

plane. To achieve an optimal focal size and efficiency the elliptical mirrors need to be manufactured to a very high degree of figure accuracy and surface smoothness (approximately 2 nm peak-to-valley figure accuracy) over the entire reflective area. The curvature of the mirrors is achieved by highly precise mechanics, allowing for a focal spot size as small as 7 nm [18]. KB mirrors are particularly attractive for nano-focusing X-rays since they are inherently non-dispersive and operate at high efficiency [102], enabling a massive increase in the incident intensity per unit area, resulting in a reduced data acquisition time. A further advantage is that the method maintains the focus with the same optical arrangement over a range of X-ray wavelengths. Higher incidence angles focus more of the incident X-ray beam with the maximum angle set by the critical angle of the reflective surface for a particular beam energy. Within the free electron approximation, the critical angle for total external reflection, θ_c, is

$$\theta_c = 2.99 \times 10^{-15} \lambda \sqrt{N} \tag{3.1}$$

where λ is the wavelength (Å) and N is the number of electrons per unit volume of reflective material. As an example, the condition for total external reflection for 10 keV X-rays ($\lambda = 1.3$ Å) reflected with a platinum-coated mirror yields a critical glancing angle of $\theta_c = 8.4$ mrad.

X-rays may be also be focused using a Fresnel zone plate, a diffraction based optic consisting of a series of "zones" arranged into a cylindrically symmetric diffraction grating. A Fresnel zone plate schematic is shown in Fig. 3.2 (b). When a zone plate is illuminated with a coherent plane wave, constructive and destructive interference results in a series of diffraction orders that are focused to particular points downstream. A detailed theoretical description of zone plate geometry and capability is provided in the review by Paganin [103]. The zone plate properties relevant to Fresnel CDI (see Chapter 4) are detailed below.

Under the projection approximation, zones of width Δ_R, with period $2\Delta_R$, diffract X-rays by an angle

$$\theta_{m=1} \approx \lambda / 2\Delta_R. \tag{3.2}$$

The focal length, f, for the outermost zone is

$$f = \frac{2R\Delta_R}{\lambda}. \tag{3.3}$$

The zone plate resolution is set by the diffraction limit (i.e. the Rayleigh criterion). The numerical aperture is

$$\mathrm{NA} = \lambda / 2\Delta_R, \tag{3.4}$$

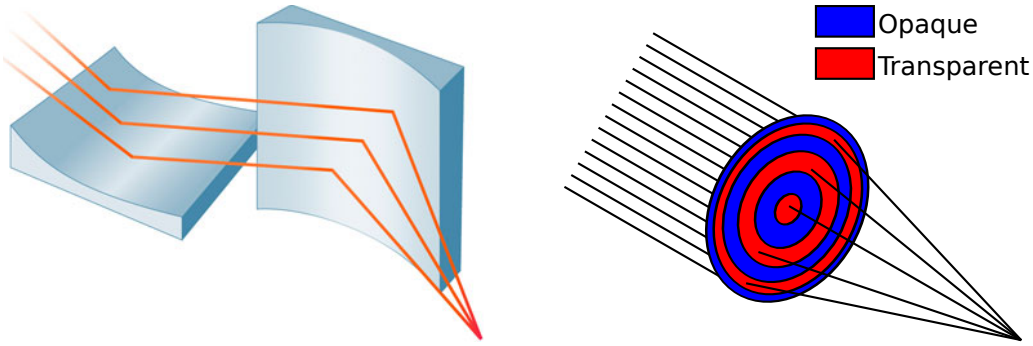

(a) (b)

Figure 3.2: Kirkpatrick Baez (KB) mirrors and Zone Plates as X-ray focusing optics. (a) Reflective KB mirrors are commonly used to focus hard X-rays. (b) A Fresnel zone plate, commonly used in focusing soft X-rays.

and the zone plate spatial resolution, Z_{res}, is

$$\begin{aligned} Z_{res} &= \frac{0.61\lambda}{\mathrm{NA}} \\ &= 1.22\Delta_R. \end{aligned} \tag{3.5}$$

A final important quality is the zone-plate efficiency. This is related to both the photon energy and the aspect ratio of the zone plate (i.e. the width to depth ratio of the zones), a quality that is ultimately restricted by the limitations in the fabrication process. At lower energies, a zone plate effectively acts as a binary mask, while at higher energies the zone plate is more transparent to the incident X-ray illumination, acting as a phase mask and operating with higher efficiency compared to the efficiency at lower energies. As an example the experiments detailed in Chapter 4 used a 2.535 keV X-ray beam to illuminate a 160 μm zone plate with an outer zone width of 50 nm and a zone plate thickness of 3.3 μm, yielding a zone plate efficiency of approximately 10% [104].

3.3 X-ray Detectors

CDI places a critical requirement on linear response and accuracy in the device used to record the diffraction data. The primary devices used in recording X-ray diffraction are image plates, Charge Coupled Devices (CCD) and more recently, photon counting detectors. Though image plates provide excellent dynamic range and linear response characteristics, a slow readout time and poor resolution make them unsuitable for CDI. The following discussion is therefore restricted to CCD's and photon counting detectors.

CCD's remain the primary device used in CDI, displaying an excellent linear response with increasing photon flux. They are used to either detect direct X-rays, or record the visible light emitted by a phosphor-coated screen (a scintillator). Incident photons interact in the CCD depletion region, creating a cascade of electron-hole pairs that move under an applied electric field toward a collector. The pixels are defined by the position of electrodes above the CCD that form potential wells to capture incoming electrons. Charge is transferred in a CCD array by shifting rows down the array into a horizontal register and reading the register out to an analogue-to-digital converter.

Despite excellent linear response characteristics, there are a number of processes that need to be accounted for when recording diffraction data using a CCD. The uncertainties in these measurements are dominated by contributions from photon counting statistics or "shot" noise, the cascading electron effect produced by the initial photon-electron interaction, as well as thermal events occurring in the CCD itself. The uncertainty in the amount of charge generated by a photon event is characterised by a Poisson distribution scaled by the Fano factor [105], F_a, an experimentally determined quantity that accounts for the correlation between pair creation events, i.e. the noise statistics are described by

$$\begin{aligned} \sigma_e^2 &= N_e F_a \\ &= E_\nu F_a / E_e \end{aligned} \tag{3.6}$$

where N_e is the number of electrons, E_ν is the photon energy, and E_e is the electron-hole creation energy.

At any temperature T, an electron-hole pair can split and provide an apparent contribution to the signal. These events occur when the detector is in either open or shuttered state and are collectively referred to as the "dark current". The probability of these events is temperature dependent and can be greatly reduced (though never completely removed) by cooling the detector. The average dark current D_{av} may be expressed in terms of the temperature T and the electron energy E_g as

$$D_{av} = CT^{3/2} e^{-E_g/(2k_b T)}, \tag{3.7}$$

where C is a constant dependent on pixel size and room temperature dark current. Dark current statistics for a number of electrons, N_e, and elapsed times τ are well described by a Poisson distribution, yielding the dark current noise per pixel as

$$\sigma_e = \sqrt{N_e} = \sqrt{D_{av}\tau}, \tag{3.8}$$

The random nature of these events means that dark-field subtraction, where the signal with the X-ray source shuttered is subtracted from the diffracted image, despite correcting for a number of undesirable contributions including thermal and stray radiation, produces an additive effect in the dark current noise with a noise contribution of $\sigma_e = \sqrt{2D_{av}Nt}$. These contributions to the dark current increase noise and consequently diminish the data quality.

Photon-counting devices are an important recent development that show great promise, primarily due to the ability to accurately detect X-rays over far greater dynamic range than CCD's, with very low read-out time. In a photon-counting detector, individual events of charge are released by X-ray absorption resulting in a signal that is amplified in the readout pixel. If the signal exceeds an adjustable threshold an absorption event is digitally counted. This removes the dark current contribution to detector noise, with superior signal-to-noise characteristics as a consequence. The photon counting is performed on the fly during exposure, achieving earliest possible digitisation and a subsequent fast and almost noise-free digital readout. This is in contrast to an integrating detector such as a CCD, where charge is accumulated during exposure and an intrinsic dark current is added to the accumulated charge. Though CCD's are presently the most widely used X-ray detection system in CDI, photon counting devices appear set to become the primary method of X-ray capture in the near future.

3.4 Coherent X-ray Diffractive Imaging

CDI seeks a solution to the paraxial wave equation through the iterative propagation of the wavefield between the sample and detector planes. The phase retrieval scheme determines a set of phases consistent with constraints including the measured diffraction intensity in the detector plane, the sample extent in the sample plane and whatever *a priori* information is available, until the iteration becomes self-consistent under free space propagation. This technique has its origins in crystallographic imaging, in that the objective lens is replaced with a numerical computation of the diffracted wave phase. The primary distinction from these techniques is that the sample image can be obtained without the requirement of crystalline forms of the target sample. Measurement of the diffraction intensity records the amplitude of the diffracted wave-field. Provided the diffraction patterns are sufficiently sampled (see §3.6), the sample transmission function may be determined through iterative recovery of the missing phase information.

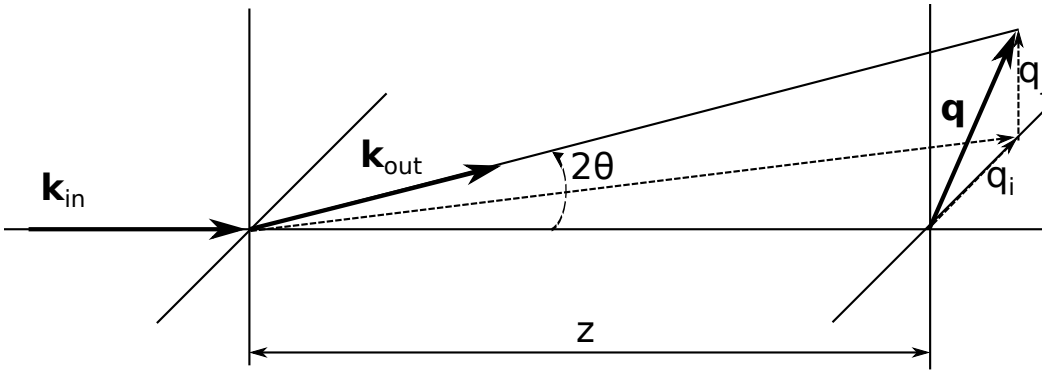

Figure 3.3: CDI scattering geometry. The far-field diffraction intensity, $I(\mathbf{q})$, is recorded a propagation distance z from the scattering sample.

3.5 Discrete Diffraction Data

The scattered wavefield intensity distribution is recorded onto an $N \times N$ Cartesian grid characterised by unit vectors $\hat{i}$ and $\hat{j}$ with pixel width Δ_D (see Fig. 3.3). The pixel location is determined by $\mathbf{q}_{ij} = \Delta_D(m\hat{\mathbf{i}} + n\hat{\mathbf{j}})$ relative to the pixel intersecting the beam, where m and n are positive integers in the range $[0, N]$. When the pixel number, N, is even, centring the grid on the zero spatial frequency requires the grid spacing along each grid axis to run from $-(N/2-1) \rightarrow N/2$, with the corresponding spatial frequencies running from $-(N/2-1) \times \Delta_D \rightarrow N/2 \times \Delta_D$. In the sample plane the grid is characterised by a spacing, Δ_S (see Eq. 3.10), and a field width $w = N\Delta_S$. The intensity, $I(q_x, q_y)$, may be written in terms of the *discrete* Fourier transform of the wavefield $\psi(x, y)$ as

$$I(q_x, q_y) = \left| \sum_x^N \sum_y^N \psi(x, y) \exp\left[-\frac{2\pi i}{N} (xq_x + yq_y) \right] \right|^2 . \tag{3.9}$$

The far-field sampling interval for an $N \times N$ array with detector plane sampling interval (i.e the pixel size), Δ_D, sample plane pixel size, Δ_S, at a wavelength, λ, with propagation distance z is determined from the scaling of the discrete Fourier transform as

$$\Delta_S = \frac{\lambda z}{N\Delta_D}. \tag{3.10}$$

This highly useful relationship is used extensively throughout this thesis.

3.6 Sampling Requirements

The determination of the wavefield phase from a recorded diffraction intensity, $I(q_x, q_y)$, requires that the diffraction pattern be sampled according to a critical sampling criterion that was first identified and discussed by Sayre in 1952 [23]. This was based on Shannon-Nyquist [106] information theory, which states that if a function $f(x)$ vanishes outside the limits, $x = \pm n/2$ (i.e. the function is "band limited"), its Fourier transform, $F(k)$, is completely determined in k space by discrete sample values at the points $k_a = \pm a/n$ ($a = 0,\ 1,\ 2, ...$). For a two dimensional exit surface wave, $\psi(x, y)$, the convolution theorem and shift invariance of the Fourier transform yields the diffracted intensity, $I(q_x, q_y)$, as

$$\begin{aligned} I(q_x, q_y) &= \left|\mathscr{F}\left[\psi(x, y)\right]\right|^2 \\ &= \mathscr{F}\left[\psi^*(x, y)\right]\mathscr{F}\left[\psi(x, y)\right] \\ &= \mathscr{F}\left[\psi^*(x, y) \otimes \psi(x, y)\right] \\ &= \mathscr{F}\left[a(h_x, h_y)\right], \end{aligned} \tag{3.11}$$

where $a(h_x, h_y)$ is the autocorrelation function (see Eq. A.5). Recovery of the scattering object from its diffracted intensity therefore requires sufficient sampling to recover the autocorrelation function. For a scattering object with a maximum width w the maximal width of the autocorrelation is $2w$, i.e. the condition to sufficiently sample the diffraction intensities corresponds to a discretely-sampled periodic autocorrelation that falls to zero along the edges of a square grid of dimension $2N \times 2N$. this is equivalent to a band-limited exit surface wave, $\psi(x, y)$ that falls to zero outside the boundary defined by half the sample plane array size in each linear dimension. The region known to contain $\psi(x, y)$ is known as the "support".

The retrieval of a complex wavefield may also be regarded as the solution of N^2 simultaneous equations with $2N_s$ unknowns, where N_s is the total number of sampling points contained in the sample extent. A reconstruction cannot be uniquely determined from a diffraction pattern if the number of degrees of freedom is larger than the number of constraints. In other words the system is under-determined unless $N_s \leq N^2/2$. This motivates the useful *oversampling ratio* [24], defined as

$$\sigma = \frac{N}{N_s} \tag{3.12}$$

Unique solutions require $\sigma \geq 2$, reducing the real-space non-zero elements in a sufficiently sampled grid to half the total array size. This condition corresponds to sampling in Fourier space at the Nyquist frequency. When recording two dimensional

diffraction patterns, the sampling condition in each linear dimension is considered independently. If both $\sigma_x \geq 2$ and $\sigma_y \geq 2$ the diffraction pattern is sufficiently oversampled, allowing the unique determination of the wavefield phase from the recorded intensity distribution. When the diffraction intensities of a finite object are sampled on a grid finer than the Nyquist frequency, the number of correlated intensities is more than the number of unknown variables in real space and the wavefield phase is uniquely encoded in the diffraction intensity. Sampling at a higher rate does not increase the information content of the measurement, though it can assist in alleviating a number of experimental issues encountered in a typical CDI experiment including data noise, coherence issues and the loss of data associated with the use of a beam stop.

When recording the diffracted intensities from a scattering object with width, w, on a detector with pixel size, Δ_D, at a wavelength λ, the oversampling places a critical criterion on the sample-detector distance, z, i.e.

$$z > \frac{2w\Delta_D}{\lambda}. \tag{3.13}$$

The detector position also determines the range of available scattering angles and hence the achievable spatial resolution.

3.7 Projections and Constraints

Iterative phase retrieval belongs to a much larger family of multiple-constraint problems wherein a solution, x, is sought, such that $x \in C_1 \cap C_2 \cap C_3...$, where C_k is a constraint set. The archetypal phase retrieval scheme is a two-constraint problem, with C_1 and C_2 representing the support and modulus constraints respectively. In the case where all constraint sets are *convex*[1], the intersection forms a contractive mapping and the convergence of algorithms can be assumed without explicit knowledge of the individual constraint sets. This type of problem has numerous applications in medical imaging and various other algorithm optimisation problems. Although many general results from convex-set theory are not applicable to non-convex sets, it is nonetheless useful to develop a similar phase retrieval framework as the reformulation of the problem into constraint sets and projections allows the development of geometric formalism and arguments. In this formalism, iterates are mapped to points within a convex space. The phase retrieval problem is now expressed as the search for the unique element that satisfies two simultaneous con-

[1] a set C is *convex* if, for any two points $x, y \in C$, $(1-\eta)x + \eta x \in C$, where $0 \leq \eta \leq 1$

straints in direct space and Fourier space. The action of a projection, $\mathbf{P}$, onto a set, E, may be described by the following definition:

> For a closed constraint set $C \in E$, a projection $\mathbf{P}$ onto the set C maps all $\mathbf{x_1} \in E$ to a point $\mathbf{x_2} = P(\mathbf{x_1}) \in C$ such that $|\mathbf{x_2} - \mathbf{x_1}|$ is minimised.

In other words, a projection onto a set determines the closest point for the set. If the set C is convex, the projection, $P(\mathbf{x_1})$, is unique [107]. Non-convex sets may in theory have more than one projection satisfying the above definition (i.e. that the projection is ill defined), though in practice the probability of this occurring is vanishingly small.

3.7.1 Support and Modulus Constraints

Most phase retrieval imaging algorithms place constraints on a wavefield, $\psi(\mathbf{r})$, using *a priori* information about the spatial extent of the scattering object through a "support" region, S, in the sample plane, and knowledge of the diffracted wavefield intensity in the detector plane. This may be expressed through the action of the support operator, π_S, acting on the wavefield in the sample plane, $\psi(\mathbf{r})$, as

$$\pi_S[\psi(\mathbf{r})] = \begin{cases} \psi(\mathbf{r}) & \mathbf{r} \in S \\ 0 & \mathbf{r} \notin S \end{cases} \tag{3.14}$$

The action of π_S on $\psi(\mathbf{r})$ leaves the wavefield unaffected inside the support boundary, while setting wavefield regions outside the support boundary to zero. The choice of support is dependant on the problem and critical in determining whether or not the algorithm converges on a solution.

Rather than setting a *static* support boundary, a *dynamic* support constraint may be applied. This allows the shape of the support to evolve throughout the iterative process. Support constraint sets of this kind can be defined by thresholding the allowable values of the exit surface wave amplitude. This description is consistent with the "shrink-wrap" algorithm proposed by Marchesini *et al.* [32]. For a minimal threshold value, t,

$$\pi_{shrink}[\psi(\mathbf{r})] = \begin{cases} \psi(\mathbf{r}) & |\psi(\mathbf{r})| \geq t \\ 0 & |\psi(\mathbf{r})| < t \end{cases} \tag{3.15}$$

Variations on this approach include the use of a low-pass filter on $|\psi(\mathbf{r})|$ prior to the application of the threshold [32], usually in the form of a Gaussian filter. This operation is not distance-minimising and is not a projection in itself, but rather the

combination of a support projection, with an additional intervention that redefines the support as the iteration evolves.

Measurement of the wavefield occurs in the detector plane, enabling a constraint on the amplitude or *modulus* of the wavefield. The amplitude rescaling operator, π_m, enforces the measured intensity while preserving the current estimate of the phase in the detector plane. This may be expressed as

$$\pi_m[\Psi(\mathbf{q})] = \Psi(\mathbf{q})\frac{\sqrt{I(\mathbf{q})}}{|\Psi(\mathbf{q})|}, \tag{3.16}$$

where $\Psi(\mathbf{q}) = \mathscr{F}[\psi(\mathbf{r})]$ is the wavefield in the detector plane and $I(\mathbf{q})$ is the recorded sample intensity. A simplification of the notation uses the modified amplitude projector, π_M, that first determines the wavefield in the detector plane by free space propagation from the sample plane to the detector plane, enforces consistency between the current estimate of the wavefield and the diffraction data, then performs the free space propagation back to the sample plane to update the current estimate of the sample exit surface wave. This may be expressed as

$$\pi_M[\psi(\mathbf{r})] = \mathscr{F}^{-1}\left[\pi_m \mathscr{F}[\psi(\mathbf{r})]\right], \tag{3.17}$$

where $\mathscr{F}$ represents the free space propagation from the sample to detector planes, provided in Eq. 2.15 or its small-angle limiting form in Eq. 2.12.

3.8 Phase Retrieval Algorithms

The foundation for modern iterative CDI methods was developed by Gerchberg and Saxton [25] in work on electron diffraction imaging. The proposed Gerchberg and Saxton (G & S) phase retrieval scheme used a measurement of the wavefield amplitude in both the sample and detector planes to retrieve the wavefield phase through the following sequential application of constraints:

1. Enforce measured amplitude of the diffracted wave.
2. Propagate from the detector plane to sample plane.
3. Enforce measured amplitude of the sample.
4. Propagate from the sample pane to the detector plane.

The algorithm cycles through these constraints until the iterate simultaneously satisfies the diffraction intensity constraint and the sample amplitude constraint to within experimental error.

A comparison between the reconstructed wavefield, $\Psi(\mathbf{q})$, and the recorded diffraction intensity, $I(\mathbf{q})$, may be determined using the error metric, χ^2, defined as

$$\chi^2 = \frac{\sum_n \left[|\psi_n| - \sqrt{I_n}\right]^2}{\sum_n I_n}, \tag{3.18}$$

where n ranges over all each element in the reconstructed array and the recorded diffraction data.

3.8.1 Error Reduction

The requirement to obtain a measurement in the sample plane (see step 3 in the G & S algorithm) severely limits the applications of the phase retrieval scheme. In a later development, Fienup lifted this restriction, proposing an algorithm that only required measurement of the diffracted data [28]. In this study, Fienup proposed a more general "finite support" constraint in addition to the "positivity" constraint, requiring that the real space density of the scattering object be real and positive. This is ensured in X-ray microscopy where the non-negative electron density forms the scattering agent, retarding the phase of the incoming X-rays relative to free space propagation. The finite support constraint is connected to the oversampling condition, requiring the object occupy less than half the field of view in real space.

The routine, known as "error reduction" [28] or "ER", involves the sequential application the magnitude of the diffracted wave, determined using the measured intensity or "modulus", and non-negative density in real space via knowledge of the object extent or "finite support". The algorithm name comes from the fact that the map is non-expanding, i.e. the distance between an iterate and the next is non-increasing, a property previously observed by Gerchberg and Saxton [25]. ER proceeds as for the G & S method with the modification that in step 3 the support constraint is enforced rather than the measured sample amplitude. The update of the k^{th} estimate of the wavefield, $\psi^k(\mathbf{r})$, using the ER algorithm may be completely described via the modified amplitude operator, π_M (Eq. 3.17), and the support operator, π_S (Eq. 3.14), as

$$\psi^{k+1}(\mathbf{r}) = \pi_S \pi_M [\psi^k(\mathbf{r})] \tag{3.19}$$

Despite a tendency towards iterative stagnation, ER retains widespread use as a highly useful tool.

3.8.2 Hybrid Input Output (HIO)

The HIO algorithm is essentially the ER algorithm with an added feedback loop such that output from the previous iterate is used to update the current iterate according to the rule

$$\psi^{k+1}(\mathbf{r}) = \begin{cases} \pi_S \pi_M[\psi^k(\mathbf{r})] & \mathbf{r} \in S \\ (1 - \beta\pi_M)\psi^k(\mathbf{r}) & \mathbf{r} \notin S, \end{cases} \tag{3.20}$$

where the parameter, β, is a real constant and is used to control the amount of feedback. The feedback mechanism pushes elements outside the support away from the current incorrect value, as opposed to ER where they are simply set to zero. HIO may also be expressed using the projection operators, π_M and π_s, as

$$\begin{aligned} \psi^{k+1}(\mathbf{r}) &= \pi_s \pi_M \psi^k(\mathbf{r}) + (1 - \pi_s)(1 - \beta\pi_M)\psi^k(\mathbf{r}) \\ &= \psi^k(\mathbf{r}) + \left[(1 + \beta)\pi_s \pi_M - \pi_s - \beta\pi_M\right]\psi^k(\mathbf{r}). \end{aligned} \tag{3.21}$$

Unlike ER, which enforces a reduction in the χ^2 error metric through the method of steepest descents, HIO is a method associated with conjugate gradient optimisation, allowing the current estimate of the error metric to fluctuate. A common routine is to alternate between the HIO and ER algorithms, enforcing two-constraint phase retrieval, while providing sufficient flexibility through HIO to overcome stagnation.

3.8.3 Difference Map

The Input-Output methods proposed by Fienup were later generalised by Elser [108] using an iterative scheme known as the "Difference Map" (DM) algorithm. DM is defined as

$$\psi^{k+1}(\mathbf{r}) = \psi^k(\mathbf{r}) + \beta[y_2\psi^k(\mathbf{r}) - y_1\psi^k(\mathbf{r})] \tag{3.22}$$

where

$$\begin{aligned} y_1 &= \pi_1\left[(1 + \gamma_2)\pi_2[\psi^k(\mathbf{r})] - \gamma_2\psi^k(\mathbf{r})\right] \\ y_2 &= \pi_2\left[(1 + \gamma_1)\pi_1[\psi^k(\mathbf{r})] - \gamma_1\psi^k(\mathbf{r})\right]. \end{aligned} \tag{3.23}$$

In the above definition π_1 and π_2 are projection operators and the control parameters β, γ_1, and γ_2 are constants and usually set to be real.

The overall convergence rate of the algorithm is largely problem dependent. Elser's optimisation of the free parameters is based on the properties of projection operators in the vicinity of fixed points. Assuming that the two projections are

locally orthogonal, one finds that the difference map converges fastest if $\gamma_1 = 1/\beta$ and $\gamma_2 = -1/\beta$. Substitution into Eq. 3.23 yields

$$\psi^{k+1}(\mathbf{r}) = \psi^k(\mathbf{r}) + \beta \left[\pi_s \left(\pi_M - \frac{1}{\beta} (\pi_M - I) \right) - \pi_M \left(\pi_s + \frac{1}{\beta} (\pi_s - I) \right) \right] \psi^k(\mathbf{r}) \tag{3.24}$$

where I is the identity operator. The special case where $\gamma_1 = -1$ and $\gamma_2 = 1/\beta$ yields the HIO algorithm in Eq. 3.20.

Precisely how these non-convex algorithms work is incompletely understood, though empirical evidence has lead to some intuitive understanding of the process [109]. Irrespective of initial conditions, iterates appear to follow a trajectory on a subspace of the search space, analogous to strange attractors encountered in the qualitative description of dynamical systems. Fixed points lying on this subspace have a basin of attraction of their own that can have the effect of terminating the progress of the iterate. In the DM and HIO schemes, the iterate is attracted rather than trapped in these minima and importantly both algorithms have the ability to move away from a close, but false, solution. This is an essential feature when searching for the intersection of non-convex constraint sets that are generally plagued by many regions of space where the distance between the constraint sets comes to a local (and false) minima.

3.9 Partially Coherent Diffractive Imaging

Recent developments have demonstrated the ability to retrieve the wavefield phase using partially coherent data by first characterising the degree of partial spatial [53, 1] or temporal [54] coherence and explicitly accounting for these in the phase retrieval scheme. Compared to fully coherent CDI, the distinction lies in propagating the dominant mode associated with fully coherent illumination along with a number of modes with lower occupancy levels. In this framework fully coherent diffractive imaging may be regarded as a limiting approximation where the occupancies for modes other than the dominant mode tend to zero.

The primary benefit of incorporating partial coherence into the phase retrieval iterative scheme is the ability to perform CDI over a broader range of experimental conditions. In particular the useable flux may be significantly increased as the requirements on full spatial coherence are relaxed. In the case of partial temporal coherence a wider beam spectrum is used [54]. These modifications can lead to significant decrease in exposure time while achieving equivalent sample scatter. Accounting for partial spatial coherence in the phase retrieval algorithms can allow

successful reconstruction for coherence lengths as low as $l_c = 0.8L_{max}$ where L_{max} is the maximal length of the scattering object [53], significantly relaxing the coherence requirement of $l_c = 2L_{max}$ suggested by Spence *et al.* [51].

The partially coherent diffractive imaging algorithm suggested by Whitehead *et al.* [53] for use with partially spatially coherent data, assumes that a modal expansion of the mutual optical intensity, $\mathbf{J}(\mathbf{r}_1, \mathbf{r}_2) = \mathbf{J}_\mathbf{x}(x_1, x_2)\mathbf{J}_\mathbf{y}(y_1, y_2)$, has been constructed using the formalism in §2.4.3, yielding the eigenvalue equation, $\mathbb{JC} = \mathbf{a}\mathbb{SC}$, where the elements of $\mathbb{J}$ and $\mathbb{S}$ are determined via Eq. 2.61 using a set of basis functions, $P_k(\mathbf{x})$. For digitally sampled data, a simple choice for $P_k(\mathbf{x})$ consists of an array of step functions of the form:

$$P_k(\mathbf{x}) = \begin{cases} \frac{1}{h^2} & \left(x_k - \frac{h}{2}\right) \leq x \leq \left(x_k + \frac{h}{2}\right) \cap \left(y_k - \frac{h}{2}\right) \leq y \leq \left(y_k + \frac{h}{2}\right) \\ 0 & \text{otherwise,} \end{cases} \tag{3.25}$$

where h may be interpreted as the pixel size in each linear dimension [1]. The basis in Eq. 3.25 has the additional advantage of reducing $\mathbb{S}$ to the identity matrix. For quasi-monochromatic synchrotron X-ray sources $\mathbf{J}(\mathbf{r}_1, \mathbf{r}_2)$ is known to be well approximated by the two-dimensional Gaussian-Schell functions in Eq. 2.67 [92, 96]. In practise the vertical coherence length is usually sufficiently long such that $\mathbf{J}_\mathbf{y}(y_1, y_2)$ may be adequately represented by a single flat mode associated with full coherence. The modal decomposition of the four-dimensional MOI is therefore entirely determined from the modal decomposition of $\mathbf{J}_\mathbf{x}(x_1, x_2)$.

The iterative retrieval of the sample transmission function using partially coherent diffraction data requires several modifications to the coherent phase retrieval schemes detailed in §3.8. Under the projection approximation, on interacting with the target sample with transmission function, $O(\mathbf{r})$, the modified modes, $\psi_k(\mathbf{r})$, can be expressed in terms of the characterised illumination modes, $\psi_{0,k}(\mathbf{r})$, as

$$\psi_k(\mathbf{r}) = T(\mathbf{r})\,\psi_{0,k}(\mathbf{r}). \tag{3.26}$$

Each mode is propagated to the detector plane using precisely the same free-space propagators (i.e. using Eq. 2.15 and Eq. 2.12) as for the fully coherent case. The modal occupancies, α_n, remain unaltered, allowing the detector plane intensity distribution, $I(\mathbf{q})$, to be written as the weighted modal sum in Eq. 2.65, i.e.

$$\begin{aligned} I(\mathbf{q}) &= \sum_n \alpha_n \Psi_n(\mathbf{q}) \Psi_n^*(\mathbf{q}) \\ &= \sum_n \alpha_n I_n(\mathbf{q}). \end{aligned} \tag{3.27}$$

The coupling of the modes means that rather than adjusting the amplitudes independently, a common rescaling function is applied such that the current estimate of the partially coherent intensity matches the recorded diffraction intensity, $I_D(\mathbf{q})$. This is written as the modified modulus constraint for each of the modes, $\Psi_k(\mathbf{q})$, as

$$\Psi'_k(\mathbf{q}) = \left[\frac{I_D(\mathbf{q})}{I(\mathbf{q})}\right]^{1/2} \Psi_k(\mathbf{q}). \tag{3.28}$$

The updated modal functions, $\Psi'_k(\mathbf{q})$ form the basis for the MOI in the detector plane.

The transfer function, $T(\mathbf{r})$, is common to all modes. It may be updated by propagating a single mode, $\Psi'_k(\mathbf{q})$, back to the sample plane, yielding the updated sample plane mode, $\psi'_k(\mathbf{r})$. Though any mode may be chosen to perform this task, a logical choice is the fundamental mode, $\Psi'_0(\mathbf{q})$, associated with the highest occupancy. This allows the transfer function to be updated via

$$T(\mathbf{r}) = \frac{\psi'_0(\mathbf{r})}{\psi_{0,0}(\mathbf{r})}. \tag{3.29}$$

where $\psi_{0,0}(\mathbf{r})$ is the fundamental mode from the known modal expansion of the source. The support and additional constraints may then be applied as for the fully coherent case. This relatively simple process allows partial coherence to be accounted for without the technical and computational difficulty of determining and propagating a four dimensional MOI. A full treatment of the technique (including an explicit modal decomposition) is provided in Chapter 7.

3.10 Ptychographic Algorithms

Ptychography is an extension of CDI where a target sample is translated step-wise across a localised probe wavefront and the resulting diffraction patterns are recorded for each sample translation. Provided the illuminated regions of the sample have sufficient overlap [71] these diffraction patterns can be used in conjunction with the iterative algorithms discussed in §3.8 to quantitatively recover the complex projected sample transmission function. Importantly, ptychography overcomes the size restrictions imposed by the oversampling condition, enabling extended samples to be imaged. The large amount of redundant information supplied by the overlapping probe regions enables iterative feedback in the overlap regions, resulting in improved robustness in the presence of noise and partial coherence when compared to standard CDI [3]. Recent developments of the ptychographic algorithm have also

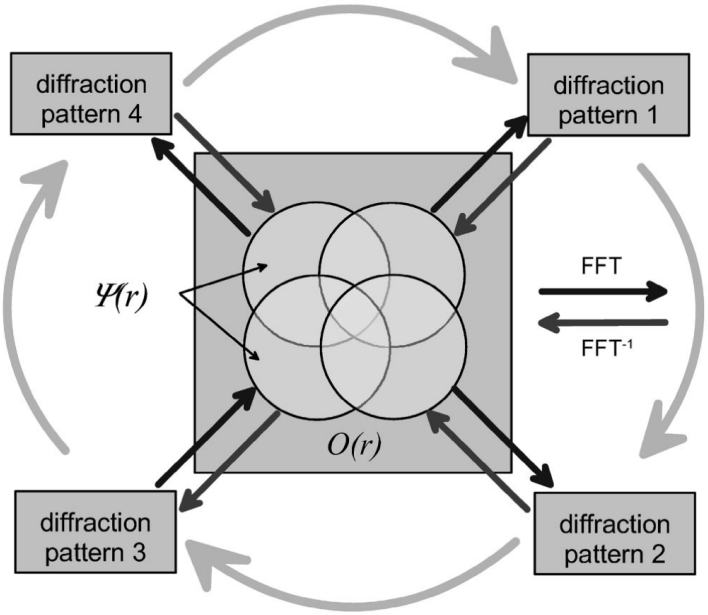

Figure 3.4: Schematic of the Ptychographic Iterative Engine (PIE) algorithm. The exit surface wave for each translated probe position (overlapping circles) is updated via the modulus projection operator π_M. This is used to update the sample transmission function (square region) via the "overlap constraint" in Eq. 3.32. Image reproduced from [67].

enabled the simultaneous retrieval of the illuminating probe [4, 68]. A rough initial probe estimate usually suffices to obtain convergence in the phase retrieval scheme. As a result of these developments ptychography has seen significant interest and development in the X-ray community [3, 4, 110]. Recent demonstrations have used electrons as the probe [74, 111] to obtain atom-scale resolution.

3.10.1 Ptychographic Iterative Engine

The ptychographic iterative engine (PIE) was originally proposed by Rodenburg *et al.* [67] to image extended samples using a known complex probe, $P(\mathbf{r})$. Under the projection approximation (see §2.2.2) the exit surface wave for the k^{th} sample position, $\mathbf{s}_k$, may be written as the product of the illuminating probe, $P(\mathbf{r})$, and the sample transmission function, $O(\mathbf{r})$, i.e.

$$\psi_k(\mathbf{r}) = P(\mathbf{r})O(\mathbf{r} - \mathbf{s}_k). \tag{3.30}$$

The coherent intensity for the k^{th} diffraction pattern, $I_k(\mathbf{q})$, is determined using free space propagation of the exit surface wave

$$\begin{aligned} I_k(\mathbf{q}) &= \left|\mathscr{F}\left[\psi_k(\mathbf{r})\right]\right|^2 \\ &= \left|\mathscr{F}\left[P(\mathbf{r})O(\mathbf{r}-\mathbf{s}_k)\right]\right|^2. \end{aligned} \tag{3.31}$$

In addition to enforcing consistency with the recorded diffraction data via the modulus constraint (Eq. 3.16), the algorithm enforces consistency between overlapping illuminated regions in the sample via the overlap constraint [67]

$$O^{j+1}(\mathbf{r}) = O^j(\mathbf{r}) + \beta \frac{|P(\mathbf{r}-\mathbf{s}_k)|}{|P(\mathbf{r}-\mathbf{s}_k)|_{max}} \frac{P^*(\mathbf{r}-\mathbf{s}_k)}{|P(\mathbf{r}-\mathbf{s}_k)|^2 + \alpha} \left[\psi'^j(\mathbf{r},\mathbf{s}_k) - \psi^j(\mathbf{r},\mathbf{s}_k)\right], \tag{3.32}$$

where the parameter α is set to $\alpha \ll 1$, forming a Wiener noise filter. The overlap constraint takes the place of the support constraint in standard CDI. For a known illumination, $P(\mathbf{r})$, the PIE algorithm can yield the sample transmission function, $O(\mathbf{r})$, using the following sequential application of constraints:

1. Using the j^{th} estimate of the sample transmission function, $O^j(\mathbf{r})$, and the known probe function, $P(\mathbf{r})$, determine the j^{th} estimate of the exit surface wave at the k^{th} scan position, $\psi^j(\mathbf{r},\mathbf{s}_k)$, where

$$\psi^j(\mathbf{r},\mathbf{s}_k) = O^j(\mathbf{r}-\mathbf{s}_k)P(\mathbf{r}).$$

2. Update the exit surface wave estimate by free-space propagation to the detector plane, imposing the recorded diffraction intensity, I_k, via the modulus constraint, π_m, and subsequent propagation back to the sample plane, i.e.

$$\psi'^j(\mathbf{r},\mathbf{s}_k) = \mathscr{F}^{-1}\pi_m\mathscr{F}\left[\psi^j(\mathbf{r},\mathbf{s}_k)\right].$$

3. Update the sample transmission function, $O^j(\mathbf{r})$, via the overlap constraint in Eq. 3.32

A single iteration is complete after all scan positions have been cycled through. The process continues until the χ^2 error metric in Eq. 3.18 has been reduced to a user defined threshold value over the entire scanning trajectory.

3.10.2 Extended Ptychographic Iterative Engine

The requirement that the probe function, $P(\mathbf{r})$, is known significantly limits the conditions under which ptychography can be performed. In a later development,

known as the *extended* Ptychographic Iterative Engine (ePIE), the PIE algorithm was adapted to recover the sample transmission function and illumination probe simultaneously [68], allowing ptychography to be performed under a broader range of experimental conditions. This important modification forms the basis for much of the work in this thesis.

The task of the ePIE algorithm is to determine a unique sample transmission function, $O(\mathbf{r})$, and illuminating probe function, $P(\mathbf{r})$, that match the recorded ptychographic dataset. This is achieved using the modified overlap constraint [68], defined as

$$O^{j+1}(\mathbf{r}) = O^{j}(\mathbf{r}) + \alpha_1 \frac{P^{*j}(\mathbf{r})}{|P^{j}(\mathbf{r})|^2_{max}} \left[\psi_k^{j+1}(\mathbf{r}) - \psi_k^{j}(\mathbf{r})\right]. \tag{3.33}$$

Retrieval of the illuminating probe is achieved via an additional application of the overlap constraint in Eq. 3.33, with the roles of the probe estimate, $P^j(\mathbf{r})$ and sample transmission function estimate, $O^j(\mathbf{r})$, exchanged (see step 4 in the following description of the ePIE algorithm). The ePIE algorithm may be summarised through the following sequential application of constraints:

1. For the k^{th} scan position, $\mathbf{s}_k$, determine the j^{th} estimate of the exit surface wave, $\psi^j(\mathbf{r}, \mathbf{s}_k)$, where

$$\psi^j(\mathbf{r}, \mathbf{s}_k) = O^j(\mathbf{r} - \mathbf{s}_k) P_n^j(\mathbf{r}).$$

2. Update the exit surface wave estimate by propagating to the detector plane, imposing the recorded diffraction intensity, I_k, via the modulus constraint, π_m, and subsequent propagation back to the sample plane, i.e.

$$\psi'^j(\mathbf{r}, \mathbf{s}_k) = \mathscr{F}^{-1} \pi_m \mathscr{F} \left[\psi^j(\mathbf{r}, \mathbf{s}_k)\right].$$

3. Update the sample transmission function, $O(\mathbf{r})$, via the overlap constraint

$$O^{m+1}(\mathbf{r}) = O^{m}(\mathbf{r}) + \alpha_1 \frac{P^{*m}(\mathbf{r})}{|P^{m}(\mathbf{r})|^2_{max}} \left(\psi'^j(\mathbf{r}, \mathbf{s}_k) - \psi^j(\mathbf{r}, \mathbf{s}_k)\right).$$

4. Update the probe function, $P(\mathbf{r})$, via a second application of the overlap constraint

$$P^{m+1}(\mathbf{r}) = P^{m}(\mathbf{r}) + \alpha_2 \frac{O^{*m+1}(\mathbf{r})}{|O^{m+1}(\mathbf{r})|^2_{max}} \left(\psi'^j(\mathbf{r}, \mathbf{s}_k) - \psi^j(\mathbf{r}, \mathbf{s}_k)\right).$$

Control of the algorithm is achieved through the feedback parameters $\alpha_1, \alpha_2 \in$

$[0, 1.5]$. A complete cycle iterates over all scan positions, $\mathbf{s}_k$, and the process is repeated until the current estimate of the sample transmission function, $O^j(\mathbf{r})$, and the probe function, $P^j(\mathbf{r})$, are consistent with the recorded diffraction dataset and the overlap constraints in steps 3 and 4. This thesis makes extensive use of the ePIE algorithm. To avoid repetition only the proposed modifications are noted, the reader is referenced back to this section where appropriate.

3.11 Conclusion

Despite the difficulty in obtaining a sufficiently coherent and bright X-ray source, CDI remains a simple experimental procedure, with minimal disturbance to the sample structure during sample preparation. Instead, provided the diffraction patterns are over-sampled according to the conditions outlined in §3.6, a quantitative measurement of the sample transmission function may be obtained using the Gerchberg and Saxton based algorithms in §3.8. The sample size limitations of CDI have been addressed using ptychography, with the additional benefit that many of the convergence issues in CDI, including robustness in the presence of noise and a higher tolerance to partial coherence in the recorded diffraction data, can be overcome by a highly overlapped, information rich ptychographic dataset.

The retrieval of the wavefield phase is essentially a global optimisation problem wherein a non-linear search is performed using the Fourier transform in conjunction with a set of constraints. The non-linear progress of the iterate in these searches can be halted by a number of points in the search space where the solution trajectory is locally parabolic, resulting in "false minima "stagnation. The ability of the HIO algorithm to "push" the iterate out of these undesirable points in the solution space has resulted in the conclusion of several studies [31, 52, 92] identifying HIO as a reliable and robust CDI phase retrieval method. Ptychographic algorithms are able to overcome these convergence issues as the points of stagnation are generally inconsistent between the overlapping wave-fields. This results in an improved robustness to intrinsic issues in X-ray data, including noise and deviations from perfect coherence. As a result ptychography is rapidly becoming a routine nanoscale X-ray imaging procedure, with some interesting recent developments in the visible regime [112] and promising work at the atom-scale using electrons [74, 75].

CHAPTER

FOUR

FRESNEL CDI TOMOGRAPHY USING PTYCHOGRAPHY

The need to understand the internal three-dimensional configurations in high resolution microscopy and structure determination has given rise to X-ray tomography, a set of techniques that uses the high penetration power of X-rays in conjunction with computed tomography [79]. High-resolution micro-tomography using synchrotron sources has delivered three-dimensional imaging techniques capable of resolving features under 100 nm, providing important three-dimensional structural information on a range of material and biological samples including single cells.

This chapter presents a demonstration of three-dimensional Fresnel CDI tomography using ptychography in the X-ray regime. The method uses a diffraction dataset recorded over a series of sample rotations, exploiting the high penetration power of X-rays and the high sensitivity of lensless imaging. The resulting series of two-dimensional reconstructions are used in conjunction with computed tomography [79] to obtain quantitative, high-contrast three-dimensional images of the sample as well as a three-dimensional map of the sample complex refractive index. The technique is used to obtain quantitative images of a lithographed borosilicate capillary, resolving features down to 70 nm.

4.1 Fresnel CDI

Providing the sampling conditions outlined by Sayre [23] are satisfied, the use of a pre-characterised, curved illumination proposed by Nugent *et al.* [55, 56] and later optimised by Quiney *et al.* [57], resolves the reflection and translation ambiguity

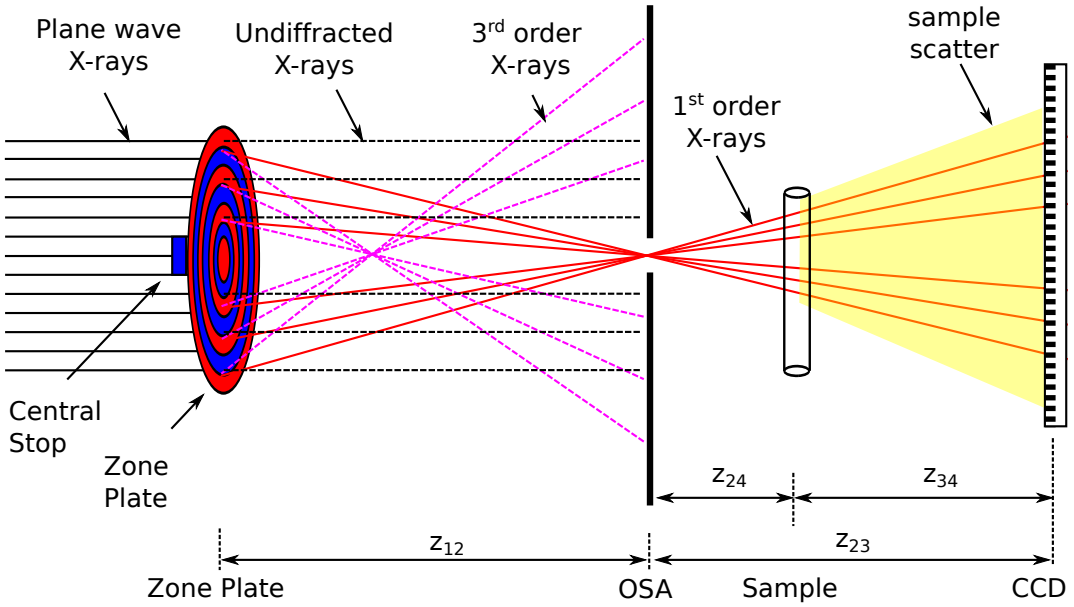

Figure 4.1: Fresnel Coherent Diffractive Imaging experimental geometry. Incident plane wave coherent X-rays illuminate a zone plate. The OSA is placed at the first-order zone plate focus allowing only first order light through and removing the need for a beamstop.

in plane wave CDI, as well as uniqueness issues associated with plane wave CDI. The latter study demonstrated that the use of an illumination with spherical phase curvature corresponding to a Fresnel number, $N_F \geq 5$, resulted in accelerated convergence of iterative algorithms compared to the plane wave case for real scattering objects with a finite support. In the method proposed by Quiney *et al.* [58], the wavefront curvature is obtained using a Fresnel zone plate in conjunction with an order sorting aperture. An independent characterisation of the illumination wavefront is obtained through a separate illumination intensity measurement and subsequent retrieval of the illumination phase. This independent characterisation is used to provide critical information in the Fresnel CDI sample reconstructions.

Fig. 4.1 shows an Fresnel CDI experimental setup where a highly coherent plane wave illuminates a Fresnel zone plate, separating the illumination into a series of orders. An Order Sorting Aperture (a pinhole) is placed at the first order zone plate focus, an arrangement that allows only the first order X-rays through, blocking all higher order contributions. Importantly, the arrangement of the zone plate "central stop" and OSA blocks the direct beam from propagating to the detector. There is therefore no need for a beam-stop and no subsequent loss of low frequency information.

The independent characterisation of the illuminating wavefield phase, as discussed in §4.2, is performed using a separate recording of the illumination intensity in the detector plane without the sample in place, consisting of a magnified image

of the focusing optic or "pupil" (see Fig. 4.3 (a)). The use of a Fresnel zone plate in conjunction with an order sorting aperture produces a wavefield that requires Fresnel propagation (Eq. 2.15) rather than the Fraunhofer propagation (Eq. 2.12) associated with plane wave CDI.

A second far-field diffraction measurement is performed with the sample placed downstream of the zone plate focus, as indicated in Fig. 4.1. As distinct from plane-wave CDI, the experimental geometry creates an inline hologram of the target sample (see Fig. 4.3 (c)), superimposed over the original magnified pupil image. This simplifies the sample alignment procedure compared to plane wave CDI experiments, but more importantly retains low frequency shape information that facilitates rapid algorithm convergence in the Fresnel CDI algorithm sample transmission reconstructions. An additional advantage, discussed in detail by Williams *et al.* [52] and demonstrated experimentally by Whitehead *et al.* [113], is an improved robustness to partial coherence compared to plane wave CDI. These qualities result in a robust mechanism for the quantitative retrieval of the sample transmission with rapid and consistent algorithm convergence for a range of biological [114] and material science samples [59, 115].

The characterisation of the illuminating wavefield phase and subsequent retrieval of the sample transmission function using Fresnel diffraction data requires a number of modifications to the CDI algorithms discussed in Chapter 3. In the discussions below the propagation distances z_{12}, z_{24} and z_{34} are as shown in Fig. 4.1. Reversal of the z subscripts indicates a switch in sign, i.e. $z_{43} = -z_{34}$.

4.2 Fresnel CDI Illumination Phase Retrieval

A fundamental assumption underpinning Fresnel CDI [58] is that a Fresnel zone plate (FZP) coupled with an Order Sorting Aperture placed at the first order zone plate focus may be considered a thin lens with focal length f. A spherically expanding wave may be written as

$$\begin{aligned}\exp(ik|\rho|) &= \exp\left[ik\sqrt{z^2+|\mathbf{r}|^2}\right] \\ &= \exp\left[ikz\sqrt{1+\frac{|\mathbf{r}|^2}{z^2}}\right] \\ &\approx \exp(ikz)\exp\left(\frac{i\pi|\mathbf{r}|^2}{\lambda z}\right), \end{aligned} \tag{4.1}$$

where the third line makes use of the paraxial approximation (Eq. 2.13). Motivated by Eq. 4.1, the wavefield exiting the zone plate, $\psi(\mathbf{r}_1, z_1)$, is expressed as the multiplication of a slow moving, complex function, $P(\mathbf{r}_1)$, that contains the amplitude and phase deviations from the ideal thin lens form, and a rapidly varying pseudo-spherical phase component, $\exp\left(-i\pi|\mathbf{r}_1|^2/\lambda z_{12}\right)$, as

$$\psi(\mathbf{r}_1, z_1) = P(\mathbf{r}_1) \exp\left(-\frac{i\pi|\mathbf{r}_1|^2}{\lambda z_{12}}\right), \tag{4.2}$$

where the sign on the exponential in Eq. 4.2 is due to the focussing of the wavefield. The free space paraxial Fresnel propagation of a quasi-monchromatic wavefield, $\psi(\mathbf{r}, z)$, from the pupil plane at z_1 to the focal plane at z_2 is determined using Eq. 2.15, yielding

$$\psi(\mathbf{r}_2, z_2) = A(\mathbf{r}_2, f)\mathscr{F}_F\left[B(\mathbf{r}_1, f)\psi(\mathbf{r}_1, z_1)\right], \tag{4.3}$$

where $\mathscr{F}_F$ is the Fresnel propagator, and $A(\mathbf{r}_2, f)$ and $B(\mathbf{r}_1, f)$ are given by

$$A(\mathbf{r}_2, f) = \left(\frac{-i}{\lambda z_{12}}\right) \exp\left(\frac{2\pi i f}{\lambda}\right) \exp\left(\frac{i\pi|\mathbf{r}_2|^2}{\lambda f}\right)$$
$$B(\mathbf{r}_1, f) = \exp\left(\frac{i\pi|\mathbf{r}_1|^2}{\lambda f}\right).$$

Substituting Eq. 4.2 into Eq. 4.3 allows the rapidly oscillating part of the wavefield exiting the zone plate that cannot be sufficiently sampled to be removed, yielding the wavefield at the focal plane as

$$\psi(\mathbf{r}_2, z_2) = A(\mathbf{r}_1, f)\mathscr{F}_F\left[P(\mathbf{r}_1)\right]. \tag{4.4}$$

Similar considerations allow the wavefield at the detector, $\psi(\mathbf{r}_3, z_3)$, to be written in terms of a rapidly oscillating phase component multiplied by a slowly varying envelope function,

$$\psi(\mathbf{r}_3, z_3) = Q(\mathbf{r}_3, z_3) \exp\left(\frac{i\pi|\mathbf{r}_3|^2}{\lambda z_{23}}\right). \tag{4.5}$$

Propagation between the focal and detector planes is determined using Eq. 2.15, i.e.

$$\psi(\mathbf{r}_2, z_2) = A(\mathbf{r}_3, z_{23})\mathscr{F}_F\left[Q(\mathbf{r}_3, z_3)\right] \tag{4.6}$$

Reconstruction of the sample transmission function using Fresnel CDI requires detailed prior knowledge of the illumination phase distribution. This is determined through independent measurement of the diffracted illumination intensity and the iterative Fresnel CDI recovery of the illumination phase [57], requiring a three-plane

propagation through the pupil (zone plate) plane at z_1, the focal plane at z_2 and the detector plane at z_3. These propagations are performed using Eq. 2.15. The finite support is enforced in the pupil plane, where the zone plate extent is known. The support constraint is usually either a disc with the same radius as the focusing optic, or is obtained by thresholding the current estimate of the reconstructed illumination in the sample plane. Additional information is provided through knowledge of the zone plate focal length, z_{12}, and the focus-detector distance, z_{23}. The algorithm involves the following sequential propagations and application of constraints:

1. Propagate $z_3 \rightarrow z_2$: $\psi(\mathbf{r}_2, z_2) = A(\mathbf{r}_2, z_{32}) \mathscr{F}_F^{-1} \left[Q'(\mathbf{r}_3, z_3) \right]$
2. Propagate $z_2 \rightarrow z_1$: $P(\mathbf{r}_1) = (-i) \exp\left(2\pi i z_{21}/\lambda\right) \mathscr{F}_F^{-`1} \left[B(\mathbf{r}_2, z_{21}) \psi(\mathbf{r}_2, z_2) \right]$
3. Apply Support Constraint: $P'(\mathbf{r}_1) = \pi_s[P(\mathbf{r}_1)]$
4. Propagate $z_1 \rightarrow z_2$: $\psi(\mathbf{r}_2, z_2) = A(\mathbf{r}_2, z_{12}) \mathscr{F}_F \left[P'(\mathbf{r}_1) \right]$
5. Propagate $z_2 \rightarrow z_3$: $Q(\mathbf{r}_3, z_3) = (-i) \exp\left(2\pi i z_{23}/\lambda\right) \mathscr{F}_F \left[B(\mathbf{r}_2, z_{23}) \psi(\mathbf{r}_2, z_2) \right]$
6. Apply Modulus Constraint: $Q'(\mathbf{r}_3, z_3) = \pi_m[Q(\mathbf{r}_3, z_3)]$

The reconstructed illuminating wavefield may be propagated to any point between the pupil and detector planes, in particular at the sample plane, using the Fresnel propagation in 2.15.

4.3 Fresnel CDI Sample Transmission Retrieval

The target sample is placed downstream of the zone plate focus, such that the pseudo-spherical phase variation across the sample corresponds to a Fresnel number (see Eq. 2.16), $N_F \geq 5$. This produces a magnified image of the sample in the central hologram region of the Fresnel diffraction patterns (see Fig. 4.3 (c)), providing low-frequency information that allows the Fresnel CDI algorithm to quickly retrieve the sample shape, accelerating the algorithm convergence. The region outside the central hologram contains high resolution sample scatter, enabling Fresnel CDI to image the scattering sample at higher resolution than that determined by the finest zone of the zone plate (see §3.2). This quality enables Fresnel CDI to obtain higher resolution images of the target sample than competing X-ray microscopy techniques such as Scanning Transmission X-ray Microscopy.

Under the Born approximation, the wavefield leaving the sample, $\psi_{esw}(\mathbf{r}_4, z_4)$, is the sum of the pre-characterised illumination function, $\psi_0(\mathbf{r}_4, z_4)$, and the scattered

wave, $\psi(\mathbf{r}_4, z_4)$, i.e.

$$\psi_{esw}(\mathbf{r}_4, z_4) = \psi_0(\mathbf{r}_4, z_4) + \psi(\mathbf{r}_4, z_4). \tag{4.7}$$

Once the illumination function, $\psi_0(\mathbf{r}_4, z_4)$, has been recovered (see §4.2), recovery of the sample image is achieved through the iterative propagation of the scattered wave, $\psi(\mathbf{r}_4, z_4)$, between the sample and detector planes described by $\mathbf{r}_4$ and $\mathbf{r}_3$ respectively. This two-plane framework is similar to plane wave phase retrieval, with the distinction that the propagation of the scattered wavefield is performed using Eq. 2.15. The retrieval of the sample image requires several modifications to the plane-wave phase retrieval algorithms detailed in Chapter 3, in particular a modification of the modulus constraint, as detailed in §4.3.2, along with a number of additional algorithm operations discussed in detail below.

4.3.1 Fresnel propagation of the Sample ESW

Eq. 2.15 yields the wavefield in the sample plane, $\psi(\mathbf{r}_4, z_4)$, as

$$\psi(\mathbf{r}_4, z_4) = A(\mathbf{r}_4, z_{34}) \int \psi(\mathbf{r}_3, z_3) \exp\left(\frac{i\pi|\mathbf{r}_3|^2}{\lambda z_{34}}\right) \exp\left(\frac{-2\pi i \mathbf{r}_3 \cdot \mathbf{r}_4}{\lambda z_{34}}\right) d\mathbf{r}_3, \tag{4.8}$$

where

$$A(\mathbf{r}_4, z_{34}) = -\frac{i\pi}{\lambda z_{34}} \exp\left[\frac{i2\pi z_{34}}{\lambda}\right] \exp\left[\frac{i\pi|\mathbf{r}_4|^2}{\lambda z_{34}}\right].$$

Substitution of the scattered wavefield, $\psi(\mathbf{r}_3, z_3)$, in Eq. 4.5, into Eq. 4.8 yields

$$\psi(\mathbf{r}_4, z_4) = A(\mathbf{r}_4, z_{34}) \int Q(\mathbf{r}_3, z_3) \exp\left[\frac{i\pi|\mathbf{r}_3|^2}{\lambda}\left(\frac{1}{z_{23}} + \frac{1}{z_{34}}\right)\right] \exp\left(\frac{-2\pi i \mathbf{r}_3 \cdot \mathbf{r}_4}{\lambda z_{34}}\right) d\mathbf{r}_3 \tag{4.9}$$

The opposite sign and similar magnitude of z_{23} and z_{34} provide a critical slow varying phase envelope over $\mathbf{r}_3$, avoiding the under-sampling issues associated with a rapidly oscillating phase terms. Eq. 4.9 may be expressed in the compact form

$$\psi(\mathbf{r}_3, z_3) = A(\mathbf{r}_3, z_{43}) \mathscr{F}_F \left[P(\mathbf{r}_4, z_4) \exp\left[\frac{i\pi|\mathbf{r}_4|^2}{\lambda}\left(\frac{1}{z_{23}} + \frac{1}{z_{43}}\right)\right]\right]. \tag{4.10}$$

Similar considerations allow the Fresnel free-space propagation between the detector and sample planes to written as

$$\psi(\mathbf{r}_4, z_4) = A(\mathbf{r}_4, z_{34}) \mathscr{F}_F \left[Q(\mathbf{r}_3, z_3) \exp\left[\frac{i\pi|\mathbf{r}_3|^2}{\lambda}\left(\frac{1}{z_{23}} + \frac{1}{z_{34}}\right)\right]\right], \tag{4.11}$$

where $z_{34} = -z_{43}$.

4.3.2 Fresnel CDI modulus constraint

The addition of the known detector plane illumination, $\psi_0(\mathbf{r}_3, z_3)$, and the estimated propagated scattered wavefront, $\psi(\mathbf{r}_3, z_3)$, yields an estimate of the detector plane intensity, $I(\mathbf{r}_3, z_3)$, via

$$I(\mathbf{r}_3, z_3) = \left|\psi_0(\mathbf{r}_3, z_3) + \psi(\mathbf{r}_3, z_3)\right|^2 . \tag{4.12}$$

For a recorded intensity distribution, $I_D(\mathbf{r}_3, z_3)$, the modified Fresnel modulus constraint is

$$\psi'(\mathbf{r}_3, z_3) + \psi_0(\mathbf{r}_3, z_3) = \left[\psi_0(\mathbf{r}_3, z_3) + \psi(\mathbf{r}_3, z_3)\right] \left[\frac{I_D(\mathbf{r}_3, z_3)}{I(\mathbf{r}_3, z_3)}\right]^{1/2} . \tag{4.13}$$

The updated estimate of the sample scatter, $\psi'(\mathbf{r}_3, z_3)$, may then be obtained by subtracting the illumination $\psi_0(\mathbf{r}_3, z_3)$.

4.3.3 Transmission Constraints

When the illuminating wavefield interacts with the sample, the resulting phase and amplitude modification may be represented by the sample transmission function, $O(\mathbf{r}_4, z_4)$. Under the projection approximation (§2.2.2), the scattered wave is written as the product of the incident illumination, $\psi_0(\mathbf{r}_4, z_4)$ and sample transmission function, $O(\mathbf{r}_4, z_4)$:

$$\psi(\mathbf{r}_4, z_4) = \psi_0(\mathbf{r}_4, z_4) O(\mathbf{r}_4, z_4). \tag{4.14}$$

Access to the transmission function, $O(\mathbf{r}_4, z_4)$, is obtained through substituting Eq. 4.14 into Eq. 4.7, yielding

$$\psi_{esw}(\mathbf{r}_4, z_4) = \psi_0(\mathbf{r}_4, z_4) \left[O(\mathbf{r}_4, z_4) + 1\right] . \tag{4.15}$$

The sample transmission function, $O(\mathbf{r}_4, z_4)$, is the linear integral through the refractive index distribution of the sample:

$$\begin{aligned} O(\mathbf{r}_4, z_4) &= \exp\left[-ik \int \left[\delta(\mathbf{r}_4, z) - i\beta(\mathbf{r}_4, z)\right] dz\right] \\ &= A(\mathbf{r}_4, z_4) \exp[i\phi(\mathbf{r}_4, z_4)]. \end{aligned} \tag{4.16}$$

i.e.

$$\begin{aligned} A(\mathbf{r}_4, z_4) &= \exp\left[-k \int \beta(\mathbf{r}_4, z) dz\right] \\ \phi(\mathbf{r}_4, z_4) &= -k \int \delta(\mathbf{r}_4, z) dz. \end{aligned} \tag{4.17}$$

The definitions in 4.17 restrict the transmission amplitude, $A(\mathbf{r}_4, z_4)$, and the transmission phase, $\phi(\mathbf{r}_4, z_4)$, to lie between the values

$$\begin{aligned} 0 \leq & A(\mathbf{r}_4, z_4) \leq 1 \\ & \phi(\mathbf{r}_4, z_4) \leq 0. \end{aligned} \tag{4.18}$$

The constraints in Eq. 4.18 are applied to prevent the algorithm from stagnating in unphysical solutions, yielding an updated transmission function $T'(\mathbf{r}_4, z_4)$. The updated exit surface wave, $\psi_{esw}(\mathbf{r}_4, z_4)$, is obtained using Eq. 4.15. This may be propagated to the detector plane using Eq. 4.10.

4.3.4 Fresnel CDI Algorithm

The retrieval of the sample transmission function is obtained through the Fresnel CDI implementation of the ER algorithm detailed in §3.8.1. In this two-plane phase retrieval scheme the propagated wavefield is determined using the Fresnel propagator in Eq. 2.15. The scattered wavefield, $\psi(\mathbf{r}_4, z_4)$, is determined by the sequential application of the following series of propagations and constraints:

1. Propagate $z_4 \rightarrow z_3$:
   $\psi(\mathbf{r}_3, z_3) = A(\mathbf{r}_3, z_{43}) \mathscr{F}_F \left[P(\mathbf{r}_4, z_4) \exp\left[\frac{i\pi |\mathbf{r}_4|^2}{\lambda} \left(\frac{1}{z_{23}} + \frac{1}{z_{43}} \right) \right] \right]$.

2. Add illumination: $\psi(\mathbf{r}_3, z_3) = \psi(\mathbf{r}_3, z_3) + \psi_0(\mathbf{r}_3, z_3)$.

3. Apply modulus constraint: $\psi'(\mathbf{r}_3, z_3) = \pi_m \left[\psi(\mathbf{r}_3, z_3) \right]$.

4. Subtract illumination: $\psi'(\mathbf{r}_3, z_3) = \psi'(\mathbf{r}_3, z_3) - \psi_0(\mathbf{r}_3, z_3)$.

5. Propagate $z_3 \rightarrow z_4$:
   $\psi(\mathbf{r}_4, z_4) = A(\mathbf{r}_4, z_{34}) \mathscr{F}_F \left[Q(\mathbf{r}_3, z_3) \exp\left[\frac{i\pi |\mathbf{r}_3|^2}{\lambda} \left(\frac{1}{z_{23}} + \frac{1}{z_{34}} \right) \right] \right]$.

6. Apply support constraint: $\psi'(\mathbf{r}_4, z_4) = \pi_s \left[\psi(\mathbf{r}_4, z_4) \right]$.

7. Divide illumination to access sample transmission function:
   $O(\mathbf{r}_4, z_4) = \frac{\psi_{esw}(\mathbf{r}_4, z_4)}{\psi_0(\mathbf{r}_4, z_4)} - 1$.

Parameter	symbol	Value
Wavelength	λ	0.489 nm
Focal Length	z_{12}	16.4 mm
Focus-Sample distance	z_{24}	1.90 mm
Focus-Detector distance	z_{23}	0.766 m
Sample-Detector distance	z_{34}	0.764 m
Cropped array size	$N \times M$	1024×1024
Detector pixel size	Δ_D	13.5 μm
Sample plane pixel size	Δ_S	27 nm

Table 4.1: Fresnel CDI experimental parameters at APS beamline 2-IDB

8. Apply transmission constraints.

9. Multiply illumination to update exit surface wave:
   $\psi_{esw}(\mathbf{r}_4, z_4) = \psi_0(\mathbf{r}_4, z_4)\,[O(\mathbf{r}_4, z_4) + 1]$.

The process is repeated until, according to the χ^2 error metric in Eq. 3.18, the current estimate of the detector intensity lies within experimental error to the measured diffraction data.

4.4 Application with X-ray data

The experiment was conducted at sector 2-ID-B at the Advanced Photon Source, Argonne National Laboratory [116], using the dedicated *in vacuo* Fresnel Imaging Endstation (FRIEND) [117]. A 2.54 keV X-ray beam was used to coherently illuminate a 160 μm Fresnel zone plate, with nominal outer zone width of 50 nm, yielding a focal length of 16.4 mm (see Eq. 3.3). The combination of the zone plate central stop and an order-sorting aperture placed at the first order focal plane blocked the direct beam and isolated the first-order portion of the illumination. The sample was placed in the diverging illumination, 1.9 mm downstream of the first order zone plate focus. The diffraction images were recorded 0.764 m downstream from the sample on a 2048×2048 Princeton Instruments CCD with 13.5 μm square pixels. The region of interest was a 1024×1024 array centred on the Fresnel diffraction data. The experimental parameters yield a sample plane sampling interval plane of 27 nm. The zone plate, sample, and CCD were maintained *in vacuo* during data collection in order to reduce air scatter. Based on previous studies of the 2-ID-B beam coherence properties [96], the exit slit settings were chosen to define an illumination with coherence length in both transverse directions larger than the sample.

The sample was provided by Dr. Eugeniu Balaur and consisted of a lithographed borosilicate capillary approximately 2.5 μm wide at the tip. A tomographic dataset

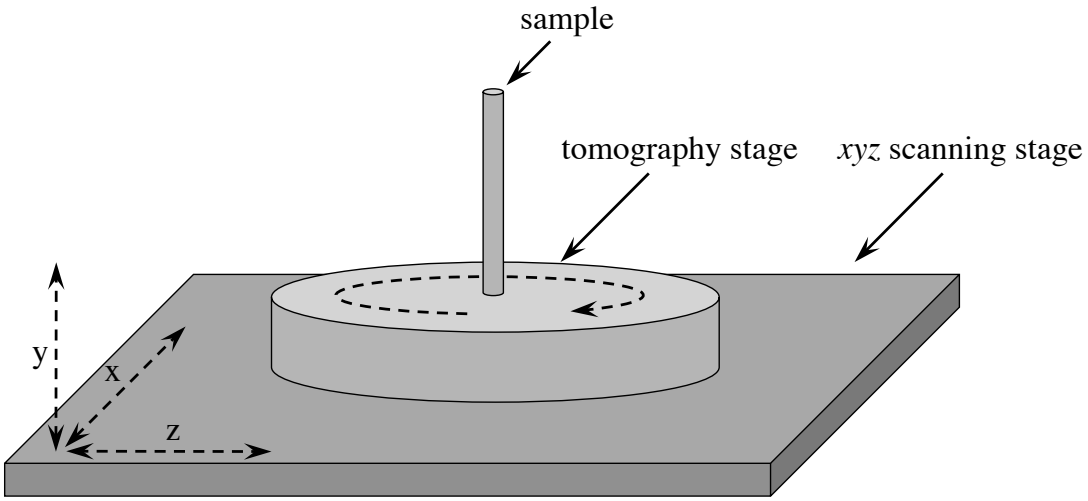

Figure 4.2: The tomographic scanning stage used at APS beamline 2-ID-B. The sample was mounted on a tomographic stage positioned above an xyz scanning stage as shown. The sample was rotated through 180° in 2° steps. Fresnel diffraction data was recorded for each sample rotation. In addition a ptychographic dataset consisting of 9 diffraction images obtained using a 3×3 grid pattern was obtained every 30°, resulting in 7 ptychographic datasets in total.

was acquired by rotating the sample in steps of 2°, over a range of $0° \leq \theta \leq 180°$. Six Fresnel diffraction images were recorded and summed for each sample rotation. An example diffraction image is provided in Fig. 4.3 (c). In addition to the tomographic Fresnel diffraction dataset, 7 Fresnel ptychographic datasets were recorded at 30° intervals over the full range of θ. Each ptychographic dataset was obtained by translating the sample over a 3×3 grid, spaced by 5 μm between adjacent scanning positions. 25 images were recorded and summed for each sample translation. The data acquisition time was 0.75 seconds for each image. The combined exposure time for the specimen was approximately 1.2 hours. The average fluence on the sample per recorded data frame was calculated to be 2.1×10^5 photons/μm^2, providing a dose of 2.17×10^5 Gy per tomographic projection, 8.1×10^5 Gy per ptychographic position, and a total dose of approximately 7.7 MGy.

The sample was mounted over a tomography stage and an xyz scanning stage in the geometry shown in Fig. 4.2. The sample was aligned with the centre of the tomographic stage using two actuator screws oriented perpendicularly to one another. An optical video camera was used to measure the sample precession after adjustment of the actuator screws. This arrangement made aligning the sample with the centre of the tomographic stage very difficult to achieve, resulting in a circular sample precession with a radius of approximately 25 μm. An important consequence of the sample precession was uncertainty in the sample-focus distance, a critical parameter in the sample reconstructions due to the magnification associated

with a spherically expanding wavefront and the evolution of the illumination under propagation.

Maintaining the sample in the illumination required correction of the sample position after each tomographic rotation. The correction was performed only in the transverse plane (i.e. the xy plane in Fig. 4.2) using the xyz sample scanning stage. Translating the sample in the transverse plane did not effect the longitudinal component of the sample precession (due to the tomographic alignment issues) as the xyz sample scanning stage translations also translated the tomography stage. It was therefore possible to calculate the longitudinal component of the sample precession using elementary geometry, and hence the change in the focus-sample distance, over the 180° sample rotation.

4.5 Fresnel CDI Reconstructions

Using the illumination phase retrieval algorithm detailed in §4.2, the illuminating wavefield phase was retrieved from the illumination intensity data. The illumination diffraction data and the resulting retrieved illumination phase (i.e the illumination wavefield at the detector) are provided in Fig. 4.3 (a) and (b) respectively. As the recorded illumination intensity, $I_0(\mathbf{r}_3, z_3)$, and the sample diffraction data, $I_D(\mathbf{r}_3, z_3)$, are obtained independently, a normalisation of $I_D(\mathbf{r}_3, z_3)$ needs to be performed such that $\psi(\mathbf{r}_3, z_3)$ may be interpreted as a perturbation to the illumination arising solely from the introduction of the sample. To achieve this the sample diffraction intensity is scaled as $I_D(\mathbf{r}_3, z_3) \rightarrow \alpha I_D(\mathbf{r}_3, z_3)$, where α is a real and positive and is determined by either using knowledge of the ring current at the time of image capture, or by performing a parameter search on α, minimising $|I_0(\mathbf{r}_3, z_3) - \alpha I_D(\mathbf{r}_3, z_3)|$, until only the hologram and the scatter that is second-order in $\psi(\mathbf{r}_3, z_3)$ are present. This operation is performed in a region where the sample scatter is negligible, such as the region indicated in Fig. 4.3 (c). The normalisation is performed by minimising the metric:

$$\sum_k |I_{0,k} - \alpha I_{D,k}|^2 \tag{4.19}$$

over the parameter α, where k ranges over the regions pixel locations. As an example the diffraction data in Fig. 4.3 (a) and (c), yielded the scaling parameter $\alpha = 0.9816$, i.e. $I(\mathbf{r}_3, z_3) \rightarrow 0.9816 I(\mathbf{r}_3, z_3)$.

The sample transmission function was retrieved using the retrieved illumination function, $\psi_0(\mathbf{r}_4, z_4)$, in conjunction with the Fresnel CDI algorithm detailed in Eq. 4.3.4. The support was updated using the shrinkwrap algorithm detailed in Eq.

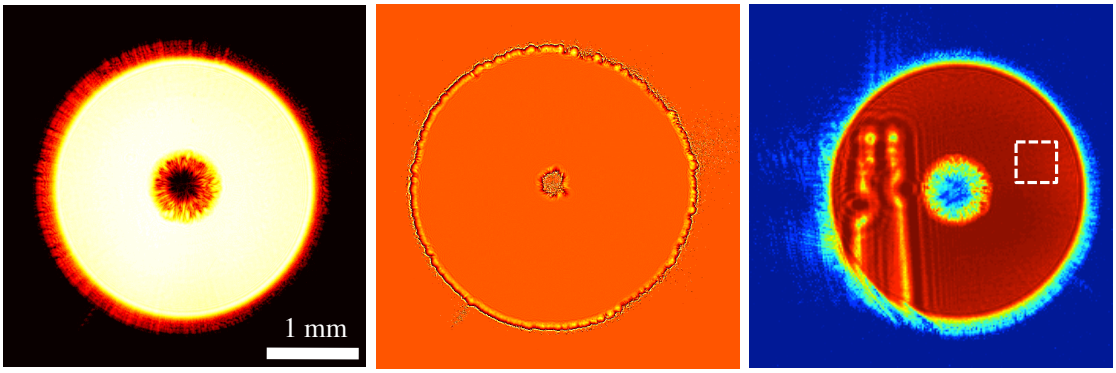

(a) (b) (c)

Figure 4.3: Fresnel CDI illumination and sample diffraction data. The recorded illumination intensity (at the detector plane) in (a) was used to reconstruct the illumination wavefield phase at the detector plane in (b). Example diffraction data with the sample in the beam is shown in (c). The white box indicates the region of negligible sample scatter used in the sample diffraction data normalisation detailed in §4.5

3.15, with the threshold, t, gradually increased from 1% to 3% of the maximal value of the magnitude of the exit surface wave. The sample transmission amplitude and phase were constrained according to Eq. 4.18, i.e. by enforcing the transmission phase to $\phi(\mathbf{r}_4, z_4) \leq 0$ and the transmission amplitude $A(\mathbf{r}_4, z_4) \leq 1$. Transmission phase and amplitude values greater than the maximum allowable values were set to 0 and 1 respectively. The Fresnel CDI algorithm was run for a total of 250 iterations. An example reconstruction for a single projection is provided in Fig. 4.4 (b). Measurement of the reconstructed sample transmission function gives a capillary wall thickness of 350 nm. The reconstruction is qualitatively similar to the SEM image in 4.4 (a), but has the important distinction that the measurement provides detailed analysis of the internal sample structure without resorting to sample sectioning. In addition the "shadowing" artefacts present at the capillary edges in the SEM image are absent in the Fresnel CDI reconstructions. These SEM artefacts are due to surface charge effects and hence are not present in the Fresnel CDI reconstructions.

Despite the ability to yield a quantitative two-dimensional map of the projected sample structure, the reconstructed sample transmission function exhibited a series of radial artefacts. These artefacts are thought to be due to stability issues, in particular instability in the beam trajectory, sample position and the OSA position. Under these conditions the illumination function is effectively evolving and the reconstructed illumination does not perfectly match the illumination during sample data acquisition. This causes artefacts both in the illumination subtraction (see Eq. 4.3.4) in the detector plane and the illumination division associated with the transmission constraints (§4.3.3) in the sample plane. The radial structures have been

previously documented at this particular beamline [118, 119], and are evidently a consequence of using the illumination to provide the reference phase. The sample was translated across the beam at several positions with diffraction data recorded for each sample translation. It was found that the radial structures in Fig. 4.4 (b) were inconsistent between the resulting sample reconstructions. The inconsistency between radial artefacts in neighbouring sample translations suggests that these artefacts may be addressed using ptychography.

4.6 Fresnel CDI ptychography

In the Fresnel CDI configuration, the extended sample transmission may be obtained using "keyhole" Fresnel CDI [115], or by using the Fresnel implementation of the PIE algorithm [118, 114]. Here the latter method was used due to the improvements offered by the dynamic feedback between overlap regions during the reconstruction process. In addition the technique offers substantially a smaller overlap requirement and rapid sample alignment [118]. In this phase retrieval scheme the pre-characterised illumination, $\psi_0(\mathbf{r}_4, z_4)$, partially illuminates the sample with an unknown transmission function, $O(\mathbf{r}_4, z_4)$, translated by $\mathbf{s}_k$. Under the projection approximation, the resulting exit-surface wave, $\psi_{esw}(\mathbf{r}_4, \mathbf{s}_k)$, at scan position $\mathbf{s}_k$, can be written via Eq. 4.15 as

$$\psi^j_{esw}(\mathbf{r}_4, \mathbf{s}_k) = \psi_0(\mathbf{r}_4, z_4)\left(O(\mathbf{r}_4 - \mathbf{s}_k) + 1\right). \tag{4.20}$$

The scattered wavefield is propagated and updated according to the methods outlined in §4.3, with the additional requirement that for each scan position, $\mathbf{s}_k$, the transmission function, $O(\mathbf{r}_4, z_4)$, is updated via a modified form of the PIE overlap constraint (see Eq. 3.32) as

$$T^{j+1}(\mathbf{r}_4, z_4) = T^j(\mathbf{r}_4, z_4) + \beta \sum_{i=1}^{I} \left(\frac{|\psi_0(\mathbf{r}_4 - \mathbf{s}_k, z_4)|}{|\psi_0(\mathbf{r}_4, z_4)|_{max}} \right) \left[\psi_i^{j+1}(\mathbf{r}_4, z_4) - \psi_i^j(\mathbf{r}_4, z_4)\right]. \tag{4.21}$$

The parameter β acts to control the degree of algorithm feedback using the current and previous estimates of the reconstructed wave field. The first term in the sum of Eq. 4.21 ensures that the object function is updated in regions where the signal is strongest. Access to the sample transmission function also allows constraint of the transmission constraints detailed in §4.3.3.

The sample transmission function was retrieved using the Fresnel implementation of the PIE algorithm and a series of ptychographic datasets taken over a series

of tomographic projections at 30° intervals. The sample scanning parameters (a 3×3 grid spaced by 5 μm) correspond to an illuminated area of the sample between 20 μm^2 and 40 μm^2, with a total probe area of 160 μm^2. The initial sample transmission function estimate consisted of a random binary estimate with phase elements randomly distributed over the interval $[-\pi, \pi]$. An example ptychographic reconstruction is provided in Fig. 4.4 (d). A comparable SEM of the target sample is provided in Fig. 4.4 (a). There is a major reduction in the radial artefacts in the ptychographic reconstruction in Fig. 4.4 (d) compared to the Fresnel CDI reconstructions in Fig. 4.4 (b) and (c), as well as an improved uniformity in the reconstructed capillary wall and weaker central regions of the projected transmission function.

4.7 Bootstrapping with Ptychography

An exploratory study in Fresnel CDI tomography [114] has shown that "bootstrapping", a process wherein a neighbouring projection reconstruction, $T_{\theta-\Delta\theta}$, is used to supplied the initial estimate for a current projection, T_θ, can improve the algorithm convergence rate and lead to greater consistency with the diffraction data, as measured by the χ^2 metric in Eq. 3.18. This study used both simulated and optical data, here the method is extended to X-ray Fresnel CDI tomography.

An initial estimate for the exit surface wave at the current projection, ψ_θ, may be determined using a recovered transmission function for a neighbouring projection, $T_{\theta-\Delta\theta}$, via

$$\psi_\theta^{est}(\mathbf{r}_4, z_4) = \psi_0(\mathbf{r}_4, z_4) T_{\theta-\Delta\theta}(\mathbf{r}_4, z_4) \tag{4.22}$$

where $\psi_0(\mathbf{r}_4, z_4)$ is the pre-characterised illumination. Recovery of the sample transmission function at the current projection, T_θ, proceeds as described in §4.5.

A series of ptychographic Fresnel CDI reconstructions, spaced at 30° intervals, were used to estimate the sample transmission function for a series of non-ptychographic projected sample transmission functions using the "bootstrapping" method in Eq. 4.22. The method was applied in steps of 2° over a range of ±15° from each ptychographic projection. The reconstructions used the same data and algorithm parameters as the non-seeded Fresnel CDI reconstruction described in §4.5. Example unseeded and seeded reconstructions for a particular projection are provided in Fig. 4.4 (b) and (c) respectively. There is a notable improvement in the uniformity of the capillary wall reconstructions and a significant reduction in the radial artefacts.

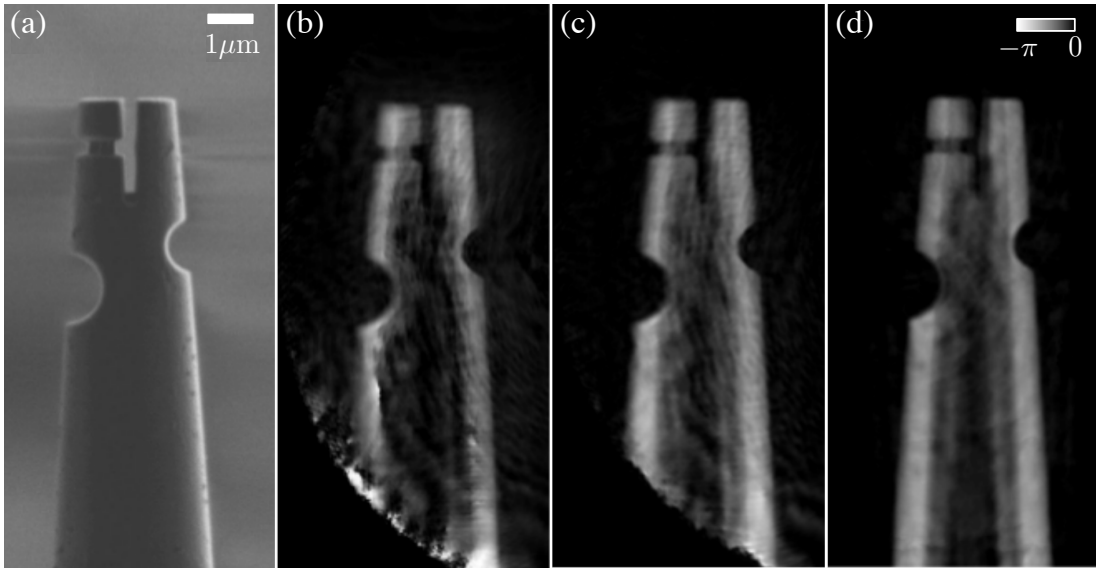

Figure 4.4: Fresnel CDI sample transmission reconstructions. (a) A SEM image of the lithographed borosilicate sample. (b) and (c) show reconstructions of the transmission phase for the same non-ptychographic sample projection without bootstrap and with bootstrap input respectively. (d) ptychographic sample transmission phase reconstruction (scale bars are common to all reconstructions).

4.8 Resolution Comparison

An estimate of the achievable reconstruction resolution may be obtained using Abbé theory [10]. In the small angle limit, the numerical aperture, NA, of the detector (defined here to be one half the sine of the detector acceptance angle), is $NA \approx N\Delta/2z$, where N is the linear dimension in pixels, Δ is the detector plane pixel size and z is the propagation distance. Using the experimental parameters detailed in §4.4, the theoretical resolution limit was determined to be $\Gamma = 0.82\lambda/NA \approx 44$ nm. The actual resolution of the reconstructions is lower than this as it is dependent on a number of experimental factors including deviations from perfect coherence, stability, and the signal-to-noise ratio of the recorded diffraction patterns. The achieved resolution can be determined using the phase retrieval transfer function (PRTF) [39] or the power spectral density. The PRTF uses the wavefield estimates from a large number of randomly initialised reconstructions. These are averaged to form the intensity estimate, I_{recon}, then compared with the recorded data via the ratio I_{recon}/I_{data}. The averaging process in the PRTF acts to minimise spatial frequencies dominated by random fluctuations. The spatial frequency corresponding to the resolution limit corresponds to the point where the PRTF drops to $1/e$ [39]. In Fig. 4.5 (a), this corresponds to an estimate of the reconstruction resolution as approximately 40 nm.

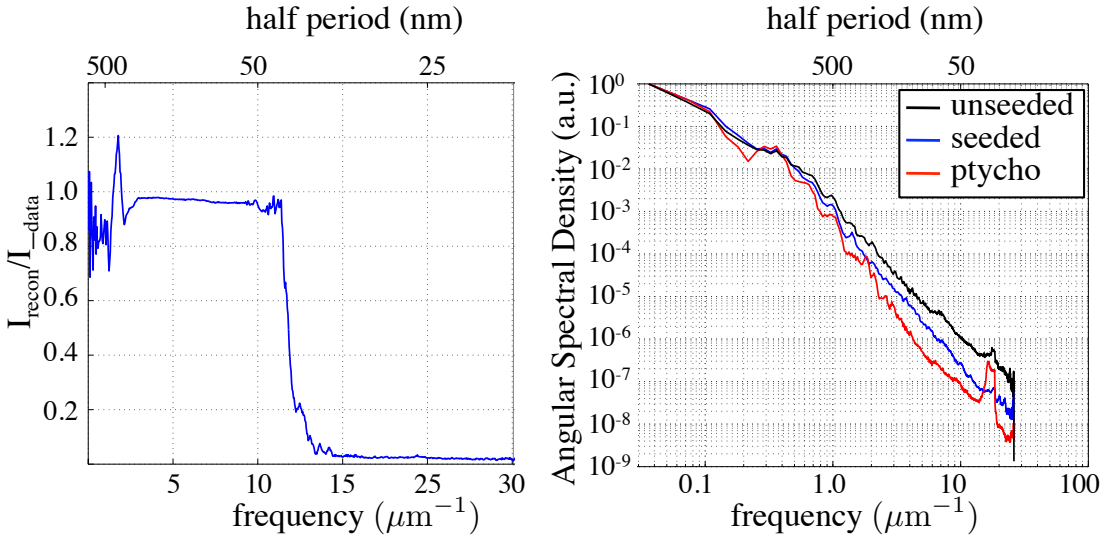

Figure 4.5: Analysis of the PRTF in (a) gives a resolution limit of 42 nm. The Power Spectral Density in (b), gives a resolution limit of 35 nm. The PSD resolution limit occurs when the PSD first deviates significantly from a power law.

Alternately the Power Spectral Density (determined via the Fourier transform) of the recovered complex sample transmission function can be used to estimate the achieved reconstruction resolution. This estimate is obtained by plotting the average angular frequencies and determining where the plot deviates from a power law of the form $y = ax^k + b$. This corresponds to deviations from linear form in the log-log in Fig. 4.5 (b), occurring at a half period of approximately 35 nm.

A one-dimensional sigmoid function (also known as a shifted logistic function) of the form

$$f(x) = \alpha + \frac{\beta}{(1 + e^{-(x-\gamma)/\delta})}, \tag{4.23}$$

can be used to the estimate the reconstruction resolution by measuring the reconstruction edge sharpness. A lithographed edge (known to be sharp) was used with a least squares minimisation with a sigmoid function of the form in Eq. 4.23 to determine the optimal values for α, β, γ and δ. The edge sharpness and can be well modelled by fitting the one dimensional Gaussian function

$$G(x) = A \exp\left[-\frac{(x-B)^2}{2\sigma^2}\right]. \tag{4.24}$$

to the bell shaped gradient of the sigmoid function in Eq. 4.23. This reduces the edge sharpness measurement to a single parameter, namely σ in Eq. 4.24. The FWHM measurement of the Gaussian in Eq. 4.24 gave an estimate of 70 nm for the

reconstruction resolution.

The sigmoid edge sharpness fitting scheme targets a specific feature and is less prone to noise and systematic artefacts that may appear as features when using the PTRF or Spectral Density resolution analysis, yielding a sample image reconstruction resolution of 70 nm.

4.9 Fresnel CDI Tomography using Ptychography

The geometry for a three-dimensional Fresnel CDI tomography experiment is an extension of the two dimensional Fresnel CDI geometry discussed in §4.4, with the additional requirement of rotating the sample through a series of projections using a tomographic stage. In three-dimensional CDI [76], the two-dimensional diffraction patterns are assembled into a three-dimensional diffraction volume and the sample is recovered using the three-dimensional implementation of the iterative phasing methods discussed in Chapter 3. As discussed in §3.6 the oversampling condition for a three-dimensional diffraction volume places a strict limitation on the useable sample size.

A critical distinction in three-dimensional tomographic CDI is the ability to assemble a series of extended sample transmission projections obtained using ptychography into a three-dimensional reconstruction. Under the projection approximation, the projected sample transmission function for a particular projected angle, θ, is written via Eq. 4.16 as a line integral through the three-dimensional complex refractive index, $n(\mathbf{r}_4, z) = 1 - \delta(\mathbf{r}_4, z) + i\beta(\mathbf{r}_4, z)$, i.e.

$$T_\theta(\mathbf{r}_4, z_4) = \exp\left[-ik \int \left[\delta(\mathbf{r}_4, z) - i\beta(\mathbf{r}_4, z)\right] dz\right]. \tag{4.25}$$

A series of projected ptychographic sample transmission reconstructions may be used with computed tomography [79] to obtain a three-dimensional mapping of the sample over an extended field of view. This technique was first performed in plane wave CDI to produce an extended three-dimensional image of a mouse femur [110]. The highly overlapped regions are exposed to a correspondingly greater radiation dose with adverse implications for *in vivo* cellular imaging.

In §4.7 it was shown that high quality ptychographic Fresnel CDI reconstructions can be used to improve neighbouring projection reconstructions. Importantly, these improvements are attained without a corresponding increase in the radiation dose for the current projection. A total of 90 bootstrapped projection reconstructions were aligned using image registration and used to obtain a series of sinograms.

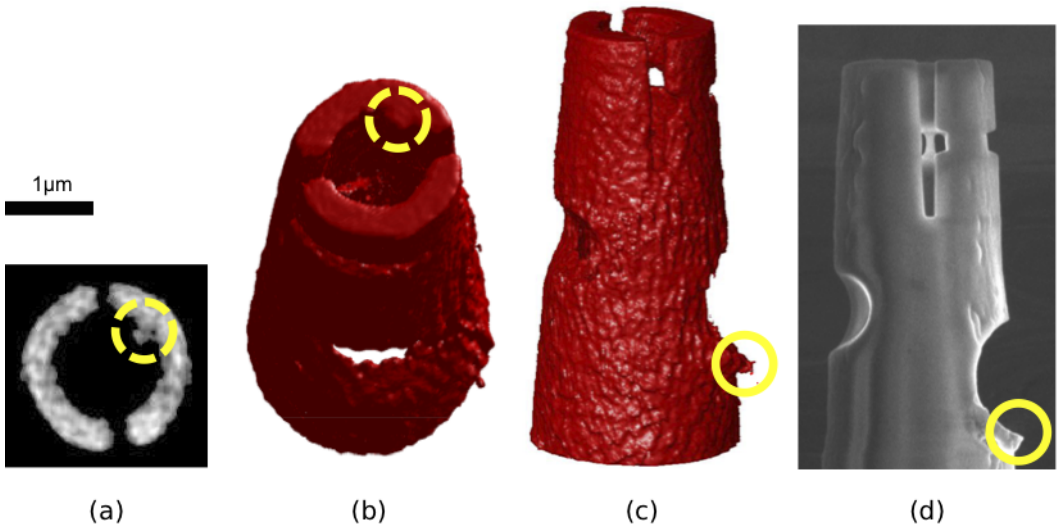

Figure 4.6: Three- dimensional reconstructed sample transmission function using ptychography with tomography. (a) Tomographic slice through the upper region of the tomographic reconstruction surface rendered in (b) and (c). The internal protrusion highlighted within the yellow dashed circle is a ridge running through the tip interior. (d) an SEM image shows the extrusion in (c) circled in yellow.

These were used to yield a total of 300 slices through the sample using the inverse radon transform via the "iradon" MATLAB routine with linear interpolation and a Hamming filter. An example reconstructed phase slice is provided in Fig. 4.6 (a). The slices were stacked into a three-dimensional quantitative map of the sample transmission phase. The final three-dimensional result is shown as a surface rendering in Fig. 4.6 (b) and (c). The etched features of the capillary, also visible in the SEM in 4.6 (d) are clearly defined. Additional features include the internal protrusion highlighted by the yellow dashed circles in (a) and (b), and the extruded material highlighted by the yellow circles in 4.6 (c) and (d). The appearance of these features demonstrates the ability of the technique to resolve nanoscale features of the internal and external sample structure.

Analysis of the tomographic slices yields the quantitative measurement of three-dimensional refractive index components, $\delta(\mathbf{r}_4, z)$ and $\beta(\mathbf{r}_4, z)$. The sample transmission phase, ϕ and sample transmission amplitude, $|T|$, are related to the components of the refractive index via

$$\begin{aligned} \phi_\theta &= -k \int_z \delta(\mathbf{r}_4, z) dz \\ \log(|T_\theta|) &= k \int_z \beta(\mathbf{r}_4, z) dz. \end{aligned} \tag{4.26}$$

Computed tomography using either ϕ_θ or $\log(|T_\theta|)$ yields the refractive index com-

ponents δ and β respectively. Accordingly, the reconstructed three-dimensional voxels for each component yield the measured refractive index components as $\delta = (5.9 \pm 1.4) \times 10^{-5}$ and $\beta = (1.5 \pm 0.4) \times 10^{-5}$, where the δ and β components are given in the form $\mu \pm \sigma$. The refractive index of typical borosilicate glass at this energy, with a density of 2.3 g/cm^3, yields $\delta = 7.23 \times 10^{-5}$ and $\beta = 6.93 \times 10^{-6}$ [120]. The discrepancy in the mean calculated δ value is attributed to the reconstruction issues noted above in §4.5, in particular the radial artefacts present in the two-dimensional series of projected sample reconstructions used to obtain the three-dimensional sample mapping. At 2.535 keV the interaction of the specimen with the incident illuminating wavefield is dominated by phase effects. The amplitude of the reconstructed transmission function for each projection was of accordingly lower quality, resulting in a poor estimate of the β component.

4.10 Discussion and Conclusions

The ability to characterise the incident illuminating wavefield is a significant advantage in Fresnel CDI experiments, enabling the extent of the sample to be defined by the illumination, as well as providing a reference phase to obtain quantitative measurements of the scattering sample. This reference phase, along with the ability to retain low spatial frequency shape information, result in rapid and consistent algorithm convergence, providing a robust mechanism for high-resolution quantitative sample image retrieval.

The improved convergence characteristics appear to be accompanied by an increased sensitivity to stability, resulting in a series of radial artefacts throughout the retrieved sample transmission function. These artefacts are thought to be responsible for the deviations from the experimentally obtained mean refractive index values ($\delta = (5.9 \pm 1.4) \times 10^{-5}$ and $\beta = (1.5 \pm 0.4) \times 10^{-5}$) compared to the expected value ($\delta = 7.23 \times 10^{-5}$ and $\beta = 6.93 \times 10^{-6}$) [120].

During the tomographic data acquisition the target sample had a radius of approximately 25 μm. Although this parameter was corrected for *post facto*, the accumulated error due to uncertainty in the focus-sample distance (a critical algorithm parameter), degraded the reconstruction quality and is therefore expected to have reduced the δ and β estimation accuracy. Through improvements to the scanning stage and tomography stage (in particular placing the tomography stage beneath the scanning stage) the sample precession radius can be reduced to 5 μm.

The radial artefacts were greatly reduced using ptychography. The use of the ptychographic reconstructions to bootstrap neighbouring non-ptychographic recon-

structions resulted in a significant improvement in the series of projected sample transmission functions and consequently an improved three-dimensional tomographic map of the sample. Despite this, the qualitative and quantitative improvements in the ptychographic phase reconstructions suggest that providing the dose lies under feature destroying levels, the best imaging results would be achieved by performing ptychography for every projection.

The motivation to perform ptychography in Fresnel geometry rather than the standard plane wave case is somewhat diminished due to the similar improvement in convergence characteristics when using ptychography in either Fresnel or plane wave geometry. Additionally, the use of a plane wave geometry resolves a number of the reconstruction issues relating to stability sensitivity. As a result, the remainder of this thesis is dedicated to research in high-resolution plane wave ptychography, proposing a number of modifications to the ptychographic algorithm that extend and improve its use in high resolution X-ray imaging.

CHAPTER

FIVE

COHERENT PLANE WAVE PTYCHOGRAPHY

Though there is a natural interest in developing ptychography as a robust nanoscale imaging method for extended, non-crystalline samples, a recent development of the ptychographic algorithm allows simultaneous retrieval of the illuminating probe [68, 121], enabling a quantitative study of the illuminating wavefield in the sample plane. In §5.2, a series of ptychographic datasets, obtained over several longitudinal sample translations, are used to quantitatively measure the evolution of the illuminating wavefield under propagation. These measurements are shown to be in strong quantitative agreement with the equivalent wavefields obtained under numerical propagation.

The fundamental mechanism underlying ptychography is the ability to use additional information supplied by translating a target sample through a constant illuminating probe and recording the resulting diffraction data [3, 67, 68, 121]. The second study in this chapter discusses a method for generating additional data redundancy by scanning the target sample through several distinct illuminating probes. Using the resulting probe-diverse ptychographic datasets, a modified form of the ePIE algorithm is used to retrieve the sample transmission function and all illuminating probes simultaneously. This is shown to yield significant improvements in the reconstructed sample transmission function compared to the standard single probe method.

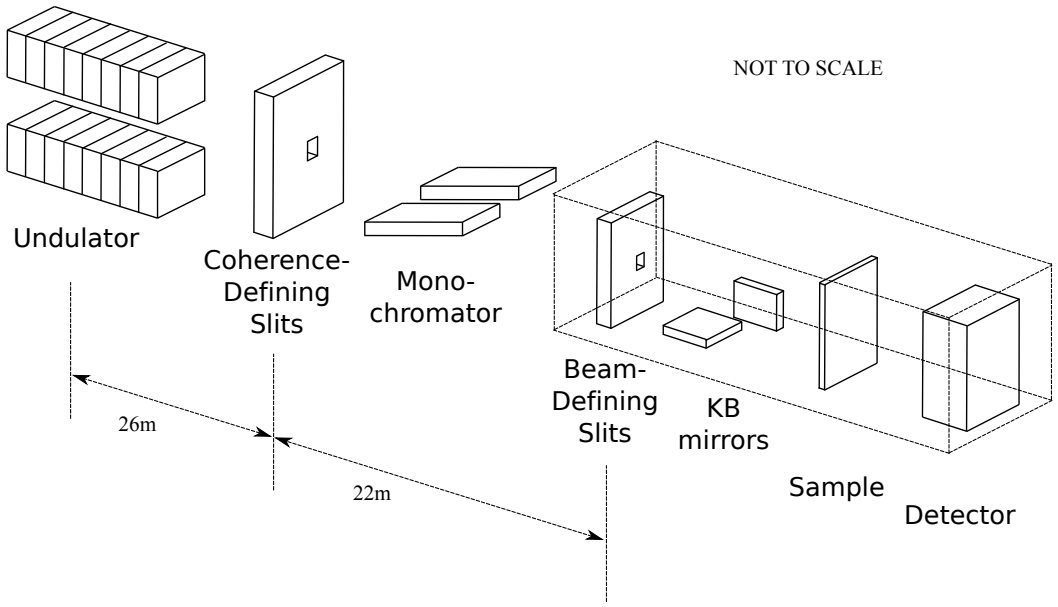

Figure 5.1: Schematic of the APS beamline 34-ID-C. A set of coherence-defining slits are used to control the coherence characteristics of the source. The beam-defining secondary slits, located within the 34-ID-C hutch, are used to select out a portion of the beam. The KB mirrors were used to focus the beam on the sample and the resulting diffraction patterns recorded with a CCD or photon-counting detector.

5.1 APS beamline 34-IDC

The experiments in this chapter were performed at the Advanced Photon Source (APS) beamline 34-ID-C. All measurements were conducted at an X-ray energy of 9 keV ($\lambda = 0.138$nm), selected out by a Si(111) double crystal monochromator [122]. A horizontal coherence-defining slit located 26 m from the undulator is used as a secondary source. A set of beam-defining secondary slits, located approximately 48 m downstream from the undulator and within the 34-ID-C experimental hutch can be used to vary the spatial coherence characteristics of the incident illumination. A beamline schematic is provided in Fig. 5.1

The beam was focused using a compact set of Kirkpatrick-Baez (KB) mirrors placed between the secondary slits and sample plane as shown in Fig. 5.1. The mirrors were coated with a 50 nm platinum layer over a 10 nm chrome base-layer to improve the reflectivity at higher energies. The incidence angle of the mirrors was 3.0 milliradians relative to the beam. The vertical and horizontal focusing mirrors were positioned approximately 0.22 m and 0.10 m upstream of the sample stage respectively. The KB mirrors were positioned to capture all of the beam, including the diffracted beam lobes, from the secondary slits. The sample was mounted on an xyz nPoint NPXY100Z25A piezo scanning stage for nano-translations in the x,

Parameter	Value
Wavelength	0.138 nm
Sample-Detector distance, position a	2.31 m
Sample-Detector distance, position b	2.30 m
Sample-Detector distance, position c	2.29 m
Detector pixel size	20 μm
Cropped array size	128×128
Sample plane pixel size	124 nm
Ptychographic scanning area	10 μm $\times$ 10 μm
Radial scan trajectory increment	0.75 μm
Ptychographic scanning points	141

Table 5.1: Probe propagation experimental parameters at APS beamline 34-ID-C

y, and z directions. Larger translations were performed using a set of step-motors mounted below the piezo scanning stage.

5.2 Probe recovery and propagation

Using the experimental geometry outlined in §5.1, with the secondary slits set to 20 μm $\times$ 20 μm (a setting known to yield a coherent beam at this beamline), and placed approximately 0.12 m upstream of the entrance side of the vertical focusing mirror, a tungsten tip was scanned across a 9 keV incident beam. The scanning trajectory covered a 10 μm $\times$ 10 μm area, consisting of a series of concentric circles with 5n equally spaced points on the n^{th} ring. The radial increment was set to be 0.75 μm between adjacent rings, resulting in a scanning array of 141 points. This scanning pattern has been shown to remove scanning artefacts associated with a raster scanning grid [121]. The resulting diffraction patterns were recorded 2.31 m downstream from the tungsten tip sample on a Princeton Instruments PI-MTE 1300B CCD with a 20 μm$\times$20 μm pixel size, summing 60 images for scan position to improve the signal statistics. The data acquisition for each image was 0.05 seconds. Two additional ptychographic datasets were obtained, with the sample translated by 10.0 mm and 20.5 mm downstream of the original sample position. The region of interest in the diffraction patterns was a 128×128 pixel array centred on the diffraction peak. At an energy of 9 keV and a propagation distance of 2.31 m, Eq. 3.10 yields the sample plane sampling interval as 124 nm. The relevant experimental parameters are summarised in Table 5.1.

Using the ePIE algorithm detailed in §3.10.2, with an initial probe estimate based on a knife edge scan of the central probe lobe and a random binary estimate of the sample transmission function, the sample transmission function and probe

were retrieved for each of the three longitudinal translations. The retrieved probe amplitudes in order of decreasing propagation distance are shown in Fig. 5.2 (a)-(c).

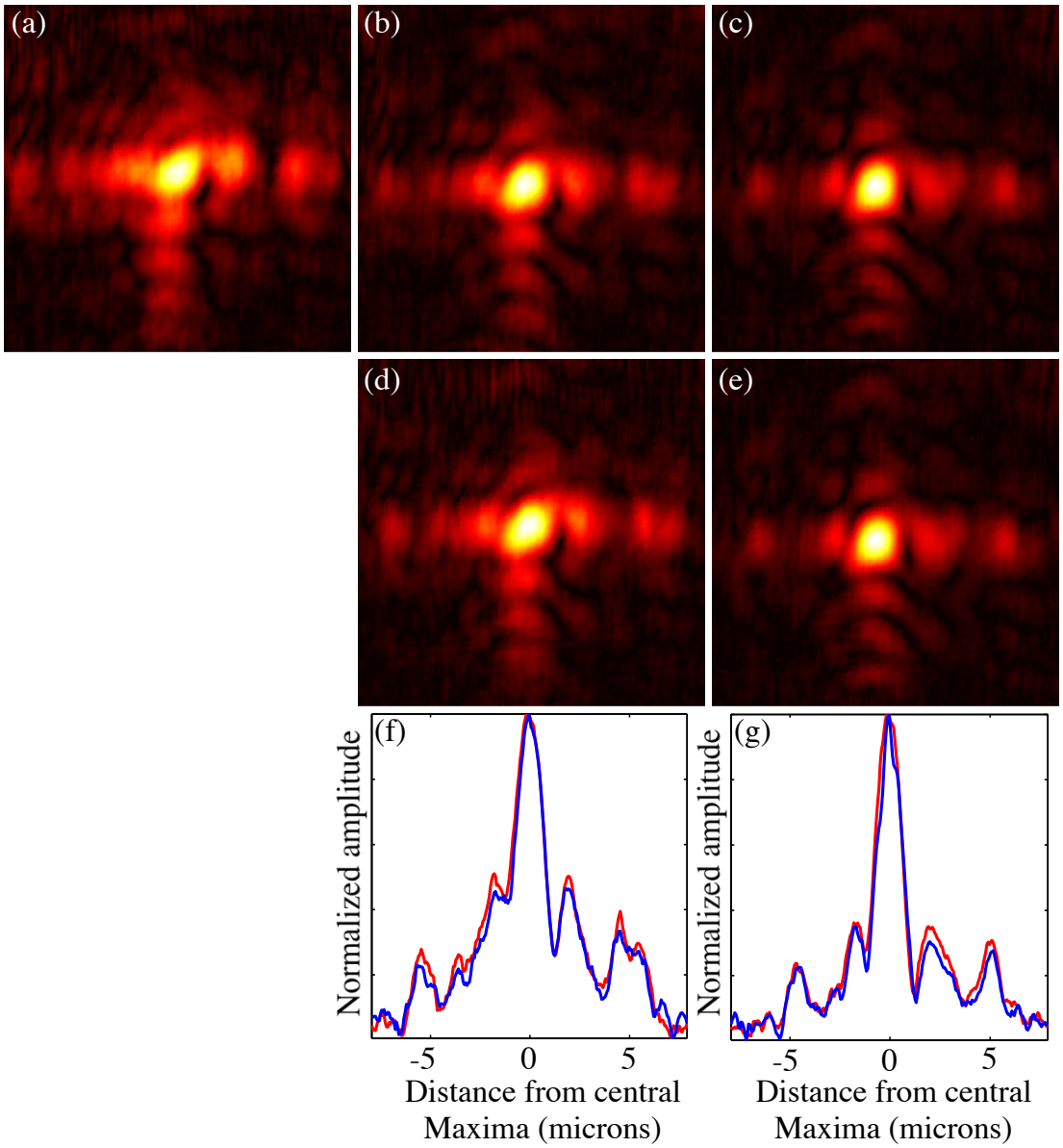

Figure 5.2: Normalized reconstructed probe amplitudes at three planes spaced longitudinally in 10 mm steps are shown in (a), (b) and (c). The wavefronts in (d) and (e) were numerically propagated to give the probe amplitudes in (d) and (e) respectively. (f) shows centre pixel amplitude plots for (b) (red) and (d) (blue). The corresponding plots for (c) and (e) are shown in (g). The scale in (f) and (g) is common to all images.

The probe wavefronts in Fig. 5.2 (a)-(c) may be numerically propagated to any plane using the Fresnel propagator in Eq. 2.15, or its near field limiting form in Eq. 2.14. This allows verification of the probe retrieval accuracy through comparison of the ptychographically retrieved wavefronts with their numerically propagated counterparts. At an energy of 9 keV and a propagation distance of approximately 10 mm,

the Fresnel number, N_F, is $N_F = (L/2)^2/\lambda z \approx 20$. In this range the angular spectrum method is valid and the numerically propagated wavefield is obtained through an application of Eq. 2.14. The reconstructed probe at the original sample position (Fig. 5.2 (a)) was numerically propagated 10 mm to obtain an estimate of the X-ray wavefront at the middle longitudinal sample translations (see Fig. 5.2 (d)). The reconstructed probe in the central longitudinal sample position (see Fig. 5.2 (b)) was numerically propagated 10 mm to the third longitudinal sample position, obtaining the numerical estimate of the X-ray wavefront in Fig. 5.2 (e). Comparison between the illumination wavefronts obtained by ptychography and their numerically propagated counterparts indicates an excellent agreement, demonstrating consistency over the tested longitudinal sample position range. This is supported by the line-out plots running in the vertical direction through the centre pixel in Fig. 5.2 (f) and (g).

For very short-range propagation (≈ 1 μm) the X-ray wavefield propagating from the KB mirrors is essentially constant. This is important when the propagation distance between the beam focus and sample varies over the sample scan trajectory as the ptychographic algorithm places a strict requirement on a constant illuminating wavefront. This is an issue in Bragg ptychography, where the sample orientation is no longer aligned perpendicular to the beam and the xy nano-translations result in the focus-sample distance varying over the scanning trajectory. The measurements show that on the scales encountered in a typical scanning trajectory the requirement of a constant probe should not impede the possibility of performing Bragg ptychography using KB mirrors as the focusing mechanism.

5.3 Multiple Probe Ptychography

The standard ptychographic method scans a target sample through a single coherent probe. The resulting ptychographic dataset may be used to the retrieve the sample transmission function and probe simultaneously [4, 68]. Here a modification to the ePIE algorithm is proposed that can use ptychographic data generated from several distinct illumination probes on a common target sample. The recovery of the sample transmission function, $O(\mathbf{r})$, using n distinct probes with a set of associated sample scan trajectories, $\{\mathbf{s}_1, \mathbf{s}_2, ..., \mathbf{s}_n\}$, requires the simultaneous retrieval of a set of probes, $\{P_1(\mathbf{r}), P_2(\mathbf{r}), ..., P_n(\mathbf{r})\}$. This is implemented by modifying the ePIE algorithm in §3.10.2 to include the exit surface waves from each of the probes on the common target sample, i.e. at the k^{th} scan position of the n^{th} scanning trajectory, $\mathbf{s}_{n,k}$, the

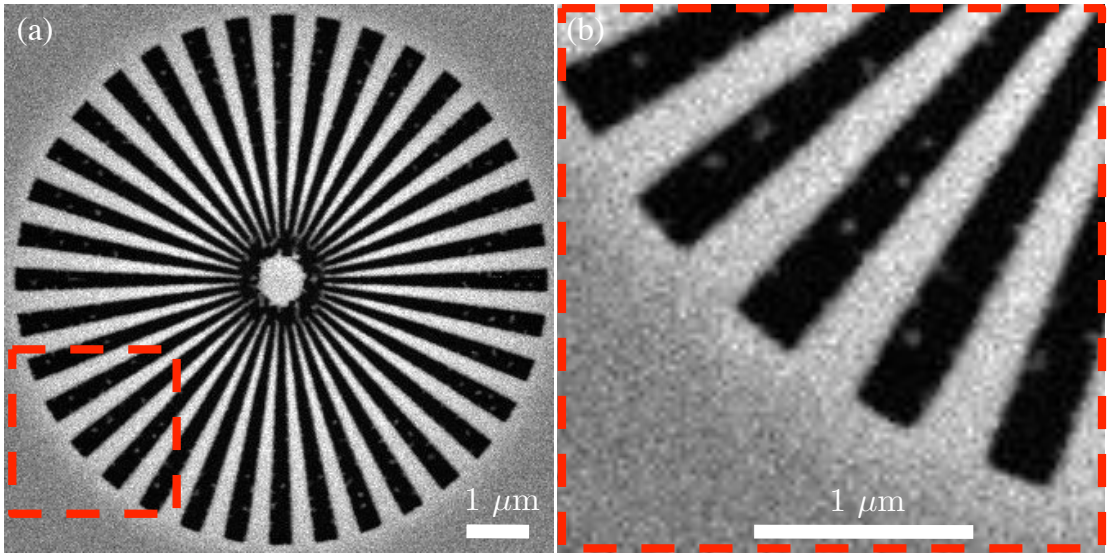

Figure 5.3: An example SEM image of the lithographed star aperture test pattern is shown in (a). The lithographed regions are shown in black. Tungsten deposits, seen as small ($\sim$ 50nm) spots in the closeup in (b) are the result of errors in the lithographing process.

j^{th} estimate of the exit surface wave, $\psi_n^j(\mathbf{r}, \mathbf{s}_{n,k})$, is written as

$$\psi_n^j(\mathbf{r}, \mathbf{s}_{n,k}) = O^j(\mathbf{r}) P_n^j(\mathbf{r} - \mathbf{s}_{n,k}).$$

The algorithm proceeds as for the ePIE algorithm detailed in §3.10.2, enabling the set of probe estimates, $\left\{P_1^j(\mathbf{r}), P_2^j(\mathbf{r}), ..., P_n^j(\mathbf{r})\right\}$ to be simultaneously updated in conjunction with the current estimate of the common sample transmission function, $O^j(\mathbf{r})$.

5.3.1 Demonstration with a mixed ptychographic dataset

The experiment was performed at the APS beamline 34-ID-C (detailed in §5.1), using a 9 keV beam. A test sample was manufactured by first depositing a 1.5 μm tungsten layer onto a 100 nm thick silicon nitride support membrane. A series of star shaped apertures were lithographed into the tungsten layer, allowing approximately 70% transmission [120] through the non-lithographed regions and full transmission through the lithographed regions. The apertures were 9 μm wide, consisting of 36 spokes arranged in a circular pattern. An example SEM image of one of the apertures is shown in Fig. 5.3. The sample was scanned through a scanning trajectory similar to that detailed in §5.2, with the scan parameters set to a 0.5 μm radial increment covering a 10 μm $\times$ 10 μm area, resulting in a scanning array of 323 points for each ptychographic dataset. The secondary slits were set to widths of 10 μm $\times$ 20 μm in

Parameter	Value
Wavelength	0.138 nm
Sample-Detector distance	3.2 m
Detector pixel size	55 μm
Cropped array size	256×256
Sample plane sampling interval	31 nm
Slit width a	10 μm $\times$ 20 μm
Slit width b	20 μm $\times$ 40 μm
Slit width c	40 μm $\times$ 50 μm
Ptychographic scanning area	10 μm $\times$ 10 μm
Radial scan trajectory increment	0.5 μm
Ptychographic scanning points	323

Table 5.2: Multiple-probe experimental parameters at APS beamline 34-ID-C

the horizontal and vertical directions respectively. The resulting diffraction patterns were recorded 3.2 m downstream from the sample using a Timepix readout chip with 55 μm square pixels. 30 images were summed for each ptychographic scan position. The acquisition time for each image was 0.04 seconds. The measurements were repeated using secondary slit widths of 20 μm $\times$ 40 μm and 40 μm $\times$ 50 μm. The region of interest (ROI) in all diffraction datasets was set to a 256×256 pixel array centred on the diffraction peak. At 9 keV with a propagation distance of 3.2 m, the sample plane sampling interval is 31 nm (see Eq. 3.10). The relevant experimental parameters are summarised in Table 5.2.

5.3.2 Standard ePIE reconstructions

Using the standard ePIE algorithm, the sample transmission function and probe were retrieved for the 10 μm $\times$ 20 μm dataset. The reconstructions used an initial random binary estimate for the sample transmission function and a probe estimate based on a knife edge scan of the central lobe. The algorithm was run for 500 iterations. The resulting reconstructed sample transmission amplitude and phase are shown in Fig. 5.4 (a) and (b) respectively. The reconstructed probe amplitude is shown in the inset in Fig. 5.4 (a). There is a correspondence between the rapid and erroneous variation in the reconstructed sample transmission amplitude and phase. The phase reconstructions are presented in wrapped form as the erroneous rapid phase transitions introduced subsequent errors in the unwrapping algorithms. The ePIE algorithm was used for a further 500 iterations, with no measurable improvement in the reconstructed sample transmission function. A second ptychographic sample transmission retrieval was performed using the 20 μm $\times$ 40 μm dataset, with the same algorithm parameters used in the 10 μm $\times$ 20 μm reconstructions. The re-

sulting probe and target sample reconstructions are provided in Fig. 5.4 (c) and (d) respectively. The reduction in reconstruction quality compared to the 10 μm$\times$20 μm dataset reconstructions may be largely attributed to the decrease in probe size and corresponding decrease in overlap ratio, an effect noted elsewhere [71].

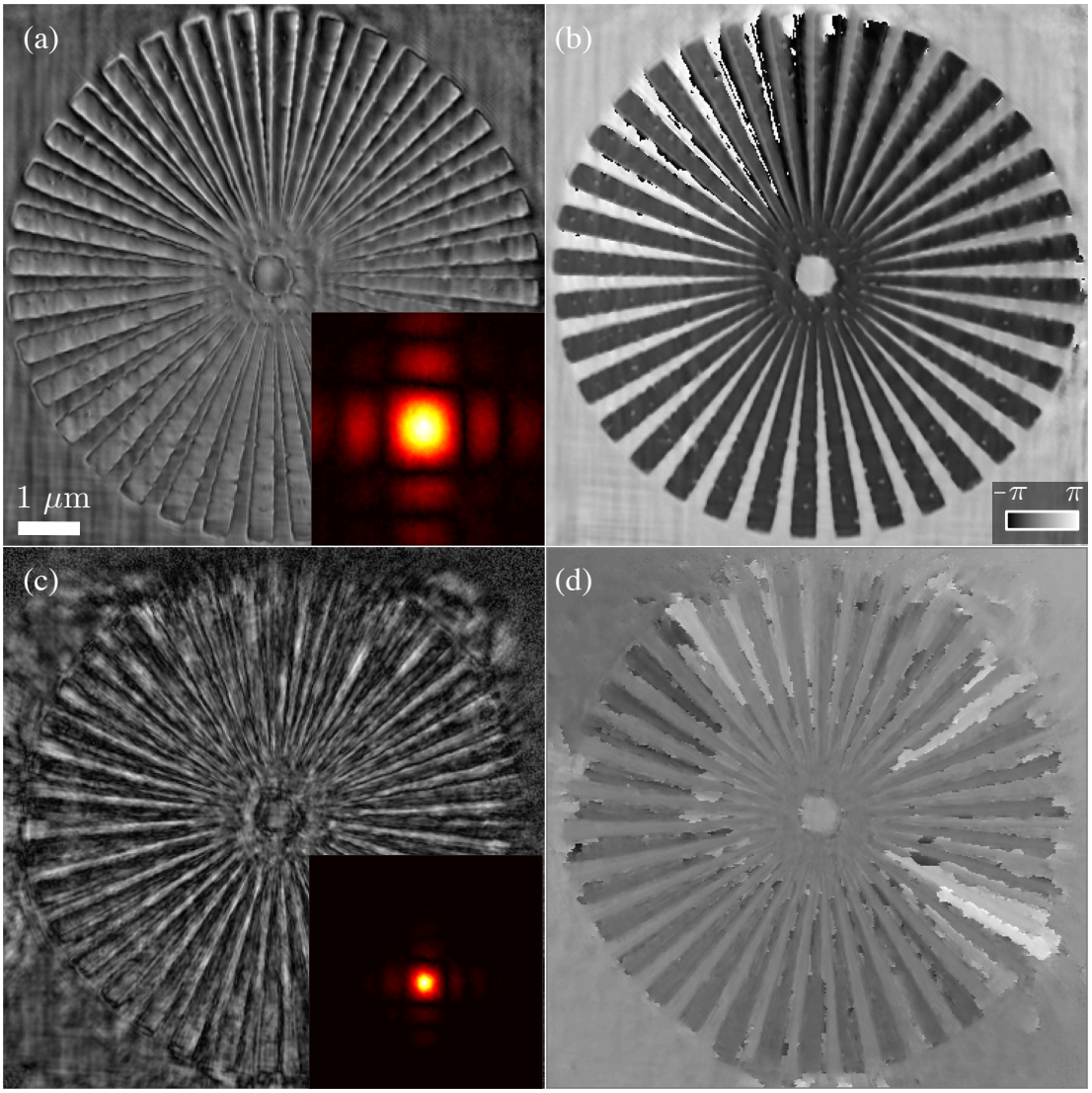

Figure 5.4: (a) and (b) show the retrieved sample transmission amplitude and phase using the 10 μm $\times$ 20 μm dataset. The probe amplitude is shown in the inset in (a). The corresponding reconstructions for the 20 μm $\times$ 40 μm dataset are shown in (c) and (d).

5.3.3 Multiple probe reconstructions

Using the multiple probe ePIE algorithm, the target sample was reconstructed using data from both the 10 μm $\times$ 20 μm and 20 μm $\times$ 40 μm ptychographic datasets. The reconstructions used a sparsely distributed dataset, where the diffraction data from every second point in each dataset was used, resulting in a mixed dataset with

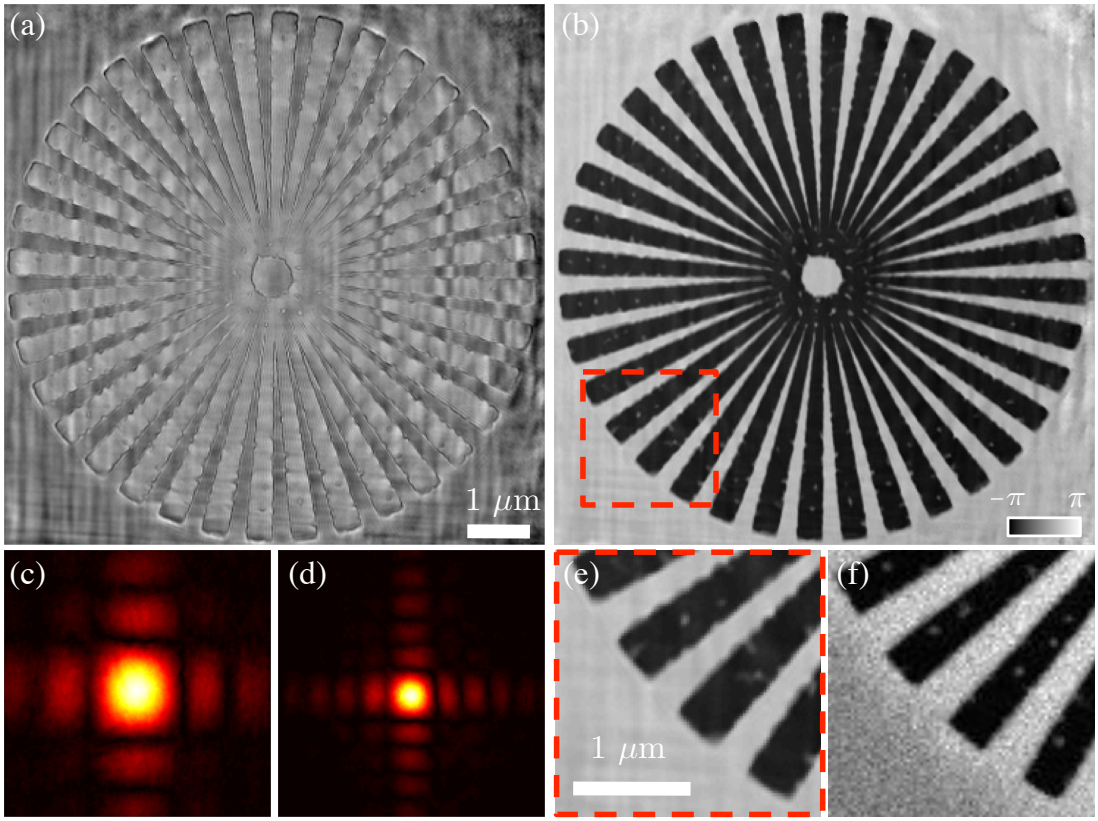

Figure 5.5: Multiple probe sample transmission amplitude and phase reconstructions using half the data from both the 10 μm $\times$ 20 μm and 20 μm $\times$ 40 μm datasets in (a) and (b) respectively. The simultaneously retrieved probes are shown in (c) and (d). The tungsten deposits, seen as small ($\sim$ 50nm) "spots" in the close-up in (e), are also present in the SEM close-up in (f). The sample contained multiple copies of the star shaped aperture and based on the spot distribution a different star was imaged by the SEM

323 diffraction images, i.e. the same amount of data used in the standard single probe ePIE reconstructions detailed in §5.3.2. As half the data was obtained using a smaller probe this *reduced* the total probe overlap compared to the 10 μm $\times$ 20 μm dataset. The reconstructions were initialised using the same algorithm parameters as the single probe reconstructions detailed in §5.3.2, in particular the same initial estimates for the sample transmission and both probes. The multi-probe ePIE algorithm was used for 500 iterations, reconstructing the sample transmission function and both probes simultaneously.

The reconstructed sample transmission function and both reconstructed probes are shown in Fig. 5.5. There is an improvement in the accuracy of the reconstructed sample image, resolving the phase wrapping artefacts present in the standard single probe ePIE reconstruction. In particular the tungsten deposits, seen as small "spots" ($\sim$ 50 nm), are clearly resolved throughout the reconstructed multiple probe ePIE sample transmission function in Fig. 5.5. According to the distribution of the

Dataset	Dataset Density	Dataset Size
10 μm $\times$ 20 μm	Full	323
20 μm $\times$ 40 μm	Full	323
10 μm $\times$ 20 μm + 20 μm $\times$ 40 μm	Sparse	323
10 μm $\times$ 20 μm + 20 μm $\times$ 40 μm	Full	646
10 μm $\times$ 20 μm + 20 μm $\times$ 40 μm + 40 μm $\times$ 50 μm	Full	969

Table 5.3: Multiple-probe ptychographic dataset parameters at APS beamline 34-ID-C

lithographed imperfections in the SEM image in Fig. 5.5 (e), the SEM image is not of the same star aperture imaged in the multiple-probe reconstructions. The improvements obtained using a sparsely distributed multiple-probe dataset data were obtained using the same amount of ptychographic data, i.e. there was no increase in the data collection time compared to the single probe reconstructions.

Using the same algorithm parameters the multi-probe ePIE algorithm was tested using all recorded data from the 10 μm $\times$ 20 μm and 20 μm $\times$ 40 μm ptychographic datasets (i.e. 626 diffraction images in total). The resulting reconstruction demonstrated no significant improvement compared to the sparsely distributed multi-probe ePIE reconstructions. A final test was performed using additional data from the 40 μm $\times$ 50 μm dataset (i.e. 969 data-points in total). Again there was no significant improvement in the reconstructed sample transmission function. A summary of the different multiple probe tests is provided in Table 5.3

5.4 Undersampling and ptychography

Until recently the sampling requirements in ptychography were assumed to be the same as those in CDI (see §3.6), i.e. that the scattered wavefield $\psi(\mathbf{r})$ is required to fall to zero outside the boundary defined by half the array size in the sample plane in each linear dimension or

$$D \leq \frac{\lambda z}{2\Delta_D} \tag{5.1}$$

where D is the maximal width of the scattered wave, λ is the illumination wavelength, z is the sample-detector propagation distance, and Δ_D is the detector pixel size. Despite the ability to image extended samples using ptychography, satisfying the criterion in Eq. 5.1 imposes a strict limitation on the useable probe size. This can be difficult to achieve at higher X-ray energies, or when the available sample-detector distance is relatively short. Recent work [123] suggests that a conventionally undersampled ptychographic dataset can artificially satisfy the criterion in Eq. 5.1 for each diffraction image by considering each recorded pixel as a sum of n synthetic

subpixels with a sum equal to the recorded pixel value, I_j, where j is an index ranging over the number of recorded pixels per diffraction image. The algorithm is known as the "sPIE" algorithm, in which the wavefield at the m^{th} subpixel, $\Psi_{j,m}$, is modified to match the recorded intensity of the j^{th} pixel, I_j, via

$$\Psi'_{j,m} = \frac{\Psi_{j,m}\sqrt{I_j}}{\sqrt{\sum_{m=1}^{n}|\Psi_{j,m}|^2}}, \tag{5.2}$$

The remainder of the algorithm proceeds as for the ePIE algorithm in §3.10.2, enabling the recovery of the sample transmission function, probe, and synthetic pixel values. The ability to retrieve these synthetic pixel values yields an estimate of the diffraction dataset sampled on a grid at a rate determined by the upsampling ratio.

The discussion below is restricted to a few observations on the consequences of reconstructing the sample transmission and probe from an undersampled ptychographic dataset. The probe lobes in Fig. 5.5 (c) and (d) extend to the edges of the reconstructed probe array. As both the probe and scattering object are greater than half the array size, the sample exit surface wave, defined by multiplication of the sample transmission and probe functions, must therefore violate Eq. 5.1. Despite this, it appears that the additional information in a ptychographic dataset enables the reconstruction of the sample transmission function when using undersampled ptychographic data and the standard ePIE algorithm.

The sample transmission amplitude and phase in Fig. 5.5 (a) and (b) are actually cropped arrays. The full sample transmission phase reconstruction is provided in Fig. 5.6 (a). The reconstructed sample transmission phase contains periodic artefacts spaced by 256 pixels, i.e the periodicity is the same as the diffraction data array size. The artefacts are most notable at the reconstructed sample transmission edges, where the probe overlaps are of low density, resulting in the "shadowing" artefacts near the edges of the reconstructed sample transmission function. The 256 pixel periodicity is shown in Fig. 5.6 (c), a 256×256 array obtained using a circular array shift of the region indicated in Fig. 5.6 (a). The reconstructions were repeated using 10 distinct random binary initial estimates of the sample transmission function, yielding the same periodic artefacts for each reconstruction, but with variation in the intensity of the artefacts. This would appear to be an indication of non-uniqueness in the solution of the sample transmission and probe functions when using undersampled ptychographic diffraction data.

The sample image was reconstructed using the sPIE algorithm (i.e. using Eq. 5.2) with an up-sampling ratio of 4, yielding an artificially upsampled wavefield estimate composed of $4 \times 256 = 1024$ pixels in each linear dimension. This is equivalent

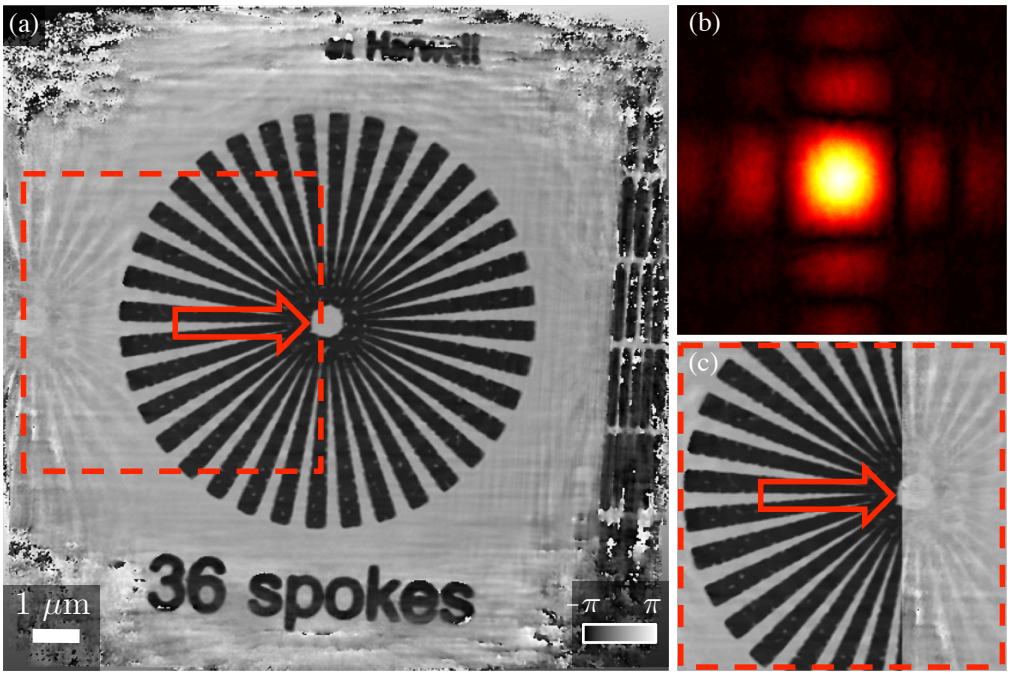

Figure 5.6: Reconstructing the sample image from an undersampled ptychographic dataset results in a series of periodic artefacts throughout the reconstructed sample image, most notable at the array edges where the probe overlaps are of lower density. The 256 pixel periodicity is shown in (c), a 256 pixel wide region obtained using a circular array shift of the highlighted region in (a).

to sampling the diffraction data on a 1024×1024 array with $55/4 = 13.75$ μm pixels. The reconstructed sample transmission phase and amplitude is provided in Fig. 5.7 (a) and (b), with an enlargement of the region in (a) provided in (c). The 256 pixel periodicity noted in the standard ePIE reconstructions in Fig. 5.6 was also present in the sPIE reconstructions, with an additional set of periodic artefacts, spaced by $2 \times 256 = 512$ pixels from the original image. The reconstructions were obtained for 10 distinct initial estimates of the sample transmission function. The periodic artefacts were present in all sample reconstructions with the same spacing, but with variation in the relative intensity of the periodic artefacts, as noted in the standard ePIE reconstructions.

The reconstructed probe amplitude corresponding to the sample transmission phase and amplitude reconstructions in Fig. 5.7 (a) and (b) is shown in Fig. 5.7 (d). The upsampling algorithm has enabled the probe to be imaged over an extended field of view, with a number of additional probe lobes not present in the standard ePIE reconstructions in Fig. 5.6 (b). This has been achieved due to the ability of the sPIE algorithm to share information acquired over a ptychographic dataset between the estimated wavefields, yielding an estimated far-field wavefield sampled at a higher rate than the recorded diffraction data. However, similarly to the reconstructed

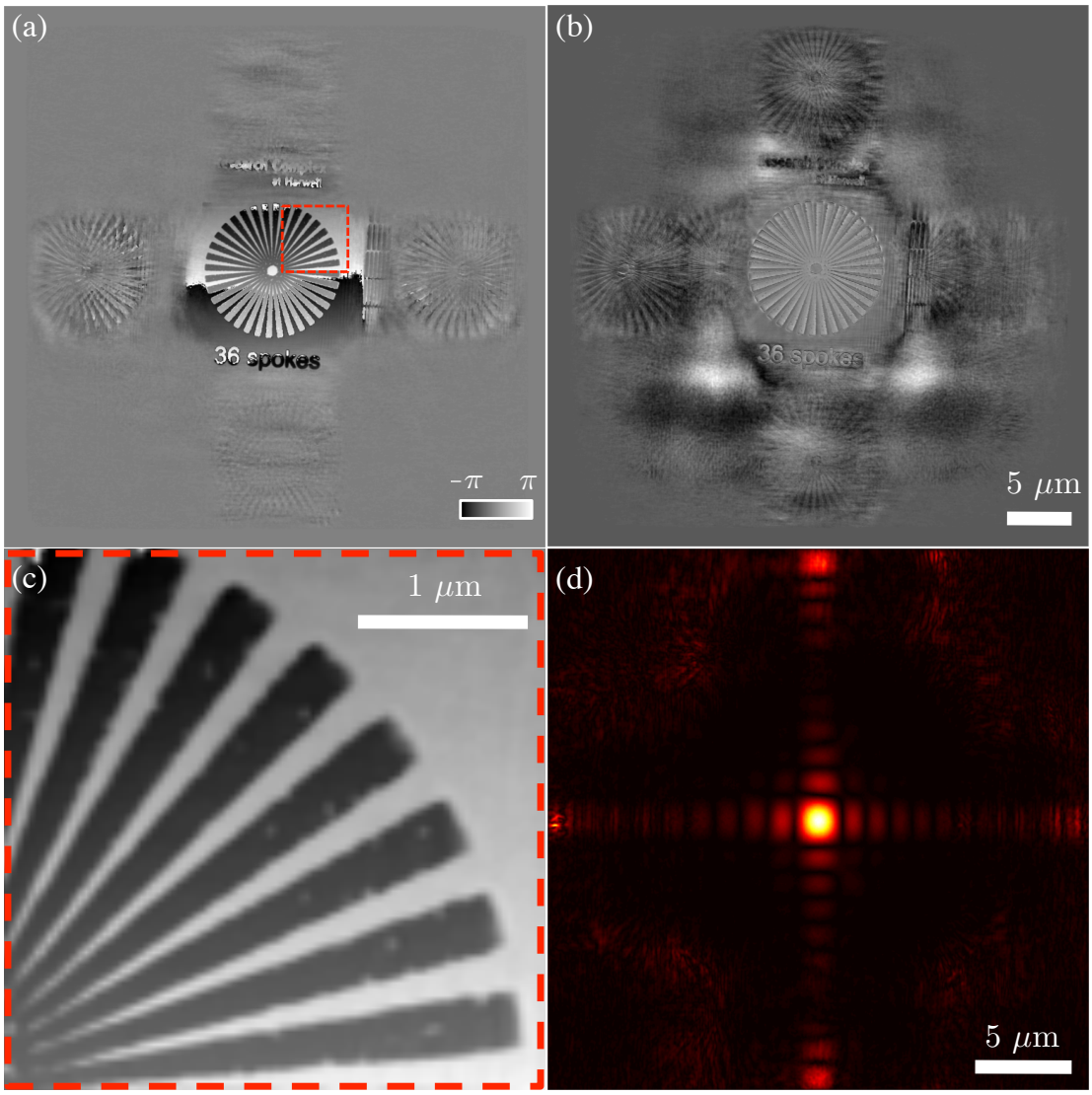

Figure 5.7: Artificially satisfying the Nyquist criterion with an upsampling ratio of 4. The reconstructed sample transmission and phase in (a) and (b) exhibit periodic artefacts spaced by 256 pixels, including a second set spaced by 512 pixels from the central sample image. An enlargement of the region indicated in (a) is provided in (c). The reconstructed probe in (d) also exhibits the 512 pixel periodicity (the upsampled probe is a 1024×1024 array).

sample, the reconstructed probe contained periodic artefacts spaced by 512 pixels. The periodic artefacts, noted in both the sample and probe reconstructions using an upsampling rate of 4, were also present when reconstructing the sample using upsampling ratios of 8 and 12.

The sample was then reconstructed using the sPIE algorithm and a dataset comprised of 2×2 binning of the original ptychographic diffraction dataset, i.e. using diffraction data binned to 128×128 pixels. The reconstructions using an upsampling ratio of 2. This results in a reconstructed sample, probe, and artificially upsampled

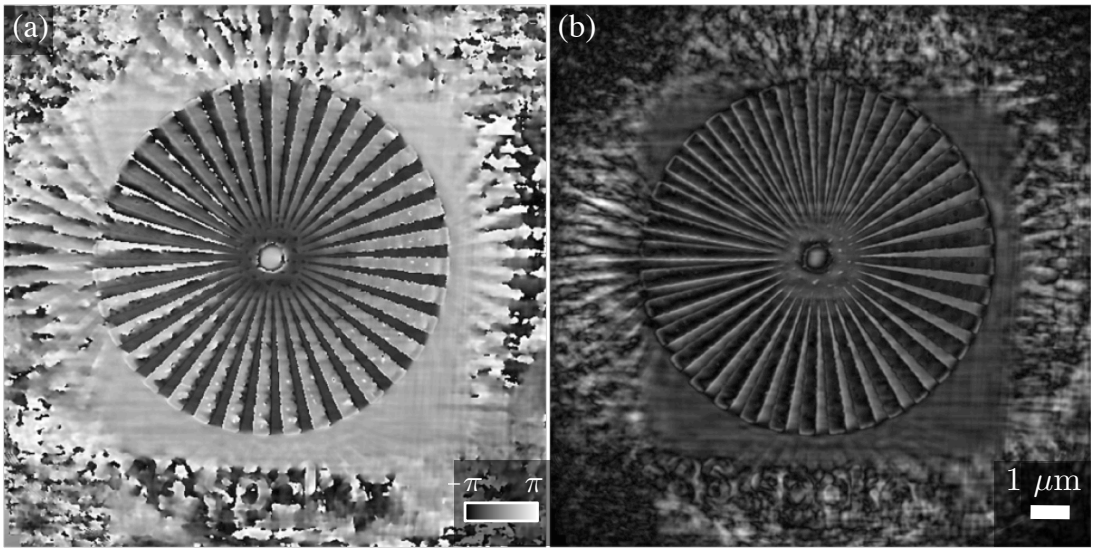

Figure 5.8: Sample transmission phase and amplitude reconstructions using a 2×2 binned ptychographic dataset (i.e. 128×128 pixels) with an upsampling factor of 2. This results in a reconstructed probe and sample of the same size as the standard ePIE reconstructions in Fig. 5.6. The periodic artefacts are now spaced by 128 pixels, i.e. the size of the binned diffraction data.

wavefield of equal size and sampled at an equal spacing to that obtained using the original, unbinned diffraction dataset and the standard ePIE algorithm shown in Fig. 5.6. The resulting reconstructed sample transmission phase and amplitude are shown in Fig. 5.8. The sample transmission phase is presented in wrapped form due to the rapid transitions in phase introducing subsequent phase wrap errors in the phase unwrapping algorithms. The reconstructions contain periodic artefacts spaced by 128 pixels, i.e. a spacing equal to the array size of the binned diffraction data. Although this is most clear at the reconstructed array edges, the overlapping of the periodic artefacts with the reconstructed sample image results in a decrease in reconstruction quality compared to the reconstructions in Fig. 5.6.

A final test was performed by embedding the 128×128 binned diffraction data in a 256×256 array of zeros. The sample was reconstructed with the sPIE algorithm and an upsampling ratio of 2. The reconstructed sample contained periodic artefacts with the same relative position as the reconstructions in Fig. 5.8. These studies indicate reconstructing the sample transmission function using an undersampled ptychographic dataset introduces a series of periodic artefacts with a periodicity determined by the array size of the diffraction data that cannot be removed regardless of the upsampling ratio.

5.5 Conclusion

The wavefield propagating from a set of KB mirrors was determined over several longitudinal translations using a plane wave ptychographic dataset and the ePIE algorithm. The measurements show that the wavefield remains constant for all practical purposes over a ptychographic scanning trajectory. For longer propagation distances $\sim$ 10mm, the retrieval of the illuminating wavefields using ptychography demonstrates excellent consistency with the numerically propagated wavefields over the tested longitudinal sample position range (i.e. approximately 20 mm). The repeated measurements provide a convincing verification that the ePIE algorithm is capable of reliably retrieving the X-ray wavefield at different longitudinal sample translations.

A modification to the ePIE algorithm was proposed that can use mixed ptychographic datasets obtained from scanning a target sample through multiple distinct illumination probes. The algorithm was tested using ptychographic X-ray data, yielding significant improvement in the reconstructed sample transmission function while using an equal sized ptychographic dataset. There was an apparent limitation in the achievable reconstruction quality that prevented further improvement in the reconstruction with additional ptychographic data. This may be explained by regarding the solution of the sample transmission function as the search for a fixed number of unknowns that can be calculated to within an accuracy determined by intrinsic experimental issues including data noise, beam coherence and uncertainty in the sample position. Once this limit is approached, additional ptychographic data only yields incremental improvements in the reconstruction quality.

Using the sPIE algorithm, it was shown that an undersampled diffraction dataset could be used to yield images of the illuminating wavefield over an extended field of view. Though it appears that the additional information in a ptychographic dataset compensates for undersampling the diffraction data, the studies presented here indicate that regardless of the amount of additional ptychographic data or increase in the up-sampling rate, the use of undersampled data introduces artefacts with a periodicity determined by the diffraction data size that cannot be removed using the standard ePIE algorithm or sPIE extension. The variation in intensity of the periodic artefacts when using distinct initial estimates of the sample transmission function would appear to be an indication of uniqueness issues in the solution of the sample transmission and probe when using an undersampled ptychographic dataset. If the sample occupies a region greater $N \times \Delta_s$, where the diffraction images are recorded on an $N \times N$ array and Δ_s is the sample plane sampling interval, it appears that the overlapping of the sample image and the periodic artefacts can have a

significant impact on the reconstruction accuracy. If the data is not of sufficient quality, the effect of these periodic artefacts may not be immediately obvious, but may have consequences in the algorithm convergence characteristics.

CHAPTER

SIX

POSITION CORRECTIONS IN PTYCHOGRAPHY

Ptychography is a robust, high-resolution phase retrieval imaging method, but the achievable resolution is limited by the precision of the measured sample translations. Uncertainty in the sample positions arises from a number of experimental issues including stage misalignment, non-linear drift, or hysteresis in the probe scan coils. Minimising the impact on the recorded sample positions can present major experimental challenges and may not be possible to address completely. Enforcing an incorrect scanning trajectory on a ptychographic reconstruction results in a conflict between the overlap constraint and resulting propagated wavefield estimate, and the diffraction dataset. This is a particular problem when the uncertainty in the recorded sample positions is greater than the sample plane sampling interval, as determined by Eq. 3.10. For the ptychographic X-ray experiments presented in this thesis, this corresponds to a uncertainty of approximately 50 nm. Stability is an even greater problem in electron ptychography [74, 75], where the electron beam must be controlled to within 50 pico-metres to ensure the uncertainty in the sample positions does not significantly impact the sample image retrievals. The failure to meet these requirements can result in a series of artefacts in the reconstructed sample image or the complete failure of the algorithm to converge.

In this chapter, an efficient iterative sample position correction scheme is proposed. The optimisation of the sample scan trajectory is performed simultaneously with the retrieval of the sample transmission function and illuminating wavefield. This operation is performed using only the ptychographic diffraction data and recorded sample translations. The algorithm operation and accuracy is first tested

Parameter	Value
Wavelength	0.138 nm
Sample-Detector distance	2.0 m
Detector pixel size	20 μm
Cropped array size	256×256
Sample plane sampling interval	54 nm
Ptychographic scanning area	10 μm $\times$ 10 μm
Radial scan trajectory increment	0.5 μm
Ptychographic scanning points	323

Table 6.1: Simulated parameters chosen to match APS beamline 34-ID-C.

using a simulated ptychographic dataset and a series of simulated distorted scan trajectories. The position optimisation is tested using synchrotron X-ray data, resulting in an improved sample image reconstruction as well as a position correction map for the sample scan trajectory.

6.1 Position errors in Ptychography

The simulated parameters were chosen to realistically model X-ray experiments conducted at the APS beamline 34-ID-C. The simulated target sample was chosen to model the star shaped aperture detailed in §5.3.1. The simulated aperture consisted of 36 equally spaced sectors, each subtending an angle of 4° on a circle of radius 4.5 μm, with a non-lithographed circular central region of radius 0.2 μm. The simulated probe was generated by near-field propagation (Eq. 2.14) of a plane wave exiting a binary circular aperture of radius 2 μm. A ptychographic diffraction dataset was simulated using a scanning trajectory based on previous studies at this beamline (see §5.3). The simulated parameters are summarised in Table 6.1.

The simulated diffraction data included Poisson noise to match the characteristics of the CCD in use at APS beamline 34-ID-C. A series of simulated distorted scanning trajectories, with jitter ranging from 1 pixel to 20 pixels, in steps of 1 pixel for each successive dataset, were used to reconstruct the probe and sample from the simulated diffraction data.

Using the standard ePIE algorithm (see §3.10.2) and the simulated ptychographic dataset, the sample transmission function and probe were reconstructed over the range of distorted scanning trajectories, resulting in 20 sample and probe reconstructions in total. The reconstructions were obtained using the ePIE algorithm for 250 iterations. The initial sample transmission and probe estimates were a random binary array and a circular binary array 10 pixels wider than the known probe dimensions respectively.

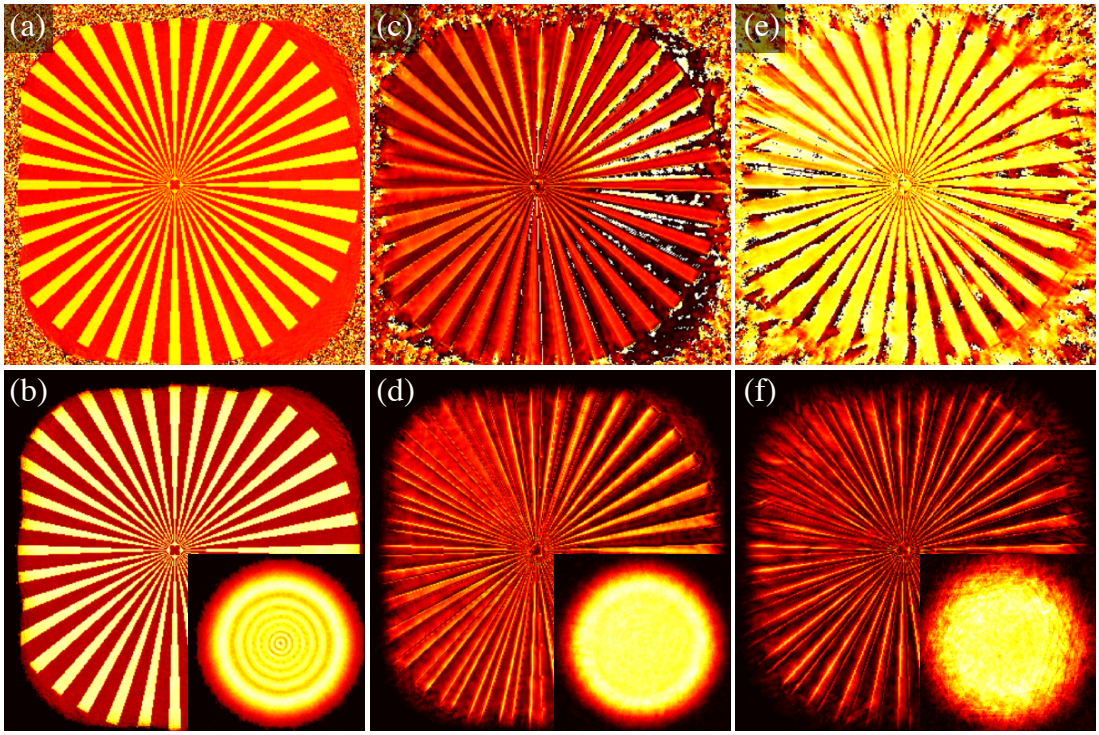

Figure 6.1: Ptychographic reconstructions in the presence of sample position jitter. The reconstructed sample transmission phase and amplitude reconstructions with 1 pixel jitter are shown in (a) and (b) respectively, with the corresponding reconstructed probe amplitude shown in the inset. The corresponding reconstructions for 5 pixel and 20 pixel jitter are shown in (c) and (d), and (e) and (f) respectively.

The sample transmission phase and amplitude reconstructions for simulated jitter of 1 pixel are shown in Fig. 6.1 (a) and (b). The reconstructed probe amplitude is provided in the inset in 6.1 (b). The corresponding reconstructions for 5 pixel and 20 pixel jitter are shown in (c) and (d), and (e) and (f) respectively. Though the sample transmission function was reasonably robust to 3 pixel jitter, significant artefacts, including the rapid and erroneous variation in the retrieved sample transmission phase and corresponding artefacts in the retrieved sample transmission amplitude were introduced for jitter above 5 pixels (see Fig. 6.1 (c)). These regions introduced additional artefacts in the phase unwrapping algorithms and therefore the retrieved phase is presented as a wrapped array. The retrieved probe demonstrated a higher sensitivity to the sample translation errors, with the algorithm failing to retrieve the probe structure for jitter above 3 pixels.

6.2 Cross Correlation Analysis

The cross correlation, $r_{fg}(x_0, y_0)$, between two two-dimensional arrays, $f(x, y)$ and $g(x, y)$, with $M \times N$ elements, is

$$\begin{aligned} r_{fg}(x_0, y_0) &= \sum_{x,y} f(x, y) g^*(x - x_0, y - y_0) \\ &= \sum_{u,v} F(u, v) G^*(u, v) \exp\left[2\pi i \left(\frac{u x_0}{M} + \frac{v y_0}{N}\right)\right] \end{aligned} \tag{6.1}$$

where $F(u, v)$ is the two-dimensional Fourier transform of $f(x, y)$ and similarly for $G(u, v)$. The cross-correlation is commonly used in image registration, where, for two image arrays, $f(x, y)$, and $g(x, y)$, the location of the cross-correlation peak determines the offset or translation between the two arrays. An efficient algorithm for determining the cross-correlation peak to sub-pixel accuracy was proposed by Guizar-Sicairos *et al.* [124]. In this algorithm, the location of the cross-correlation peak is first determined using Eq. 6.1, then refined by up-sampling the cross-correlation by a factor κ in a small neighbourhood about this initial estimate, enabling the location of the cross-correlation peak to be determined to within $1/\kappa$ pixel accuracy. The calculation can be iteratively refined via repeated upsampling, resulting in a highly efficient and accurate algorithm to determine the cross-correlation peak. This algorithm was used to obtain the cross-correlation peaks locations used in the proposed algorithm.

6.2.1 Cross correlation analysis with simulated data

Using the same simulated ptychographic dataset and distorted scanning trajectories, $\mathbf{s}'$, detailed in §6.1, the cross-correlation peak locations were determined using the previous and current estimates of the sample transmission function, $O(\mathbf{r})$, at the *same* scan position, $\mathbf{s}'_k$, i.e. setting $f(x, y) = O^j(\mathbf{r} - \mathbf{s}'_k)$ and $g(x, y) = O^{j+1}(\mathbf{r} - \mathbf{s}'_k)$ in Eq. 6.1, where j denotes the current iteration. The operation was performed for each scan position, $\mathbf{s}'_k$, yielding a vector, $\mathbf{e}$, containing the cross-correlation peaks for a particular iteration. Example mean cross-correlation peaks for jitter of 5 and 10 pixels are shown in Fig. 6.2 (a) and (b) respectively. The magnitude of the cross-correlation peak locations are very small (< 0.01 pixels), placing high demands on the accuracy of the registration algorithm.

The sample translation errors can be written as the difference between the true scan trajectory used to obtain the diffraction data, $\mathbf{s}$, and the distorted scanning trajectory, $\mathbf{s}'$, used to reconstruct the sample transmission function and probe from

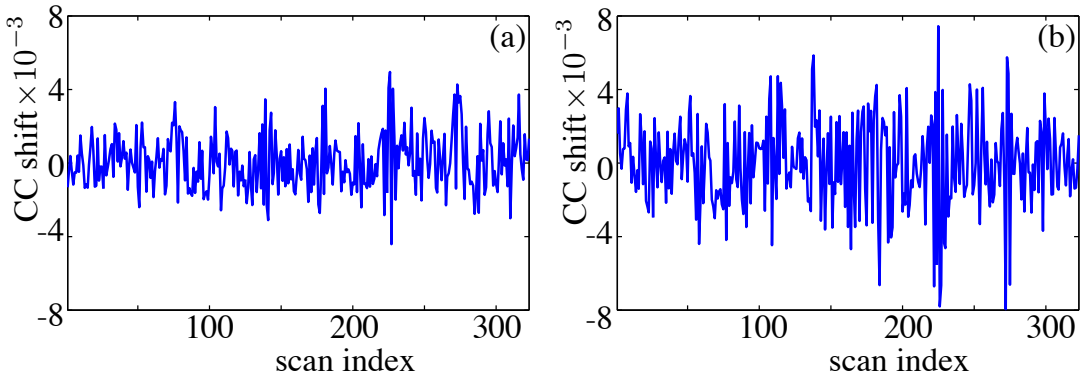

Figure 6.2: Mean cross-correlation shifts over the scanning trajectory for 5 and 10 pixel jitter in (a) and (b) respectively.

the ptychographic diffraction data, i.e.

$$f(\mathbf{s}, \mathbf{s}') = |\mathbf{s} - \mathbf{s}'|. \tag{6.2}$$

The ptychographic reconstructions and cross-correlation calculations were obtained using information on the distorted trajectories, $\mathbf{s}'$, i.e. the true scan trajectory, $\mathbf{s}$, was not provided to the algorithm.

Fig. 6.3 compares the mean of the cross-correlation peaks, $\mathbf{e}$, with the gradient function of the known sample translation errors, $\nabla f(\mathbf{s}, \mathbf{s}')$. These quantities differ by several orders of magnitude and the plots are normalised for clarity, yielding the result that is central to the operation of the proposed position correction algorithm:

$$\begin{aligned} \nabla f(\mathbf{s}, \mathbf{s}') &= \nabla |\mathbf{s} - \mathbf{s}'| \\ &\approx \mathbf{c}_k \mathbf{e}_k. \end{aligned} \tag{6.3}$$

The cross-correlation vector, $\mathbf{e}$, can therefore be used to approximate the gradient function of the scanning trajectory errors, $\nabla f(\mathbf{s}, \mathbf{s}')$, yielding information on the true scanning trajectory, $\mathbf{s}$. This information is obtained using only the diffraction data and the distorted scanning trajectory, $\mathbf{s}'$, without knowledge of the true scan trajectory. This allows the cross-correlation vector to be used to retrieve the true scan trajectory using the "gradient descent" algorithm, discussed below.

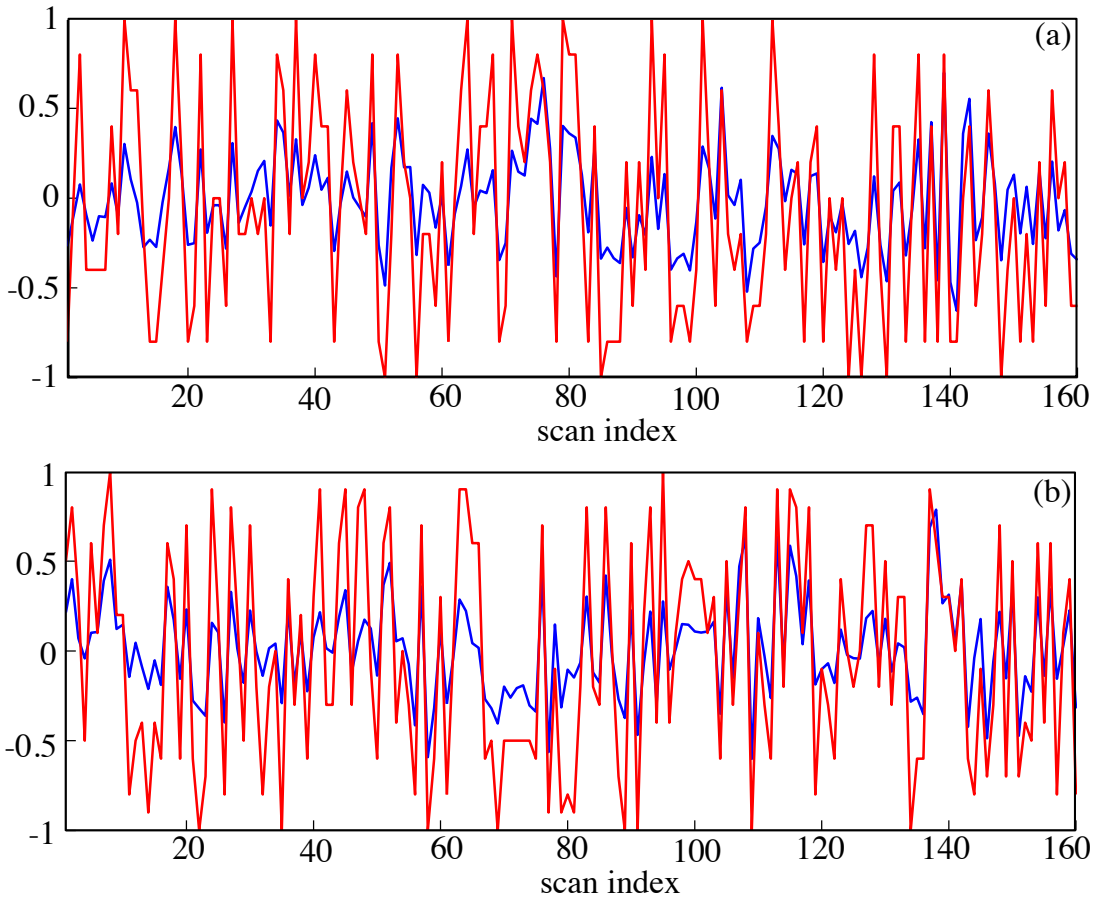

Figure 6.3: Comparison between the (normalised) horizontal components of the calculated cross-correlation peaks (blue) and the position errors (red) for for 5 and 10 pixel jitter shown in (a) and (b) respectively. For clarity only the first 160 positions in each scan trajectory are shown.

6.3 Scan Trajectory Optimisation

Iterative correction of the sample scan trajectory may be classed as a non-linear optimisation problem that minimises the residual function

$$f(\mathbf{s}, \mathbf{s}') = |\mathbf{s} - \mathbf{s}'|, \tag{6.4}$$

where $\mathbf{s}$ is the true trajectory and $\mathbf{s}'$ is the current trajectory estimate. If $f(\mathbf{s}, \mathbf{s}')$ is approximately quadratic near a local minimum, an optimisation may be performed using a general class of iterative techniques known as methods of descent. These include gradient descent, steepest descents, Newton-Raphson, and conjugate gradient methods. Though these iterative optimisation schemes vary in their complexity and convergence rate, they are variants on the following general iterative algorithm:

1. Determine a descent direction, Δx^j.

2. Choose a step size, α^j, where $\alpha^j > 0$.

3. Update the current iterate, x^j, via the relation $x^{j+1} = x^j + \alpha^j \Delta x^j$.

The sequence is repeated until $\Delta x^j \to 0$. Choosing the descent direction to be the negative gradient, i.e. setting $\Delta x^j = -\nabla f(x^j)$, results in the "gradient descent" algorithm. In the special case that f is a Euclidean norm (e.g. the residual function in Eq. 6.4), the optimisation belongs to the class of "steepest descent" methods, a group that possesses improved convergence characteristics compared to the general gradient descents group.

It was demonstrated in §6.2.1 that the gradient residual function, $\nabla f(\mathbf{s}, \mathbf{s}')$, can be estimated using the cross-correlation peak location vector detailed in §6.2. This allows the scanning trajectory estimate to be refined using gradient descent optimisation, with the descent direction determined by the cross-correlation peak vector, $\mathbf{e}$. The current estimate of the scanning trajectory, $\mathbf{s}'$, is updated by first choosing a step size, α_k^j, such that

$$\begin{aligned} \mathbf{s}_k'^{j+1} &= \mathbf{s}_k'^{j} + \alpha_k^j \nabla f(\mathbf{s}_k, \mathbf{s}_k') \\ &\approx \mathbf{s}_k'^{j} + \beta_k^j \mathbf{e}_k^j, \end{aligned} \tag{6.5}$$

where β_k^j is a new set of multiplicative constants. In the proposed modification to the ePIE algorithm, the cross-correlation between previous and current estimates of the sample transmission function, $O^j(\mathbf{r} - \mathbf{s}_k')$ and $O^{j+1}(\mathbf{r} - \mathbf{s}_k')$, at an estimated sample position $\mathbf{s}_k'$, yields a small shift signal, $\mathbf{e}_k^j$, that is used to update the sample trajectory estimate via Eq. 6.5. The optimisation is performed for each position estimate, $\mathbf{s}_k'^j$, simultaneously with the probe and sample transmission retrievals.

6.4 Algorithm Performance with Simulated Data

The cross-correlation position correction ePIE algorithm was tested using the simulated ptychographic dataset and series of distorted scanning trajectories discussed in §6.1. The reconstructions used the same algorithm parameters, in particular the same initial probe and sample transmission estimates, as well as the same number of iterations. The cross-correlation position correction was initialised on the 25^{th} iteration. The feedback parameter, β, defined in Eq. 6.5, was set to $\beta = 100$ in all the reconstructions. Example position error retrievals for 5, 10, and 20 pixel jitter are shown in Fig. 6.4 (a), (b) and (c) respectively. The total residual errors, calculated as $f(\mathbf{s}, \mathbf{s}') = |\mathbf{s} - \mathbf{s}'|$, for 5, 10, and 20 pixel jitter are shown in Fig. 6.4 (d), (e) and (f) respectively. Though the cross-correlation position optimisation has

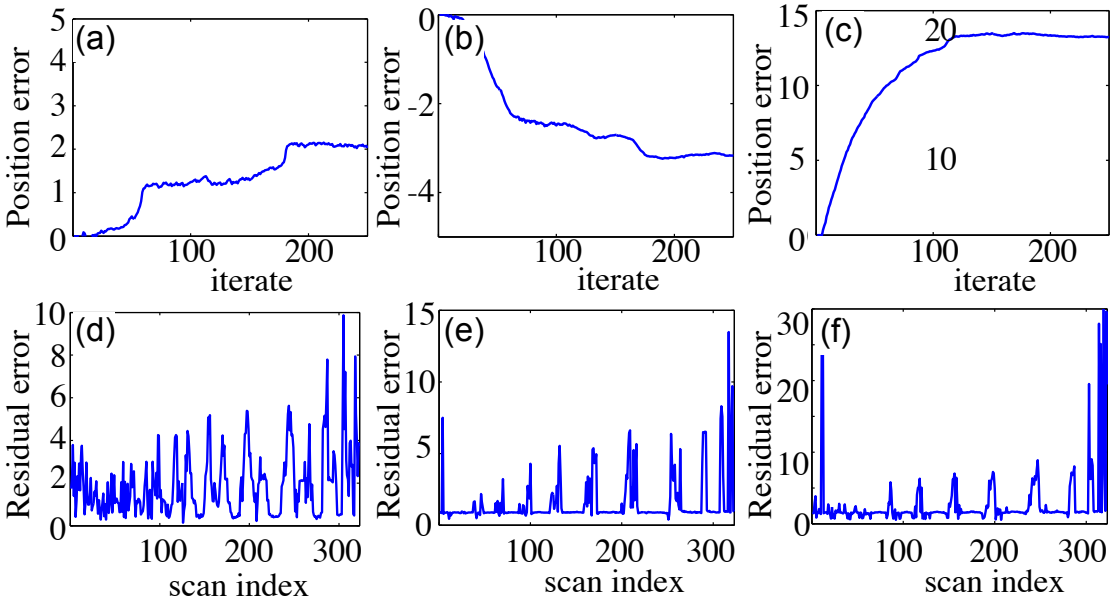

Figure 6.4: Position retrievals for a series of distorted scanning trajectories. (a), (b), and (c) show example position retrievals over 250 iterations for 5, 10, and 20 pixel jitter respectively. The residual errors the full scanning trajectories for 5, 10, and 20 pixel jitter are shown in (d), (e), and (f) respectively. The feedback parameter was set to $\beta = 100$ for all reconstructions.

improved each of the scanning trajectories, there remain a number of residual position errors. It appears that the residual errors propagate between overlap regions, resulting in the regularity in the residual error peaks (the scanning points lie on a series of concentric circles).

6.4.1 Feedback Parameter Optimisation

The feedback parameter, β, is of particular importance as it governs the step-size and consequentially the convergence characteristics of the position retrieval. A poor choice for β can result in the algorithm converging very slowly, or not at all. In the implementation described above, β_k was naively set to be a constant ($\beta = 100$). This is a special (and non-optimal) case. In the optimisation scheme proposed by Zhang *et al.* [125], β is adjusted globally (i.e. though the value for beta is allowed to evolve, the same value for beta is used for the entire scanning trajectory) by comparing previous and current calculated shifts across the entire scanning trajectory. This enables the adjustment of β in a manner similar to negative feedback in control theory, but is nonetheless not an optimal choice as the optimal value for β must vary between each individual position optimisation trajectory.

An optimisation scheme is proposed that optimises the feedback parameter for each individual position estimate. This conforms to the gradient descent algorithm

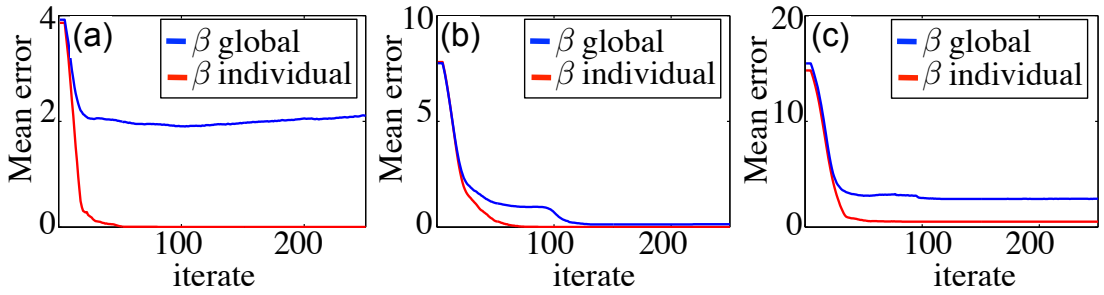

Figure 6.5: Comparison between mean residual errors for position correction feedback parameter optimisation methods with 5, 10 and 20 pixel jitter in (a), (b) and (c) respectively.

in Eq. 6.5. The β_k^j parameter is individually optimised by comparing the current and previous cross-correlation peak calculation, $\mathbf{e}_k^j$ and $\mathbf{e}_k^{j-1}$ for a particular scan position $\mathbf{s}_k$. If $\mathbf{e}_k^j$ and $\mathbf{e}_k^{j-1}$ have the same sign (i.e. the shift is in the same direction), the step-size is increased by setting $\beta_k^j \rightarrow a\beta_k^j$ where $a > 1$. If the sign of $\mathbf{e}_k^j$ and $\mathbf{e}_k^{j-1}$ switches (indicating oscillation) the step-size is reduced by setting $0 < a < 1$. This allows the radius of convergence for each scan position to be individually optimised, leading to improved global convergence characteristics. Fig. 6.5 shows a comparison between the two optimisation methods, demonstrating a clear improvement in the convergence rate and accuracy. Using individual β adjustment, the position errors were retrieved to within less than 0.01 pixel accuracy for all retrievals up to 15 pixel jitter. The 20 pixel jitter mean position retrievals were correct to within 0.5 pixels.

6.5 Algorithm Performance with X-ray Data

The algorithm was tested with X-ray data obtained at the Advanced Photon Source beamline 34-ID-C using the experimental setup detailed in §5.1. The target sample was scanned in a 9 keV beam using an nPoint NPXY100Z25A piezo stage. The sample consisted of a test pattern lithographed into a tungsten layer with the same specifications as those described in §5.3.1. The test pattern is shown in the SEM image of the target sample provided in Fig. 6.6. The scanning trajectory was the same as the trajectory detailed in §5.3. The diffraction dataset was collected by a Princeton Instruments CCD with 20 μm square pixels, placed 2.0 m downstream of the sample. The acquisition time for each image was 0.5 seconds. The region of interest (ROI) in the diffraction patterns was set to be 256×256 pixels. The experimental parameters are summarised in Table 6.2.

The standard ePIE algorithm (i.e. without position correction) was used to reconstruct the sample transmission and probe over 500 iterations, beginning with a random binary sample transmission function estimate and an estimate for the

Parameter	**Value**
Wavelength	0.138 nm
Sample-Detector distance, position c	2.0 m
Detector pixel size	20 μm
Cropped array size	256×256
Sample plane sampling interval	54 nm
Ptychographic scanning area	10 μm $\times$ 10 μm
Radial scan trajectory increment	0.5 μm
Ptychographic scanning points	323

Table 6.2: Position correction parameters at APS beamline 34-ID-C

probe function based on a knife edge scan of the illuminating probe. The resulting sample transmission phase and amplitude are provided in Fig. 6.8 (a) and (b). The cross-correlation correction ePIE algorithm was used to reconstruct the sample transmission and probe functions. An initial estimate of the sample transmission function was determined using the standard ePIE algorithm for the first 50 iterations, followed by 450 iterations using the cross-correlation position correction.

The optimisation scheme was unstable for a small subset of the scanning trajectory positions (< 10), resulting in a rapid rise in the χ^2 metric and sharp peaks in the position correction map at these positions. To address this issue the position updates were only accepted when they reduced in the χ^2 metric for a particular position, resulting in a robust and efficient position-correction mechanism. The unreliability in the cross-correlation optimisation may be partly attributed to noise dominating a very small cross-correlation shift signal. The corrected sample scan trajectory is shown in Fig. 6.7 (c). A comparison between the χ^2 metric across the entire scanning trajectory is provided in Fig. 6.7 (d). The series of scan trajectory positions with the greatest position error correction (i.e. for the deviation for positions with scan trajectory index $190 - 200$) correspond to the region with greatest improvement in the χ^2 metric.

The retrieved sample transmission phase and amplitude using cross-correlation position correction are provided in Fig. 6.8 (c) and (d). There is an improvement in the reconstructed lettering, a reduction in erroneous shadowing near regions of rapid phase change (i.e. in regions near the spoke and lettering edges), and an improvement in the "spot" features in the spokes. These features are remaining tungsten deposits ($\sim$ 50nm) and are also present in the SEM in Fig. 6.6 (the reconstructions in §5.3 also share these tungsten deposit features).

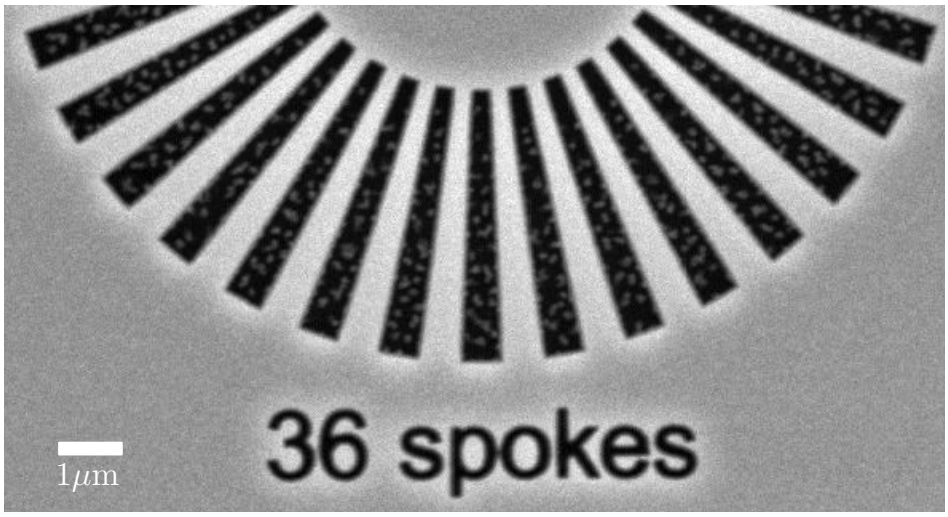

Figure 6.6: SEM image of the sample used in the position correction tests. The sample was manufactured by depositing a tungsten layer on a silicon nitride membrane, then lithographing the tungsten layer. The lithographed features (in black) are transparent to X-rays. The "spot" features in the spokes are remaining tungsten deposits ($\sim$ 50nm).

6.6 χ^2 minimisation position correction

A standard iterative method for correcting the position errors uses the χ^2 metric as the search parameter. For an estimated scan position, $\mathbf{s}'^j_k$, sample transmission estimate, $O^j(\mathbf{r})$ and probe estimate $P^j(\mathbf{r})$, m trial position offsets, $\mathbf{t}^j_{k,m}$, are used to generate m trial exit surface waves, $\psi_{k,m}(\mathbf{r})$, via

$$\psi_{k,m}(\mathbf{r}) = O^j(\mathbf{r} - (\mathbf{s}'^j_k + \mathbf{t}^j_{k,m}))P^j(\mathbf{r}). \tag{6.6}$$

An estimate of the far field intensity distribution is obtained using the usual far-field propagation in Eq. 2.12. The optimal trial position offset, $\mathbf{t}_{k,n}$, is chosen such that the χ^2 metric in Eq. 3.18 is minimised and the current estimate of the scan position $\mathbf{s}^{j+1}_k$ is updated via

$$\mathbf{s}'^{j+1}_k = \mathbf{s}'^j_k + \mathbf{t}^j_{k,n}. \tag{6.7}$$

The operation is performed for all scan position estimates. The χ^2 position correction method was recently optimised by Maiden *et al.* [126].

The χ^2 position-optimisation was tested using the X-ray data described in §6.5. Initial estimates of the sample transmission and probe function were obtained using the standard ePIE algorithm for the first 100 iterations. The χ^2 position-correction was initialised on the 100$^{\text{th}}$ iteration and used to refine the scan trajectory estimate for the remaining 400 iterations. The position search radius was initially set to 5

pixels and gradually reduced to a 1 pixel radius by the 500^{th} iteration for all scan positions. The resulting position correction maps are provided in Fig. 6.7 (a)-(c), indicating a strong agreement between the cross-correlation position correction maps and the χ^2 position correction. As shown in Fig. 6.7 (d), both mechanisms resulted in a reduction of the χ^2 metric, with the χ^2 position correction algorithm demonstrating a small improvement compared to the cross-correlation method. The corrected trajectory in Fig. 6.7 (c) indicates a rotational correction. As the scan trajectory consists of a series of concentric rings, this results in the sinusoidal form of both the horizontal and vertical position correction maps in Fig. 6.7 (a) and (b) respectively, as well as the χ^2 correction maps in Fig. 6.7 (d). The coupling between these quantities is explored in a later study in §7.5.2.

The reconstructed sample transmission amplitude and phase using χ^2 correction are shown in Fig. 6.8 (e) and (f). There is a significant improvement in the reconstructed features compared to the uncorrected sample transmission reconstructions in Fig. 6.7 (a) and (b). There is a small improvement compared to the cross-correlation correction reconstructions in Fig. 6.7 (c) and (d). In particular there is some improvement in the erroneous shadowing around the feature edges and the retrieved "spot" features.

6.7 Conclusion

It was shown that in the presence of scan trajectory errors the vector containing the cross-correlation peaks for successive estimates of the sample transmission function can be used to approximate the gradient function of the scanning trajectory errors. This information was used in a modification to the ePIE algorithm to iteratively correct the scanning trajectory simultaneously with the probe and sample transmission retrievals.

Using simulated data, the algorithm retrieved the correct sample positions to a very high accuracy (< 0.01 pixels) in approximately 50 iterations. When using X-ray data it was necessary to restrict the position updates using the χ^2 metric. This resulted in a robust position correction algorithm with demonstrated improvements in the reconstructed sample transmission function using ptychographic X-ray diffraction data. The accuracy in the position retrieval maps was verified using a χ^2 position optimisation scheme, with highly correlated position retrieval maps for the two position correction mechanisms. The χ^2 position correction method demonstrated a small improvement in the retrieved sample image quality and the χ^2 metric compared to the cross-correlation method. The primary advantages of

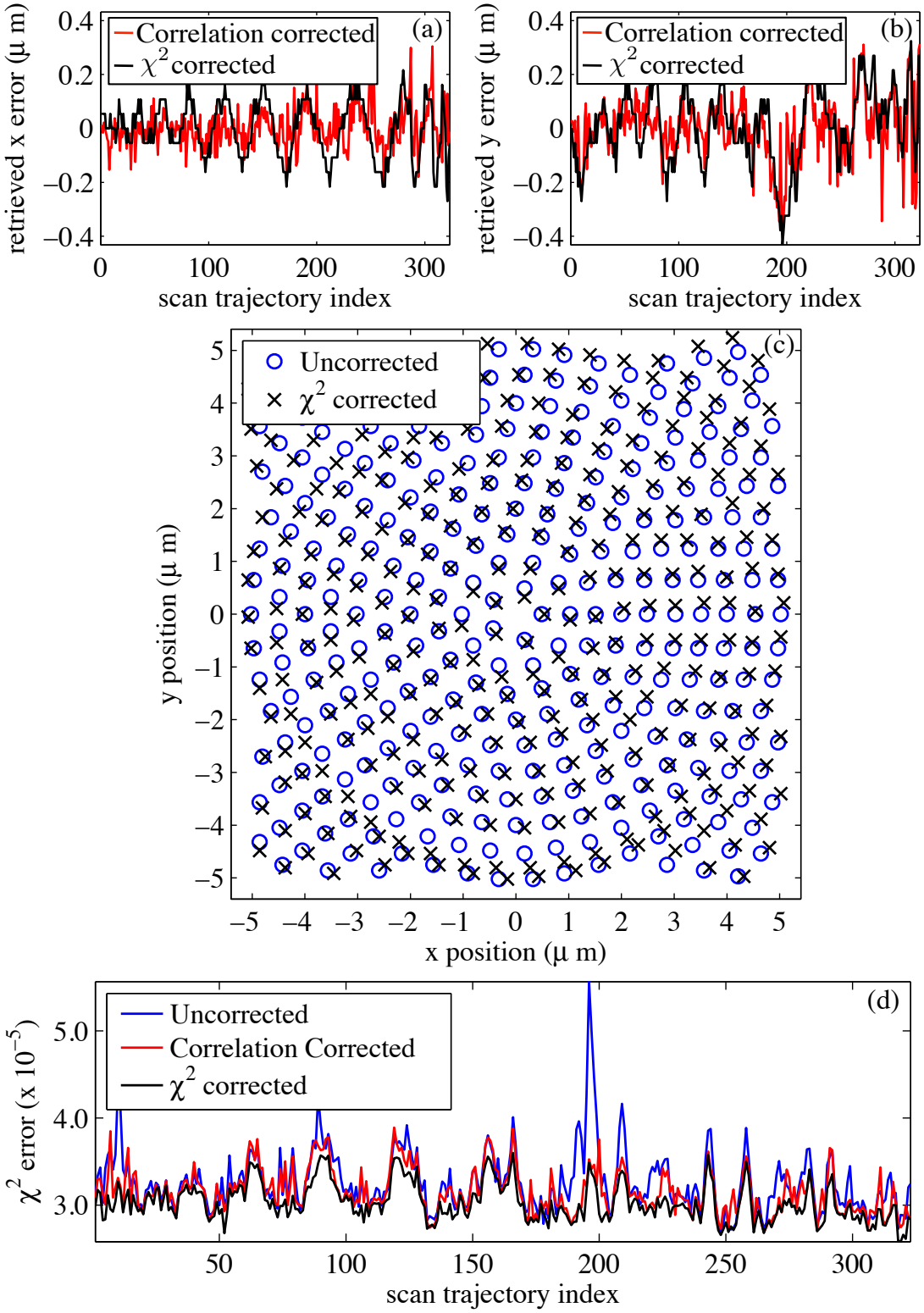

Figure 6.7: Retrieved position errors using χ^2 correction and cross-correlation correction for horizontal and vertical error corrections in (a) and (b) respectively. The χ^2 corrected scan trajectory is shown in (c). A comparison of the total χ^2 metric is shown in (d).

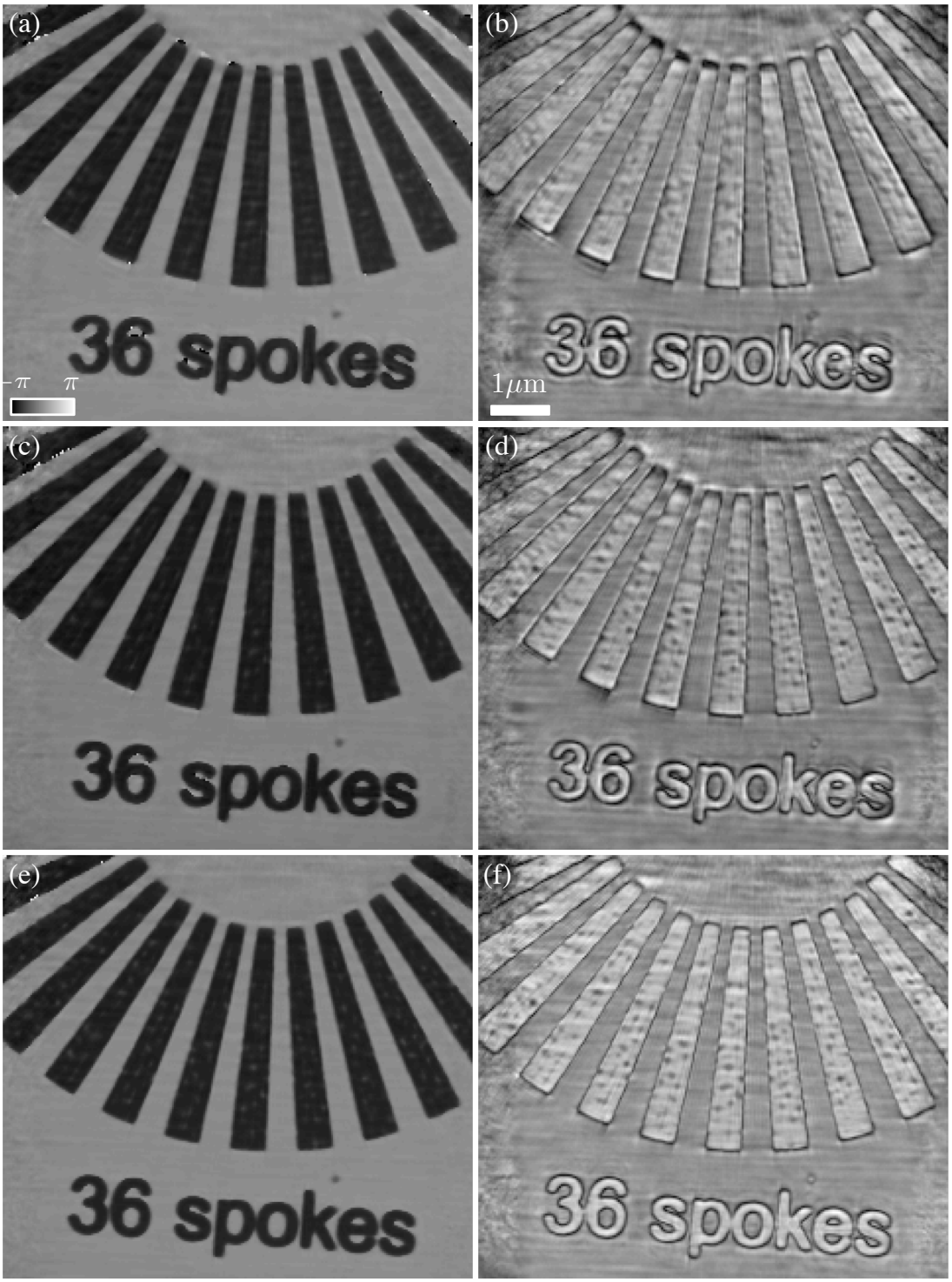

Figure 6.8: (a) and (b) show phase and amplitude reconstructions without position correction. The corresponding cross-correlation and χ^2 position corrected reconstructions are shown in (c) and (d), and (e) and (f) respectively. The scale bar is common to all reconstructions.

the cross-correlation method compared with the χ^2 method are the efficiency in the calculation, the ability to provide a direction in the position search, and the ability to efficiently correct the position errors to sub pixel accuracy. Though this can result in a rapid retrieval of the scan trajectory, the cross-correlation signal demonstrated some sensitivity to noise in the X-ray data.

The mechanism underlying the gradient estimation using the cross-correlation method is currently based on empirical observation rather than a theoretical understanding. A proper understanding of why the mechanism works may lead to a more successful implementation of the scan trajectory optimisation. An alternate position correction mechanism could use the cross-correlation calculation in conjunction with the Fletcher-Reeves algorithm or its variants. These non-linear conjugate-gradient optimisation algorithms offer the generality of gradient optimisation with the improved convergence characteristics associated with a quasi-Newton-Raphson method and may resolve the stability issues in the proposed gradient-descents position correction algorithm.

CHAPTER

SEVEN

PARTIALLY COHERENT PTYCHOGRAPHY

The role of coherence in CDI was discussed in a study by Spence *et al.* [51], concluding that in order to reconstruct the sample from the diffraction data the coherence length is required to encompass the autocorrelation of the object [51], i.e. to be at least twice the maximal dimension of the scattering sample. A later study [52] noted the need for a well-defined distribution of asymptotic zeroes in the diffraction patterns to ensure the finite support of the object, concluding that a small departure from full spatial coherence is sufficient to formally render the scattered wave irretrievable from the recorded diffraction data using any conventional iterative method based on coherent propagation. The failure to meet these requirements can result in a series of artefacts in the reconstructed sample image or the complete failure of the algorithm to converge. These issues have been recently addressed by incorporating the beam coherence properties into the phase retrieval algorithms [1, 52, 53, 127], enabling CDI to be performed over a broader range of experimental conditions, in particular when using higher source flux, than previously thought possible. In the broadband case, incorporating the temporal coherence properties can lead to a 60 fold reduction in data acquisition times [54], an impressive achievement. In this thesis the discussion is limited to the use of a quasi-monochromatic X-ray source exhibiting partial spatial coherence.

This chapter extends previous work on partially coherent diffractive imaging to ptychography, presenting two modifications to the ptychographic algorithm where partial coherence is accounted for by incorporating the illumination coherence properties into ptychographic phase retrieval algorithms. In the first proposed algorithm,

pre-characterised illumination coherence properties are used to decompose the illumination into a series of Gaussian-Schell modes. The subsequent modal propagation of the sample exit surface wave yields an estimate of the partially coherent diffracted intensity using the partially coherent propagation algorithms in §3.9. These algorithms are used in conjunction with the ePIE algorithm in §3.10.2. The resulting partially coherent modal ePIE algorithm is tested using simulated partially coherent ptychographic data over a range of spatial coherence characteristics, demonstrating the ability to accurately retrieve the sample transmission and probe for each partially coherent dataset.

In the second proposed modification to the ePIE algorithm the spatial coherence is assumed to be uncharacterised. Instead, using a known representation of the mutual optical intensity, the coherence characteristics (specifically the coherence length) are determined simultaneously with the sample transmission function and probe retrievals, removing the requirement for a separate coherence measurement. The effectiveness of this algorithm is tested using simulated partially coherent data over a range of spatial coherence characteristics, demonstrating accurate retrieval of the coherence parameters, sample transmission function and probe for each dataset. A further demonstration of the coherence retrieval and correction is performed using partially coherent ptychographic X-ray data, resulting in significant improvement in both the probe and sample transmission reconstructions as well as performing a series of coherence measurements across the entire ptychographic scanning trajectory. The proposed algorithms allow ptychography to be performed over a greater range of experimental conditions than possible under the assumptions of full spatial coherence, in particular when using a high-flux ptychographic dataset.

7.1 Partial Spatial Coherence

Many of the characteristics of a quasi-monochromatic, partially coherent synchrotron source may be accounted for by assuming a source with a Gaussian-Schell model for the mutual coherence function [95, 97]. Under this approximation the four-dimensional mutual optical intensity, $J(\mathbf{r}_1, \mathbf{r}_2)$, takes a Gaussian form, separable in Cartesian co-ordinates, i.e.

$$J(\mathbf{r}_1, \mathbf{r}_2) = \sqrt{I_0(\mathbf{r}_1)}\sqrt{I_0(\mathbf{r}_2)} \exp\left[-\frac{|x_1 - x_2|^2}{l_x^2}\right] \exp\left[-\frac{|y_1 - y_2|^2}{l_y^2}\right], \tag{7.1}$$

where I_0 is the sample plane illumination intensity. Eq. 7.1 allows the spatial coherence properties of the X-ray source to be quantified via the spatial coherence

lengths, l_x and l_y, a concept that reduces the characterisation of the four-dimensional MOI to a single parameter in each transverse dimension. The coherence length is typically measured using fringe visibility measurements (a measure of the correlation between two spatially separated points). A number of methods for performing a spatial coherence measurement have been proposed, including inline holographic methods [128], a uniformly redundant array (URA) [129] and prism interferometry [130]. A common technique for measuring the fringe visibility employs a Young's Double Slit (YDS) measurement of the illumination. This method has been used to characterise the coherence properties at third generation synchrotron sources [52, 53, 131] and more recently at fourth generation X-ray free-electron sources [132]. A coherence measurement of this kind is detailed in Appendix B, using YDS data collected at the SPring-8 BL20XU beamline in Japan.

7.2 Modal Decomposition

When $\mathbf{J}(\mathbf{r}_1, \mathbf{r}_2)$ takes the separable form in Eq. 7.1 and the vertical coherence length is sufficiently long such that the illumination may be regarded as fully coherent in the vertical direction, $\mathbf{J}_\mathbf{y}(y_1, y_2)$ is adequately represented by a single flat mode and the modal decomposition need only be performed on the function, $\mathbf{J}_\mathbf{x}(x_1, x_2)$, where

$$\mathbf{J}_\mathbf{x}(x_1, x_2) = \sqrt{I_0(\mathbf{r}_1)} \exp\left[-\frac{|x_1 - x_2|^2}{l_x^2}\right]. \tag{7.2}$$

$\mathbf{J}_\mathbf{x}(x_1, x_2)$ may be expressed via Eq. 2.57 as the expansion into a set of mutually incoherent and orthonormal modes, ψ_n, i.e.

$$\mathbf{J}_\mathbf{x}(x_1, x_2) = \sum_n \alpha_n \psi_n(x_1) \psi_n^*(x_2), \tag{7.3}$$

where α_n are the modal occupancies and the modes themselves are expanded via a complete basis, P_k, chosen to be the pixel basis in Eq. 3.25, reducing the eigenvalue equation in Eq. 2.60 to

$$\mathbb{J}_\mathbf{x} \mathbb{C}_\mathbf{x} = \mathbf{a} \mathbb{C}_\mathbf{x}, \tag{7.4}$$

where the matrix elements of $\mathbb{J}_\mathbf{x}$ are as defined in Eq. 2.61, the modal occupancies, α_n, are the diagonal elements of the matrix, $\mathbf{a}$, and $\mathbb{C}_\mathbf{x}$ is a matrix composed of the modes, $\psi_n(x)$.

For a coherence length, l_x, Eq. 7.4 enables the coherence function, $\mathbf{J}_\mathbf{x}(x_1, x_2)$,

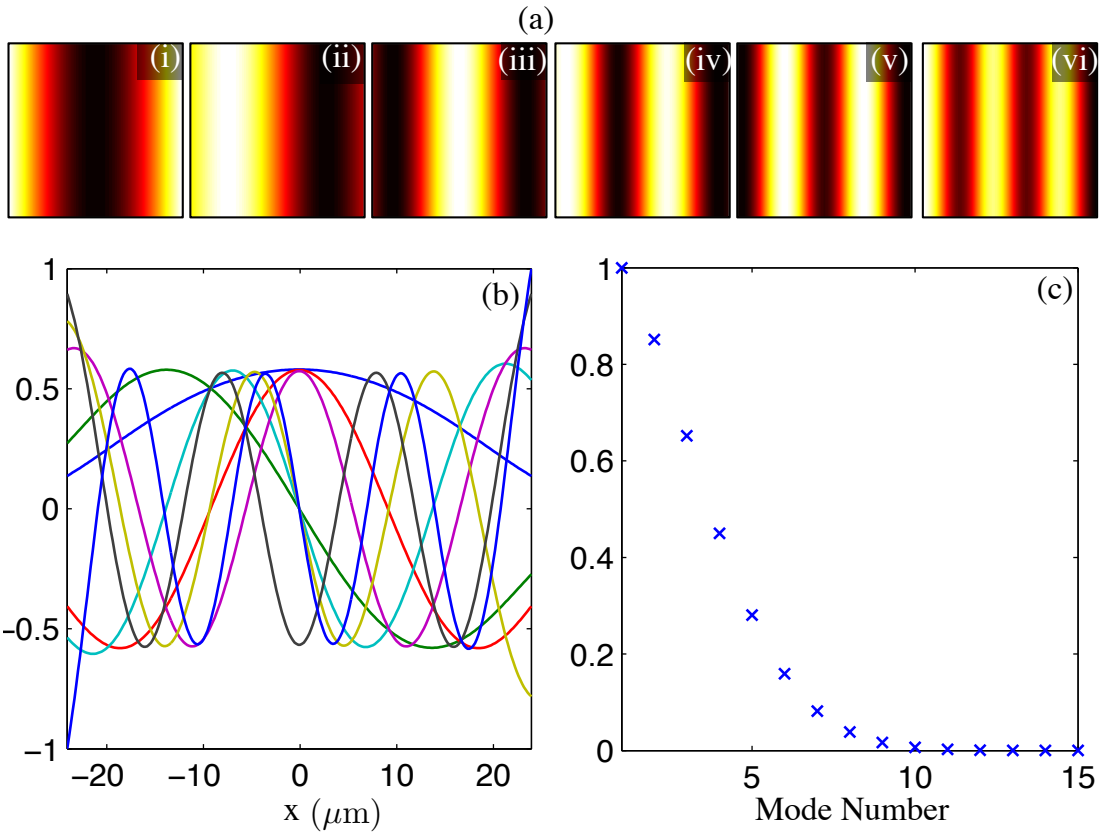

Figure 7.1: Decomposition of the illumination wavefront at SPring-8 beamline BL20XU into a series of Gaussian-Schell modes for a Gaussian coherence function with the form in Eq. 7.2. The modal series in (a) (i)-(vi) show the six highest occupancy modes contributing to $\mathbf{J_x}(x_1, x_2)$, in order of decreasing occupancy, i.e. the mode with highest occupancy is assigned the mode number (i). A centre pixel lineout through the normalised modes in (a) is shown in (b). The corresponding modal occupancies are shown in (c).

to be decomposed into a set of n Gaussian-Schell modes, $\psi_n(x)$, with associated occupancies, α_n. As an example, for the coherence study in Appendix B, the horizontal sample plane spatial coherence length, l_x, of the SPring-8 beamline BL20XU was determined to be $l_x = (18.6 \pm 1.7)$ μm, with a 40 μm pinhole placed 37 mm upstream of the sample plane. The resulting modes are shown in Fig. 7.1 (a), with a line-out for each of the modes provided in Fig. 7.1 (b). The associated normalised modal occupancies are provided in Fig. 7.1 (b).

The rapid decline in the modal occupancies suggests that $\mathbf{J_x}$ may be adequately represented with a finite number of modes. Fig. 7.2 (a) shows the coherence function, $\mathbf{J_x}$, with the form in Eq. 7.2 and with $l_x = (18.6 \pm 1.7)$ μm. The series of two-dimensional surface plots in Fig. 7.2 (b) - (i) demonstrate the ability to approximate the coherence function of the BL20XU wavefield using a successively greater number of modes, numbering from three to ten respectively. The series indicates that with the use of 7 modes, the mean difference per pixel between the modal estimation,

$\mathbf{J}_{\mathbf{x},\text{est}}$, and the actual values of $\mathbf{J}_{\mathbf{x}}$, is 1% of the maximal value of $\mathbf{J}_{\mathbf{x}}$, where the difference is calculated as $\sum_n |\mathbf{J}^n_{\mathbf{x}} - \mathbf{J}^n_{\mathbf{x},\text{est}}|/N$, where N is the total number of pixels in $\mathbf{J}_{\mathbf{x}}$. The use of 10 modes reduces the mean difference per pixel to 0.007% of the maximal value of $\mathbf{J}_{\mathbf{x}}$. This is essentially indistinguishable from $\mathbf{J}_{\mathbf{x}}$, as can be seen by comparing the 10-mode estimation in Fig. 7.2 (i) to the image of $\mathbf{J}_{\mathbf{x}}$ in Fig. 7.2 (a). Additional modes do not significantly contribute to the modal sum and $\mathbf{J}_{\mathbf{x}}$ may therefore be adequately represented with 10 Gaussian-Schell modes.

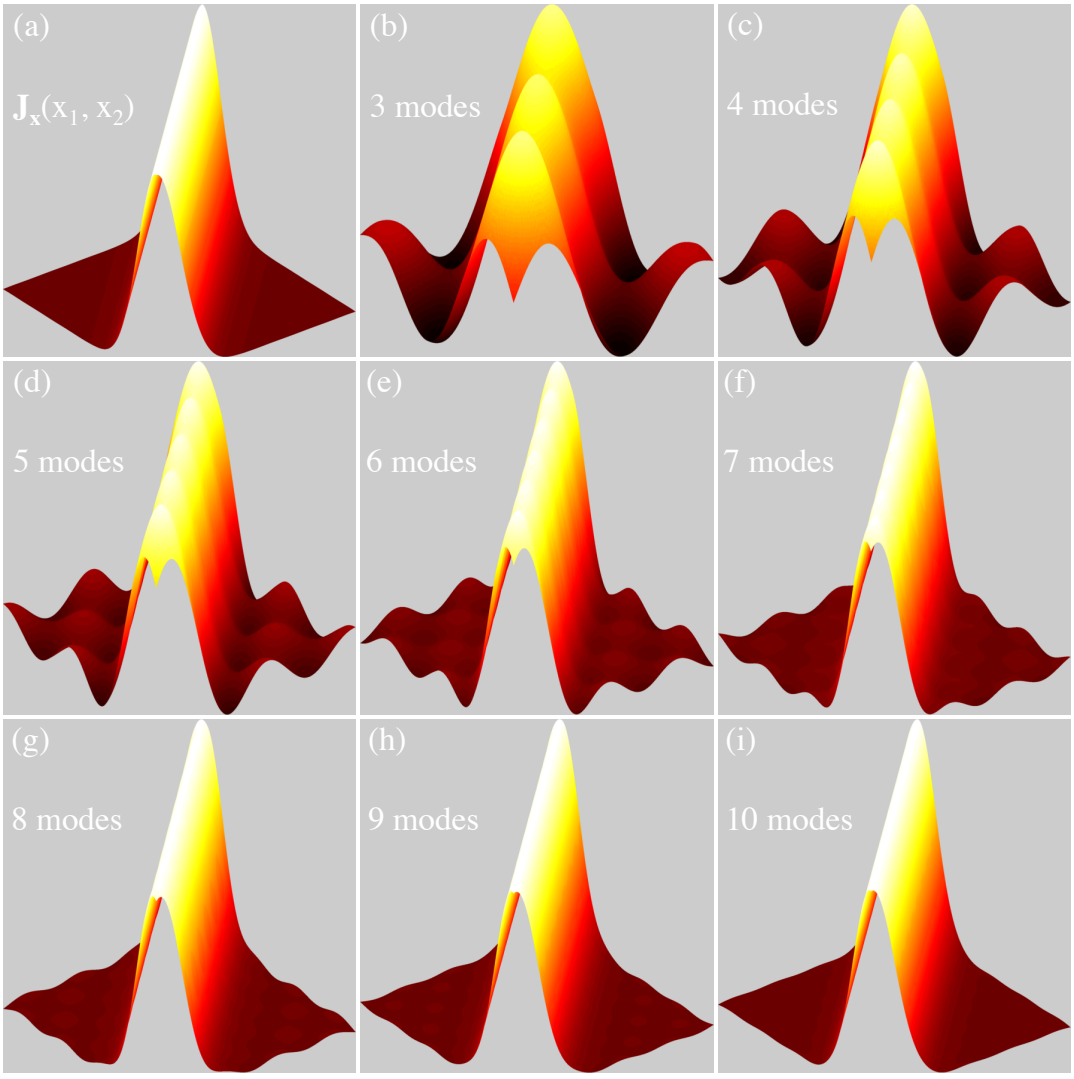

Figure 7.2: The Mutual Optical Intensity, $\mathbf{J}_{\mathbf{x}}(x_1, x_2) = \exp[-(x_1 - x_2)^2/l_x]$, where $l_x = 18.6$ μm, shown in (a), is approximated using the incoherent sum of a successively greater number of Gaussian-Schell modes, numbering from three to ten, in (b)-(i) respectively.

7.3 Partially Coherent Modal Propagation

The far-field diffracted intensity, $I(\mathbf{q})$, resulting from a quasi-monochromatic, partially coherent illumination with MOI, $J(\mathbf{r}_1, \mathbf{r}_2)$, incident on a thin sample with transfer function, $T(\mathbf{r})$, can be described by

$$I(\mathbf{q}) \propto \int J(\mathbf{r}_1, \mathbf{r}_2) T(\mathbf{r}_1) T^*(\mathbf{r}_2) \exp\left[i\mathbf{q} \cdot (\mathbf{r}_1 - \mathbf{r}_2)\right] \mathrm{d}\mathbf{r}_1 \mathrm{d}\mathbf{r}_2, \tag{7.5}$$

where $\mathbf{q}$ and $\mathbf{r}$ are co-ordinate vectors in the far-field and sample planes respectively. Under the projection approximation, for a probe, $P(\mathbf{r})$, and a sample with transmission function, $O(\mathbf{r})$, translated by, $\mathbf{s}_k$, the transfer function $T(\mathbf{r})$ is

$$T(\mathbf{r}) = O(\mathbf{r} - \mathbf{s}_k) P(\mathbf{r}). \tag{7.6}$$

Substitution of Eq. 7.3 and Eq. 7.6 into Eq. 7.5 yields

$$\begin{aligned}
I(\mathbf{q}) &= \int \sum_n \alpha_n \psi_n(\mathbf{r}_1) \psi_n^*(\mathbf{r}_2) T(\mathbf{r}_1) T^*(\mathbf{r}_2) \exp\left[i\mathbf{q} \cdot (\mathbf{r}_1 - \mathbf{r}_2)\right] \mathrm{d}\mathbf{r}_1 \mathrm{d}\mathbf{r}_2 \\
&= \int \sum_n \alpha_n \psi_n(\mathbf{r}_1) \psi_n^*(\mathbf{r}_2) O(\mathbf{r}_1 - \mathbf{s}_k) P(\mathbf{r}_1) O^*(\mathbf{r}_2 - \mathbf{s}_k) P^*(\mathbf{r}_2) \exp\left[i\mathbf{q} \cdot (\mathbf{r}_1 - \mathbf{r}_2)\right] \mathrm{d}\mathbf{r}_1 \mathrm{d}\mathbf{r}_2 \\
&= \sum_n \alpha_n \int \psi_n'(\mathbf{r}_1) \psi_n'^*(\mathbf{r}_2) \exp\left[i\mathbf{q} \cdot (\mathbf{r}_1 - \mathbf{r}_2)\right] \mathrm{d}\mathbf{r}_1 \mathrm{d}\mathbf{r}_2 \\
&= \sum_n \alpha_n \left|\Psi_n(\mathbf{q})\right|^2,
\end{aligned} \tag{7.7}$$

where α_n absorbs the constant of proportionality and $\psi_n'(\mathbf{r})$ are a set of modified modes, defined by

$$\begin{aligned}
\psi_n'(\mathbf{r}) &= \psi_n(\mathbf{r}) T(\mathbf{r}) \\
&= \psi_n(\mathbf{r}) O(\mathbf{r} - \mathbf{s}_k) P(\mathbf{r}).
\end{aligned} \tag{7.8}$$

The modal decomposition of the MOI allows the coherence properties of the illumination to be accounted for by the incoherent sum of a series of propagated illumination modes, $\Psi_n(\mathbf{q})$, weighted by their associated occupancies, α_n. In this framework full coherence is regarded as a limit in which the occupancies for modes other than the dominant mode are sufficiently small such that these modes contribute a negligible amount to the modal sum.

7.4 Partially Coherent Modal Ptychography

If the modal decomposition of the source has been performed using the methods detailed in §7.2, the partially coherent CDI algorithms detailed in §3.9 may be used to perform CDI with less stringent requirements on the beam coherence [52, 53]. In the context of ptychography, with an illuminating probe function, $P(\mathbf{r})$, sample transmission function, $O(\mathbf{r})$, and scanning trajectory, $\mathbf{s}_j$, propagation of a partially coherent wavefield from the sample plane to detector plane is determined using the methodology detailed in §7.3. The modified sample plane modes, $\psi'_{n,k}(\mathbf{r})$ are determined using Eq. 7.8, these may be propagated using Eq. 2.15 or its small angle limiting form in Eq. 2.12. An estimate of the partially coherent diffraction intensity may be calculated using Eq. 7.7. The coupling of the modes means that rather than adjusting the amplitudes independently, a common rescaling function is applied such that the current estimate of the intensity matches the diffracted intensity, $I_j(\mathbf{q})$. This leads to the modified modulus constraint

$$\Psi'_{j,n}(\mathbf{q}) = \left[\frac{I_j(\mathbf{q})}{I'_j(\mathbf{q})}\right]^{1/2} \Psi_{j,n}(\mathbf{q}), \tag{7.9}$$

where $I_j(\mathbf{q})$ is the recorded partially coherent diffracted intensity with the sample at position, $\mathbf{s}_j$.

As the transfer function, $T(\mathbf{r})$, is common to all modes, updating the current estimate of the transfer function requires a single mode to be propagated back to the sample plane. This is chosen to be the fundamental mode, $\Psi'_{j,0}(\mathbf{q})$, associated with the highest occupancy α_0. An estimate of the transfer function, $T(\mathbf{r})$ is obtained using the known fundamental mode, $\psi_0(\mathbf{r})$, from the known expansion of the source, such that

$$T_{j,0}(\mathbf{r}) = \frac{\psi'_{j,0}(\mathbf{r})}{\psi_0(\mathbf{r})}. \tag{7.10}$$

Incorporating the above modal structure into the standard ePIE algorithm in §3.10.2 requires a sufficient number of modifications to warrant a full description of the modified algorithm and its implementation. For a partially coherent source with a known coherence function, $\mathbf{J}(\mathbf{r}_1, \mathbf{r}_2)$, and subsequent set of source modes, $\{\psi_0(\mathbf{r}), ..., \psi_n(\mathbf{r})\}$, retrieval of the sample transmission function, $O(\mathbf{r})$, and illuminating probe function, $P(\mathbf{r})$, is achieved through the sequential application of the following constraints:

1. Using the known source modes, $\{\psi_0(\mathbf{r}), ..., \psi_n(\mathbf{r})\}$, for the j^{th} scan position, $\mathbf{s}_j$,

determine the set of modified modes, $\left\{\psi'^{m}_{j,0}(\mathbf{r}), ..., \psi'^{m}_{j,n}(\mathbf{r})\right\}$, where

$$\psi'^{m}_{j,n}(\mathbf{r}) = O^{m}(\mathbf{r} - \mathbf{s}_j)P^{m}(\mathbf{r})\psi_n(\mathbf{r}).$$

2. Determine the detector plane modes, $\left\{\Psi^{m}_{j,0}(\mathbf{q}), ..., \Psi^{m}_{j,n}(\mathbf{q})\right\}$, using the coherent propagator, $\mathscr{F}$, where

$$\Psi^{m}_{j,n}(\mathbf{q}) = \mathscr{F}\left[\psi'^{m}_{j,n}(\mathbf{r})\right].$$

3. Determine the partially coherent detector plane intensity estimate, $I'^{m}_{j}(\mathbf{q})$, via

$$I'^{m}_{j}(\mathbf{q}) = \sum_n \alpha_n \left|\Psi^{m}_{j,n}(\mathbf{q})\right|^2.$$

4. Update the fundamental detector plane mode, $\Psi^{m}_{j,0}(\mathbf{q})$, using the j^{th} recorded partially coherent diffraction data, $I_j(\mathbf{q})$, in the modified modulus constraint

$$\Psi'^{m}_{j,0}(\mathbf{q}) = \left[\frac{I_j(\mathbf{q})}{I'^{m}_{j}(\mathbf{q})}\right]^{1/2} \Psi^{m}_{j,0}.$$

5. Determine the revised estimate of the modified fundamental mode, $\psi'^{m+1}_{j,0}(\mathbf{r})$, via

$$\psi'^{m+1}_{j,0}(\mathbf{r}) = \mathscr{F}^{-1}\left[\Psi'^{m}_{j,0}(\mathbf{q})\right].$$

6. Determine the current estimate of the transfer function, $T(\mathbf{r})$, using the known fundamental source mode, $\psi_0(\mathbf{r})$

$$T^{m+1}(\mathbf{r}) = \frac{\psi'^{m+1}_{j,0}(\mathbf{r})}{\psi_0(\mathbf{r})}.$$

This provides access to the sample transmission function, $O(\mathbf{r})$, and probe function $P(\mathbf{r})$, via $T(\mathbf{r}) = O(\mathbf{r} - \mathbf{s}_j)P(\mathbf{r})$.

7. Update the sample transmission function, $O(\mathbf{r})$, through the overlap constraint

$$O^{m+1}(\mathbf{r} - \mathbf{s}_k) = O^{m}(\mathbf{r} - \mathbf{s}_k) + \alpha_1 \frac{P^{m*}(\mathbf{r})}{\left|P^{m}(\mathbf{r})\right|^2_{max}}\left[T^{m+1}(\mathbf{r}) - T^{m}(\mathbf{r})\right].$$

8. Update the illumination function, $P(\mathbf{r})$, through the overlap constraint

$$P^{m+1}(\mathbf{r}) = P^{m}(\mathbf{r}) + \alpha_2 \frac{O^{m+1*}(\mathbf{r}-\mathbf{s}_k)}{|O^{m}(\mathbf{r}-\mathbf{s}_k)|^2_{max}} \left[T^{m+1}(\mathbf{r}) - T^{m}(\mathbf{r})\right].$$

A complete iteration cycles over all scan positions, $\mathbf{s}_j$. The process is repeated until the current estimate of the sample transmission function, $O(\mathbf{r})$, and the probe function, $P(\mathbf{r})$, are consistent with the recorded partially coherent diffraction dataset and the overlap constraint.

7.4.1 Demonstration with simulated partially coherent data

Assuming a Gaussian-Schell source with the form in Eq. 7.1, the modal decomposition of the simulated partially coherent wavefield was performed for a series of sample plane coherence lengths of 1 μm, 3 μm, and 5 μm. When the MOI takes the form in Eq. 7.1, the modes are the Gaussian-Schell modes described in §7.2. The simulated parameters were chosen to model experiments performed at the APS beam-line 34-ID-C and are provided in Table 7.1.

Parameter	**Value**
Wavelength	0.138 nm
Sample-Detector distance	3.2 m
Detector pixel size	55 μm
Cropped array size	256×256
Sample plane sampling interval	31 nm
Coherence length range	1 μm $\rightarrow$ 5 μm
Ptychographic scanning area	10 μm $\times$ 10 μm
Radial scan trajectory increment	0.5 μm
Ptychographic scanning points	323

Table 7.1: Simulated partially coherent parameters to match APS beamline 34-ID-C

The simulations assume the central region of a partially coherent X-ray beam with FWHM of 100 μm was selected out by a 5 μm pinhole, placed 5 mm upstream of the sample. The probe was propagated to the sample plane using the near-field propagation (Eq. 2.14). Partial coherence was incorporated by assuming a MOI with the form in Eq. 7.2 and propagating a set of Gaussian-Schell modes with the highest 100 occupancy levels. The pinhole aperture was assumed to truncate each mode, blocking regions outside the central region defined by the circular aperture. Under the assumption that the source coherence function is of the form in Eq. 7.1 with subsequent modal expansion, $\{\psi_0(\mathbf{r}, ..., \psi_n(\mathbf{r})\}$, and associated modal occupancies, α_n, the partially coherent diffraction intensity resulting from a probe, $P(\mathbf{r})$, incident

on a sample with transmission function, $O(\mathbf{r})$, at scan position $\mathbf{s}_k$, is determined using Eq. 7.7.

The simulated target sample was chosen to model the lithographed star aperture detailed in §5.3.1, with parameters described in §6.1. The simulated scanning trajectory parameters are provided in Table 7.1. Three partially coherent ptychographic datasets were simulated with coherence lengths of 1 μm, 3 μm, and 5 μm.

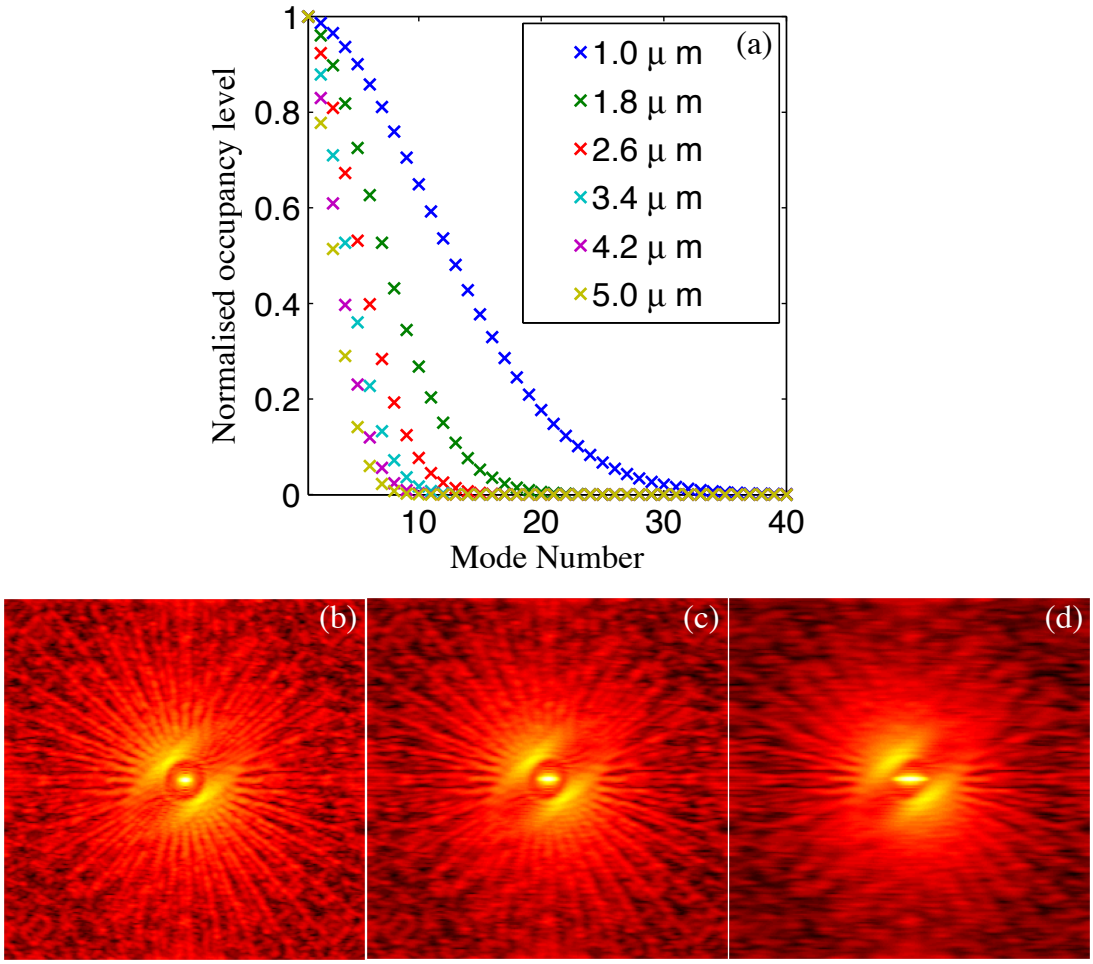

Figure 7.3: Partially coherent diffraction intensity for a range of coherence parameters using a simulated star aperture. (a) modal occupancies for coherence lengths ranging from 5 μm to 1 μm. (b) - (d) show simulated partially coherent data for coherence lengths of 5 μm, 3 μm and 1 μm

The effect of partial coherence on the diffraction data, with the sample placed at the central ptychographic position is shown in Fig. 7.3 (b)-(d) for coherence lengths of 5 μm, 3 μm and 1 μm respectively. The reduction in coherence length results in an increasingly blurred diffraction intensity. As the simulated MOI was of the Gaussian form in Eq. 7.1, an equivalent partially coherent diffraction intensity estimate may be obtained using the convolution of the coherent diffraction intensity associated with coherent propagation with a Gaussian blurring kernel provided by the known

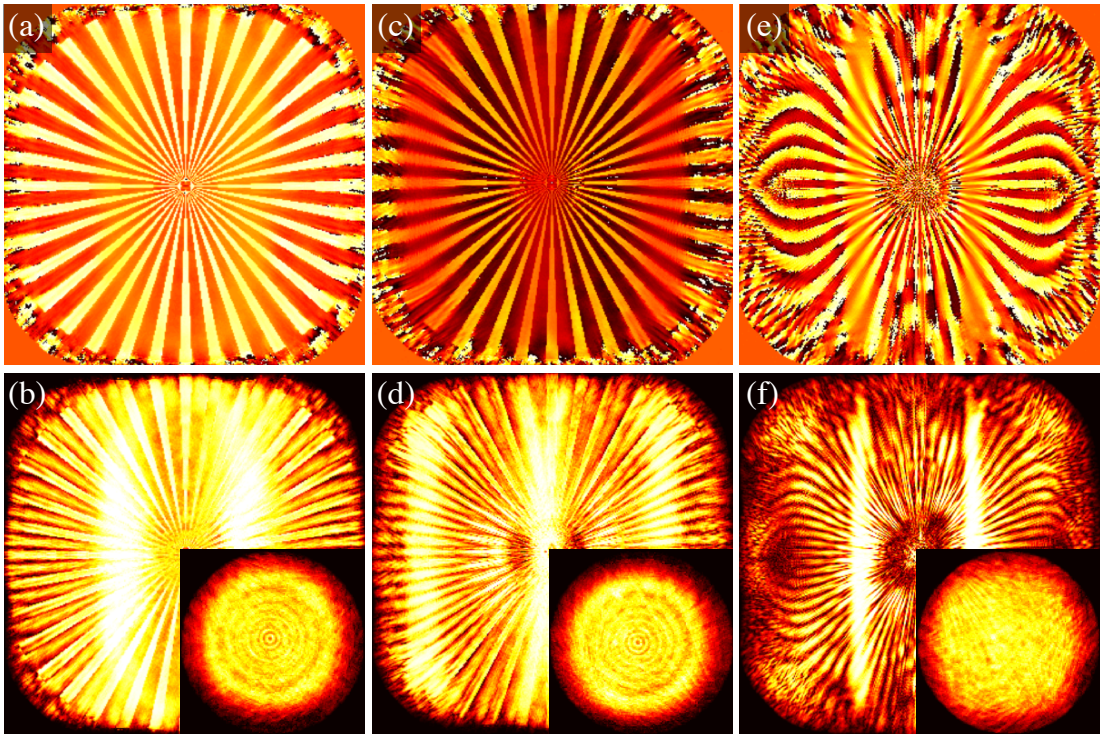

Figure 7.4: The retrieved sample transmission phase and amplitude using the standard ePIE algorithm and simulated partially coherent ptychographic data with coherence length of 5 μm are shown in (a) and (b), with the retrieved probe amplitude provided in the inset. The corresponding reconstructions for the 3 μm and 1 μm coherence length datasets are shown in (c) and (d), and (e) and (f) respectively.

representation for the MOI in Eq. 7.1. This property is used in §7.5 to perform partially coherent CDI without prior knowledge of the illumination coherence characteristics. Fig. 7.3 (a) shows a comparison between the normalised occupancies over a series of coherence lengths from 1 μm to 5 μm. As the coherence length is decreased, the associated spread across a greater number of occupancy levels means that an increasing number of modes are required to adequately approximate the partially coherent wavefront.

The standard ePIE algorithm (i.e. assuming full coherence) was used to reconstruct the sample transmission function and probe for the three simulated partially coherent ptychographic datasets. The initial estimates for the sample transmission and probe were a random binary distribution and a circular binary array respectively. The ePIE algorithm was used for 500 iterations on each simulated partially coherent ptychographic dataset. The reconstructed sample transmission phase and amplitude for the 5 μm dataset are shown in Fig. 7.4 (a) and (b), with the reconstructed probe amplitude shown in the inset. The corresponding reconstructions for the 3 μm and 1 μm datasets are provided in Fig. 7.4 (c) and (d), and Fig. 7.4 (e)

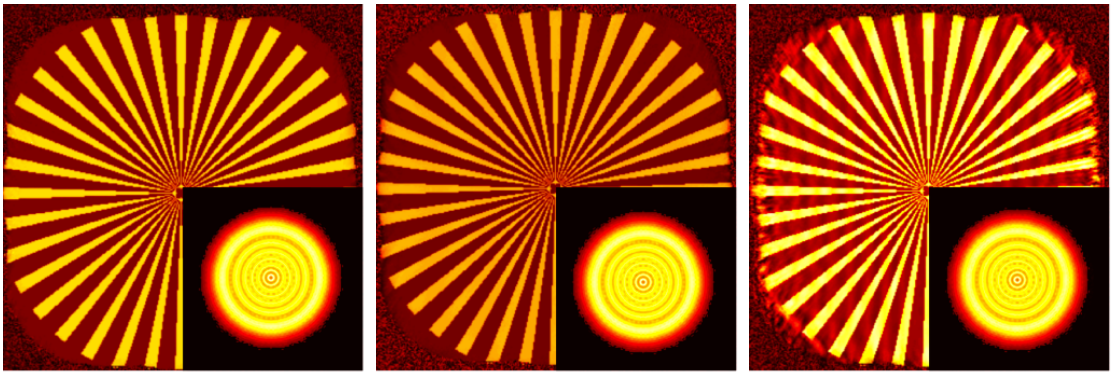

(a) (b) (c)

Figure 7.5: Sample and probe amplitude reconstructions incorporating partial coherence correction via a modal decomposition of the incident wavefield. The reconstructions were obtained using the same datasets as those presented in Fig. 7.4, i.e. using partially coherent data with coherence lengths of 5 μm, 3 μm and 1 μm in (a)-(c) respectively. For compactness, only the amplitude is presented.

and (f) respectively. The reconstructed sample transmission amplitude appears to display a higher degree of sensitivity to the degrading coherence than the retrieved sample transmission phase. This is also evident in the retrieved probe amplitude structure through the series.

Using the modified partially coherent modal ePIE algorithm, the sample transmission function and probe were reconstructed for the series of simulated partially coherent ptychographic datasets. The reconstructions were obtained using the same algorithm parameters, in particular the same initial sample transmission and probe estimates, as for the standard ePIE reconstructions. Only the modes with an occupancy level above 1% of the highest modal occupancy were used, yielding a number of modes, ranging from 7 to 32 for coherence lengths of 1 μm to 5 μm respectively.

Initial estimates of the sample transmission function and probe were generated using only the fundamental mode associated with coherent propagation for the initial 20 iterations. For the remaining 480 iterations the modified partially coherent modal ePIE algorithm was used. The resulting reconstructions are provided in Fig. 7.5. For compactness, only the amplitude is presented as the modification to the phase of the incoming wavefield results in a phase reconstruction with precisely the same form as the amplitude.

Incorporating the known coherence characteristics into the algorithm, specifically a coherence function with the Gaussian form in Eq. 7.1 and known coherence length, along with the subsequent modal expansion, enabled the highly accurate retrieval of the sample transmission function for the entire series of simulated partially coherent ptychographic datasets. In particular, the ability to retrieve the sample

transmission function using the 1 μm simulated dataset corresponds to a retrieval for a coherence length at just 25% of the exit surface wave dimensions. This is a significant improvement over previous work in CDI, with a reported minimal coherence length requirement of approximately 80% of the scattering object size [53].

7.5 *in situ* Coherence Characterisation

Measurement of the illumination coherence properties can add considerable additional complexity to a synchrotron experiment. Changes in the beamline optics, in particular variation of the coherence-defining and beam-defining slits, can result in changes to the coherence characteristics, requiring a new coherence measurement to be performed. The available experimental geometry may also mean the fringe measurements cannot be sufficiently sampled and a coherence measurement cannot be performed. Evolution of the beam coherence characteristics, for example over a ptychographic data acquisition, may make it difficult or impossible to adequately measure the coherence function. The following discussion extends a method suggested for CDI [127] to ptychography, in which a coherence measurement is performed using only the diffraction data. Using data obtained at the APS beamline 2-ID-B, the method was shown to yield a recovered coherence length in very close agreement with a previous coherence characterisation performed at the beamline 2-ID-B using a YDS measurement [53]. The extension to ptychography enables the retrieval of the coherence length and correction for partial coherence to be performed in conjunction with the sample and probe retrievals using only the partially coherent ptychographic diffraction data, i.e. without performing a separate coherence measurement.

For a Gaussian-Schell source $\mathbf{J}(\mathbf{r}_1, \mathbf{r}_2)$ takes form in Eq. 7.1, i.e.

$$\begin{aligned}\mathbf{J}(\mathbf{r}_1, \mathbf{r}_2) &= \sqrt{I_0(\mathbf{r}_1)}\sqrt{I_0(\mathbf{r}_2)}\exp\left[-\frac{|x_1 - x_2|^2}{l_x^2}\right]\exp\left[-\frac{|y_1 - y_2|^2}{l_y^2}\right], \\ &= \sqrt{I_0(\mathbf{r}_1)}\sqrt{I_0(\mathbf{r}_2)}g(\mathbf{r}_1 - \mathbf{r}_2), \end{aligned} \tag{7.11}$$

where $g(\mathbf{r}_1 - \mathbf{r}_2)$ is referred to as the complex coherence function. Substitution of Eq. 7.11 into Eq. 7.5 yields the convolution relation

$$\begin{aligned} I(\mathbf{q}) &= \int g(\mathbf{r}_1 - \mathbf{r}_2)T(\mathbf{r}_1)T^*(\mathbf{r}_2)\exp\left[i\mathbf{q}\cdot(\mathbf{r}_1 - \mathbf{r}_2)\right]\mathrm{d}\mathbf{r}_1\mathrm{d}\mathbf{r}_2 \\ &= |\Psi(\mathbf{q})|^2 * \hat{g}(\mathbf{q}), \end{aligned} \tag{7.12}$$

where $\Psi(\mathbf{q})$ is the coherent far-field wavefield, the illumination amplitude, $\sqrt{I_0(\mathbf{r})}$, is now a component of $T(\mathbf{r})$ and $\hat{g}(\mathbf{q})$ is the Fourier transform of the complex coherence function, $g(\mathbf{r}_1 - \mathbf{r}_2)$. A partially coherent diffraction intensity estimate equivalent to the incoherent modal sum in Eq. 2.65 may therefore be obtained through the convolution of a single propagated coherent wave with $\hat{g}(\mathbf{q})$, i.e. without the requirement for a modal decomposition of the illumination and subsequent modal propagation.

In the method proposed by Clark *et al.* [127], in place of the usual modulus constraint (Eq. 3.16), if the form of the coherence function, $g(\mathbf{r}_1 - \mathbf{r}_2)$, is known, the coherent wavefield, $\Psi(\mathbf{q})$, and coherence function, $\hat{g}(\mathbf{q})$, can be simultaneously determined using a two-step system consisting of the minimisation of the metric

$$\Delta = \sum_k \left| I(\mathbf{q}) - |\Psi(\mathbf{q})|^2 * \hat{g}(\mathbf{q}) \right|, \tag{7.13}$$

followed by the modified modulus constraint,

$$\Psi'(\mathbf{q}) = \left[\frac{I(\mathbf{q})}{||\Psi(\mathbf{q})|^2 * \hat{g}(\mathbf{q}, l_x, l_y)|} \right]^{1/2} \Psi(\mathbf{q}). \tag{7.14}$$

where $I(\mathbf{q})$ is the recorded partially coherent diffraction intensity. The updated estimate of the coherent wavefield, $\Psi'(\mathbf{q})$ is propagated to the sample plane using the standard coherent propagators in using Eq. 2.15 or its small angle limiting form in Eq. 2.12.

When the coherence function, $g(\mathbf{r}_1 - \mathbf{r}_2)$, has the form in Eq. 7.11, $\hat{g}(\mathbf{q})$ is also Gaussian, with widths $1/l_x$ and $1/l_y$ in the horizontal and vertical directions respectively. The minimisation in Eq. 7.13 is therefore performed using the coherence lengths l_x and l_y as the free parameters in the minimisation scheme, allowing the spatial coherence to be characterised simultaneously with the sample transmission retrieval, removing the need to perform a separate coherence measurement. The partial spatial coherence in the diffraction data is accounted for via the deconvolution in Eq. 7.14, yielding an updated estimate of the coherent wavefield, $\Psi'(\mathbf{q})$.

At the Advanced Photon Source (and at the majority of synchrotron sources) the vertical coherence length is sufficiently long such that the illumination may be considered fully coherent in the vertical direction for many experiments. Under these conditions the operation need only be performed horizontally, resulting in a simple one-parameter parametrisation scheme to determine the horizontal coherence length, l_x, and corresponding coherence function $\hat{g}(\mathbf{q}, l_x)$.

Under the assumption that the coherence function is adequately represented by $g(\mathbf{r}_1 - \mathbf{r}_2, l_x)$, the extension to ptychography requires that the coherent modulus

constraint is replaced by the two-step system comprised of the coherence length estimation using in Eq. 7.13, followed by the modified modulus constraint in Eq. 7.14. For a probe, $P(\mathbf{r})$, and sample transmission function, $O(\mathbf{r})$, at position, $\mathbf{s}_j$, with partially coherent diffraction intensity, $I_j(\mathbf{q})$, where j is an index associated with each sample translation, this yields a set of estimates, $\{l_{x,1}, ..., l_{x,j}\}$ that are determined independently of one another. The coherence characterisation and partial coherence correction are performed simultaneously with the sample and probe retrievals.

The deconvolution in Eq. 7.14 yields an updated estimate of the coherent scattered wave, $\Psi'(\mathbf{q})$, which is independent of the coherence function $\hat{g}(\mathbf{q}, l_{x,j})$. The coherent scattered wave may be propagated to the sample plane using the usual coherent propagation via Eq. 2.15, enabling updates on the sample transmission function, $O(\mathbf{r})$, and probe, $P(\mathbf{r})$. If the coherence function $g(\mathbf{r}_1 - \mathbf{r}_2, l_x)$ is evolving over the scanning trajectory (e.g. if the illumination coherence function is evolving with time), the proposed algorithm can account for this evolution, independently characterising and correcting for deviations from full spatial coherence at each scan position. Alternately, provided the coherence function is sufficiently stable during the ptychographic data acquisition, estimating the coherence length over the entire scanning trajectory introduces a large amount of redundancy in the coherence characterisation, allowing the coherence function to be updated using the mean retrieved coherence length. The ability to estimate the coherence length parameter over a large number of measurements reduces the possibility of noise dominating the coherence characterisation, resulting in an improved robustness compared to a single measurement.

7.5.1 Analysis with simulated data

Using the coherence-correction ePIE algorithm, the sample transmission function and probe were reconstructed for the simulated partially coherent ptychographic datasets detailed in §7.4.1. The initial algorithm parameters, in particular the initial sample transmission and probe estimates were as for the reconstructions using the modal ePIE algorithm detailed in §7.4, with the distinction that no information on the coherence parameters was used. Instead, under the assumption that the coherence function, $g(\mathbf{r}_1 - \mathbf{r}_2, l_x)$, had the form in Eq. 7.11, with full spatial coherence in the vertical direction, the coherence length was iteratively estimated for each scan position simultaneously with the sample transmission and probe retrievals using the metric in Eq. 7.13.

The standard ePIE algorithm was used for the first 20 iterations to obtain an

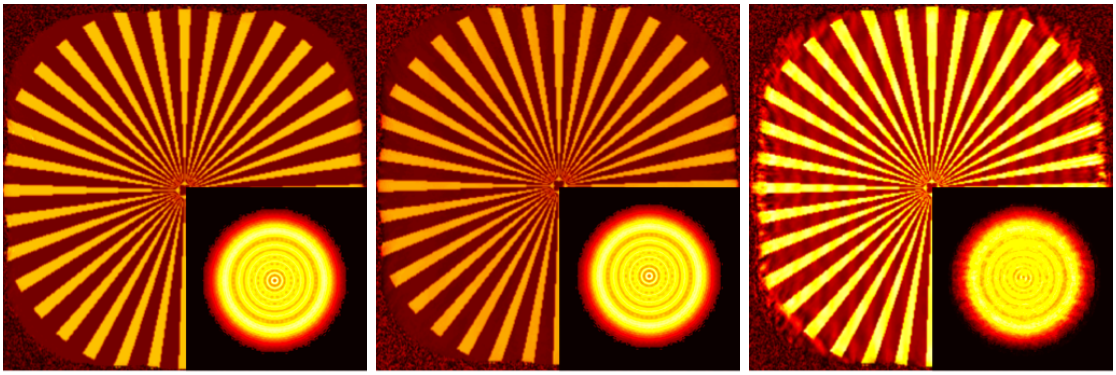

(a) (b) (c)

Figure 7.6: *in situ* retrieval of the coherence length and partial coherence correction on simulated partially coherent ptychographic datasets. The sample transmission amplitude and probe amplitude reconstructions in (a)-(c) were obtained using the same datasets as those presented in Fig. 7.4, i.e. using partially coherent ptychographic data with coherence lengths of 5 μm, 3 μm and 1 μm respectively. For compactness, only the amplitude is presented.

estimate of the sample transmission and probe functions. For the remaining 230 iterations the coherence-correction ePIE algorithm was used. The retrieved sample transmission and probe amplitudes for coherence lengths of 5 μm, 3 μm and 1 μm are shown in Fig. 7.6, demonstrating the ability to obtain highly accurate retrievals of the sample transmission function and probe functions. Due to the similarity between the phase and amplitude, only the amplitudes are shown. The retrieved coherence lengths for the reconstructions in Fig. 7.6 were determined to be (5.00 ± 0.01) μm, (3.00 ± 0.01) μm, (1.00 ± 0.01) μm, where the errors are the maximal deviation from the mean.

7.5.2 Analysis with X-ray data

The experiment was performed at the Advanced Photon Source beamline 34-ID-C (see §5.1 for details) using the experimental parameters in Table 5.2. All measurements were conducted using X-rays with an energy of 9 keV ($\lambda = 0.138$ nm). A set of secondary slits, located approximately 48 m downstream from the undulator and within the end-station, were used to vary the spatial coherence characteristics of the incident illumination (see Fig. 5.1). The slits were initially set to 60 μm $\times$ 50 μm in the horizontal and vertical directions respectively. The resulting probe was focused onto the target sample using a set of compact Kirkpatrick-Baez (KB) mirrors in the geometry outlined in §5.1, where it is noted that the mirrors focused the entire beam, including the diffracted lobes, onto the sample without cutting any of the beam (i.e. preserving the coherence characteristics). The star shaped aperture de-

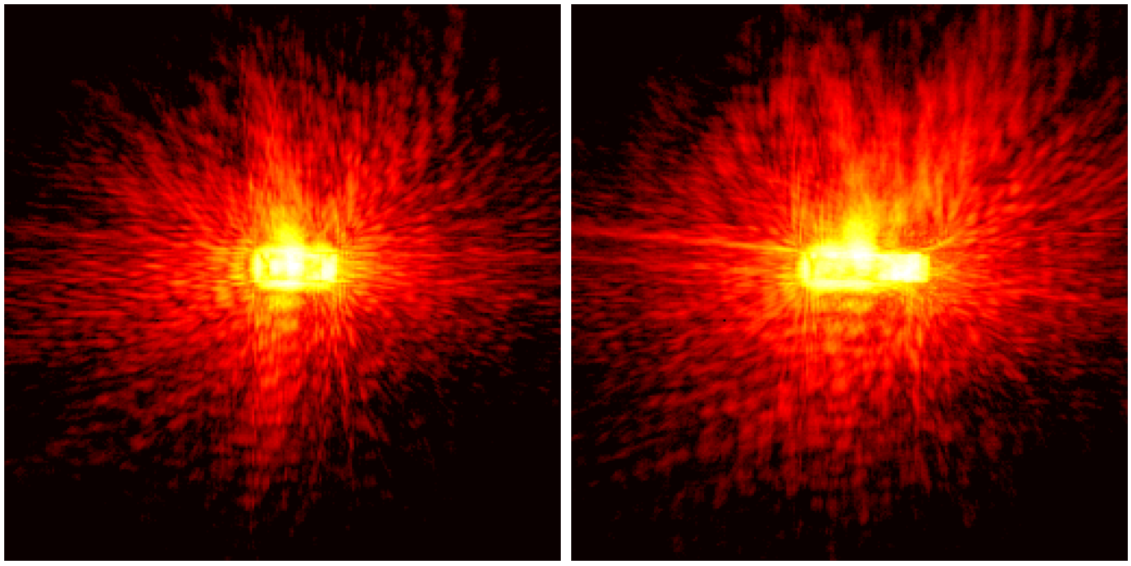

(a) (b)

Figure 7.7: Partially coherent diffraction data from a star shaped aperture with beam-defining slits set to 60 μm $\times$ 50 μm and 100 μm $\times$ 50 μm in the horizontal and vertical directions respectively. The data collection time was 0.12 seconds for all images.

tailed in §5.3.1 and shown in Fig. 5.3 was scanned through the resulting probe using the scanning trajectory parameters provided in Table 5.2. A second ptychographic dataset was obtained using horizontal and vertical slit settings of 100 μm $\times$ 50 μm.

Example diffraction data with the sample placed in the centre of the scanning trajectory for the two slit settings is shown in Fig. 7.7 (a) and (b). Varying the slit width impacts on several experimental parameters. The number of photons incident on the sample increases as the slits are widened. This causes a corresponding increase both in the fully transmitted beam, seen by the widening of the central bright region in Fig. 7.7 (a) and (b), but more importantly in the number of sample scattering events, resulting in the increased scattering angle as the slits are widened. The increase in slit width is also accompanied by a corresponding increase in blurring of the diffraction data.

The sample transmission function and probe were reconstructed using the standard ePIE algorithm (i.e. under the assumption of full spatial coherence) with the 60 μm $\times$ 50 μm ptychographic dataset for 1000 iterations. The initial sample transmission function estimate was a random binary distribution with an initial probe estimate determined from previous studies at this beamline (see §5.3). The resulting reconstructed sample transmission amplitude and phase are shown in Fig. 7.8 (a) and (b). The phase reconstruction is presented in wrapped form as the rapid, erroneous variation in phase introduced subsequent errors in the phase unwrapping algorithms. There is a correspondence between erroneous variation across

the lithographed regions in both the amplitude and phase reconstructions. The lithographed regions are transparent to X-rays and are expected to have uniform density.

The sample transmission function and probe were then retrieved using the standard ePIE algorithm on the 100 μm $\times$ 50 μm dataset for 1000 iterations. The resulting sample transmission amplitude and phase are shown in Fig. 7.9 (a) and (b). The reduction in the phase retrieval accuracy compared to the reconstructions in Fig. 7.8 (a) and (b) may be largely attributed to the decrease in the beam coherence associated with wider slit settings.

Using the coherence-correction ePIE algorithm, the sample transmission function and probe were retrieved simultaneously with the iterative coherence characterisation and correction for both of the 60 μm $\times$ 50 μm and the 100 μm $\times$ 50 μm datasets. In both cases, the standard ePIE algorithm was used for 300 iterations to estimate the sample transmission function and probe and the coherence-correction ePIE algorithm was used for the remaining 700 iterations. The coherence-corrected sample transmission amplitude and phase for the 60 μm $\times$ 50 μm dataset are shown in Fig. 7.8 (c) and (d) respectively. The corresponding reconstructions for the 100 μm $\times$ 50 μm dataset are shown in Fig. 7.9 (c) and (d). In both cases there is a significant improvement compared to the standard ePIE reconstructions. The reduction in artefacts corresponds to a reduction in the χ^2 metric across the entire scanning trajectory for both datasets as seen in Fig. 7.10 (a) and (b).

The mean retrieved coherence length, $l_{\bar{x}}$, was initially used to estimate a coherence function, $\hat{g}(\mathbf{q}, l_{\bar{x}})$, used in the modified modulus constraint in Eq. 7.14 to obtain each updated far-field wavefield $\Psi'_j(\mathbf{q})$. For the final 500 iterations the coherence length estimation was refined using individual retrieval of the coherence lengths, $l_{x,j}$, and corresponding set of coherence functions, $\hat{g}(\mathbf{q}, l_{x,j})$. This method yielded improved accuracy in the coherence length estimation, as well as the sample transmission and probe retrievals when compared to the results obtained using only independent estimation. The mean coherence length estimation was performed for 200 iterations. The retrieved coherence lengths for the 60 μm $\times$ 50 μm and the 100 μm $\times$ 50 μm ptychographic dataset are provided in Fig. 7.10 (c), yielding coherence length estimates of 1.6 ± 0.2 μm and 1.2 ± 0.1 μm respectively, where the estimates are given in the form $\mu_{l_x} \pm \sigma_{l_x}$.

The coherence length estimation scheme in Eq. 7.13 and the χ^2 calculation are both dependent on the accuracy in the the coherent far-field intensity estimate, $|\Psi(\mathbf{k})|^2$. As discussed in Chapter 6, errors in the scan trajectory can have a major impact on the sample transmission and probe estimates, and consequentially on

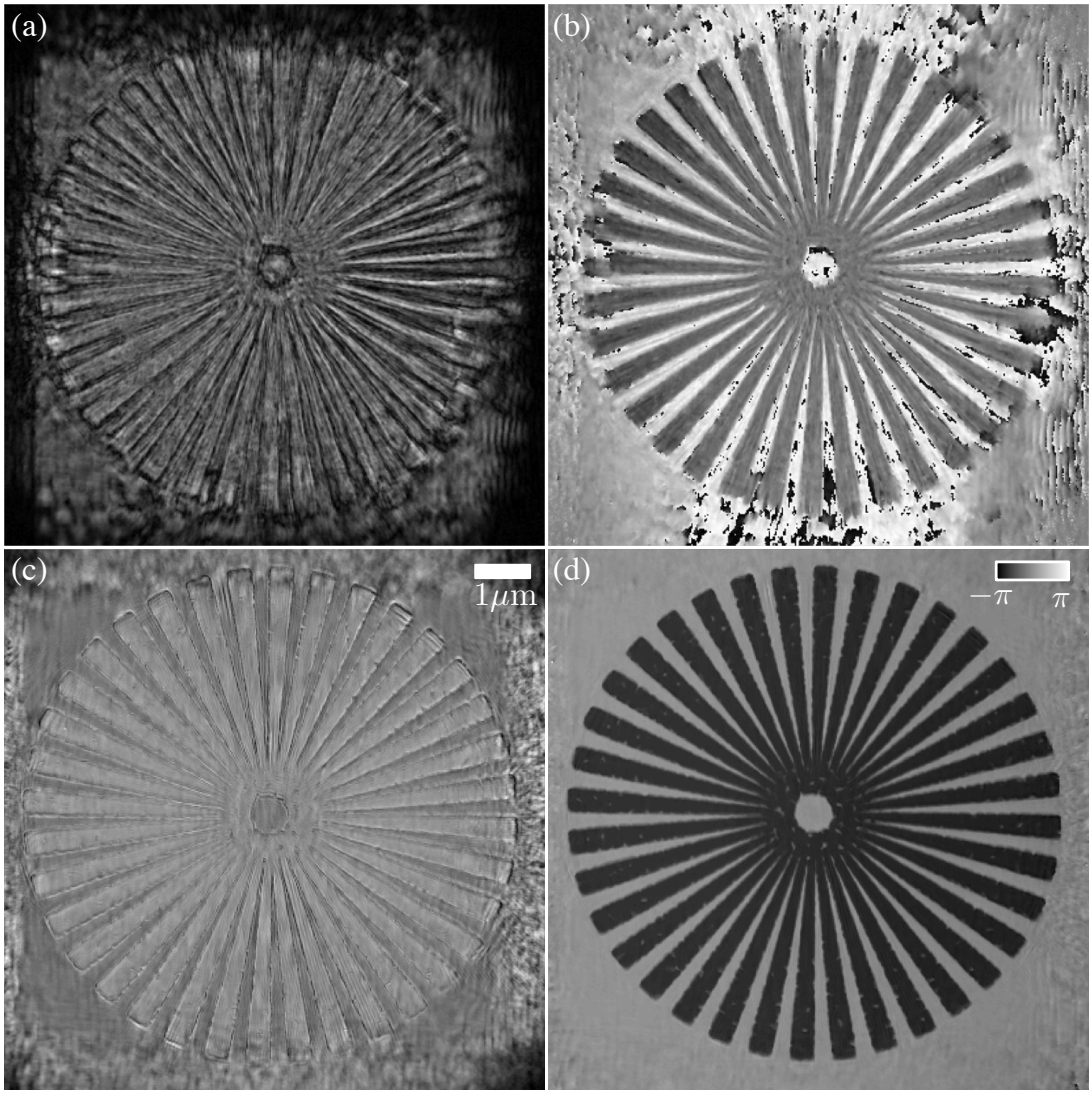

Figure 7.8: (a) and (b) show the retrieved sample transmission amplitude and phase using the standard ePIE algorithm on datasets obtained with beam-defining slit settings of 60 μm $\times$ 50 μm. The sample transmission amplitude and phase using coherence correction are shown in (c) and (d) respectively

the accuracy of the wavefield, $\Psi(\mathbf{k})$. It is therefore to be expected that errors in the scan trajectory would impact both the coherence-length estimation and the χ^2 calculation. The normalised magnitude of the horizontal scan trajectory error vector, $|\Delta x|$, retrieved using the χ^2 error correction algorithm described in §6.6, is shown in Fig. 7.10 (d). The sinusoidal form of the position error retrieval is indicative of a rotational misalignment between the scanning stage and the detector. Fig. 7.10 (d) indicates a coupling between the retrieved horizontal position errors, the retrieved coherence lengths and the χ^2 plots (all quantities are normalised). This variation is present in both the standard ePIE and coherence-corrected χ^2 plots in Fig. 7.10 (a) and (b). The variation is therefore independent of the coherence retrieval and

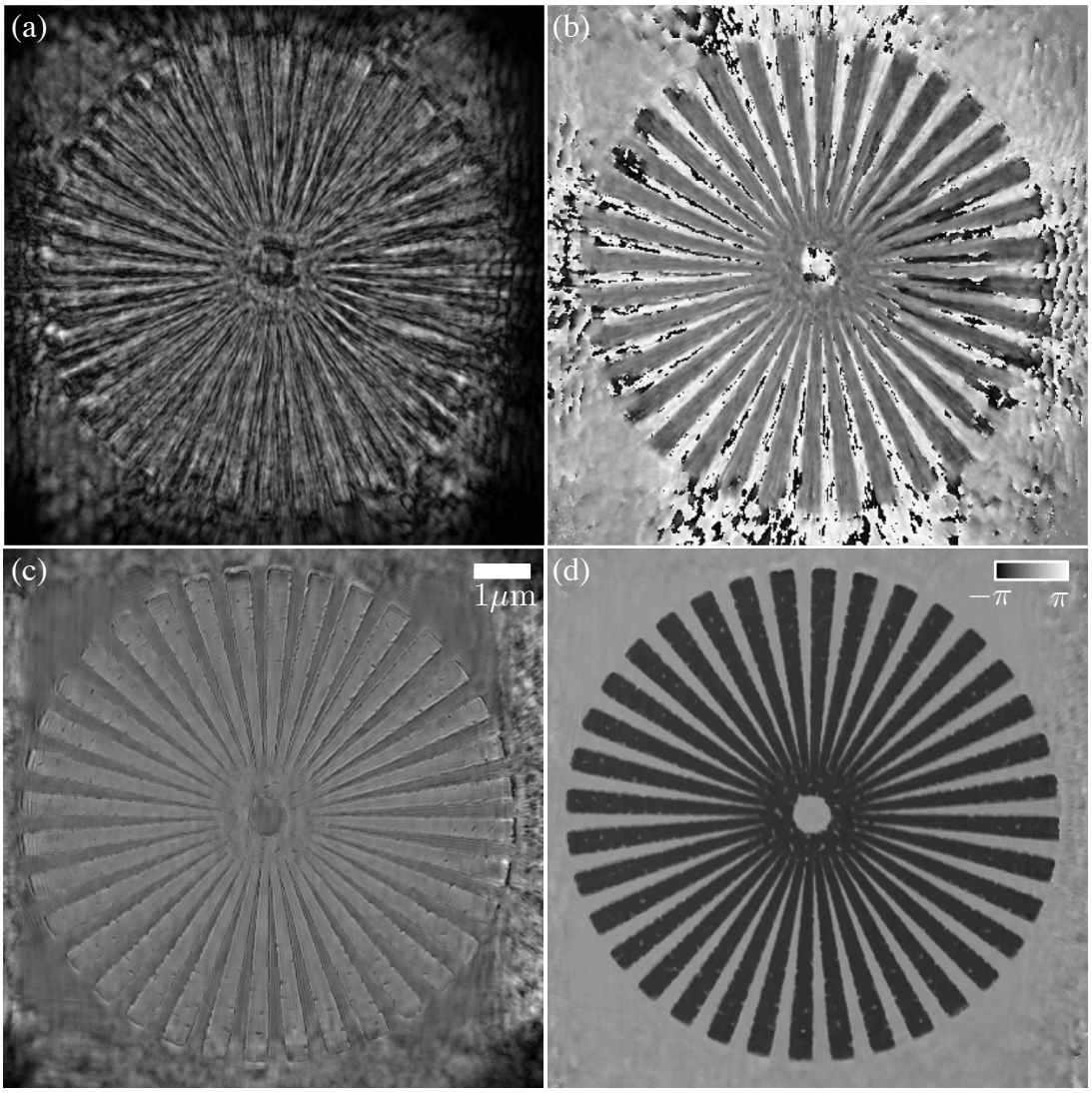

Figure 7.9: (a) and (b) show the retrieved sample transmission amplitude and phase using the standard ePIE algorithm on datasets obtained with beam-defining slit settings of 100 μm $\times$ 50 μm. The sample transmission amplitude and phase using coherence correction are shown in (c) and (d) respectively.

correction scheme. It is also noted that the coherence-correction algorithm corrects for a number of factors that contribute to blurring in the diffraction data, including the detector point spread function as well as stability in the sample and detector positions during the acquisition of each individual diffraction image. It is expected that the blurring contribution from these factors would yield a lower estimate of the coherence length.

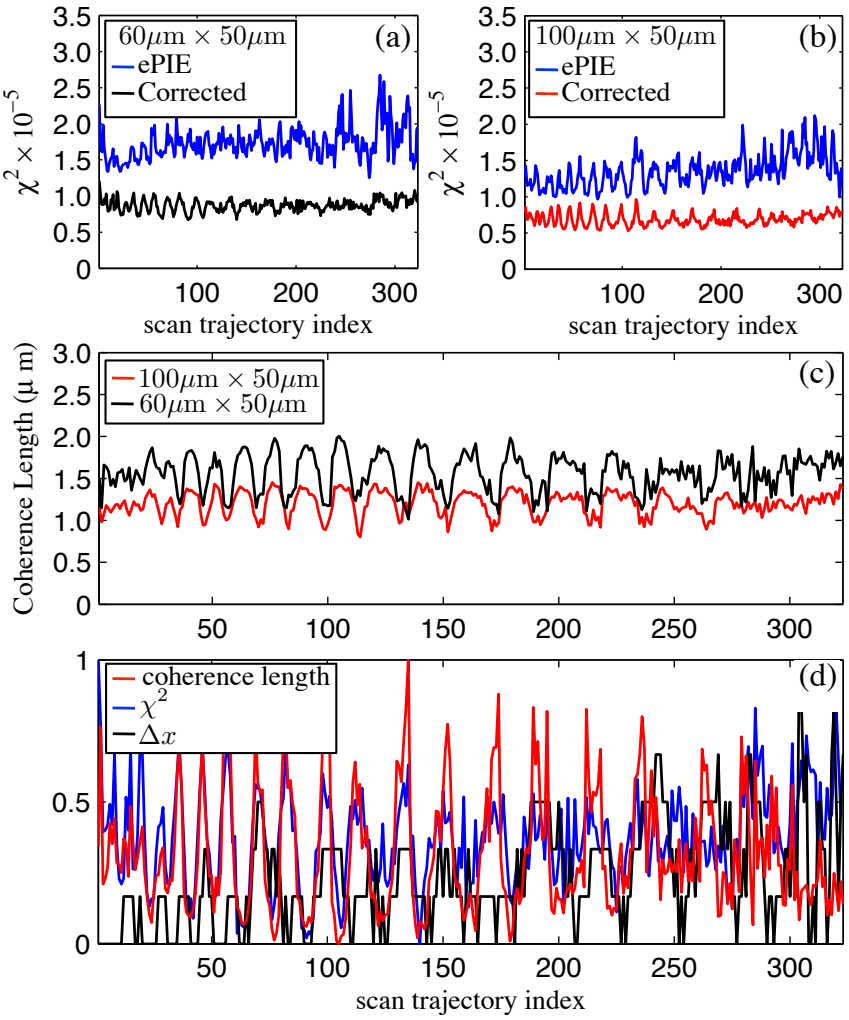

Figure 7.10: Retrieved coherence lengths for high flux data. (a) and (b) compare the uncorrected and coherence-corrected χ^2 metric for the 60 μm $\times$ 50 μm and 100 μm $\times$ 50 μm datasets respectively. (c) shows the retrieved coherence lengths for both datasets. (d) shows a comparison of the 100 μm $\times$ 50 μm retrieved width of the coherence function, $\hat{g}(\mathbf{q}, l_{\bar{x}})$, the χ^2 metric, and magnitude of the horizontal scan position, Δx (normalised).

7.6 Conclusion

This chapter proposed two modifications to the ptychographic algorithm that enable high-resolution images of an extended sample to be obtained using a high flux, partially coherent ptychographic dataset. It was demonstrated that if the spatial coherence properties are well characterised, the partial coherence in a partially coherent ptychographic dataset can be accounted for by decomposing the illumination into a series of Gaussian-Schell modes. Using simulated partially coherent ptychographic data obtained under the assumption of a Gaussian coherence function over a range of coherence characteristics, the proposed modal partially coherent ptychographic algorithm obtained accurate retrievals of the sample transmission function

and probe, with the minimum tested coherence length at 25% of the linear dimensions of the illumination. The advantage of the modal approach is to provide an additional constraint on the partially coherent ptychographic algorithm. This requires a separate spatial coherence measurement to be performed, placing additional demands in a synchrotron experiment. This can be a particular issue where the coherence characteristics evolve over the ptychographic data acquisition.

If the illumination coherence cannot be adequately measured, this study has shown that under the assumption of a Gaussian coherence function, a coherence-characterisation can be performed simultaneously with the ptychographic sample transmission and probe retrievals, using only the ptychographic diffraction data. The primary advantage of this approach is that there is no need to perform an independent characterisation of the MOI. The algorithm accurately retrieved the coherence length simultaneously with the sample transmission function and probe from the simulated partially coherent data used in the modal reconstructions. The coherence-correction ePIE algorithm was also tested with partially coherent ptychographic X-ray data using two partially coherent ptychographic datasets with distinct coherence characteristics. The 60 μm $\times$ 50 μm and 100 μm $\times$ 50 μm ptychographic datasets yielded horizontal coherence lengths of 1.6$\pm$0.2 μm and 1.2$\pm$0.1 μm respectively. As expected, the retrieved coherence length was reduced when using wider slit settings. Although a separate coherence characterisation was not performed to confirm these measurements, it has been previously shown in CDI [127] using data obtained at the APS beamline 2-ID-B that the mechanism used to perform the coherence characterisation yielded a recovered coherence length in very close agreement with a YDS spatial coherence measurements performed at beamline 2-ID-B [53]. The coherence-correction mechanism was shown to be a useful tool to correct for a number of factors that contribute to blurring in the diffraction data - as confirmed by the significant reduction in the χ^2 metric across the entire scanning trajectory and the improvements in the accuracy of the reconstructed sample image. The coherence-correction ePIE algorithm demonstrated significant improvement in the retrieved sample transmission image for both partially coherent ptychographic datasets, resulting in a high-resolution sample image retrieval using high-flux ptychographic data.

CHAPTER

EIGHT

CONCLUSION

The past decade has seen a great deal of research on high-resolution imaging using coherent X-ray diffraction data from finite scattering objects. These techniques have their foundations in crystallography, in particular iterative phase-retrieval algorithms, with the majority of applications employing a variant on the iterative schemes proposed by Fienup. The result is a promising form of high-resolution lensless X-ray microscopy with the potential to make significant contributions to structural biology and the material sciences. The sample size restrictions imposed by spatial frequency sampling requirements have been addressed by ptychography, a data rich development of CDI capable of imaging extended samples and rapidly becoming an established nanoscale X-ray imaging procedure.

Chapter 4 presented a demonstration of Fresnel CDI tomography using ptychography. Fresnel diffraction data was obtained over a series of sample rotations and the resulting set of projected sample transmission reconstructions were used with computed tomography to obtain a three-dimensional quantitative map of the sample. The study noted a sensitivity to stability, resulting in a series of radial artefacts throughout the series of reconstructed sample images and resulting errors in the three-dimensional tomographic mapping of the sample. These artefacts are thought to be responsible for the deviations from the experimentally obtained mean refractive index values ($\delta = (5.9 \pm 1.4) \times 10^{-5}$ and $\beta = (1.5 \pm 0.4) \times 10^{-5}$) compared to the theoretical value ($\delta = 7.23 \times 10^{-5}$ and $\beta = 6.93 \times 10^{-6}$). It was found that the radial artefacts could be reduced using Fresnel CDI ptychography. The ptychographic reconstructions were used to bootstrap neighbouring projections. Despite the improvements offered by this technique, the qualitative and quantitative improvements of the ptychographic reconstructions suggest that ptychography should

be performed for every projection when performing Fresnel CDI tomography.

The fundamental mechanism underlying ptychography is the ability to use additional information obtained by translating the target sample through an illuminating probe. In Chapter 5, an algorithm was proposed that can use ptychographic data obtained by scanning the target sample through several distinct probes rather than the standard, single probe method. The algorithm was tested using probe-diverse ptychographic X-ray data, demonstrating the ability to retrieve the sample transmission function and all illuminating probes simultaneously. This resulted in a significant improvement in the reconstructed sample transmission function compared to the standard single probe ptychographic retrievals while using an equal sized ptychographic dataset. No further improvements were observed with additional ptychographic data. As the amount of data reaches a certain limit, additional ptychographic data will only lead to incremental improvements in the reconstruction quality as the achievable reconstruction quality is primarily affected by intrinsic experimental issues including uncertainty in the sample position, the beam coherence characteristics and noise in the recorded diffraction data. It was also shown that although the additional information in a ptychographic dataset compensates for undersampling the diffraction data, the use of undersampled data introduces artefacts with a periodicity determined by the diffraction data size that cannot be removed using the standard ePIE algorithm or by artificially upsampling the diffracted wavefield with the sPIE extension. If the sample occupies a region greater $N \times \Delta_s$, where the diffraction data is recorded on an $N \times N$ grid and Δ_s is the sample plane sampling interval, it appears that the overlapping of the sample image and the periodic artefacts can have a significant impact on the reconstruction accuracy.

Ptychography is a robust, high-resolution imaging method capable of imaging extended samples, but these advances are accompanied by a number of additional experimental challenges compared to CDI, including the need to control the sample translations to nanoscale accuracy when using X-rays and additional sensitivity to sample drift and stage misalignment. The uncertainty in the sample positions limits the achievable sample image resolution, resulting in artefacts in the reconstructed sample image or the complete failure to converge. This is a significant problem when using X-rays, and an even greater problem when using electrons as the probe. In Chapter 6 an iterative cross-correlation gradient-descent position optimisation scheme was proposed, allowing the scan trajectory to be corrected simultaneously with the retrieval of the sample transmission function and illuminating wavefield. The primary advantage of the proposed method compared with the standard χ^2 error correction method is an improved position retrieval efficiency. In particular,

the cross-correlation gradient estimation yields a search direction that minimises the difference between the true scan trajectory and the estimated scan trajectory. The method can be used to correct for the scan positions to a very fine accuracy (< 0.01 pixels) using simulated data. The algorithm operation and accuracy was tested using synchrotron X-ray data, resulting in an improved sample image reconstruction compared to the reconstructions obtained with no position error correction. However, the cross-correlation signal demonstrated some sensitivity to noise when using X-ray data and it was necessary to restrict the position updates to those that reduced the χ^2 metric. This sensitivity is thought to be due to noise dominating the cross-correlation calculation. The results were compared with a standard χ^2 position correction scheme, demonstrating highly correlated position retrieval maps with the cross-correlation method and a small improvement in the sample image retrieval.

In Chapter 7, two modifications to the ptychographic algorithm were proposed, enabling ptychography to be performed using a high flux, partially coherent ptychographic dataset. If the spatial coherence properties are well characterised, the partial coherence can be accounted for by decomposing the illumination into a series of Gaussian-Schell modes. The advantage of the modal approach is to provide an additional constraint on the partially coherent ptychographic algorithm. The primary issues with this approach are the need to perform a separate spatial coherence measurement and the inability to account for evolving coherence characteristics during the data acquisition. A second proposed algorithm demonstrated that, under the assumption of a Gaussian coherence function, a coherence characterisation and correction can be performed simultaneously with the sample transmission and illumination probe retrievals, using only the partially coherent ptychographic diffraction data. The effectiveness of the algorithm was tested using simulated partially coherent data over a range of spatial coherence characteristics, demonstrating accurate retrieval of the coherence parameters, sample transmission function and probe for each dataset. The algorithm was tested using two high-flux, partially coherent ptychographic X-ray datasets with distinct coherence characteristics. The algorithm demonstrated the ability to retrieve an estimate of the coherence length simultaneously with the sample image and probe retrievals. The coherence-correction resulted in a significant improvement in the accuracy of the reconstructed sample image as well as a significant reduction in the χ^2 metric across the entire scanning trajectory for two partially coherent ptychographic datasets. Both of the proposed algorithms enable ptychography to be performed over a greater range of coherence characteristics than possible under the assumptions of full spatial coherence, with the *in*

*situ*coherence-characterisation and correction demonstrating the ability to obtain high-resolution images of the target sample when using high-flux ptychographic X-ray data.

This thesis has proposed a number of high-resolution ptychographic X-ray imaging techniques, using manufactured samples as a metric to gauge the success of a particular method. The greater aim is to use these methods to obtain high-resolution images of material and biological samples, providing information that will assist in nano-characterisation when using X-rays and atom scale characterisation when using electrons as the probe.

APPENDIX

A

PRELIMINARIES

The Fourier transform is defined as:

$$\tilde{f}(q) = \mathscr{F}[f] = \int_{-\infty}^{\infty} f(x) e^{iq\mathbf{x}} d\mathbf{x} \tag{A.1}$$

A quantity expressed as a function of spatial coordinates $\mathbf{r} = (x, y, z)$ is termed to be in "direct space". The Fourier transform of direct space functions are said to be in "Fourier space" or "reciprocal space" with co-ordinates $\mathbf{q} = (q_x, q_y, q_z)$. The convolution of two functions f and g is defined as

$$(f \star g)(x) = \int f(x') g(x - x') dx', \tag{A.2}$$

with closely related operation know as the cross-correlation, defined as

$$(f \otimes g)(x) = \int f(x') g^*(x - x') dx' \tag{A.3}$$

$$= \mathscr{F}^{-1}\left[\mathscr{F}[f]\ (\mathscr{F}[g])^*\right]. \tag{A.4}$$

An important special case of Eq. A.3 is the autocorrelation function, defined as

$$(f \otimes f)(x) = \mathscr{F}^{-1}\left[|\mathscr{F}[f]|^2\right]. \tag{A.5}$$

The properties of the Fourier transform used throughout this thesis are briefly detailed below. The conservation of the L_2 norm (i.e. energy conservation) is expressed through Parseval's theorem, which may be written as

$$\int |\tilde{f}(q)|^2 dq = \int |f(x)|^2 dx. \tag{A.6}$$

By Eq. A.1, the Fourier transform of a translated function produces a phase ramp

$$\mathscr{F}\left[f(x+a)\right] = e^{iqa}\mathscr{F}\left[f(x)\right] \tag{A.7}$$

For a two-dimensional function, $f(x,y)$, the projection $p(x)$ of $f(x)$ onto the x-axis is

$$p(x) = \int_{-\infty}^{\infty} f(x,y)dy. \tag{A.8}$$

The slice $s(k_x)$ through Fourier space parallel to the projection $p(x)$ and through the origin in Fourier space is

$$\begin{aligned} s(k_x) &= F(k_x, 0) \\ &= \int_{-\infty}^{\infty}\int_{-\infty}^{\infty} f(x,y)e^{-2\pi i(xk_x+yk_y)}dxdy \\ &= \int_{-\infty}^{\infty}\left[\int_{-\infty}^{\infty} f(x,y)dy\right]e^{-2\pi ixk_x}dx \\ &= \int_{-\infty}^{\infty} p(x)e^{-2\pi ixk_x}dx. \end{aligned} \tag{A.9}$$

This is the one dimensional Fourier transform of the projection, $p(x)$, in the direction of the x-axis. Rotating $f(x,y)$ by an angle θ simply rotates the Fourier transform, $\mathscr{F}[f(x,y)]$, by the same angle θ and the above argument holds. The proof for higher dimensions is easily generalised from the above formulation.

APPENDIX

B

SPATIAL COHERENCE MEASUREMENT AT SPRING-8 BEAMLINE BL20XU

The SPring-8 BL20XU beamline is a hard X-ray microscopy and micro-tomography imaging beamline used for applications including medical imaging. A schematic of the BL20XU beamline is provided in Fig. B.1. The beamline was maintained *in vacuo* from the monochromator to the entrance of the downstream hutch, a total propagation distance of approximately 200 m.

Although the long source-sample propagation distance yielded an improved beam coherence in accordance with the Van Cittert-Zernike theorem [10], it also had the effect of exacerbating instability in the beam trajectory. This effect was particularly noticeable at this beamline as the double crystal monochromator was cooled in a pool of liquid nitrogen. Heat transfer from the monochromator caused the nitrogen pool to boil, resulting in continual beam jitter. A measurable effect of the beam jitter was to reduce the spatial coherence length over time. This may be explained by regarding the effects of partial spatial coherence as equivalent to Gaussian uncertainty in the beam position.

To produce a more regular beam intensity a spinning paper diffuser, positioned upstream of the sample, was used to diffuse the X-rays. The diffuser had a spin period much smaller than the data acquisition time. This scenario is well approximated by incoherent averaging over an ensemble of spatially-random transverse phase screens. The addition of many speckled interference fringe images over an exposure yields a sum of fringes with reduced visibility.

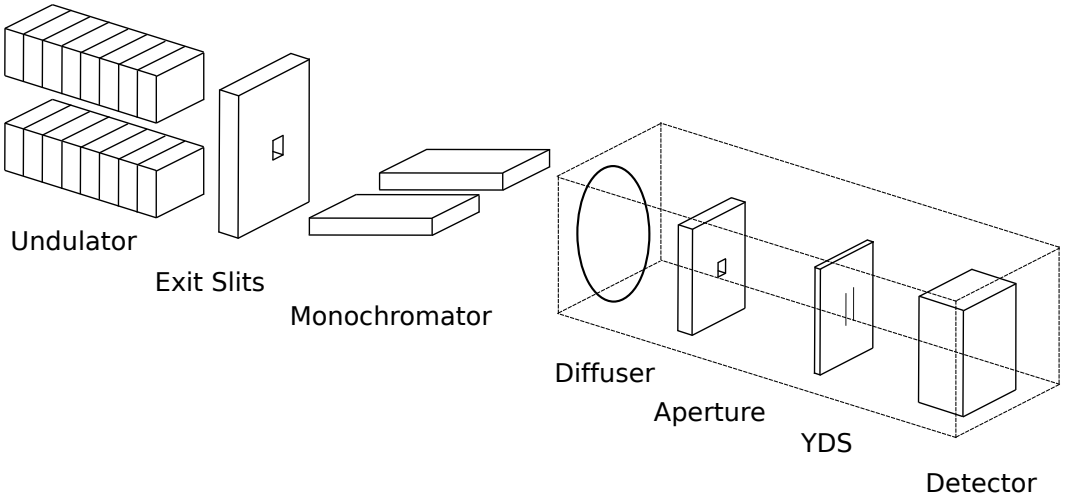

Figure B.1: SPring-8 BL20XU beamline schematic. The beamline features a 200 m propagation distance between the monochromator and the experimental hutch. The beam intensity was smoothed using a spinning paper diffuser. A 40 μm platinum aperture selected out a central portion of the beam. A YDS apparatus containing a series of YDS slits was used to measure the coherence characteristics of the illuminating wavefield.

The experiment was performed using X-rays at an energy of 9 keV. A central region of the beam was selected using a 40 μm platinum pinhole aperture, positioned approximately 37 mm upstream of the sample. The experimental geometry is shown in Fig. B.1. The coherence characteristics were measured using a YDS apparatus consisting of six YDS pairs with slit separations ranging from 6 μm to 16 μm, in steps of 2 μm. The YDS apparatus was manufactured using a focused ion beam. The slits were 1 μm wide, 50 μm high, and milled into an 8 μm thick layer of gold deposited on a silicon nitride window. The slits were oriented parallel to the exit slits of the monochromator and placed in the arrangement shown in Fig. B.1.

The data was collected on a 1340 $\times$ 1300 Hamamatsu phosphor coupled CCD with 3.3 μm square pixels, placed approximately 7.1 m downstream of the YDS apparatus. The fringe intensity patterns for each slit separation are shown in Fig. B.2. The intensity peak at the centre of the interference patterns is due to 70% [120] X-ray transmission through the 8 μm gold layer. The asymmetry in the two-slit diffractions in Fig B.2 is due to a path length difference introduced by a small rotational offset in the slit position.

The ideal two-slit fringe intensity distribution, $I\left(x\right)$, recorded on a detector with pixel width, δ, located at a distance, z, from the slits for light of wavelength, λ, with wavelength spread, $\Delta\lambda$, incident upon slits of width, α, and separation, β, is [10]

$$I\left(x\right) = A(x)I_0\left[1 + \mu_{12}\left(\frac{\sin\left(\frac{\pi\Delta\lambda}{\lambda z}x\right)}{\frac{\pi\Delta\lambda}{\lambda z}x}\right)\left(\frac{\sin\left(\frac{\pi\delta\beta}{\lambda z}\right)}{\frac{\pi\delta\beta}{\lambda z}}\right)B\left(x\right)\right], \tag{B.1}$$

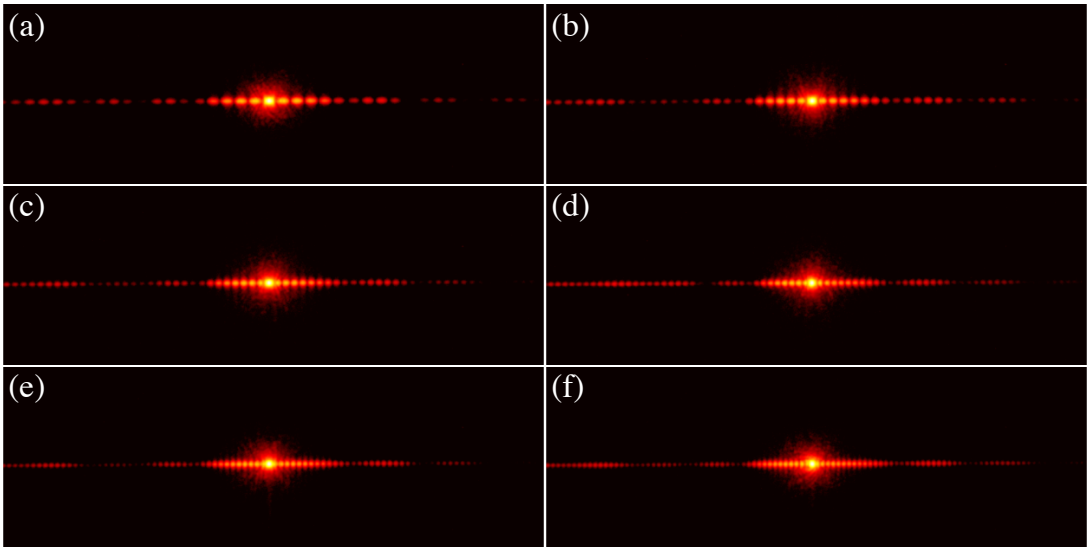

Figure B.2: Young's Double Slit data at SPring-8 beamline BL20XU. (a)-(f) show YDS interference fringes for 6 μm to 16 μm slits in steps of 2 μm (shown in logscale).

where I_0 is the central intensity of the light and μ_{12} is the degree of coherence (see Eq. 2.46). The envelope function, $A(x)$, and fringe interference function, $B(x)$, are

$$A(x) = \left[\frac{\sin\left(\frac{\pi\alpha}{\lambda z}x\right)}{\frac{\pi\alpha}{\lambda z}x}\right]^2,$$

and

$$B(x) = \cos\left(\frac{2\pi}{\lambda z}\beta x\right).$$

The degree of coherence, $\mu_{12}(x)$, is obtained by fitting the two-slit diffraction data to the ideal distribution in Eq. B.1.

A least square regression fit was performed using Eq. B.1 for each slit separation over the range 6 μm to 16 μm. The central peak was excluded from the data as it is due to direct beam transmission rather than two-slit interference. The degree of coherence for each slit separation was determined using the data on each side of the central peak and averaging the results. The measured values differed by no more than 5% for each slit separation. An example fit using the 16 μm slit data is provided in Fig. B.3 (a). The resulting set of visibility measurements are provided in the plot in Fig. B.3 (b).

The assumption that $\mathbf{J}(\mathbf{r}_1, \mathbf{r}_2)$ is of Gaussian form is supported by previous coherence measurements at this beamline [130], using the same apparatus, in particular when using a spinning paper diffuser. The horizontal coherence length, l_x, may

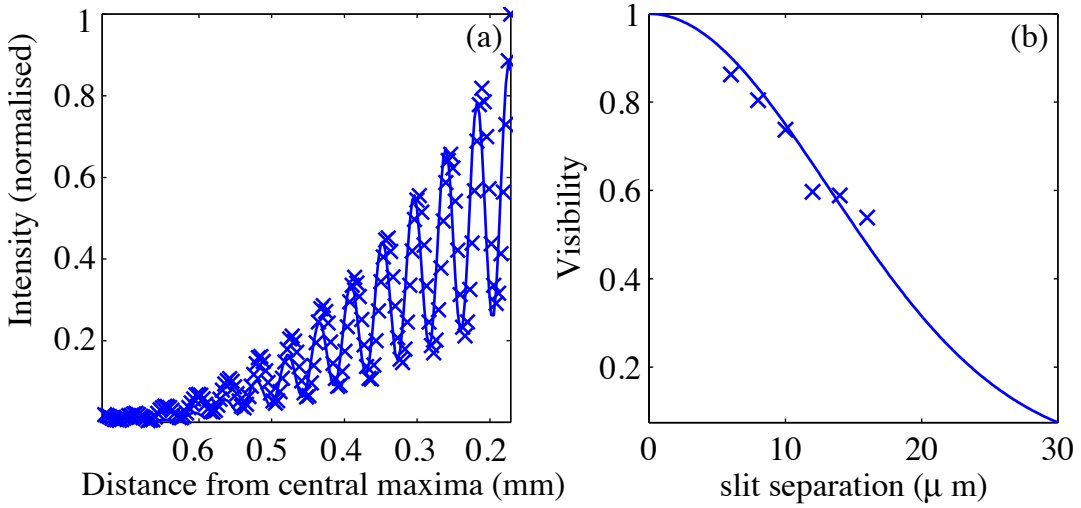

Figure B.3: Coherence characterisation at SPring-8 beamline BL20XU. (a) shows an example fitting to Eq. B.1 for the 16 μm data. (b) shows a plot of the visibility of each dataset against the slit separation. Assuming a Gaussian MOI this may be used to determine the coherence length.

therefore be determined via the one-dimensional Gaussian coherence model

$$\mu_{12}(x) = \exp\left[-\frac{x^2}{l_x^2}\right], \tag{B.2}$$

where $\mu_{12}(x)$ is measured over a range of slit separations. A least squares regression fit to the Gaussian coherence function in Eq. B.2 was performed using the visibility measurements across the range of slit separations, yielding the horizontal coherence length at the sample plane as $l_x = (18.6 \pm 1.7)$ μm, where the errors were determined at the 95% confidence interval.

BIBLIOGRAPHY

[1] S. Flewett, H.M. Quiney, C.Q. Tran, and K.A. Nugent. Extracting coherent modes from partially coherent wavefields. *Opt. Lett.*, 34(14):2198–2200, JUL 2009.

[2] H.N. Chapman, A. Barty, M.J. Bogan, S. Boutet, M. Frank, S.P. Hau-Riege, S. Marchesini, B.W. Woods, S. Bajt, H. Benner, R.A. London, E. Plonjes, M. Kuhlmann, R. Treusch, S. Dusterer, T. Tschentscher, J.R. Schneider, E. Spiller, T. Moller, C. Bostedt, M. Hoener, D.A. Shapiro, K.O. Hodgson, D. Van der Spoel, F. Burmeister, M. Bergh, C. Caleman, G. Huldt, M.M. Seibert, F.R.N.C Maia, R.W. Lee, A. Szoke, N. Timneanu, and J. Hajdu. Femtosecond diffractive imaging with a soft-x-ray free-electron laser. *Nat. Phys.*, 2(12):839–843, DEC 2006.

[3] J.M. Rodenburg, A.C. Hurst, A.G. Cullis, B.R. Dobson, F. Pfeiffer, O. Bunk, C. David, K. Jefimovs, and I. Johnson. Hard-x-ray lensless imaging of extended objects. *Phys. Rev. Lett.*, 98(3):34801, JAN 2007.

[4] P. Thibault, M. Dierolf, A. Menzel, O. Bunk, C. David, and F. Pfeiffer. High-resolution scanning x-ray diffraction microscopy. *Science*, 321(5887):379–382, JUL 2008.

[5] M. Dierolf, A. Menzel, T. Thibault, P. Schneider, C.M. Kewish, R. Wepf, O. Bunk, and F. Pfeiffer. Ptychographic x-ray computed tomography at the nanoscale. *Nature*, 467(7314):436–439, September 2010.

[6] Roshdi Rashed. A pioneer in anaclastics. ibn sahl on burning mirrors and lenses. *Isis*, 81(308):464–491, 1990.

[7] R. Hooke. *Micrographia: or, Some physiological descriptions of minute bodies made by magnifying glasses.* J. Martyn and J. Allestry, 1667.

[8] Robert Koch. *Aetiology of tuberculosis*. William R. Jenkins, 1890.

[9] Robert Koch. A further communication on a remedy for tuberculosis. *British medical journal*, 1(1568):125, 1891.

[10] Max Born and Emil Wolf. *Principles of optics: electromagnetic theory of propagation, interference and diffraction of light*. CUP Archive, 1999.

[11] Michael J Rust, Mark Bates, and Xiaowei Zhuang. Sub-diffraction-limit imaging by stochastic optical reconstruction microscopy (storm). *Nature methods*, 3(10):793–796, 2006.

[12] H Bornfleth, Kurt Saetzler, R Eils, and C Cremer. High-precision distance measurements and volume-conserving segmentation of objects near and below the resolution limit in three-dimensional confocal fluorescence microscopy. *Journal of microscopy*, 189(2):118–136, 1998.

[13] P Lemmer, M Gunkel, D Baddeley, R Kaufmann, A Urich, Y Weiland, J Reymann, P Müller, M Hausmann, and C Cremer. Spdm: light microscopy with single-molecule resolution at the nanoscale. *Applied Physics B*, 93(1):1–12, 2008.

[14] J. Kirz, C. Jacobsen, and M. Howells. Soft x-ray microscopes and their biological applications. *Q. Rev. Biophys.*, 28(1):33–130, FEB 1995.

[15] P. Horowitz and J.A. Howell. A scanning x-ray microscope using synchrotron radiation. *Science*, 178(4061):608, 1972.

[16] B. Niemann, D. Rudolph, and G. Schmahl. X-ray microscopy with synchrotron radiation. *Applied Optics*, 15(8):1883–1884, 1976.

[17] W.L. Chao, B.D. Harteneck, J.A. Liddle, E.H. Anderson, and D.T. Attwood. Soft x-ray microscopy at a spatial resolution better than 15 nm. *Nature*, 435(7046):1210–1213, 2005.

[18] Kazuto Yamauchi, Hidekazu Mimura, Takashi Kimura, Hirokatsu Yumoto, Soichiro Handa, Satoshi Matsuyama, Kenta Arima, Yasuhisa Sano, Kazuya Yamamura, Koji Inagaki, et al. Single-nanometer focusing of hard x-rays by kirkpatrick–baez mirrors. *Journal of Physics: Condensed Matter*, 23(39):394206, 2011.

[19] Weilun Chao, Jihoon Kim, Senajith Rekawa, Peter Fischer, and Erik H. Anderson. Demonstration of 12 nm resolution fresnel zone plate lens based soft x-ray microscopy. *Opt. Express*, 17(20):17669–17677, 2009.

[20] L. Marton. Internal report. Technical report, RCA Laboratories, Princeton, New Jersey, NJ, 1939.

[21] M. Von Ardenne. Zur leistungsfhigkeit des elektronen-schattenmikroskopesa und uber ein rontgenstrahlen-schattenmikroskop. *Naturwiss*, 27:485–486, 1939.

[22] M. Von Ardenne. *Elektronen-Ubermikroskopie*. Springer, 1940.

[23] D. Sayre. Some implications of a theorem due to shannon. *Acta Crystallogr.*, 5:843, 1952.

[24] J.W. Miao, P. Charalambous, J. Kirz, and D. Sayre. Extending the methodology of x-ray crystallography to allow imaging of micrometre-sized noncrystalline specimens. *Nature*, 400(6742):342–344, JUL 1999.

[25] R.W. Gerchberg. Super-resolution through error energy reduction. *Optika Acta*, 21(9):709–720, 1974.

[26] J.R. Fienup. Space object imaging through the turbulent atmosphere. *Opt. Eng.*, 18(5):529–534, 1979.

[27] R.H.T. Bates. Fourier phase problems are uniquely solvable in more than one dimension. 1. underlying theory. *Optik*, 61:247–262, 1982.

[28] J.R. Fienup. Iterative method applied to image-reconstruction and to computer computer-generated holograms. *Opt. Eng.*, 19(3):297–305, 1980.

[29] J.R. Fienup. Phase retrieval algorithms: a comparison. *Appl. Optics*, 21(15):2758–2769, August 1982.

[30] R.P. Millane. Phase retrieval in crystallography and optics. *J. Opt. Soc. Am. A*, 7(3):394–412, March 1990.

[31] S. Marchesini. A unified evaluation of iterative projection algorithms for phase retrieval. *Rev. Sci. Instrum.*, 78(1):011301, JAN 2007.

[32] S. Marchesini, H. He, H. N. Chapman, S. P. Hau-Riege, A. Noy, M. R. Howells, U. Weierstall, and J. C. H. Spence. X-ray image reconstruction from a diffraction pattern alone. *Phys. Rev. B*, 68(14):140101, Oct 2003.

[33] S. Marchesini. Phase retrieval and saddle-point optimization. *J. Opt. Soc. Am. A*, 24(10):3289–3296, OCT 2007.

[34] J. Miao, D. Sayre, and H.N. Chapman. Phase retrieval from the magnitude of the fourier transforms of nonperiodic objects. *J. Opt. Soc. Am. A.*, 15(6):1662, JUN 1998.

[35] R.H.T Bates. Uniqueness of solutions to two-dimensional fourier phase problems for localized and positive images. *Comput. Vision Graph.*, 25(2):205–217, 1984.

[36] P. Thibault, V. Elser, C. Jacobsen, D. Shapiro, and D. Sayre. Reconstruction of a yeast cell from x-ray diffraction data. *Acta Crystallogr. A*, 62:248–261, JUL 2006.

[37] J.W. Miao, T. Ishikawa, B. Johnson, E.H. Anderson, B. Lai, and K.O. Hodgson. High resolution 3d x-ray diffraction microscopy. *Phys. Rev. Lett.*, 89(8):088303, AUG 2002.

[38] J.W. Miao, K.O. Hodgson, T. Ishikawa, C.A. Larabell, M.A. LeGros, and Y. Nishino. Imaging whole escherichia coli bacteria by using single-particle x-ray diffraction. *Proc. Nat. Acad. Sci. U.S.A.*, 100(1):110–112, JAN 7 2003.

[39] D. Shapiro, P. Thibault, T. Beetz, V. Elser, M. Howells, C. Jacobsen, J. Kirz, E. Lima, H. Miao, A.M. Neiman, and D. Sayre. Biological imaging by soft x-ray diffraction microscopy. *Proc. Nat. Acad. Sci. U.S.A.*, 102(43):15343–15346, OCT 2005.

[40] K. Giewekemeyer, P. Thibault, S. Kalbfleisch, A. Beerlink, C. Kewish, M. Dierolf, F. Pfeiffer, and T. Salditt. Quantitative biological imaging by ptychographic x-ray diffraction microscopy. *Proc. Nat. Acad. Sci. U.S.A.*, 107(2):529–534, Jan. 2010.

[41] X.J. Huang, J. Nelson, J. Kirz, E. Lima, S. Marchesini, H.J. Miao, A.M. Neiman, D. Shapiro, J. Steinbrener, A. Stewart, J.J. Turner, and C. Jacobsen. Soft x-ray diffraction microscopy of a frozen hydrated yeast cell. *Phys. Rev. Lett.*, 103(19):198101, NOV 6 2009.

[42] E. Lima, L. Wiegart, P. Pernot, M. Howells, J. Timmins, F. Zontone, and A. Madsen. Cryogenic x-ray diffraction microscopy for biological samples. *Phys. Rev. Lett.*, 103(19):198102, NOV 6 2009.

[43] Y. Nishino, Y. Takahashi, N. Imamoto, T. Ishikawa, and K. Maeshima. Three-dimensional visualization of a human chromosome using coherent x-ray diffraction. *Phys. Rev. Lett.*, 102(1):018101, JAN 9 2009.

[44] K Giewekemeyer, M Beckers, T Gorniak, M Grunze, T Salditt, and A Rosenhahn. Ptychographic coherent x-ray diffractive imaging in the water window. *Optics express*, 19(2):1037–1050, 2011.

[45] IA Vartanyants, JA Pitney, JL Libbert, and IK Robinson. Reconstruction of surface morphology from coherent x-ray reflectivity. *Physical Review B*, 55(19):13193, 1997.

[46] I.K. Robinson, I.A. Vartanyants, G.J. Williams, M.A. Pfeifer, and J.A. Pitney. Reconstruction of the shapes of gold nanocrystals using coherent x-ray diffraction. *Phys. Rev. Lett.*, 87(19):195505, NOV 5 2001.

[47] IK Robinson, JL Libbert, IA Vartanyants, JA Pitney, DM Smilgies, DL Abernathy, and G Grübel. Coherent x-ray diffraction imaging of silicon oxide growth. *Physical Review B*, 60(14):9965, 1999.

[48] I A Vartanyants and I K Robinson. Partial coherence effects on the imaging of small crystals using coherent x-ray diffraction. *Journal of Physics: Condensed Matter*, 13(47):10593, 2001.

[49] G.J. Williams, M.A. Pfeifer, I.A. Vartanyants, and I.K. Robinson. Three-dimensional imaging of microstructure in au nanocrystals. *Phys. Rev. Lett.*, 90(17):175501, MAY 2 2003.

[50] M.A. Pfeifer, G.J. Williams, I.A. Vartanyants, R. Harder, and I.K. Robinson. Three-dimensional mapping of a deformation field inside a nanocrystal. *Nature*, 442(7098):63–66, JUL 6 2006.

[51] J.C.H. Spence, U. Weierstall, and M. Howells. Coherence and sampling requirements for diffractive imaging. *Ultramicroscopy*, 101:149–152, NOV 2004.

[52] G.J. Williams, H.M. Quiney, A.G. Peele, and K.A. Nugent. Coherent diffractive imaging and partial coherence. *Phys. Rev. B*, 75(10):104102, MAR 2007.

[53] L.W. Whitehead, G.J. Williams, H.M. Quiney, D.J. Vine, R.A. Dilanian, S. Flewett, K.A. Nugent, A.G. Peele, E. Balaur, and I. McNulty. Diffractive imaging using partially coherent x rays. *Phys. Rev. Lett.*, 103(24):243902, December 2009.

[54] B. Abbey, L.W. Whitehead, H.M. Quiney, D.J. Vine, G. Cadenazzi, C.A. Henderson, K.A. Nugent, E. Balaur, C.T. Putkunz, A.G. Peele, G.J. Williams, and I. McNulty. Lensless imaging using broadband x-ray sources. *Nat. Phot.*, 5:420–424, 2011.

[55] K.A. Nugent, A.G. Peele, H.N. Chapman, and A.P. Mancuso. Unique phase recovery for nonperiodic objects. *Phys. Rev. Lett.*, 91(20):203902, NOV 2003.

[56] K.A. Nugent, A.G. Peele, H.M. Quiney, and H.N. Chapman. Diffraction with wavefront curvature: a path to unique phase recovery. *Acta Crystallogr. A*, 61:373–381, MAY 2005.

[57] H.M. Quiney, K.A. Nugent, and A.G. Peele. Iterative image reconstruction algorithms using wave-front intensity and phase variation. *Opt. Lett.*, 30(13):1638–1640, JUL 1 2005.

[58] H.M. Quiney, A.G. Peele, Z. Cai, and D. Nugent K.A. Paterson. Diffractive imaging of highly focused x-ray fields. *Nat. Phys.*, 2(2):101–104, FEB 2006.

[59] G.J. Williams, H.M. Quiney, B.B. Dhal, C.Q. Tran, K.A. Nugent, A.G. Peele, D. Paterson, and M.D. de Jonge. Fresnel coherent diffractive imaging. *Phys. Rev. Lett.*, 97(2):025506, JUL 2006.

[60] J.N. Clark, G.J. Williams, H.M. Quiney, L. Whitehead, M.D. de Jonge, E. Hanssen, M. Altissimo, K.A. Nugent, and A.G. Peele. Quantitative phase measurement in coherent diffraction imaging. *Opt. Express*, 16(5):3342, MAR 3 2008.

[61] J.N. Clark, C.T. Putkunz, M.A. Pfeifer, A.G. Peele, G.J. Williams, B. Chen, K.A. Nugent, C. Hall, W. Fullagar, S. Kim, and I. McNulty. Use of a complex constraint in coherent diffractive imaging. *Opt. Express*, 18(3):1981, MAR 3 2010.

[62] G.J. Williams, E. Hanssen, A.G. Peele, M.A. Pfeifer, J.N. Clark, B. Abbey, G.A. Cadenazzi, M.D. de Jonge, S. Vogt, L. Tilley, and K.A. Nugent. High-resolution x-ray imaging of plasmodium falciparum-infected red blood cells. *Cytom. Part A*, 73A(10):949–957, OCT 2008.

[63] W. Hoppe. Beugung im inhomogenen Primärstrahlwellenfeld. III. Amplituden- und Phasenbestimmung bei unperiodischen Objekten. *Acta Crystallographica Section A*, 25(4):508–514, Jul 1969.

[64] J.M. Rodenburg and R.H.T Bates. The theory of supperresolution electron-microscopy via wigner-distribution deconvolution. *Philos. Trans. R. Soc. London, Ser. A*, 339(1655):521–553, JUN 1992.

[65] P.D. Nellist, B.C. McCallum, and J.M. Rodenburg. Resolution beyond the 'information limit' in transmission electron-microscopy. *Nat. Lett.*, 374(6523):630–632, APR 1995.

[66] H.N. Chapman. Phase-retrieval x-ray microscopy by wigner-distribution deconvolution. *Ultramicroscopy*, 66:153–172, DEC 1996.

[67] J.M. Rodenburg and H.M.L Faulkner. A phase retrieval algorithm for shifting illumination. *App. Phys. Lett.*, 85(20):4795–4797, NOV 2004.

[68] Andrew M. Maiden and John M. Rodenburg. An improved ptychographical phase retrieval algorithm for diffractive imaging. *Ultramicroscopy*, 109(10):1256 – 1262, 2009.

[69] Cameron M. Kewish, Pierre Thibault, Martin Dierolf, Oliver Bunk, Andreas Menzel, Joan Vila-Comamala, Konstantins Jefimovs, and Franz Pfeiffer. Ptychographic characterization of the wavefield in the focus of reflective hard x-ray optics. *Ultramicroscopy*, 110(4):325–329, 2010.

[70] AJ D'Alfonso, AJ Morgan, AWC Yan, P Wang, H Sawada, AI Kirkland, and LJ Allen. Deterministic electron ptychography at atomic resolution. *Physical Review B*, 89(6):064101, 2014.

[71] O. Bunk, M. Dierolf, S. Kynde, I. Johnson, O. Marti, and F. Pfeiffer. Influence of the overlap parameter on the convergence of the ptychographical iterative engine. *Ultramicroscopy*, 108(5):481–487, APR 2008.

[72] F.B. de la Cuesta, M.P.E. Wenger, R.J. Bean, L. Bozec, M.A. Horton, and I.K. Robinson. Coherent x-ray diffraction from collagenous soft tissues. *Proc. Nat. Acad. Sci. U.S.A.*, 106(36):15297–15301, SEP 8 2009.

[73] A Schropp, R Hoppe, J Patommel, D Samberg, F Seiboth, S Stephan, G Wellenreuther, G Falkenberg, and CG Schroer. Hard x-ray scanning microscopy with coherent radiation: Beyond the resolution of conventional x-ray microscopes. *Applied Physics Letters*, 100(25):253112, 2012.

[74] C.T. Putkunz, A.J. D'Alfonso, A.J. Morgan, M. Weyland, C. Dwyer, L. Bourgeois, J. Etheridge, A. Roberts, R.E. Scholten, K.A. Nugent, and L.J. Allen.

Atom-scale ptychographic electron diffractive imaging of boron nitride cones. *Phys. Rev. Lett.*, 108:073901, Feb 2012.

[75] F. Hüe, J.M. Rodenburg, A.M. Maiden, and P.A. Midgley. Extended ptychography in the transmission electron microscope: Possibilities and limitations. *Ultramicroscopy*, 111(8):1117–1123, 2011.

[76] H.N. Chapman, A. Barty, S. Marchesini, A. Noy, S.R. Hau-Riege, C. Cui, M.R. Howells, R. Rosen, H. He, J.C.H. Spence, U. Weierstall, T. Beetz, C. Jacobsen, and D. Shapiro. High-resolution ab initio three-dimensional x-ray diffraction microscopy. *J. Opt. Soc. Am. A.*, 23(5):1179–1200, MAY 2006.

[77] D. Paganin. *Coherent X-Ray Optics*. Oxford University Press, 2006.

[78] A. Barty, S. Marchesini, H. N. Chapman, C. Cui, M. R. Howells, D. A. Shapiro, A. M. Minor, J. C. H. Spence, U. Weierstall, J. Ilavsky, A. Noy, S. P. Hau-Riege, A. B. Artyukhin, T. Baumann, T. Willey, J. Stolken, T. van Buuren, and J. H. Kinney. Three-dimensional coherent x-ray diffraction imaging of a ceramic nanofoam: Determination of structural deformation mechanisms. *Phys. Rev. Lett.*, 101:055501, Jul 2008.

[79] A.C. Kak and M. Slaney. *Principles of Computerized Tomographic Imaging*. Society for Industrial Mathematics, 1988.

[80] A Ravasio, D Gauthier, FRNC Maia, M Billon, JP Caumes, D Garzella, M Géléoc, O Gobert, Jean-François Hergott, AM Pena, et al. Single-shot diffractive imaging with a table-top femtosecond soft x-ray laser-harmonics source. *Physical review letters*, 103(2):028104, 2009.

[81] Eiji J Takahashi, Tsuneto Kanai, Kenichi L Ishikawa, Yasuo Nabekawa, and Katsumi Midorikawa. Coherent water window x ray by phase-matched high-order harmonic generation in neutral media. *Physical review letters*, 101(25):253901, 2008.

[82] Emily A Gibson, Ariel Paul, Nick Wagner, David Gaudiosi, Sterling Backus, Ivan P Christov, Andy Aquila, Eric M Gullikson, David T Attwood, Margaret M Murnane, et al. Coherent soft x-ray generation in the water window with quasi-phase matching. *Science*, 302(5642):95–98, 2003.

[83] M-C Chen, P Arpin, T Popmintchev, M Gerrity, B Zhang, M Seaberg, D Popmintchev, MM Murnane, and HC Kapteyn. Bright, coherent, ultrafast soft

x-ray harmonics spanning the water window from a tabletop light source. *Physical review letters*, 105(17):173901, 2010.

[84] Bo Chen, Ruben A Dilanian, Sven Teichmann, Brian Abbey, Andrew G Peele, Garth J Williams, Peter Hannaford, Lap Van Dao, Harry M Quiney, and Keith A Nugent. Multiple wavelength diffractive imaging. *PHYSICAL REVIEW A: atomic, molecular, and optical physics*, 79(2):23809, 2009.

[85] R. Neutze, R. Wouts, D. van der Spoel, E. Weckert, and J. Hajdu. Potential for biomolecular imaging with femtosecond x-ray pulses. *Nature*, 406(6797):752–757, AUG 2000.

[86] MJ Bogan, S Boutet, A Barty, WH Benner, M Frank, L Lomb, R Shoeman, D Starodub, Marvin M Seibert, SP Hau-Riege, et al. Single-shot femtosecond x-ray diffraction from randomly oriented ellipsoidal nanoparticles. *Physical Review Special Topics-Accelerators and Beams*, 13(9):094701, 2010.

[87] Russell Fung, Valentin Shneerson, Dilano K Saldin, and Abbas Ourmazd. Structure from fleeting illumination of faint spinning objects in flight. *Nature Physics*, 5(1):64–67, 2009.

[88] OM Yefanov and IA Vartanyants. Orientation determination in single-particle x-ray coherent diffraction imaging experiments. *Journal of Physics B: Atomic, Molecular and Optical Physics*, 46(16):164013, 2013.

[89] DK Saldin, VL Shneerson, R Fung, and A Ourmazd. Structure of isolated biomolecules obtained from ultrashort x-ray pulses: exploiting the symmetry of random orientations. *Journal of Physics: Condensed Matter*, 21(13):134014, 2009.

[90] AP Mancuso, A Schropp, B Reime, L-M Stadler, A Singer, J Gulden, S Streit-Nierobisch, C Gutt, G Grübel, J Feldhaus, et al. Coherent-pulse 2d crystallography using a free-electron laser x-ray source. *Physical review letters*, 102(3):035502, 2009.

[91] K.A. Nugent. Coherent methods in the x-ray sciences. *Adv. Phys.*, 59(1):1–99, 2010.

[92] H.M. Quiney. Coherent diffractive imaging using short wavelength light sources - a tutorial review. *J. Mod. Optics*, 57(13):1109–1149, 2010.

[93] J.D. Jackson. *Classical Electrodynamics*. John Wiley and Sons, 3 edition, 1999.

[94] Jens Als-Nielsen and Des McMorrow. *Elements of modern X-ray physics*. John Wiley & Sons, 2011.

[95] Leonard Mandel and Emil Wolf. *Optical coherence and quantum optics*. Cambridge university press, 1995.

[96] C. Q. Tran, A. G. Peele, A. Roberts, K. A. Nugent, D. Paterson, and I. McNulty. Synchrotron beam coherence: a spatially resolved measurement. *Opt. Lett.*, 30(2):204–206, Jan 2005.

[97] C.Q. Tran and K.A. Nugent. Recovering the complete coherence function of a generalized schell model field. *Opt. Lett.*, 31(22):3226–3227, NOV 2006.

[98] A Starikov and E Wolf. Coherent-mode representation of gaussian schell-model sources and of their radiation fields. *JOSA*, 72(7):923–928, 1982.

[99] A. Thompson, D. Attwood, E. Gullikson, M. Howells, K.J. Kim, J. Kirz, J. Kortright, I. Lindau, P. Pianetta, A. Robinson, J. Scofield, J. Underwood, D. Vaughan, G. Williams, and H. Winick. *X-ray data booklet*, chapter Characteristics of synchrotron radiation. Lawrence Berkeley National Laboratory, 2001.

[100] P. Kirkpatrick and A.V. Baez. Formation of optical images by x-rays. *Journal of the Optical Society of America*, 38:766–771, 1948.

[101] P. Kirkpatrick. X-ray images by refractive focussing. *Journal of the Optical Society of America*, 39:796–796, 1949.

[102] Olivier Hignette, Peter Cloetens, Gérard Rostaing, P Bernard, and Ch Morawe. Efficient sub 100nm focusing of hard x rays. *Review of scientific instruments*, 76(6):063709, 2005.

[103] D. Paganin, T.E. Gureyev, S.C. Mayo, A.W. Stevenson, Y.I. Nesterets, and S.W. Wilkins. X-ray omni microscopy. *J. Microsc.*, 214:315–327, JUN 2004.

[104] Xradia Inc. www.xradia.com, 2009.

[105] Ugo Fano. Ionization yield of radiations. ii. the fluctuations of the number of ions. *Physical Review*, 72(1):26, 1947.

[106] C.E. Shannon. Communication in the presence of noise. *Proc. Inst. Radio Engrs.*, 37(1):10, 1949.

[107] Heinz H Bauschke and Jonathan M Borwein. On projection algorithms for solving convex feasibility problems. *SIAM review*, 38(3):367–426, 1996.

[108] V. Elser. Phase retrieval by iterated projections. *J. Opt. Soc. Am. A*, 20(1):40–55, JAN 2003.

[109] Veit Elser, I Rankenburg, and P Thibault. Searching with iterated maps. *Proceedings of the National Academy of Sciences*, 104(2):418–423, 2007.

[110] M. Dierolf, P. Thibault, A. Menzel, C.M. Kewish, K. Jefimovs, I. Schlichting, K. Von Konig, O. Bunk, and F. Pfeiffer. Ptychographic coherent diffractive imaging of weakly scattering specimens. *New J. Phys.*, 12:035017, 31 2010.

[111] MJ Humphry, B Kraus, AC Hurst, AM Maiden, and JM Rodenburg. Ptychographic electron microscopy using high-angle dark-field scattering for sub-nanometre resolution imaging. *Nature communications*, 3:730, 2012.

[112] Joanne Marrison, Lotta Räty, Poppy Marriott, and Peter O'Toole. Ptychography-a label free, high-contrast imaging technique for live cells using quantitative phase information. *Scientific reports*, 3, 2013.

[113] L.W. Whitehead, G.J. Williams, H.M. Quiney, K.A. Nugent, A.G. Peele, D. Paterson, M.D. de Jonge, and I. McNulty. Fresnel diffractive imaging: Experimental study of coherence and curvature. *Phys. Rev. B*, 77(10):104112, Mar 2008.

[114] C.T. Putkunz, J.N. Clark, D.J. Vine, G.J. Williams, M.A. Pfeifer, E. Balaur, I. McNulty, K.A. Nugent, and A.G. Peele. Phase-diverse coherent diffractive imaging: High sensitivity with low dose. *Phys. Rev. Lett.*, 106(1):013903, Jan 2011.

[115] B. Abbey, K.A. Nugent, G.J. Williams, J.N. Clark, A.G. Peele, M.A. Pfeifer, M. De Jonge, and I. McNulty. Keyhole coherent diffractive imaging. *Nat. Phys.*, 4(5):394–398, MAY 2008.

[116] I. McNulty, A. Khounsary, Y.P. Feng, Y. Qian, J. Barraza, C. Benson, and D. Shu. A beamline for 1-4 kev microscopy and coherence experiments at the advanced photon source. *Rev. Sci. Instrum.*, 67:3372, 1996.

[117] D.J. Vine, G.J. Williams, J.N. Clark, C.T. Putkunz, M.A. Pfeifer, D. Legnini, C. Roehrig, E. Wrobel, E. Huwald, G. van Riessen, B. Abbey, T. Beetz, J. Irwin, M. Feser, B. Hornberger, I. McNulty, K.A. Nugent, and A.G. Peele. An

in-vacuum x-ray diffraction microscope for use in the 0.7-2.9 kev range. *Rev. Sci. Instrum.*, Accepted 8th Feb, 2012.

[118] D.J. Vine, G.J. Williams, B. Abbey, M.A. Pfeifer, J.N. Clark, M.D. de Jonge, I. McNulty, A.G. Peele, and K.A. Nugent. Ptychographic fresnel coherent diffractive imaging. *Phys. Rev. A*, 80(6):063823, DEC 2009.

[119] C.T. Putkunz, M.A. Pfeifer, A.G. Peele, G.J. Williams, H.M. Quiney, B. Abbey, K.A. Nugent, and I. McNulty. Fresnel coherent diffraction tomography. *Opt. Express*, 18(11):11746–11753, 2010.

[120] Burton L Henke, Eric M Gullikson, and John C Davis. X-ray interactions: Photoabsorption, scattering, transmission, and reflection at E = 50-30,000 eV, Z= 1-92. *Atomic data and nuclear data tables*, 54(2):181–342, 1993.

[121] P. Thibault, M. Dierolf, O. Bunk, A. Menzel, and F. Pfeiffer. Probe retrieval in ptychographic coherent diffractive imaging. *Ultramicroscopy*, 109(4):338–343, MAR 2009.

[122] Tom Kupp, Basil Blank, Alex Deyhim, Curtis Benson, Ian Robinson, and Paul Fuoss. Development of a double crystal monochromator. In *Synchrotron Radiation Instrumentation*, volume 705, pages 651–654, 2004.

[123] DJ Batey, TB Edo, C Rau, U Wagner, ZD Pešić, TA Waigh, and JM Rodenburg. Reciprocal-space up-sampling from real-space oversampling in x-ray ptychography. *Physical Review A*, 89(4):043812, 2014.

[124] M. Guizar-Sicairos and J.R. Fienup. Phase retrieval with transverse translation diversity: a nonlinear optimization approach. *Opt. Express*, 16(10):7264–7278, MAY 2008.

[125] Fucai Zhang, Isaac Peterson, Joan Vila-Comamala, Ana Diaz, Felisa Berenguer, Richard Bean, Bo Chen, Andreas Menzel, Ian K. Robinson, and John M. Rodenburg. Translation position determination in ptychographic coherent diffraction imaging. *Opt. Express*, 21(11):13592–13606, Jun 2013.

[126] A.M. Maiden, M.J. Humphry, M.C. Sarahan, B. Kraus, and J.M. Rodenburg. An annealing algorithm to correct positioning errors in ptychography. *Ultramicroscopy*, 120(0):64 – 72, 2012.

[127] J.N. Clark and A.G. Peele. Simultaneous sample and spatial coherence characterisation using diffractive imaging. *App. Phys. Lett.*, 99:154103, 2011.

[128] V. Kohn, I. Snigireva, and A. Snigirev. Direct measurement of transverse coherence length of hard x rays from interference fringes. *Phys. Rev. Lett.*, 85:2745–2748, Sep 2000.

[129] JJA Lin, David Paterson, Andrew Gareth Peele, PJ McMahon, CT Chantler, Keith A Nugent, B Lai, N Moldovan, Z Cai, DC Mancini, et al. Measurement of the spatial coherence function of undulator radiation using a phase mask. *Physical review letters*, 90(7):60, 2003.

[130] Kaye S. Morgan, Sarah C. Irvine, Yoshio Suzuki, Kentaro Uesugi, Akihisa Takeuchi, David M. Paganin, and Karen K.W. Siu. Measurement of hard x-ray coherence in the presence of a rotating random-phase-screen diffuser. *Optics Communications*, 283(2):216 – 225, 2010.

[131] D. Paterson, B.E. Allman, P.J. McMahon, J. Lin, N. Moldovan, K.A. Nugent, I. McNulty, C.T. Chantler, C.C. Retsch, T.H.K. Irving, and D.C. Mancini. Spatial coherence measurement of x-ray undulator radiation. *Opt. Commun.*, 195:79–84, AUG 1 2001.

[132] I. A. Vartanyants, A. Singer, A. P. Mancuso, O. M. Yefanov, A. Sakdinawat, Y. Liu, E. Bang, G. J. Williams, G. Cadenazzi, B. Abbey, H. Sinn, D. Attwood, K. A. Nugent, E. Weckert, T. Wang, D. Zhu, B. Wu, C. Graves, A. Scherz, J. J. Turner, W. F. Schlotter, M. Messerschmidt, J. Lüning, Y. Acremann, P. Heimann, D. C. Mancini, V. Joshi, J. Krzywinski, R. Soufli, M. Fernandez-Perea, S. Hau-Riege, A. G. Peele, Y. Feng, O. Krupin, S. Moeller, and W. Wurth. Coherence properties of individual femtosecond pulses of an x-ray free-electron laser. *Phys. Rev. Lett.*, 107:144801, Sep 2011.